Brunel University

Magnetic DNA Detection sensor for Point-of-care Diagnostics

Doctor of Philosophy (PhD) Thesis

Sara Chaychian

Supervisor: Professor W. Balachandran

Brunel University

School of Engineering and Design

August, 2014

ABSTRACT

This thesis focuses on inductive base sensor design at MHz range frequency. The background theory, design, experiments and results for a new magnetic particles sensor is presented.

A new magnetic sensor based on a planar coil was investigated for DNA pathogen detection. Change in inductance of the planar coil due to the presence of magnetic particles with varying mass was measured. The experimental set-up consisted of different sized planar coil with associated electronics for inductance measurements. The best sensor performance was accomplished using two different inductors while oscillating at frequencies 2.4MHz using 9.5μH inductor and 7.2MHz with 85μH inductor. The sensor has very large signal to noise ratio (580×10^3), while the average amount of frequency drift was 0.58.

This sensor was tested with various types of magnetic particles. In addition, iron-oxide nanoparticles were synthesized through water in oil microemulsion method and with an average size of 25nm. The best sensitivity achieved for detection of 50μg iron-oxide particles was with the bead size of 10nm. 81Hz frequency shift was attained in regard to that amount of particles.

This research shows that increasing the resonance frequency to 7.2MHz can cause the larger output signal difference (frequency shift) in the presence of magnetic particles; however, the sensor stability is the most important factor for determining the detection resolution and sensitivity.

The sensitivity is better if the sensor can detect smaller amount of magnetic sample. The results of this research demonstrate that while the sample consists of smaller size particles, the sensor can detect the lower amount of sample. This is due to the heating effect of nanoparticles. On the other hand the sample distance from the sensor has a major impact on the sensitivity too; the shorter the distance, the higher the sensitivity.

This technique can potentially be extended to detect several different types of bacterial pathogens and can be modified for multiplex quantitative detection. This sensing technique will be incorporated into a handheld, disposable microfluidic chip for point-of-care diagnostics for sexually transmitted diseases.

Key words: Point of care diagnostics, Magnetic particle Detection, Molecular detection, Inductive sensing

CONTENTS

LIST OF TABLES

LIST OF FIGURES

ACKNOWLEDGEMENT

This thesis would not have been completed without help and support I received from a number of people inside and outside the School of Engineering and Design.

I would like to thank my first supervisor, Professor Wamadeva Balachandran, for his support and continued guidance throughout my PhD research. He has done a great part on keeping my focus on the primary target, and I have genuinely enjoyed our many hours of scientific discussion.

I would like to thank Professor Chris Hudson for his valued technical discussions, which have always been helpful to me. He has known the answers to the trickiest questions.

I also like to thank Brunel DocLab group and in particular, my valuable friends and colleagues , Dr. Ruth Mackay and Dr Nada Manivannan, for their never ending support and help during my research.

Finally, Special thanks to my family, who have always supported and encouraged me and stood by me during all parts of this Ph.D. work.

DECLARATION

I declare that no part of the work referred to in this thesis has been submitted in support of an application for another degree or qualification in this or any other university or other institution of learning.

CHAPTER 1: **GENERAL INTRODUCTION**

1.1 Microbial diagnosis strategies

Existing technologies for diagnosing infectious diseases require culturing bacteria in a lab and for both bacterial and viral types of infections, the molecular method of polymerase chain reaction (PCR) is currently widely used [1, 2]. The process of culturing involves high quality equipment with expensive software, and the analysis time normally takes days, which is considered very long in clinical contexts, delaying the initiation of treatment. All of these are drawbacks of culturing method which make it difficult for miniaturization and integration into a portable system [2]. Conversely, the PCR is robust, sensitive and quick, but it is expensive and its sensitivity to contamination can slow it down or stop the process [3-4]. Therefore there is a need for fast, portable, accurate and sensitive pathogen detection method that can give a diagnosis within few hours.

The common way of diagnosing diseases is immunoassays. This technique is based on the detection of specific antibodies bound to antigens in the analyte. Labels such as enzyme and fluorescent are conjugated with either antibody or its antigen and used to detect the protein molecule. This method is fast and reliable, but in the case of specificity and sensitivity there is still room for improvement while using the real sample [5].

Another detection technique is based on using DNA sequence information, which can lead to more accurate analysis. DNA is a double-stranded molecule wherein the strands run in opposite directions; hence DNA is a polarized molecule. The backbone structure of DNA is the sugar/phosphate components of the nucleotides. The nucleotide attaches to the anti-parallel nucleotide via hydrogen bonds between the two bases (A to T and C to G). Adenine and guanine are the most electro-active nucleobases of DNA and they can easily oxidize on carbon electrodes. The sequence of these nucleobases along the backbone encodes information, which is known as the genetic code. As DNA carries the genetic code it can be useful to detect infectious diseases caused by viruses or bacteria by means of identifying specific sequences unique to the target organism; this diagnostic approach is called molecular detection [6-9], which is more sensitive and specific when compared to traditional microbiological methods.

According to the Watson-Crick base pairing rule; the double helix structure of DNA is formed by hybridization of two complementary single strands of DNA (ssDNA). By breaking hydrogen bonds between the two nucleobases under high pressure or temperature, double-stranded DNA is denatured and separated, therefore two ssDNA are produced. The study of DNA hybridization

chemistry led to the emergence of probe technology and PCR technique, of which the latter is the method of DNA amplification and quantification based on thermal cycling. As mentioned earlier, one of the most useful applications of PCR is in diagnoses of diseases by detecting infection agents and the ability to separate pathogenic strains from non-pathogenic ones. This method is very sensitive; however it involves time-consuming processes with expensive equipment and requires a high level of expertise to operate the equipment [2].

Therefore, there is a great demand for rapid and sensitive pathogen detection is for point-of-care diagnostics [11, 1-3]. Molecular DNA diagnostic or nucleic acid testing (NAT) is much faster, more accurate and specific compare to the aforementioned diagnostic methods. Some specific types of pathogens (such as culture-negative pathogens) that cannot be detected by other culturing methods can be identified with molecular detection [12]. This technique can also provide quantitative detection with access to genomic information, which was inaccessible previously, and it shows the highest sensitivity and specificity of all detection methods (Figure 1.1).

Land et al [10] represented the technical development trends of detecting Chlamydia trachomatis disease from cell culture to NAT. They compared the available methods of detection in terms of sensitivity and specificity and summarized the mostly used commercial tests for C. trachomatis detection (Figure 1.1). As illustrated in Figure 1.1, only the cell culture method has 100% specificity, which means definite proof of the disease, but it is expensive and lacks sensitivity comparing to the NAT tests. In terms of sensitivity and detection limit, NAT is clearly preferable. One of the other detection assays is point of care (POC) testing, which is the fastest method available (30-minute detection time). This technique does not require complex equipment and it is not expensive or laborious. However it is mostly based on the enzyme-immunoassay (EIA), which results in low sensitivity and specificity output [10].

Test	Sensitivity (%)	Specificity (%)	Detection limit (no. of organisms)
NAAT[a]	90–95	>99	1–10
DFA[b]	80–85	>99	10–500
EIA[c]	60–85	99	500–1000
DNA-probe[d]	75–85	>99	500–1000
Cell culture	50–85	100	5–100
POC[e]	25–55	>90	>10 000

[a]Nucleic Acid Amplification Test. DNA-based: PCR Amplicor assay (Roche Diagnostics, Basel, Switzerland), LCR (Abbott Laboratories, Abbott Park, IL, USA), currently the Abbott m2000rt; SDA (Becton Dickinson, Franklin Lakes, NJ, USA), currently BD ProbeTec. RNA-based: TMA, AMP-CT (Gen-Probe, San Diego, CA, USA), current system from Gen-Probe is named TIGRIS; NASBA (Organon Teknika, Boxtel, the Netherlands, currently BioMerieux, Marcy l'Etoile, France).
[b]Direct Fluorescence Assay. Syva MicroTrak (Syva Co, Palo Alto, CA, USA).
[c]Enzyme Immuno Assay. Vidas (BioMérieux, Craponne, France).
[d]DNA-based: hybrid capture assay (Qiagen, Hilden, Germany), Ampliprobe system (ImClone Systems, New York City, NY, USA); RNA-based: PACE 2 assay (Gen-Probe, San Diego, CA, USA).
[e]Point of care test. Handilab-C (Zonda Incorporated, Dallas, TX, USA), Biorapid Chlamydia Ag test (Biokit, Barcelona, Spain), QuickVue Chlamydia test (Quidel Corporation, San Diego, CA, USA).

Figure 1.1: Sensitivities and specificities of C. trachomatis detection methods [10]

The integration of molecular diagnostic techniques instead of immunoassay provides a promising solution for POC diagnostic. Also, using microfluidic technologies alongside POC method can offer obvious advantages because of the ability to handle small sample sizes and saving valuable reagents used in the assays. Many microfluidics systems are integrated with sensing modules or sample-pre-treatment modules, which increase the efficiency of the assays and reduce cross contamination. These diagnostic devices attract enormous interest in order to automate genetic tests on an integrated microchip via molecular detection [2-3, 13]. These devices are intended for use in the detection of sexually transmitted diseases (STDs) among the key target population of young adults.

1.2 Point of care diagnostic and lab on a chip

Point of care testing (POCT) is becoming a preferred strategy over standard clinical testing for diagnosis of infectious and genetic diseases. Miniaturization of laboratory protocols and sensors integration can lead to reduced time of diagnosis, cost reduction and smaller-sized disposable devices with low reagent consumption and better process control. The patient outcome in emergency settings can improve by rapid and early treatment due to the short time of diagnosis [14]. Development of microelectromechanical systems (MEMS) helps this system to fabricate complicated mechanical and electronic components at the micro-scale within a single device.

Lab-on-a-chip (LOAC) technology has also developed during the past decade through shrinking the laboratory processes and techniques into an automated integrated microchip (Figure 1.2) [15]. This kind of automation can reduce the human error and the risk of sample contamination during the test.

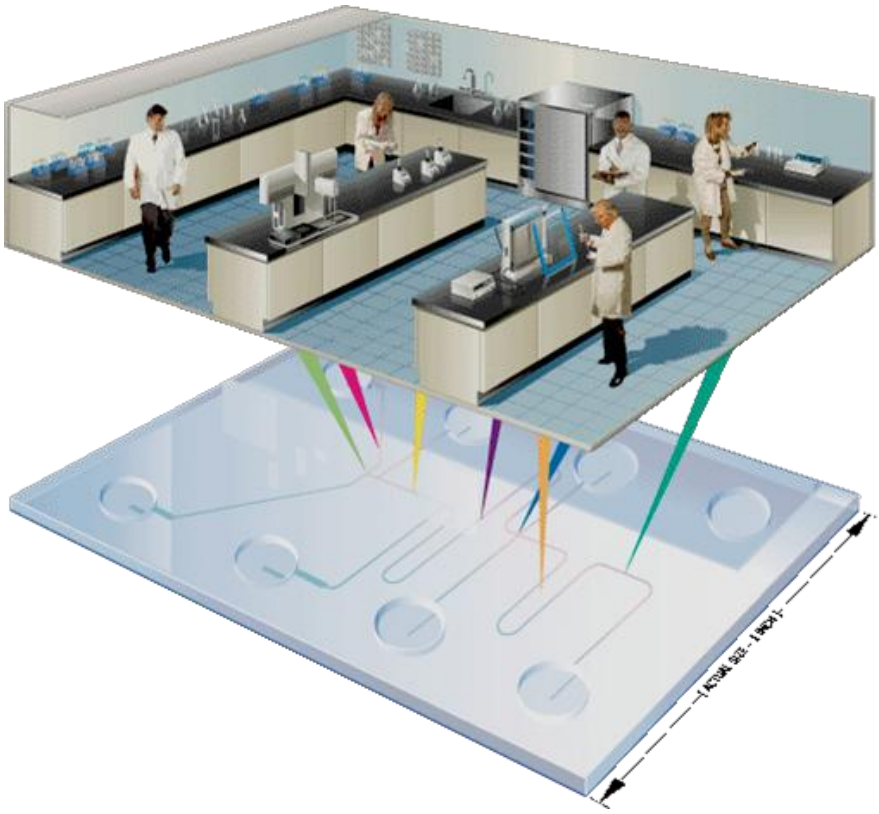

Figure 1.2: Miniaturization of the conventional laboratory to a lab-on-a-chip device [16]

LOAC diagnostics have developed quickly and are accelerating towards a "sample-in answer-out" platform for molecular diagnostics. A number of reviews have investigated the possibility of LOAC technology usage in areas such as, personalized medicine, clinical diagnostics and global health [11, 13, 17-18]. In Sub-Saharan Africa, point of care testing is becoming generally accessible as a cutting-edge testing strategy where access to laboratory services is restricted. For instance, HIV diagnostics and sexually transmitted diseases have been identified by the World Health Organisation as critical areas requiring POCT advancement to expand access to treatment [19].

The aim of this project is to develop a portable, handheld device capable of accepting a raw sample and providing disease specific diagnosis within a few minutes. This study is part of the DOC Lab research project which is based at Brunel University and is part of the esti2 consortium [http://www.esti2.org.uk]. The sample will be analysed using LOAC technologies such as molecular diagnostics. This project is seeking to achieve multiple pathogen detection with rapid results (in less than 30 minutes). The long-term vision is to incorporate this microchip with a mobile phone to provide a self-testing device (Figure 1.3).

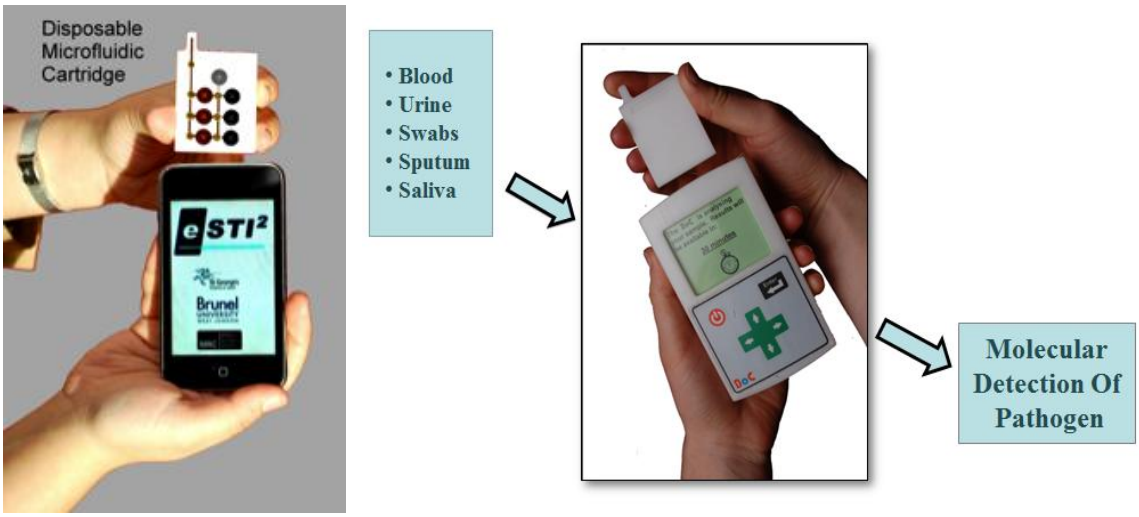

Figure 1.3: A small microfluidic chip which can interface with a wireless communication device Source: [http://bruneldoclab.com/]

The modular system overview is illustrated in Figure 1.4. Here the sample is injected into the disposable cartridge from sample collection device and after mixing with specific reagents it is directed to the lysis section for extraction of the particular DNA. Because the amount of extracted DNA is insufficient for high sensitivity detection, amplification is needed to increase the concentration of DNA. All of these actions are controlled by the electronic and control system designed for this purposes. Ultimately, the results can be sent (e.g. online) to the doctor or patient.

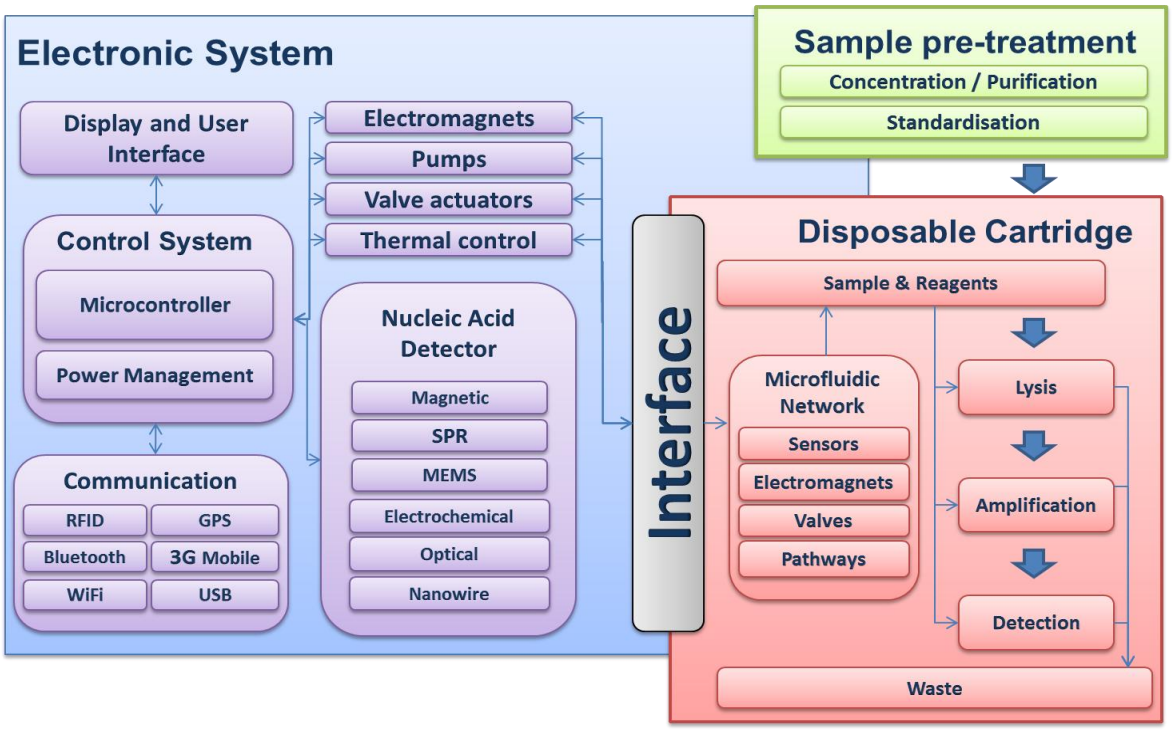

Figure 1.4: Modular system overview

1.3 LOAC procedures

An overview of the LAOC procedure is outlined in Figure 1.5 from sample input to results, starting with sample collection and preparation, extraction, amplification and then detection methods, the latter of which is the chief concern of this research.

The first step of LOAC system is sample collection and processing, which must incorporate a simple and easy procedure for all patients. Sample collection and processing is based on macro/microfluidic devices because of their potential for complex fluidic handling. Samples could be invasive (e.g. swabs or blood samples) or non-invasive (saliva, urine or stool) depending on the type and volume of sample required (from 25µl to 4ml).

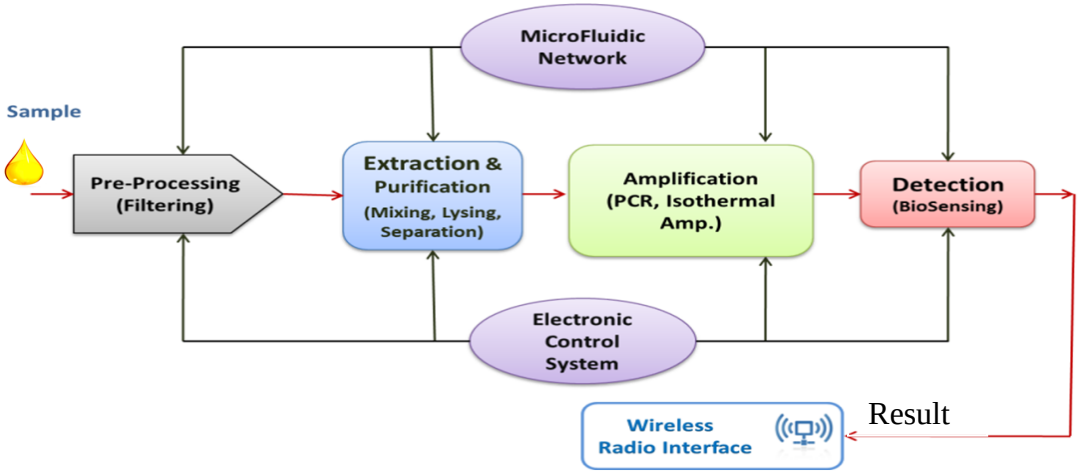

Figure 1.5 Overview of LOAC processes from sample to answer

The sample processing via microfluidic devices is the critical stage in point of care NAT devices. For achieving the required sensitivity and accurate analysis, the DNA must be isolated prior to the detection and amplification. These functions are carried on at the extraction and purification section through mixing the sample with specific reagents (based on the type of the extraction). There are different extraction methods available such as using membrane filters or silica based surface interaction affinity [41].

After nucleic acid isolation, there is an amplification step which can increase the concentration of the purified DNA molecule to achieve the desirable level before the detection stage. The common methods of amplification are PCR and isothermal methods. The exiting method for amplification is reviewed in [12].

The next and final step is detection. Detection of bio-molecular interaction in medical and biosensor research is of fundamental importance. These biosensors are used in different types of application such as: public health, clinical and environmental analysis [11, 13, 17-18]. High

sensitivity, specificity and short processing time are the most important characteristics of DNA biosensors. The DNA detection technique is based on immobilizing a specific single strand DNA (probe) on the sensor surface and then introducing the amplified sample containing the complementary target DNA, which results in hybridization. Then the signal generated from the hybridization action needs to be detected by the biosensor. In the following section three major types of detection methods are introduced: optical sensing, electrochemical detection and magnetic detection (a more thorough review of literature pertaining to magnetic detection is presented in chapter 2).

1.4 Bio-sensing techniques

A tremendous amount of research and development has been made in both parts of biosensor technology, particularly in terms of transduction devices or signal transduction and biological recognition elements or detection technique.

Due to the negative charge of the DNA, it is an outstanding option for signal transduction. Currently, most DNA specific-sequence detection methods implement affinity-based sensing, such as hybridization of ssDNA with a complementary molecule that can be peptide-nucleic acid or other base-pairing molecules [2,20-21]. The flexibility of the DNA and the nano-scale size of the DNA double helix (about 2nm diameters with the persistence length of about 50nm ≈150 base pair) make them an attractive subject for pathogen detection for point of care systems [20-22].

The signal transducer determines the sensitivity of the diagnostic technique; it converts the sequence-specific recognition event to a quantitatively measurable signal. This signal can be electrical (resistance, current or voltage change), optical (fluorescent, colorimetric, luminescent, etc.) or electrochemical (by changing one of the parameters in a chemical solution). Overall, the sensitive transduction method and the high efficiency of biochemical reactions are the factors which determine the performance of a pathogen sensor.

The general detection of biological targets can be divided into two categories; label-free detection and detection with markers. In both methods there is a target molecule that should hybridize with a probe molecule. This hybridization event generates a signal measured-by-signal transducer. In detection with markers, the target molecule is labelled with special micro or nanoparticles (depending on the sensing system). Although adding a label needs an additional step, because labels can be easily distinguished from other materials in the sample, a larger output signal is obtained with lower noise. In the label-free method, hybridization event is detected directly without any labels attached to the target molecules and the signal is generated by changing the mass or charge of

those molecules. For example, surface plasmon resonance (SPR) is one of the most common methods in label free detection, which detects the presence of a hybridization or binding event by changing the concentration of biomolecules [24, 25]. Field effect transistor (FET) sensors and acoustic technologies like quartz crystal microbalance (QCM) [26] are other types of sensing techniques used for label-free pathogen detection.

With advances in nanostructure materials, a group of researchers at the University of Southern California studied the effect of different parameters on performance of nanowire-based FET biosensors for label-free pathogen detection [2]. Besides all the advantages of label-free detection methods, the sample preparation, sensor cost and multiplex detection is quite challenging. Also, because there is no label added to the sample, signals generated from single-strand and hybridized DNA is inherently the same, which causes more complexity in detection processes.

To improve the performance of the detection techniques and achieve rapid, sensitive, accurate results and multiplex pathogen detection, using nanostructures sounds promising. Combining nanotechnology with clinical detection opens new avenues for ultra sensitive and early detection. Their unique chemical and physical properties make them attractive for clinical diagnostics. The small size enables detection of very small volume samples and diagnosis within a single cell and at the molecular level. Table 1.1 shows a summary of most useful nanoparticles for pathogen detection and their applications, such as superparamagnetic nanoparticles, quantum dots (QD) and gold nanoparticles (Au), which are currently the most useful and successful structures [27-29].

Table 1.1: Nanoparticles for pathogen detection

Nanoparticle	Application
Quantum dots [QD]	Immunoassays, optical detection
Nanowire	Optical & electrical detection
Carbon nanotube	Nucleic acid detection
Magnetic beads	Immunoassays & nucleic acid detection
Gold nanoparticle	Immunoassays & nucleic acid detection
Silver nanoparticle	Ramman scattering method [SERS]

Nanoparticles can be attached to the biomolecules as a label and make the detection easier. Optical, electrochemical and magnetic biosensors are currently the most widely used methods for detecting biomolecules.

Over the last decade, several optical biosensor platforms have been developed for pathogen detection. They became popular and attractive because there was no direct contact between the detector and the sample analyte for light measurement, therefore thousands of samples can be analysed within one experiment. For instance, microarray scanners, ELISA readers and spectrophotometric devices used for protein, enzymatic and DNA analysis are all based on optical detection [30]. They are created for both label-free (direct detection such as surface plasmon resonance) and indirect detection (with labelled molecule). A measurable optical signal based on the concentration of target analyte is produced after interaction between the analyte and biomolecule, This signal can be colorimetric, fluorescent or luminescent.

Colorimetric biosensors are widely deployed because of their cost-effective system and easy measurement set-up **[**31]. Comparing fluorescent and luminescent biosensors, the latter have faster and more sensitive detection whilst the former have more rapid light emission and low thermal loss [31]. Fluorescence sensing is based on the excitation of electrons at a particular wavelength from their ground state to an excited singlet state and they can be used *in vivo* or *in vitro* (including exogenous fluorescence element). Typically in fluorescent labelling method a small molecule of protein is used and therefore quantification of protein is necessary. In the method based on fluorescence molecular probe [31], whereby fluorescence dye is attached to one end of ssDNA and fluorescence quencher to the other end, photo bleaching steps are needed, which are not stable over time. On the other hand, chemical property and photo physical characteristics of the protein-based fluorophores and organic dye add additional limitations to such biosensors [30, 31, 32]. The ability to detect molecular interaction based on different optical methods has been tested [30] and compared with the conventional culturing method. Experiments demonstrated that although these methods can be fast with low cost, their lack of sensitivity is still an issue, and culturing methods remain more specific and sensitive. As a result, optical detection does not seem to be the optimal solution for point of care NAT system, due to the aforementioned concerns and also problems with portability and mass production [1].

Compared to optical sensors, electrochemical biosensors are more suited for point of care diagnostics due to the elimination of light in the signal transducer and because electrochemical reaction can produce an electrical signal directly [33]. Therefore there is no need for expensive and bulky transduction instrument, which can promise a better level of integration [33]. DNA-based electrochemical biosensors comprise the combination of nucleic acid layer with electrochemical transducer. In these sensors, probe DNA can be immobilized on a range of electrode substrates, such as gold or carbon substrate, immersed in an electrolyte. This means detection can be achieved with low-cost electrochemical analyser. After hybridization of ssDNA onto the probes, electronic

activity caused by redox reaction of DNA bases, will be measured. There are different principles available for electrochemical detection. One of the most common ways is by having fixed voltage across the two working electrodes and then monitor the output current for a direct measurement of analyte concentration changes as a result of electron-transfer reactions (amperometric method [34]). It should be noted that other methods are available, such as voltammetric, conductometric and FET-based methods. Several reviews and designs of these methods have been published [33-35], these sensors can also be integrated and miniaturized within microfluidic devices [36], but optical detection method is still more sensitive than electrochemical method [4].

In recent years researchers have discovered applications for using magnetic beads in clinical detection. Magnetic beads are an important source of labels for clinical diagnosis. The use of these labels provides advantages such as long-term stability, easy miniaturization and elimination of interference effects and noise from the sample background.

A volume-amplified magnetic nano-bead detection assay (VAM-NDA) has been used for detecting bacterial DNA in a clinical analyte in a substrate-free method [39, 1]. This molecular detection and amplification method is able to detect few numbers of *Escherichia coli* bacteria. The detection strategy is based on Brownian relaxation sensors and a superconducting quantum interference device (SQUID) magnetometer and is used for measuring the hydrodynamic volume of the magnetic beads, which are increased after binding of the DNA probe to oligonucleotide-functionalized magnetic beads. Although this technique has long processing times and requires trained personnel, it could also be automated by replacing the current detection method with magnetic field sensor [1].

As mentioned previously, current nucleic acid detection technologies include three core parts; sample preparation, amplification and detection [20]. Table 1.2 shows some examples of commercially available or close to market POC NAT platforms. In the majority of these platforms, real-time fluorescence detection is used beside PCR amplification (Table 1.2), which requires complex and pricey instrumentation. Magnetic detection can be the preferred method for use in this field due to easy miniaturization, low cost, long-term stability and no interference from background samples.

Table 1.2: Commercially available POC NAT platforms [20]

Platform	Manufacturer	Sample prep included?	Amplification	Detection	Time to result (min)[a]	Website
GeneXpert	Cepheid	Y	PCR	RTF	<120	www.cepheid.com
Liat Analyzer	IQuum	Y	PCR	RTF	<60	www.iquum.com
MDx	Biocartis	Y	PCR	RTF	Unknown	www.biocartis.com
FL/ML	Enigma	Y	PCR	RTF	<45	www.enigmadiagnostics.com
FilmArray	Idaho technologies	Y	PCR	RTF	60	www.idahotech.com
Razor	Idaho technologies	N	PCR	RTF	<60	www.idahotech.com
R.A.P.I.D.	Idaho technologies	N	PCR	RTF	<30	www.idahotech.com
LA-200	Eiken	N	Isothermal (LAMP)	RTT	< 60	www.eiken.co.jp
Twista	TwistDX	N	Isothermal (RPA)	RTF	< 20	www.twistdx.co.uk
BART	Lumora	N	Isothermal (LAMP)	RTB	< 60	lumora.co.uk/
Genie II	Optigene	N	Isothermal (LAMP)	RTF	< 20	www.optigene.co.uk
SAMBA	Diagnostics for the Real World	N	Isothermal (similar to NASBA)	NALF	> 60	Not available
BESt Cassette[b]	BioHelix/ Ustar Biotech	N	Not included, but typically isothermal	NALF	N/A	www.biohelix.com; www.bioustar.com

Abbreviations: RTB real-time bioluminescence; RTF real-time fluorescence; RTT real-time turbidimetry; NALF nucleic acid lateral flow

1.5 Motivation and research objectives

The main objective in this research is to investigate and develop a magnetic detection sensor with high sensitivity and reliability, which is able to detect the presence of magnetic particles attached to DNA molecules. The idea of using magnetic particles as a DNA label in this research requires a magnetic field sensor strong enough to sense 10^6-10^7 number of magnetic nanoparticles (there are large numbers of DNA in 25µL of biological sample). Considering mass production and a self-testing device, the sensor should be fabricated in very small size with the lowest price and fast response [short detection time < 5 min] overcoming the conventional detection methods wherein the detection analysis could have taken hours or days [2]. In order to design an optimised magnetic detection sensor, most of the available literature has been reviewed (the review is presented in chapter 2).

A wide variety of sensors have been already employed for magnetic label detection in which many of them take advantage of the magneto-resistive materials to fabricate their sensor. These sensors have been designed with different specification based on their application and mostly fabricated by CMOS technology [40]. For instance Micro Magnetics Company has designed a magnetic field micro-sensor [STJ-001] in 1.9mm^2 die form, able to detect a single micron-size magnetic bead. This sensor has high sensitivity (5 nT) to the magnetic field and is the good candidate for point of care diagnostic devices; however, the overall cost for each sensor is prohibitively expensive at $425 [37].

Another approach to designing magnetic biosensor is using frequency-based systems. Two groups of researchers have implemented a detection scheme based on LC resonance circuit alongside a differential sensing technique. Although they are using same principle but their circuit design are completely different in terms of operating frequency range, detection resolution and sensitivity. Wang et al [38] implemented a 16-cell sensor array in a 45nm CMOS process with Gigahertz range of resonance frequency based on differential sensing scheme which it was able to detect a single bead (4.5μm in diameter). Richardson et al [10] designed their biosensor based on a voltage-controlled oscillator and a phase-locked loop circuit in a frequency range of KHz, with the detection limit of up to three million beads (2.8μm in diameter); the amount of frequency shift they obtained was quite low, with 3.5 Hz difference for 10^5 numbers of magnetic particles.

The aim of this research is to implement an inexpensive magnetic biosensor system (costing less than $10) being able to detect the presence of magnetic beads. This also means that the amount of frequency shift should be in the range that can be detected easily without requirement of expensive equipment.

In summary, the specific goals of this research are to:

- Design and develop a suitable sensor to perform magnetic particle detection;
- Carry out experimental investigation of sensor calibration to determine the optimal frequency of detection with low noise level for higher accuracy and sensitivity;
- Synthesize magnetic particle based on the project specification; and
- Examine the sensor with actual magnetic sample and investigate the effect of different frequencies on the sensor sensitivity.

1.6 Contribution to knowledge

This study makes the following contributions to research in this area:

- Innovation of a relatively inexpensive sensor for quantifying multiple magnetic particles in small volume or mass, using phase lock loop (PLL) in a resonance circuit.

  A new scheme is introduced to detect a range of sizes of magnetic beads using an integrated PLL- IC operating at Megahertz resonance frequency with a newly designed 3D spiral coil for point-of-care diagnostics applications.

- The sensor fabrication method is proposed for detection of magnetic beads attached to the DNA strands based on using aluminium planar spiral coil on Si and gold substrates.

- A new air-core wire-wound inductor is implemented within the PLL-resonance sensor and characterized.
- Determination of the optimised sensor components for achieving the maximum frequency shift due to the presence of small mass of magnetic particles with lowest noise floor using numerical investigation and experimental validations.

A new scheme is proposed, implemented and tested by integrating commercial magnetoresistive sensor, to detect magnetic beads (μm) for the point-of-care diagnostic application.

1.7 Summary of methodology used and thesis structure

The thesis starts with a general introduction regarding the point of care diagnostic techniques and continues with the idea of molecular detection methods. **Chapter 2** gives an overview on the magnetic particle detection methods with the emphasis on the induction based and frequency based magnetic sensor including different types of magnetoresistive sensor. The last section of chapter 2 gives us the background information regarding the previous work done. This work was based on the COMSOL multiphysic software [simulation only] investigating the best inductor shape and size for detection and presenting the effect of different parameters on this sensor.

A brief description is given in **chapter 3** of different types of magnetic materials and magnetism. The discussion continues by studying magnetic particles from different aspects including their behaviour under the exposure of an external magnetic field and the forces inducing on them, plus the heat and temperature effect. Attention then shifts to synthesising magnetic particles and a full description is given regarding the iron oxide particles made for this research. At the end of this chapter the magnetic samples utilized for the experiments described in chapter 6 are introduced in detail.

Chapter 4 is dedicated to the design description of the sensors developed so far, starting with the Colpitts oscillator sensor and ending with the full explanation of phase lock loop-resonance circuit. Within this chapter the coil design is studied numerically and simulation is performed using the COMSOL multiphysic software. The experimental set up and the way this sensor is calibrated suitable for magnetic beads detection is the emphasis of **chapter 5**. Determining the appropriate detection time with the lowest level of noise is presented, corresponding to several experimental investigations.

Chapter 6 shows the validation of the design and calibration by showing the results of magnetic particle detection experiments. Firstly, the design and experiments based on GMR sensor are presented, then the tests conducted with the resonance sensor are described, whereby the detection

was performed in frequency range 2.4 - 7.2MHz, and the system was examined with four types of magnetic samples.

Chapter 7 gives an overall conclusion of the results and provides some ideas for future work on this subject, which may improve the performance of the magnetic particle detection and increase the sensitivity and resolution of this system for use in point of care diagnostic devices.

CHAPTER 2: **MAGNETIC BIOSENSOR**

2.1 Introduction

The key to prevention and early stage identification of health problems is the detection of pathogenic bacteria or molecules, such as protein and nucleic acids (DNA & RNA) in a body fluid (e.g. blood, swab and urine). The presence of a particular disease can be distinguished by biomarkers (the specific molecule or molecules symptomatic of that disease). Latest developments in ultrasensitive devices have allowed the detection of single molecules (molecular diagnosis). Pathogen detection based on DNA (molecular) diagnostics is much faster than conventional culture-based methods and sufficiently precise, in addition to providing genomic information.

Modern healthcare needs non-invasive and fast molecular diagnosis that is able to detect minute amounts of biomarkers. Most of the commercially available DNA detection methods use fluorescent labelling (optical method) for bimolecular quantification. For achieving high signal to noise ratio they need large numbers of molecules ($>10^4$), which reduces their sensitivity. The optical system requirements, such as bleaching, cannot be adequately quantifiable, therefore a portable, sensitive and low-cost detection technique is required, which can open new avenues for molecular diagnostics [42].

It was about two decades ago the first magnetic biosensor was proposed by Kriz et al [43]. Since then, a large amount of research has been conducted on biosensors using magnetic particles as labels for the biomarkers. These magnetic labels have a wide range of applications in clinical diagnostics and their stable properties over time, besides their other advantages, make them increasingly popular these days. High sensitivity as well as selectivity are the main considerations for magnetic biosensors to be beneficial in molecular assay. These kinds of biosensors and biochips have already been employed for molecular detection [42, 44, 47-49]. Their detection time is short (< 2 hours) and multiplex detection is achievable by integration of microfluidics and CMOS technology. Up to 1 million sensors per cm^2 can be fabricated with integrated CMOS circuitry [42]. Therefore, advantages and based on the reasons presented above it is wise to consider the magnetic based biosensor as a best detection method candidate for point of care molecular diagnostics.

Biosensors have the potential to shorten the time span between sample uptake and results, but their future lies in reaching the desired selectivity and sensitivity comparable to established methods at a fraction of the cost. The smallest amount of biomolecule or labels that can be detected by the sensor defines its ‘sensitivity’, whereas ‘selectivity’ defines how well the sensor

can detect and distinguish between specific molecules or labels and other impurities inside the complex fluid sample. Utilizing magnetic particles as biomarker tags can increase the sensor selectivity, because they are not inherently optically responsive to some blood components, and their effect cannot be influenced by any chemical reaction in body fluids, therefore the background signals and interference effect are reduced significantly.

This chapter gives an overview of the various sensors that have been developed for magnetic particle detection with their special features. However, the main focus here is on types of sensors in which their detection method is based on electromagnetic induction. A brief introduction to magnetoresistive sensors is given in the following section then a full description of frequency-based methods is presented.

2.2 Induction-based detection

Quantitative and fast pathogen detection is very important for point of care diagnostics. Since magnetic particles have been chosen as a reliable label for DNA detection due to their advantages over commonly used labels, magnetic field sensors can be the best option for detecting the presence of small magnetic or magnetizable particles. In general, induction-based biosensors can be categorized into two mains methods for detecting the magnetic particles: the strategy of using magnetoresistive materials (MR) as a transducer, whereby adding magnetic labels to the sample can result in resistance change; and frequency-based techniques such as using different types of oscillators. Both methods are reviewed in the following sections. Although the transducer used in these methods is completely different, the DNA detection design and principle is the same. This principle is illustrated in Figure 2.1 [50]. Designing biosensors based on DNA hybridization can be divided into the following steps:

1. Immobilizing probe DNA on top layer of the sensor.
2. Adding target DNA labelled with biotin (or any other types of tags), which leads to the hybridization occurrence (in presence of DNA complementary strands).
3. Adding magnetic particles coated with streptavidin, which are attached to the hybridized DNA on the sensor surface through biotin-streptavidin binding.
4. Finally detection of magnetic beads. The latter is engineered whilst the previous parts are more biological and biochemical. Attaching magnetic beads to the hybridized DNA alter one of the sensor elements, such as voltage, resistance, inductance or current (depends on the transducer type), that can generate measurable electrical signals. Therefore, different types of experiments are needed to design such a sensor.

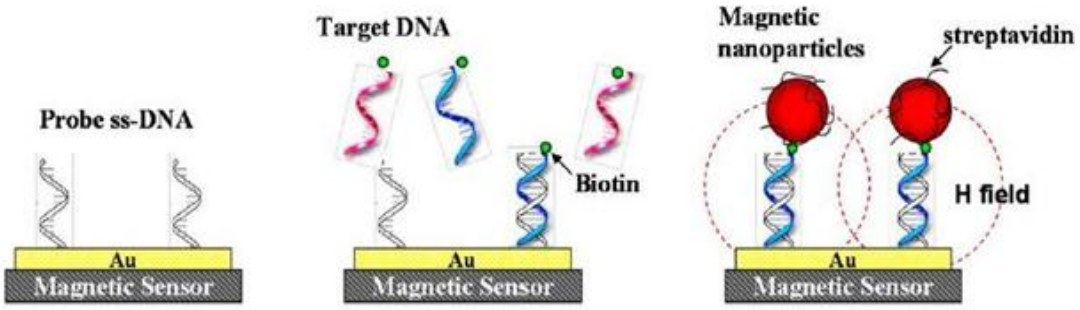

Figure 2.1: Principle of magnetic DNA detection [50]

Currently, many researchers are only focusing on designing a sensor that is sensitive to the presence of the magnetic beads, and they claim that their sensors can give accurate detection of biomolecules labelled with magnetic particles. The sensitivity of those sensors is highly related to the number of micro or nano magnetic beads they can detect; a lower numbers of beads means higher sensitivity.

2.3 Magnetoresistive (MR) sensor

Magnetoresistive effect was first discovered in the 1850s, and due to the development of microelectronics during the last century it has come to be used extensively in industry. The basic effect is that the presence of an external magnetic field, applied in the domain, is full of moving electrons, which results in a change in their paths and accordingly a change of the electrical resistance of the medium [51].

A large amount of research has been done to employ MR sensor for the detection of magnetic labels. These sensors are linear magnetic field transducers, which have a wide dynamic range with high sensitivity. The MR sensors can be fabricated using two different types of structures: either based on the natural resistance anisotropy in the 3D ferromagnetic material, which results in anisotropic magnetoresistance (AMR) sensors or on ferromagnetic/non-magnetic heterostructures, such as giant magnetoresistance (GMR) and tunnelling magnetoresistance (TMR) [49]. The attractive aspect of MR sensors is its capability to detect very weak magnetic fields (nT) at room temperature.

These devices are accurate, sensitive, inexpensive and portable and they can be made on a single chip and integrated in microsystems, thus many of them have been used for biomolecular detection due to their ability for single micron or submicron-sized magnetic label detection which is comparable with few micron cell sizes.

The most popular types of these sensors are; Hall effect sensor [44], tunnelling magnetoresistive sensor [46], Giant magnetoresistive sensor (GMR) [47] and spin-valve sensor [45], which have been widely studied and developed for bio-molecular detection.

The tunnelling magnetoresistive effect takes place within a three-layer structure; a pair of ferromagnetic layers (FM) and an intermediate insulation layer (Figure 2.2). The idea is that the insulation layer should be thin enough that electrons can tunnel (quantum mechanically) through this thin layer. This structure is called magnetic tunnel junctions (MTJ).

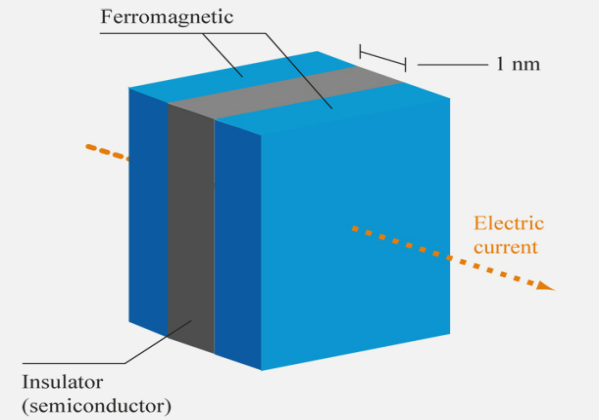

Figure 2.2: Tunnel magnetoresistance effect [153]

Shen et al [46] designed a series of micron size MTJ sensors able to detect a single magnetic M-280 bead. The bead is transported through the microfluidic channel to the sensing area (≈1.4µm), and after passing each bead over the MTJ sensor, real-time measurement shows voltage signal drop. The amplitude of the signal is dependent on the effective bead-to-sensor distance. Shorter distances can result in larger signals. Generally, 80µV is obtained for a single bead with 24 dB signal to noise ratio. Figure 2.3 illustrates the sensor images and results diagrams.

Another sensor recently used for magnetic bead detection is based on an array of Hall effect sensors designed for biomedical application [52]. This sensor is able to detect a single 4.5µm bead in less than a second, and the sensor's active area is chosen to be $4x4\mu m^2$, similar to the size of the single bead. According to the superparamagnetic nature of the beads chosen and the ability of the Hall sensor to detect magnetic field, the bead has to polarize prior to the detection and this is done using on-chip wires carrying currents. For achieving the satisfactory sensitivity by Hall sensor, the active sensing area should be as small as the bead size. Therefore, an array of several Hall sensor units is required for quantifying individual beads, and it must be ensured that each bead is going to be detected by at least one of the sensor units anywhere on the surface. Figure 2.4 illustrates the magnetic image of sensor array versus the optical image. The next section is dedicated to Giant

magnetoresistive sensors; this type has been chosen over the other magnetoresistive sensors because of its large output signal compared to Hall Effect or AMR sensors.

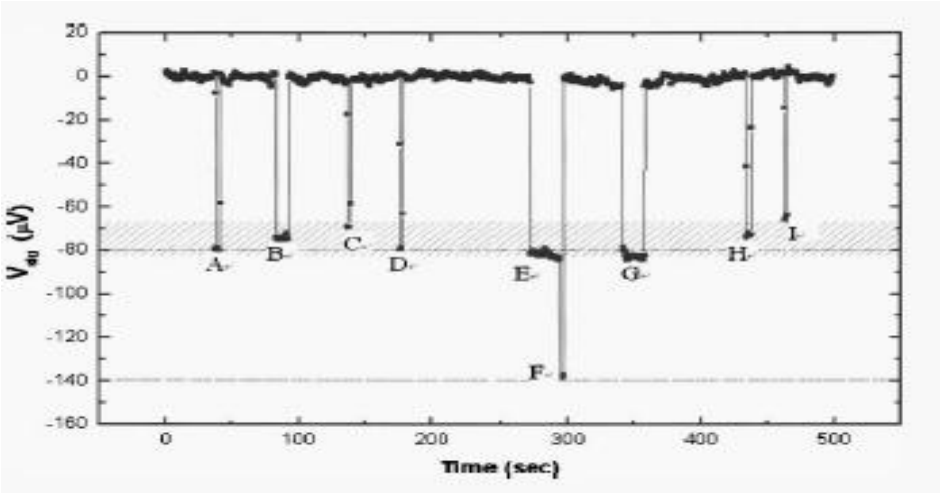

1)

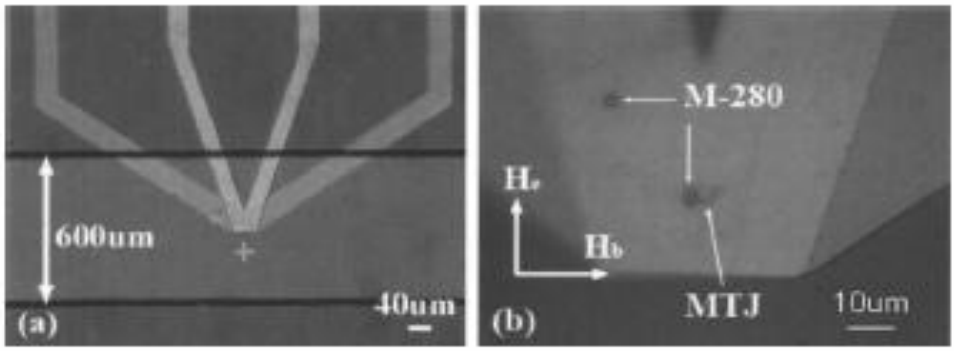

2)

1) The single-bead detection is demonstrated with real-time voltage data. When a single bead passes by the sensor, a sharp signal drop is observed (points A, C, D, H, and I). When a bead becomes stuck on the sensor area for an extended length of time, a plateau signal is obtained (points B and G). Two step signals (point E and F) correspond to a situation wherein two beads are attached to the junction at the same time. The shadowed band indicates the typical signal range measured for a single bead.
2) Optical images of (a) a single 2×6 μm MTJ sensor sealed inside a 600μm wide microchannel and (b) an identical sensor with two single M-280 beads in close proximity. The orientation of the two external fields H_e and H_b are also shown in (b).

Figure 2.3: Single bead detection with Magnetic Tunnel Junctions (MTJ) sensor [46]

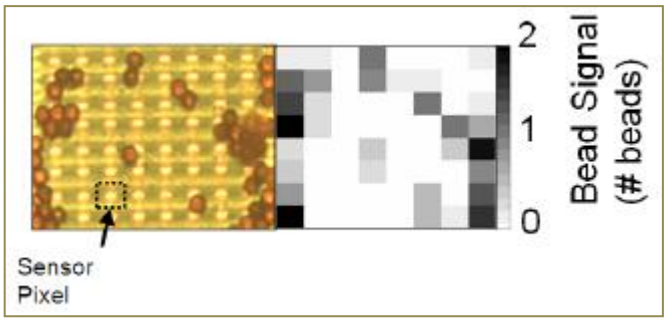

Figure 2.4: The Hall sensor arrays with magnetic beads on top alongside the optical image [52]

- **Giant magnetoresistive sensor**

GMR sensors are capable of detecting molecular identification process (using nanoparticles) and they have high sensitivity to very weak magnetic field. According to the GMR effect, the exposure of a magnetic field to the sandwich layers of ferromagnetic and nonmagnetic materials can cause the resistance change from 4% to over 20%, depending on the material used for GMR films. They can easily be integrated into microarrays, microfluidics and electronics for multiplex pathogen detection. Comparing GMR sensors with other DNA detection sensors such as optical type, the former can be fabricated with very low cost and achieves high sensitivity and good portability. However, there are some limitations to using GMR sensors, such as the maximum resistance change, which is limited to about 15%, after which range higher magnetic field will not result in a bigger output signal. Nevertheless, they are good options for the detection of single bead or beads with very low magnetic permeability.

Figure 2.5 shows that before applying an external magnetic field to the GMR sensor, the magnetic moment of ferromagnetic layers have opposite direction due to the anti-ferromagnetic coupling and thus high resistance to the current passing through the sensor [53]. By applying external magnetic field, both ferromagnetic layers will align and face the same magnetic moment direction; this means that the external field can overcome the anti-ferromagnetic coupling and therefore, resistance decrease.

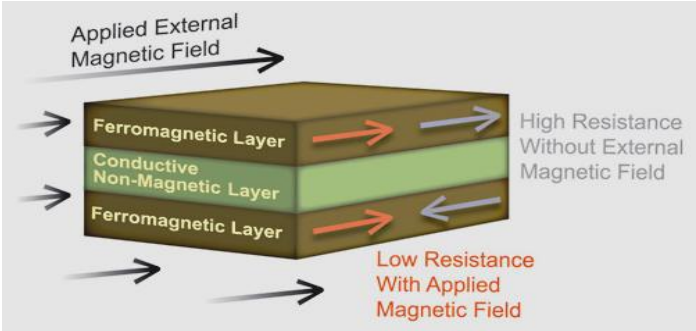

Figure 2.5: GMR sensor effect

An alternate strategy to change the alignment of the magnetic moments of FM layers is to "pin" one of this layers according to its magnetization direction. Therefore, exposure of magnetic field cannot change the magnetization direction of this pinned layer and only the other FM layer (namely "free layer") will change its direction. This type of material used in a sensor is known as a GMR "spin valve" sensor.

As an example, Jeong Suh et al designed and fabricated a GMR spin valve ring sensor able to detect at least 12 magnetic micro beads [48]. Magnetic field in the range of ± 10mT is applied to the sensor (Figure 2.6) and dc output signal of the sensor is measured between that ranges with a nano-voltmeter [48]. Increasing concentration of magnetic beads on the sensor will reduce the net field (sum of the external magnetic field and stray field of magnetic beads which is in opposite direction with external applied field) and finally change the abrupt transition field position of the sensor; consequently the sensor output signal will reduce compared to the response without magnetic beads.

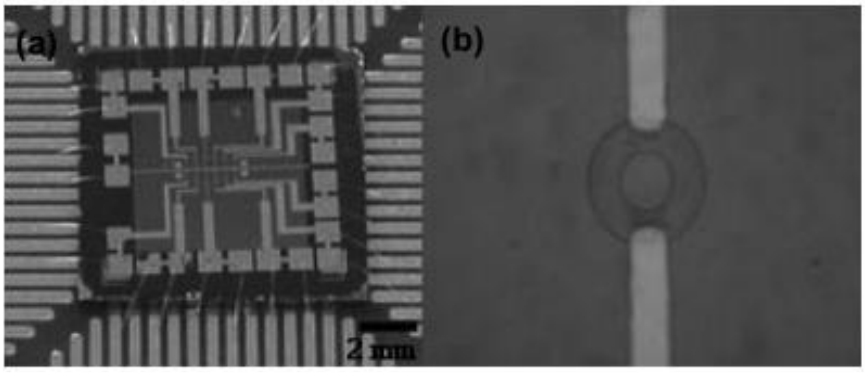

Figure 2.6: (a) Sensor chip, (b) Ring sensor element with 18µm diameter and width of 6µm

Another group of researchers demonstrated a novel spin valve ring shape sensor for detecting superparamagnetic beads. By applying external magnetic field and current to the micro-ring, they direct magnetic beads towards the sensing area for more precise detection [54].

Shu-Jen Han, and Shan Wang [50], proposed a nucleic acid biochip which is sensitive to DNA concentration ranging from 10pM to 10nM. They used spin valve sensor with an indirect labelling technique, which can detect electrical signal directly with off-die or on-die circuitry. At first, cells are labelled with biotinylated primary ligand. Then superparamagnetic beads functionalized with streptavidin will be magnetically added to the cells as label. After applying a magnetic field these target cells will remain in the solution while unlabelled cell will flow through, and remained magnetic beads will change the resistance of the sensor. As illustrated in Figure 2.7, the M_p is the pinned magnetization layer in *y* direction while M_f can freely rotates around the *x* plane [50]. Sensor resistance changes when the angle between M_f and M_p changed, and this will happen by magnetic

bead adsorption on the sensor surface. For better orientation of free layer they applied a dc current along the *x* direction.

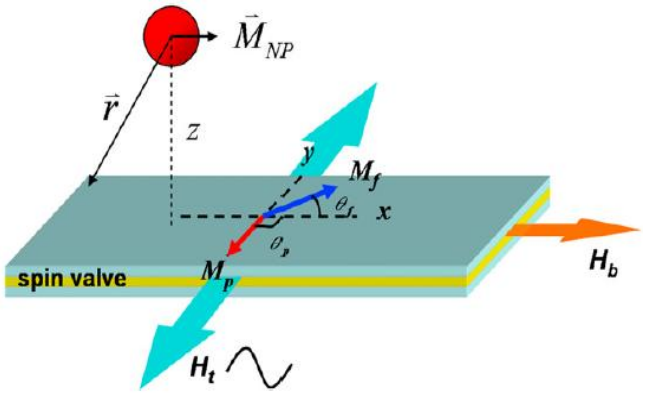

Figure 2.7: The configuration of a rectangular spin valve sensor with a magnetic nanoparticle bound to the sensor surface [50]

A sensor has been designed by Feng et al [55] for the detection of magnetic beads and ferrofluid using multilayer GMR sensors ([Cu 2.1nm/NiFeCo 1.5nm]) with 1µm diameter magnetic bead and Fe_3O_4 particles of ferrofluid. A GMR-bridge was employed for this study by connecting two GMR sensors and two external adjustable resistors also integrated with microfluidic for dynamic detection of ferrofluid. The sensor's layers were made of 3 inches Si wafers, 200nm SiO_2 passivation layer and a final coating of SU-8 photoresist (Figure 2.8).

A vertical DC magnetic field of 240 Oe was applied for magnetic bead detection beside the 70 Oe (7mT) in-plane field for ferrofluid detection. While the sensing area of GMR sensor is free of beads, the magnetic field cannot make any changes in the GMR-bridge, according to the demagnetizing effect.

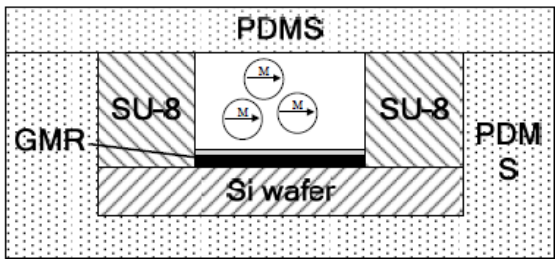

Figure 2.8: The schematic of GMR sensor [55]

The ferrofluid and water were pushed into the micro channel via a syringe pump connected to a PDMS lid. This sensor is capable of detecting a minimum of 100 magnetic beads with signal output of 8µv. The GMR bridge signal is inversely proportional to the surface coverage of magnetic beads and again the same proportion exists between the sensitivity of the GMR bridge and the size of the sensor. Therefore, for having a more sensitive sensor, AC magnetic field should be applied to this system.

In 2007 for the first time Shu-Jen et al [56-57] proved that the GMR sensor can be used in biomedical applications. They presented a biochip based on DNA microarray and spin valve sensor using magnetic particle labels as a sensitive DNA detection method for Human Papillomavirus (HPV) genotyping. Each chip consisted of 32 pairs of GMR sensors and each sensor included 32 spin valve strips, all of which are connected in series together. The resistance of each sensor is about 35 kΩ before applying magnetic field. This chip demonstrated an accuracy of 90% and is able to detect the small DNA concentrations (<1pM).

As a proof of concept in this research, the author designed and conducted an experiment for detecting the presence of magnetic bead using a commercially available GMR sensor from NVE Corporation. The selected GMR has high temperature stability; low power consumption and its output is independent of frequency [29]. With NVE GMR sensor the resistance change decrease by 14% -16% and this value is calculated using equation (2-1).

$$\%\ GMR = (Change\ in\ Resistance \times 100\%) / Minimum\ Resistance \qquad (2\text{-}1)$$

The GMR sensor chosen for these experiments is AA002-02 series, which has a planar square shape and is only able to sense magnetic fields. This sensor has an axis of sensitivity in the plane of the IC, not orthogonal [53] (Figure 2.9).

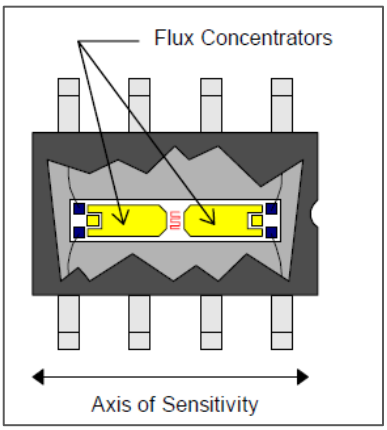

Figure 2.9: Planar sensitive magnetic axis; GMR AA002-02 Series Sensor with a cut away view of the die orientation

This sensor has been chosen because of its linear magnetic field coverage in the range of 0.15mT - 1mT [53] (Table 2-1), which is expected to cover the range of field that magnetic beads are going to induce to the sensor after placing them close enough to the GMR.

Table 2.1: GMR sensor specification

Part Number	*Linear Range (|mT|)*		*Maximum Nonlinearity (% Uni.2)*	*Maximum Hysteresis (% Uni.2)*	*Maximum Operating Temp (°C)*	*Typical Resistance (Ohms)*
	Min	Max				
AA002-02	0.15	1.05	2	4	125	5K

1 Oersted (Oe) = 1 Gauss in air = 0.1mT

Using a Wheatstone bridge configuration and the bridge resistor in the middle of the die, the magnetic flux is gathered and focused on the resistor by flux concentrators along the axis as shown above. If the external magnetic field applied is parallel to this axis then the largest output signal can be obtained.

Figure 2.10 shows how the resistance of the GMR sensor reduces by applying the magnetic field [53]. The resistance changes are equal whether a directionally positive or negative field is applied to the sensor; in both cases the material used in the GMR sensor will provide the same output and change in resistance. This characteristic is called unipolar.

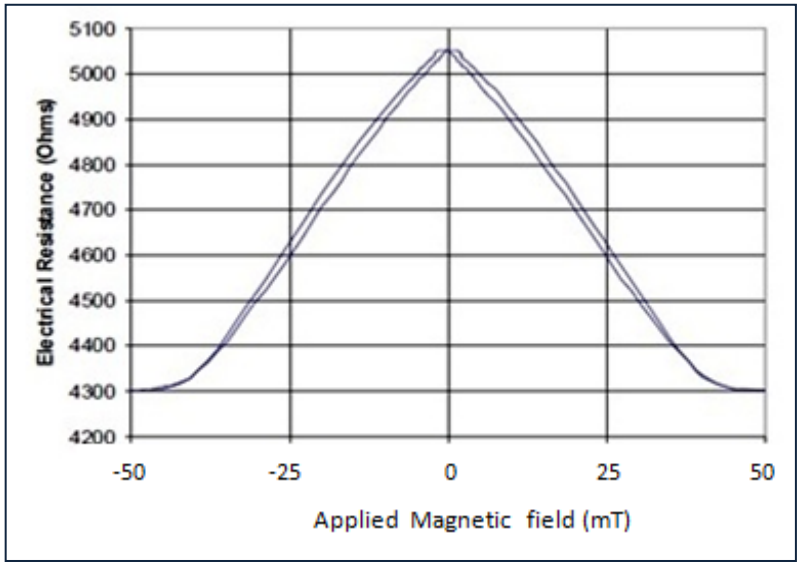

Figure 2.10: Typical characteristic for an NVE GMR material including hysteresis

Magnetic hysteresis can be found on all magnetic materials such as nickel, iron and so on, and GMR sensors are made of these materials, so they are liable to hysteresis impacts. A minor hysteresis loop is achieved when a magnetic field is applied to the sensor, which is always in the same direction (unipolar field) [53] (Fig. 2.11). In the event that the applied field to the sensor has a different magnitude, then an error is caused in the output signal, which depends on the amount of hysteresis in the sensor. This error will appear as a voltage offset in the sensor output.

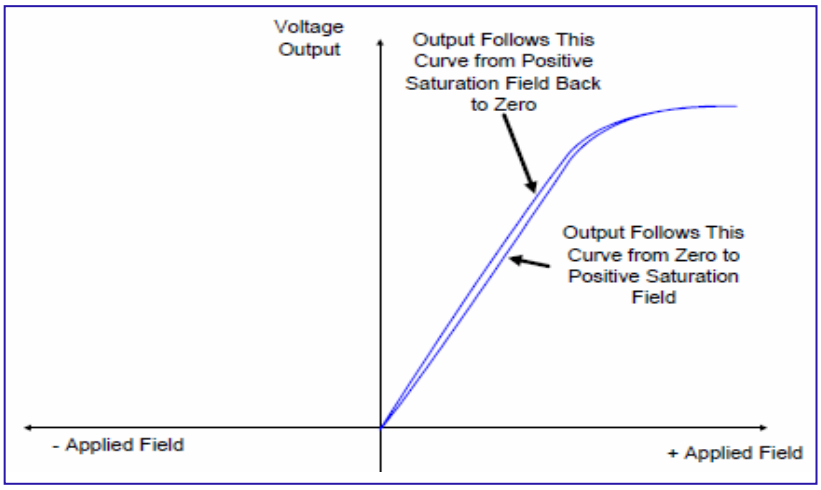

Figure 2.11: Exposure of a saturating unipolar field to an NVE AA-Series sensor

The NVE GMR application note [53] presented the output voltage signal behaviour to the applied magnetic field in the graph shown in Figure 2.12. The slope of each line indicates the *sensor sensitivity* to the magnetic field. Thus sensitivity of this sensor can be defined by the ratio of output voltage in millivolts per applied magnetic field in mT. Each graph on the Figure 2.12 represents one sensor: AA002, AA004 and AA005.

In this research the experiment was designed and conducted based on NVE GMR AA002, and its results are presented in chapter 6.

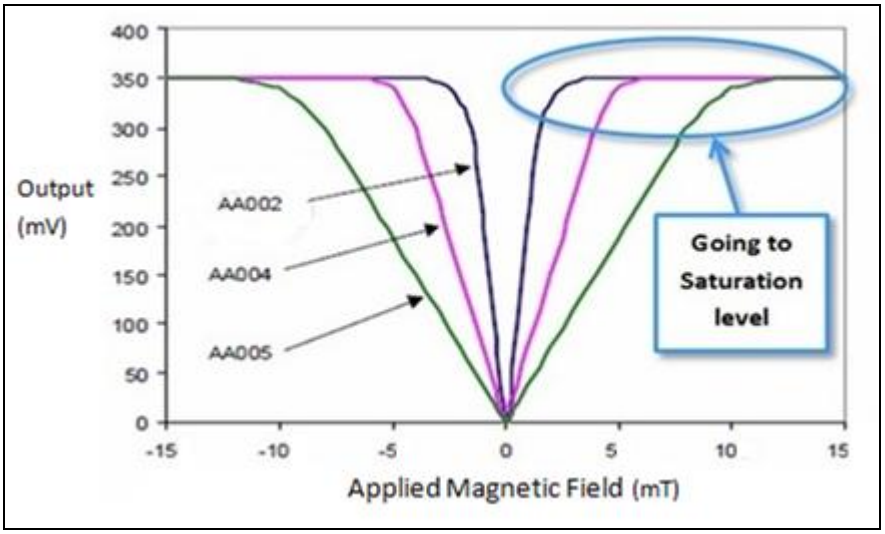

Figure 2.12: GMR sensors sensitivity to the magnetic field

2.4 Frequency-based detection systems

According to the advantages of magnetic particles comparing to the unstable enzymes and photo-based labels, they became popular to use as a label in many applications. Detecting such labels is mostly based on their magnetization response, which can be measured by different types of sensors; resonance frequency measurements of an LC oscillator, impedance or bridge

measurements and by inductive coupling between two coils. Currently, simple and fast hand-held bio-detection system with low power consumption in portable devices is highly desired [43, 58-61]. Most magnetic biosensors presented so far still needs external magnetic field or complicated processing for bimolecular detection, which affects the cost of the system. The following section reviews the development of frequency-based magnetic biosensors, which do not require external magnetic field.

Kriz et al (1996) proposed a magnetic transducer based on Maxwell B

ridge for direct ferromagnetic detection [43] (Fig. 2.13). Here the Coil L_4 is used to sense the presence of magnetic particles in a balance bridge. Introducing the ferromagnetic particles into the coil changes the magnetic permeability of these particles and accordingly the coil inductance, which unbalances the Maxwell Bridge and consequently the differential output voltage across the bridge increases. The voltage output difference is proportional to the amount of ferromagnetic material.

They attempted different methods for determining coil inductance including resonance frequency measurement but Maxwell Bridge shows 100-1000 times more sensitivity than others. They achieved sensitivity of 21 ± 4μv/(μg Fe/mL) measuring the sample of 1.5 mL buffer solution (0-50μg Fe/mL)[43, 58].

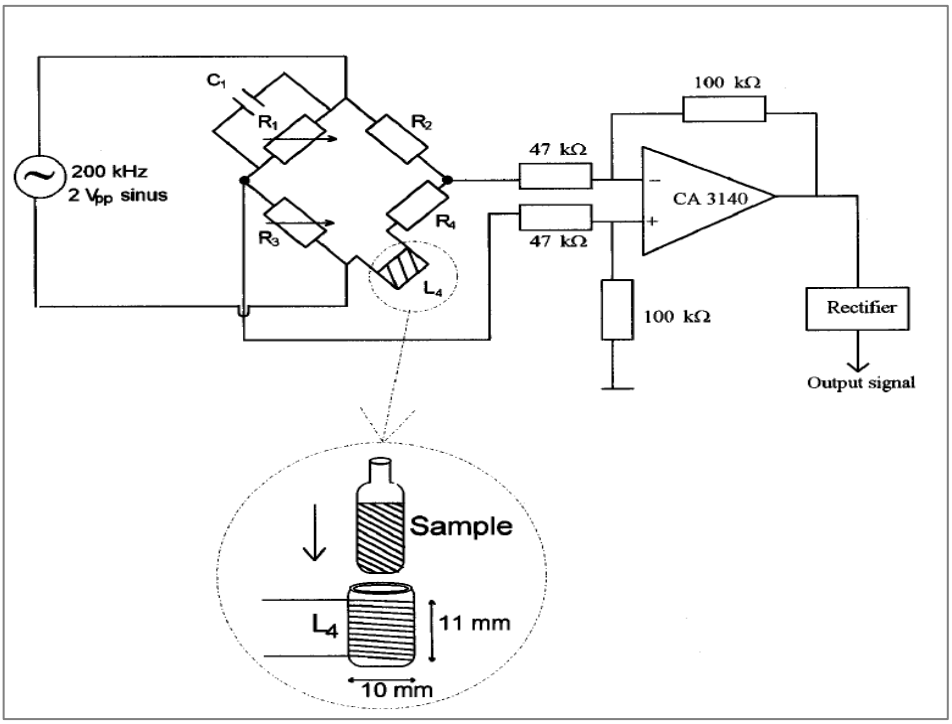

Figure 2.13: Transducer set up; Maxwell Bridge

In another approach, Richardson et al (2001) presented paramagnetic particles detection on a plastic strip based on a LC resonator circuit for magneto-immunoassay application [62]. The principle of LC detector increases the overall inductance of the circuit by applying magnetic beads close to the sensor surface and consequently decreases the resonance frequency of the circuit. The amount of Fe on each magnetic particles and total numbers of particles are factors that can directly control the frequency shift. In their proposed instrument the detection limit is between 1×10^5 to 3.33×10^6 numbers of particles, assuming that each magnetic particle (2.8μm in diameter) contains 10% Fe (1.3 g/cm^3).

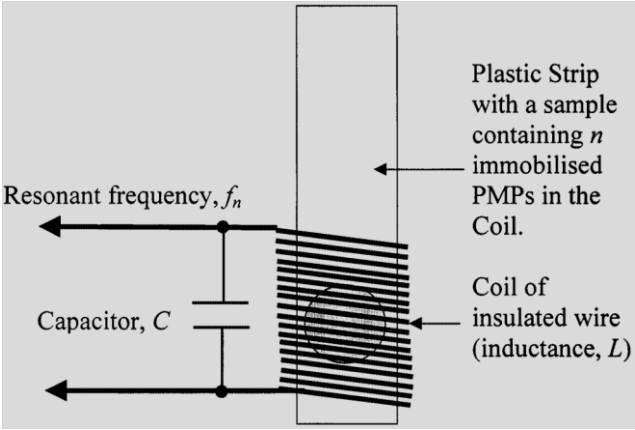

Figure 2.14: Electronic circuit for measuring the number of magnetic particles

Figure 2.14 shows their sensor in which a plastic strip with immobilized beads on it is inserted into the coil [62]. The paramagnetic particles (PMP) have been coated with streptavidin as a label and immobilized on the polyethylene terephthalate (PT) solid phase strip by a sandwich immunoassay [63]. The inductance of the coil is calculated by:

$$L = \mu\mu_0 m^2 dA \qquad (2\text{-}2)$$

$\mu_0 = 4\pi\times10^7$,μ is the total effective relative permeability of magnetic particles and the plastic strip in the core including the coil former; m is the number of turns per unit length; d is the length and A is the cross-sectional area of the coil.

Assuming that permeability of plastic strip, coil former and air space in the coil are negligible, equation (2-2) may be rewritten:

$$L = L_0 + Kn \qquad (2\text{-}3)$$

Where L_0 is inductance without any magnetic particles, n is a number of beads and $K = c\mu_p\mu_0 m^2 dA$, is a constant (μ_p; the permeability of the plastic in the strip and c is a constant which relates the permeability of individual magnetic particles to the contribution they make toμ). Therefore, Eq. (2-3) shows that increasing the number of beads cause linear increase in the coil

inductance. This sensor works with the resonance frequency of f_n = 500kHz and $f_n = \{2\pi(LC)^{-1/2}\}^{-1}$, by replacing **L** from Eq. (2-3) and using the binomial theorem:

$$f_n = f_0\{1-\tfrac{1}{2}(K/L_0)n\} \qquad (2\text{-}4)$$

f_0 is the resonance frequency of the oscillator without magnetic particles. Three important results and prediction can be made based on Eq. (2-4):

- Higher f_0 will results in better sensitivity of the circuit;
- The resonance frequency decreases linearly with increasing number of magnetic beads; and
- The sensitivity of the measuring circuit would increase with a higher resonant frequency of the coil.

In their experiments, a few hertz frequency down-shift was observed in the present of PMPs on the plastic strip. Therefore, a very stable oscillator circuit is required for having reliable measurement in this type of detection. In contrast, very easy and precise measurement of frequency is an advantage of this method. For overcoming the stability issue, phase-locked loop (PLL) oscillator circuit was designed with sensitivity of < 1 Hz in $f_n \approx$500KHz.

One of the most important factors for increasing the sensitivity of oscillators is the coil shape and dimensions. Here they tested three different types of coil design (Figure 2.15) and the results can be found in Table 2.2, which shows that the coil in Figure 2.15a has very poor sensitivity. In Figure 2.15b they used ferrite core and therefore a smaller number of turns (n=120) but this was still not sensitive enough, and Figure 2.15(c) with air core and no former shows the best sensitivity in these designs.

Richardson et al continued to improve their sensing system by investigating different types of planar coils with more stable and reliable circuits, using it in immunoassay [64]. The results did not differ significantly from their first attempt in 2001.

In 2009 Wang et al [65] presented low-power frequency-shift CMOS magnetic sensor with a PDMS microfluidic structure to make a hand-held device for magnetic bead detection. Their sensing system (Figure 2.16a) was based on LC oscillator, in which AC current is passed through the inductor to produce a magnetic field. Applied magnetic beads will then be polarized in the presence of the magnetic field and therefore the total inductance of the coil will increase, which changes the resonance frequency (f_0) of the oscillator: $f_0=1/(2\pi(LC)^{1/2})$. This sensor has single bead detection sensitivity and can be fabricated in planar form. Each micron size magnetic bead can shift the frequency, up to a few parts per million (ppm) of the resonance frequency, which in this oscillator is

around 1GHz. For instance, a magnetic bead of diameter 2.4µm can cause frequency shift of 2.6 ppm (≈ 384 Hz).

Figure 2.15	*Inductance (L) µH*	*Wire diameter µm*	$f_{resonance}$ *KHz*	*Sensitivity Hz/10³ MP*
Coil a	71	193	275	0.16
Coil b	880	121	206	0.3
Coil c	131	101	529	3.5

(MP= Magnetic Particle)

Table 2.2: Coil inductance, diameter, resonance and sensitivity

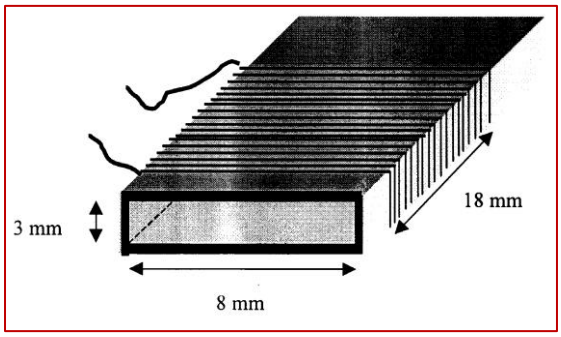

a

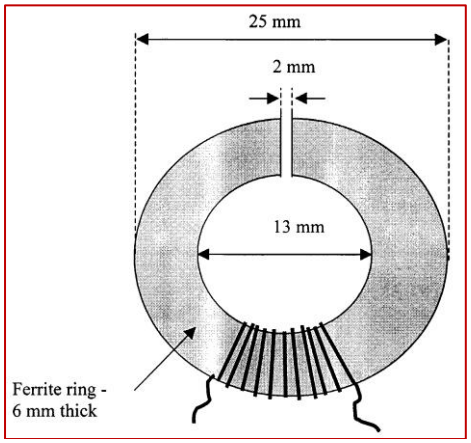

b

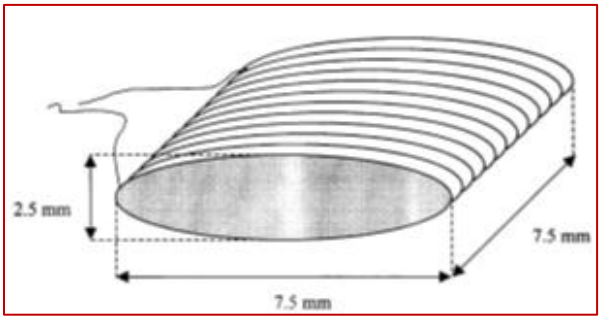

c

Figure 2.15: Different coil designs for LC resonator circuit [62]

Given the small scale frequency shift, to achieve accurate detection with long-term stable frequency behaviour, this system needs to be isolated from any kind of noise and temperature variations. For this purpose different architectures consist of PMOS and NMOS used for:

- On-chip temperature control;
- Down-conversion of system frequency from 1GHz to below 10kHz; and
- Suppressing the flicker and supply noise and any low-frequency perturbations.

This sensor can be fabricated as an array with eight parallel sensor cells [65] (Figure 2.16b), in which each cell contains a pair of differential oscillators (active and reference sensors).

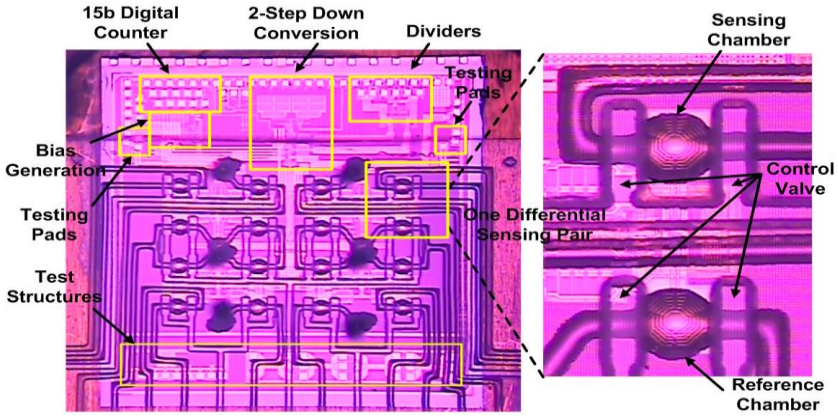

a LC resonators sensing mechanism

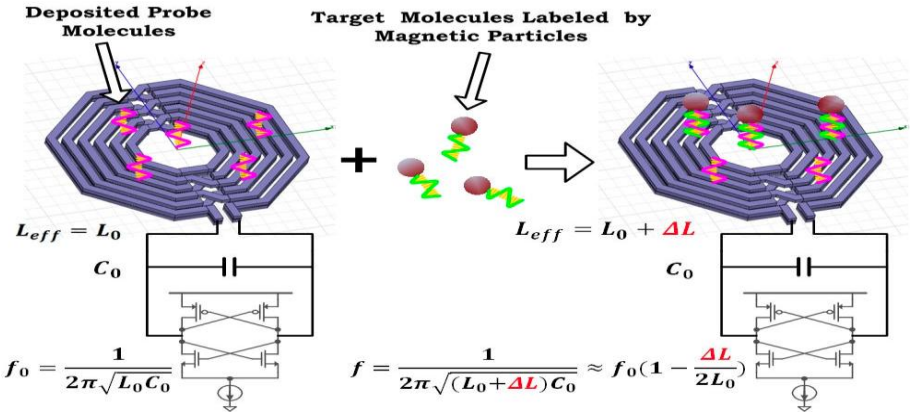

b sensor array with integrated microfluidic structures

Figure 2.16: CMOS frequency-shift-based magnetic sensor

Hua Wang [66] used the abovementioned sensing technology for real-time detection of chemical agents. Their magnetic sensor is based on periodic and autonomous beating of cardiac progenitor cells, which might have tens of microns displacement on CMOS chip. The cells were coated with magnetic particles and when the physiology of the cells was changed its pulsatile movement was recorded by the magnetic sensor. Any changes in cell position can reallocate the magnetic particles, which results in periodic pulses of resonance frequency shift in the sensor signal output. The

magnetic beads increase the inductance and cause the frequency down-shift. This frequency changes will then be modelled as a transducer gain of the sensor.

For having accurate and sensitive detection (sub-ppm frequency shift) for each LC resonator, a low noise oscillator with correlated-double-counting (CDC) noise suppression technique has been used. The fundamental noise floor was modelled in [38] and by implementing CDC method 6dB noise reduction was achieved. The differential sensing scheme was achieved by pairing the sensing and reference oscillators [38] (Figure 2.17a). The sensor output will be their frequency difference. The minimum sensor noise according to the calculation in [38] was $1/f^3$ phase noise which cannot be reduced beyond a certain level. This noise is caused by several factors, such as the waveform properties of the oscillators and mainly by the flicker noise of the active devices used in the CMOS oscillator [38]. In the normal differential scheme, using two oscillators doubled the noise power because of the uncorrelated jitters between them; however, by sharing the active core between the reference and sensing oscillators, the correlation of flicker noise ($\approx 1/f^3$) between them will increase, therefore this correlated $1/f^3$ noise can be subtracted using CDC scheme (where subtracting one frequency count from the other) from the total noise power (Fig. 2.17(b)).

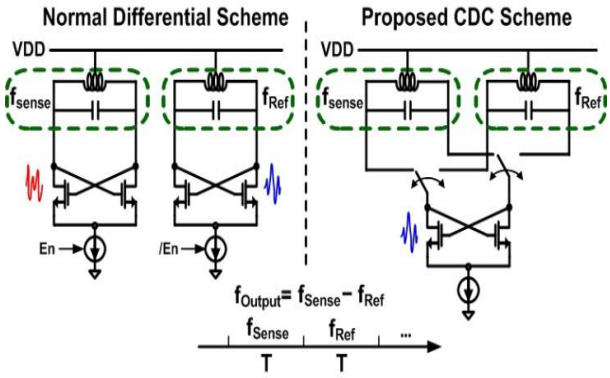

a

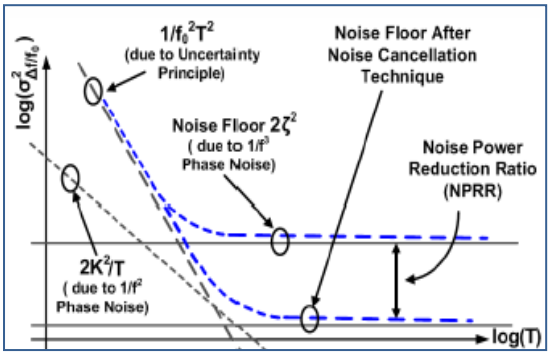

b

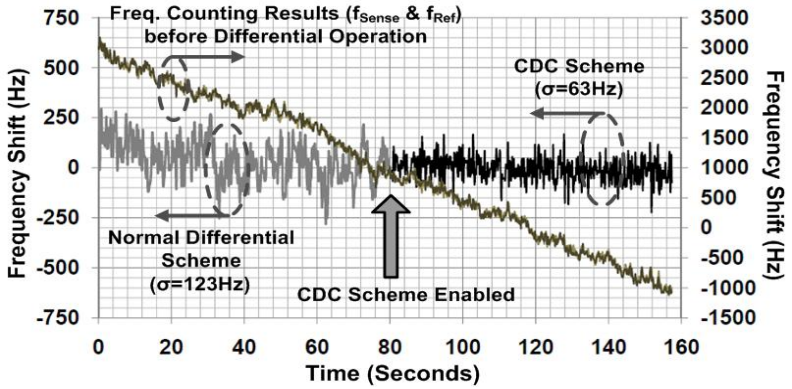

c

Figure 2.17: Proposed CDC scheme based on active core sharing [38], ***a*** *CDC scheme; σ = jitter for setting noise floor,* ***b*** *Oscillator's noise floor,* ***c*** *Frequency counting results in time domain*

The average detection time of this sensor is about three minutes and the sensing area is 120µm. Each cardiac cell is coated with ten magnetic beads (D=2.4µm). Although this sensor performs direct real-time detection, its sensing unit needs to be under physiological conditions (Figure 2.18a, b, d).

One of the sensitivity limitations and weaknesses of this type of sensing method is according the inhomogeneous distribution of magnetic beads on the inductor or sensor surface (Figure 2.18c). Therefore, detecting a small number of beads with different distribution will produce various output signals, which results in noise floor.

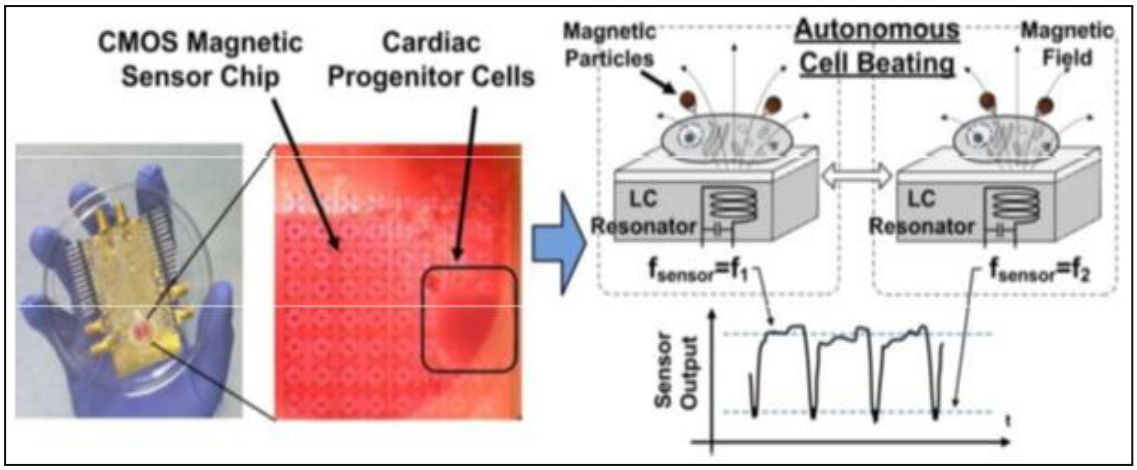

a **b**

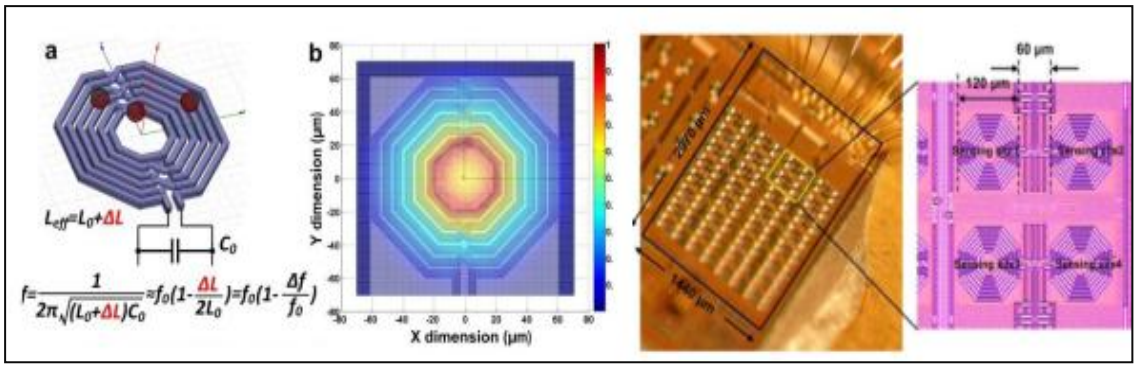

Figure 2.18: Magnetic cell-based sensor [66], ***a*** the sensor module with PDMS reservoir, **b** cells beating cause displacement of magnetic beads and periodic shift in resonance frequency is detected as a result, **c** LC resonator and the normalized transducer gain (sensitivity to magnetic particle) of the CMOS, **d** Sensor array with 64 (8×8) independent sensing site.

For overcoming this problem, Wang's group proposed new bowl-shaped inductor design, which can improve the sensor gain uniformity across the sensing area. Figure 2.19 illustrates three different physical models of inductors for magnetic particles' detection. Conventional symmetric spiral coil (Figure 2.19a), which because of non-uniform field distribution does not have linear sensing area, is mostly sensitive only at the centre. In Figure 2.19b a dual layer bowl shape inductor is proposed, in which the spacing between two layers causes the magnetic field strength to distribute uniformly on the inductor surface.

At the connecting point of two layers the non-homogeneous field distribution occurs because of the current crowding effect. Therefore, to achieve the uniform current distribution, the interconnecting trace and the floating shimming metal were proposed (Figure 2.19c). The magnetic field of this metal changes the total magnetic field strength and has a negligible influence on the coil inductance (Inductance = 1.61nH). They fabricated an array sensor with 16 parallel sensing sites in 45nm CMOS process. Each of four sensing sites (LC tank) makes one quad-core sensor cell [67] (Figure 2.20a). The inductor outer diameter is 110μm with six turns and an oscillator resonance frequency of 1.13GHz. According to their experiments, for a single 4.5μm Dynabead, frequency-shift of 18kHz with a noise floor of 388 Hz was achieved. Figure 2.20b shows the sensor frequency changes for different number of beads.

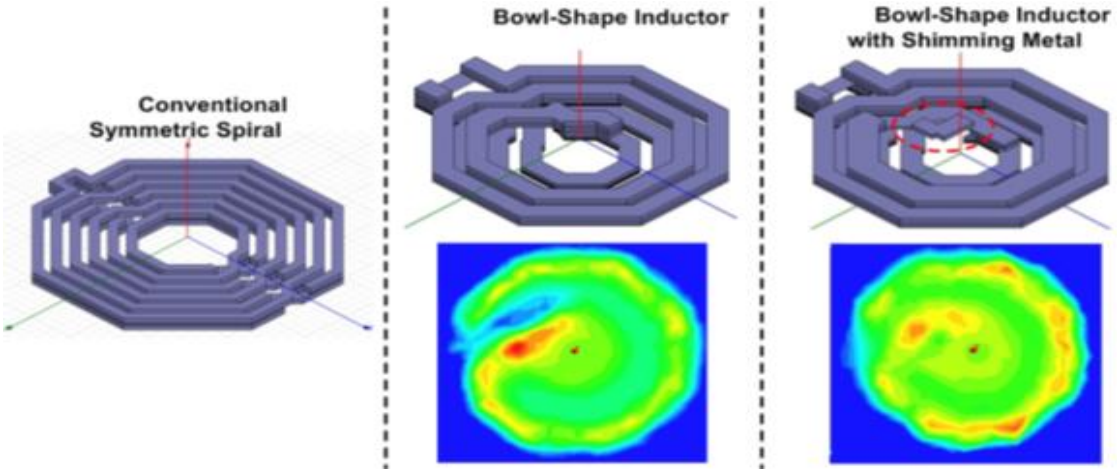

a b c

Figure 2.19: Inductor design for uniform sensor gain, the normalized magnetic field strength |B| is plotted to compare the spatial uniformity [67]

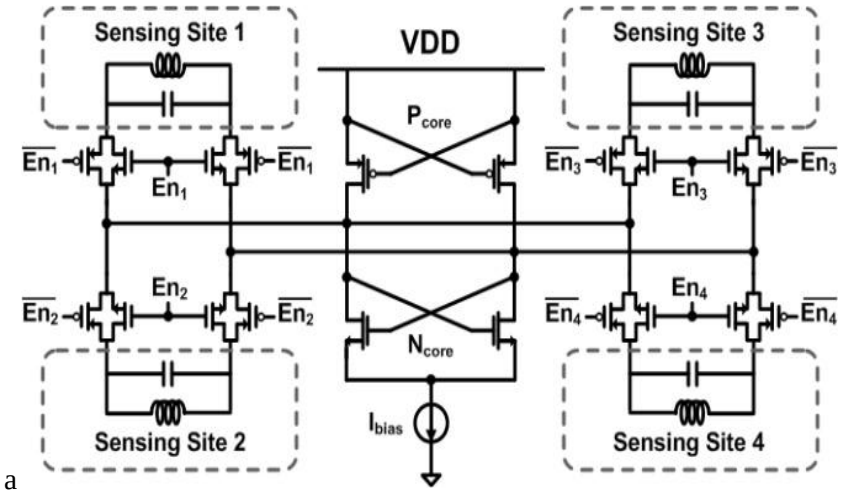

a

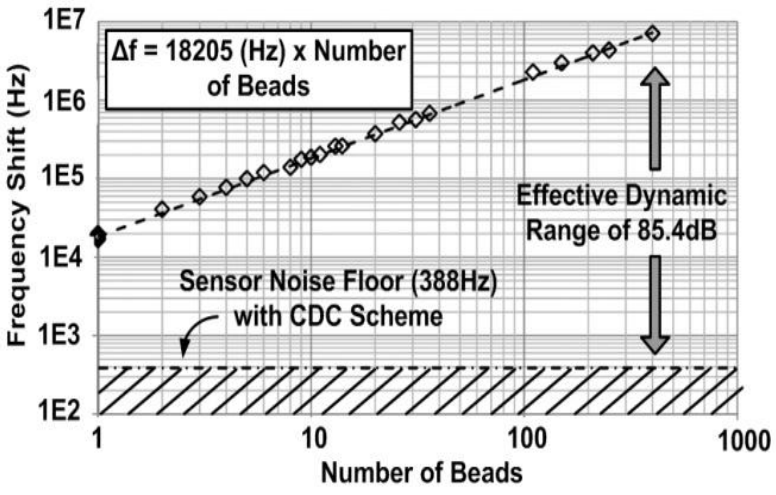

b

Figure 2.20: (a) Quad-core sensor schematic, (b) Sensor dynamic range for different bead numbers [67]

Another lab-on-a-chip inductive device was proposed using immunoassay technique by a group of researchers from the University of Catania in Italy [68-69]. Their device is based on a coreless transformer with one primary coil and two secondary coils, which have opposite winding directions

(Figure 2.21a). In this sensor the magnetic flux is generated by a primary coil, therefore equal voltage is induced in secondary coils in the opposite direction. The output signal of this senor is the differential voltage between two secondary coils. At first when there are no magnetic beads on the coils, output signal is zero, because both secondary voltages are the same, as soon as magnetic beads located on one of the secondary coils, the voltage value on two coils are not the same, hence the output signal is nonzero, as shown in Figure 2.21b.

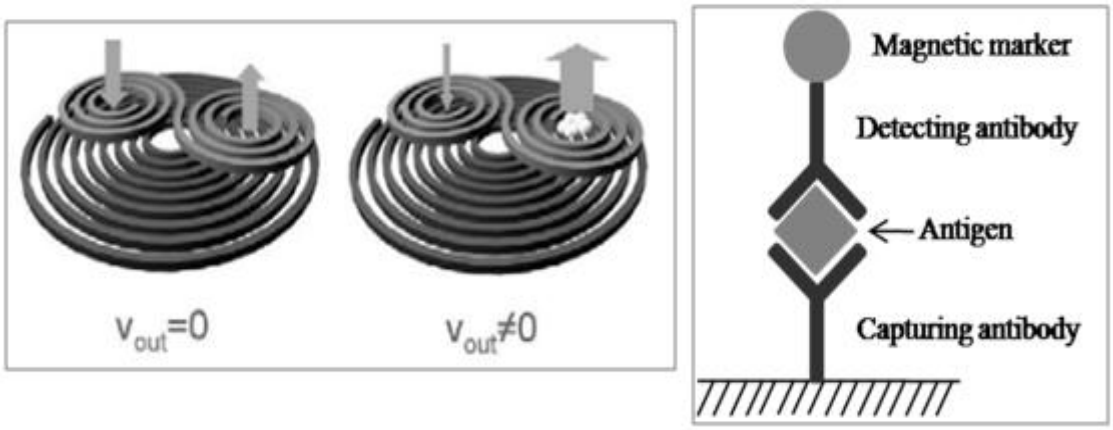

(a) (b)

Figure 2.21: (a) Working principle of the differential transformer, (b) Configuration of magnetic immunoassay bonding[68-69]

2.5 Theoretical background of magnetic DNA sensor using planar coil

Magnetic sensor using planar spiral inductor was proposed for DNA hybridization detection by Azimi et al (2007) at Brunel University [70, 71]. Their work was based on COMSOL multi-physic simulation in which the performance of the sensor has been investigated for detection of magnetic particles. This sensor was able to produce output signal much higher than the GMR sensors. Figure 2.23 illustrates the concept of using a planar spiral coil for detection of DNA hybridization. At first the single strand probe DNA is immobilized on the sensor surface. This surface is coated with the permeable layer (gold coating or SiO_2) to which DNA can be attached (Figure 2.23a), then target DNA tagged with biotin is added. If the target and probe DNA strands are complementary they will hybridize together (Figure 2.23b). In the final step magnetic beads coated with streptavidin are added, which results in biotin-streptavidin strong bond, and a layer of magnetic beads is formed on a surface in the proximity of a spiral coil.

By adding one washing step, unbound magnetic beads are removed from the sensor surface, therefore only beads bound to the hybridized DNA remain. This bead layer has high magnetic

permeability and, with permalloy layer in the bottom, can act as a magnetic core for the inductor and complete the magnetic circuit. This circuit is driven by an AC constant current and the coil voltage is the sensor output (V_s) [35] (Figure 2.22). Formation of the bead layer, increased coil inductance, and the variation of inductance can be translated to the output voltage differences, which the output amplitude is the sensor response. Assuming R_c is constant, thus the voltage only depends on the inductance $L_{c,}$ and the voltage variation is defined as Figure 2.22b.

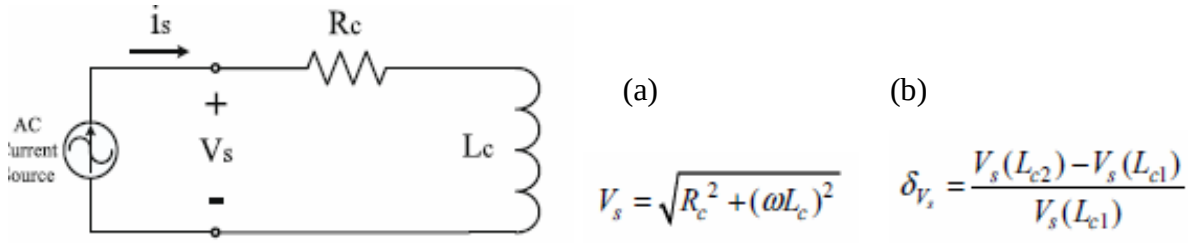

Figure 2.22: Sensor electrical model, (a) V_s amplitude equation, (b) $\delta_v = V_s$ normalized variation

Azimi investigated the optimal coil parameters and expected inductance variation by applying different coils of different size and permeability of magnetic beads. The summary of the simulation results are presented in this section.

Depending on the coil geometry and physical parameters, the inductance can differ significantly. Figure 2.24 shows the geometrical details of the coil and the sensor used in simulations [71]. Some of these important parameters are defined in table 2.3 and also here:

d_{out}: Coil outer diameter, d_{in}: Coil inner diameter, μ_{rB}: The relative permeability of magnetic beads, t_B: the thickness of the bead layer, FF: The effect of inter-winding space (S) and the conductor thickness (W).

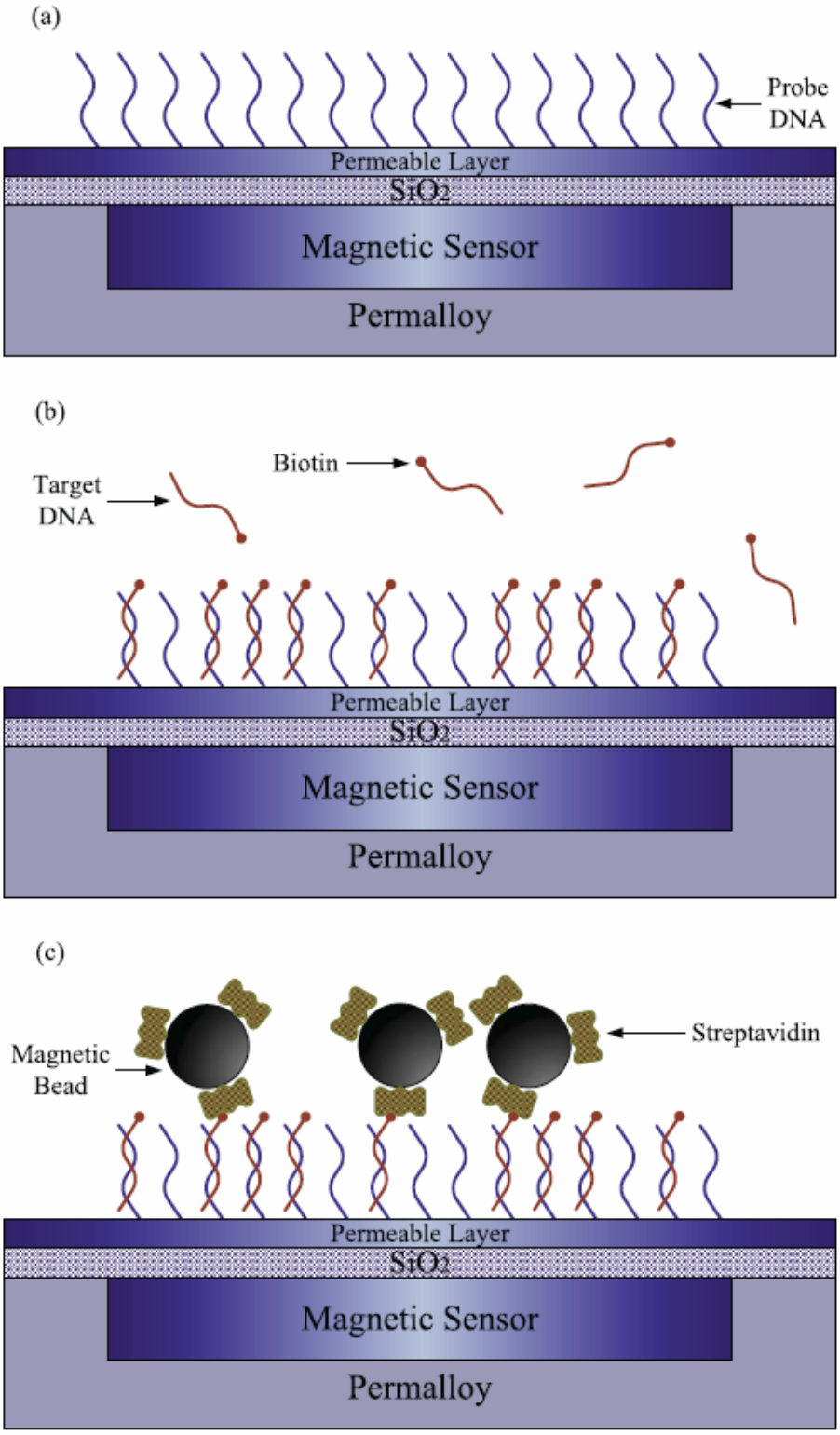

Figure 2.23: DNA detection sensor [70]

(a) Immobilized probe DNA on the sensor surface, (b) Hybridization of target DNA to the probe (c) Attachment of magnetic beads to the duplex DNA via Streptavidin- Biotin binding and construction of a magnetically permeable layer on top of the coil.

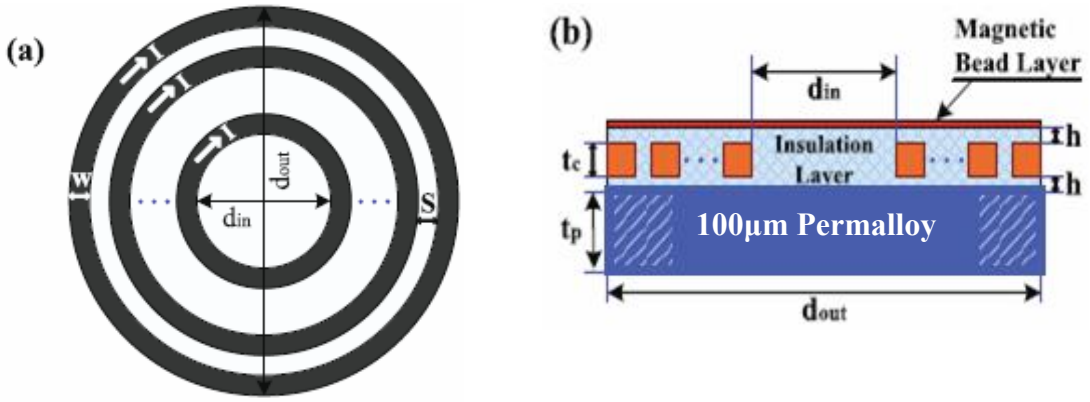

Figure 2.24: Sensor model, (a) Top view of the coil (b) lateral cross section of the sensor

Table 2.3: Coil physical parameters

Parameter	Explanation	Quantity
t_c	Thickness of Conductor	20 µm
W_c	Width of Conductor	20 µm
S	Space Between Conductors	30 µm
t_p	Thickness of Permalloy	100 µm
FF	Fill Factor (occupied area of conductors of the coil to the total coil area)	80 %
h	Gap between coil and bead layer which is occupied with insulator	10 µm

The normalized variations of the coil inductance $\boldsymbol{\delta_L}$ are defined here as a percentage of output variations (inductance changes) calculated based on the permeability of the magnetic layer formed on the sensor surface. The result diagrams illustrated in this section present the parameters causing maximum output variations as a design curve.

The normalized change in the inductance is then calculated as follows [70]:

$$\delta_L = \frac{L(d_{out}, t_c, t_p, \mu_{rB}, t_B) - L(d_{out}, t_c, t_p, \mu_{rB} = 1, t_B = 0)}{L(d_{out}, t_c, t_p, \mu_{rB} = 1, t_B = 0)} \times 100 \qquad (2\text{-}5)$$

COMSOL Simulation was done with the assumption that the magnetic beads layer thickness is about t_B = 2µm, and with no fringing effect, which means the surface of the magnetic sensor is completely covered with magnetic beads. Simulation results are described in the following subsections.

2.5.1 Effect of d_{out} on δ_L

Figure 2.25 shows that, for the given values of the relative permeability, $\boldsymbol{\delta_L}$ is maximum at a specific value of d_{out}, which is called D_{max} and this value of D_{max} is larger for higher permeability μ_{rB} [70].

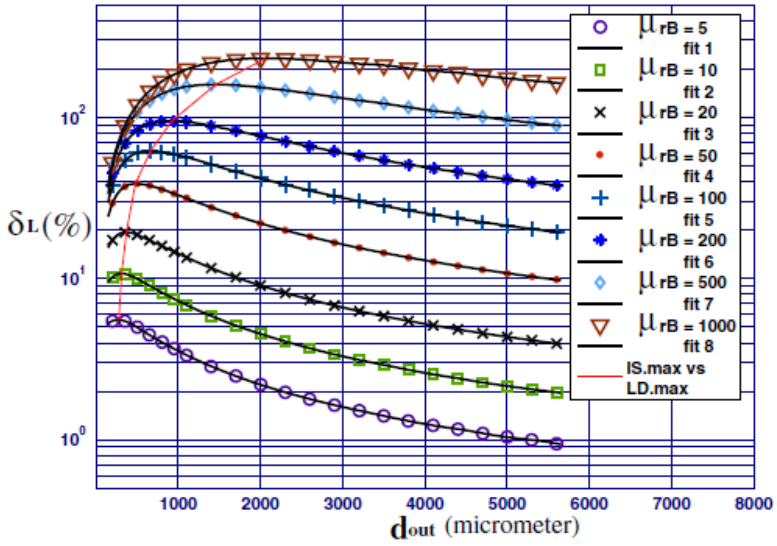

Figure 2.25: δ_L versus coil outer diameter for different bead permeability [70]

Conductor and gap thicknesses are, tc=20μm, h =10μm

2.5.2 Effect of beads' permeability μ_{rB} on δ_L

For having maximum response, it is helpful to consider the optimal coil diameter (D_{max}) in terms ofμ_{rB} and $\boldsymbol{t_C}$ (Figure 2.26a). It can be derived from this diagram that value of D_{max} increases with increase in$\boldsymbol{\mu_{rB}}$. After the best values (D_{max}, $\boldsymbol{t_C}$) are known, Figure 2.23b illustrates the maximum variations of $\boldsymbol{\delta_L}$ versus different value of the relative permeability with respect to the different value of D_{max} and the conductor thickness ($\Delta_{Lmax} = \boldsymbol{\delta_L}$ (*at* D_{max})) [70]. Simulation outcomes show that the sensor output is maximum for each value ofμ_{rB}, at a specific value of D_{max} while the conductor thickness is as small as possible.

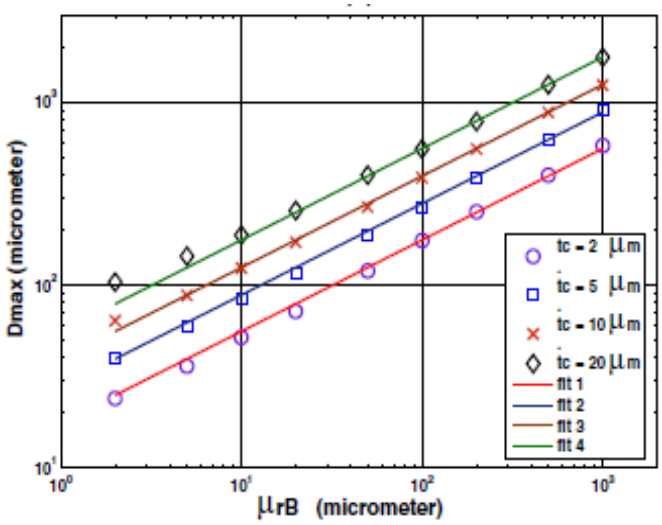

a

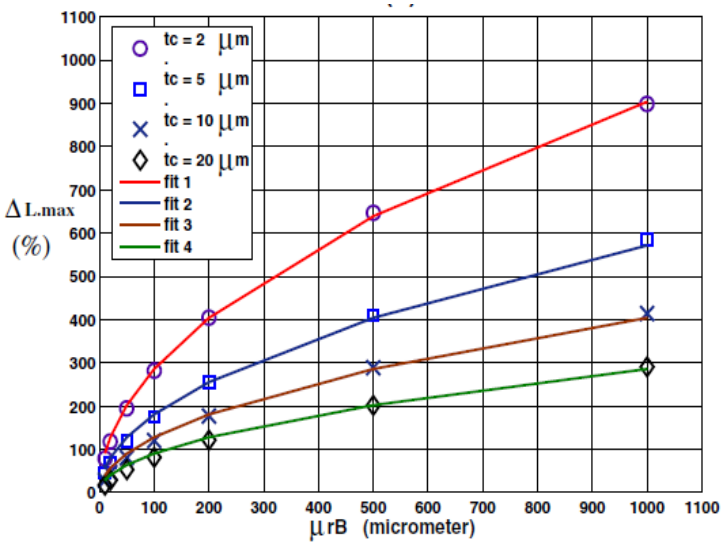

b

Figure 2.26: Comsol simulation (a) Dmax Vs.μ_{rB}, for different $t_{C,}$ while output signal is maximized (b) Maximized inductance percentage change

2.5.3 Effect of conductor thickness t_C on δL

Figure 2.26 shows the effect of conductor thickness on the normalized change by simulating four different values of t_C; decreasing conductor thickness = increasing Δ_{Lmax} (= $\boldsymbol{\delta_L}$ (at D_{max})).

Although D_{max} increases with increasing t_C for a specific value of μ_{rB}.

2.5.4 Effect of thickness of magnetic beads t_B on δ_L

According to the simulation results [70], the magnetic reluctance of the bead layer decreases to half of its original value by doubling the thickness of this layer, which means doubling the amount of bead permeability. Higher magnetic flux can pass through the coil with the bead layer of lower

reluctance. This causes better coupling between coil windings and thus a larger output.As a result, D_{max} and ΔL_{max} will increase in the presence of thicker magnetic bead layer.

2.5.5 Effect of frequency on sensor output

As illustrated in Figure 2.22, the normalized variation of the sensor output amplitude (δ_{Vs}) is the indicator of hybridization occurrence. According to the effect of ohmic resistor of the coil on the output signal, frequency of the current source (input signal) should be selected carefully and in the way that keep the *Rc* as a constant. Substituting Vs from the equation in Figure 2.22a into the equation in Fig. 2.22b results in:

$$\delta_{V_s} = \frac{\sqrt{(R_c)^2 + (\omega L_{c2})^2} - \sqrt{(R_c)^2 + (\omega L_{c1})^2}}{\sqrt{(R_c)^2 + (\omega L_{c1})^2}} \qquad (2\text{-}6)$$

Equation (2-6) indicates that for the real coil, the output variation is a function of input frequency. The behaviour of the sensor output with respect to frequency is plotted in Figure 2.24 [71]. For each value of frequency and μ_{rB}, the output signal is maximum at a specific value of outer diameter (D_{max}). Figure 2.24a shows the relationship between these values and that optimum diameter of the coil decrease by increasing the frequency. In Figure 2.24b, the sensor output $\Delta Vs = \delta Vs$ (at D_{max}) is normalized by

$$\Delta L_{max} = \lim_{\omega \to \infty} (\Delta vs)^1$$

According to this graph, higher sensitivity can be achieved at higher frequency, and even less permeable beads can result in a more sensitive sensor at higher frequency.

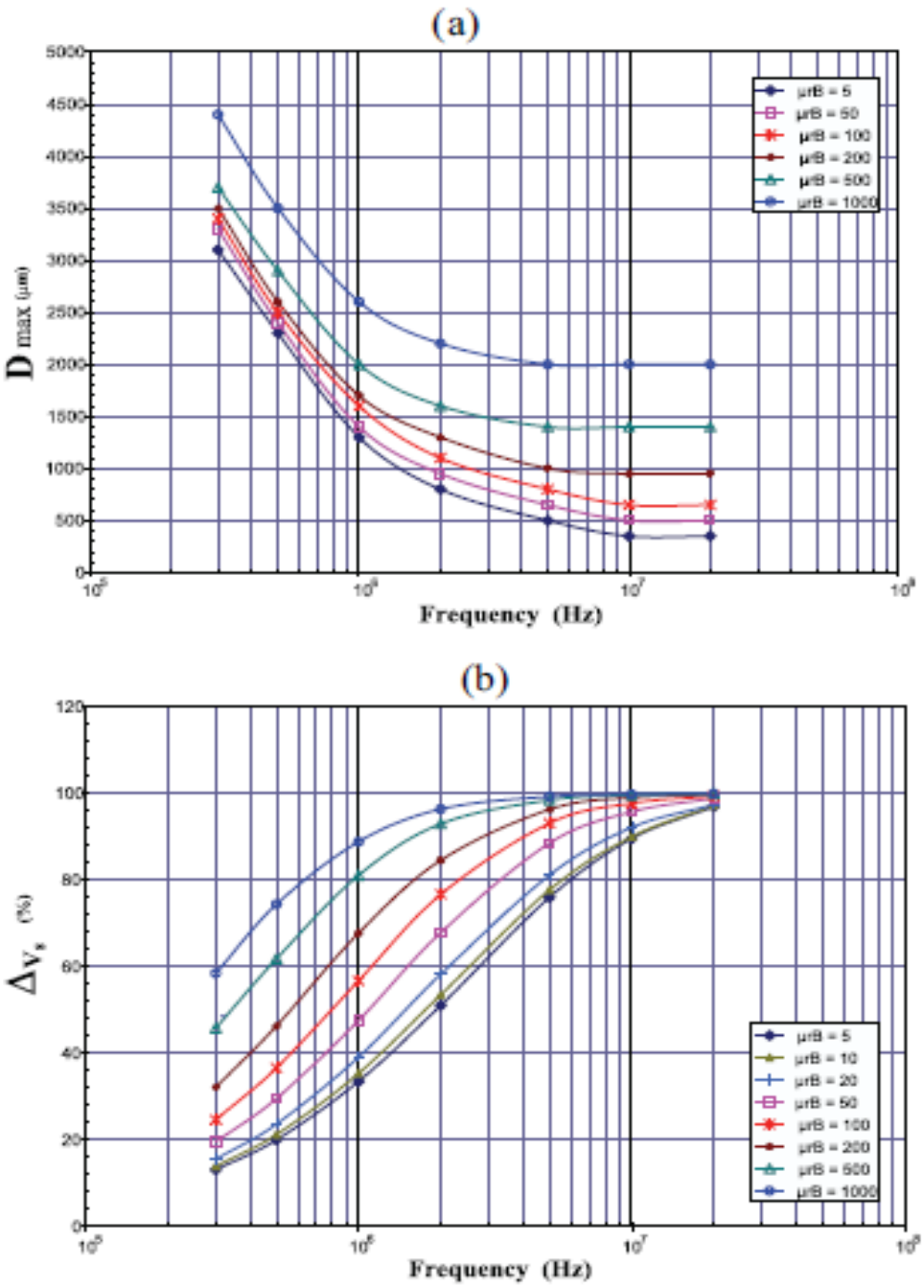

Figure 2.27: Effect of source's frequency on (a) Coil outer diameter (b) Percentage of maximized sensor voltage

In the case of sensitivity, although the sensor is affected by physical parameters (permeability of the beads) and geometrical parameters but after fabrication, sensor size is fixed and cannot be changed, therefore only magnetic permeability and thickness of the magnetic beads layer can alter the output signal and influence on sensitivity.

2.6 Summary

A review of well-known methods in the area of magnetic beads detection presented in this chapter emphasised frequency-based sensors, which are the chief concern of this research. In-depth description of the biosensor based on spiral inductor has been presented. Although the work was

based on simulation only, the results and ideas were taken to consider for starting this project and trying to make them real and demonstrate them experimentally.

For having an overall impression of most of the works done in frequency-based sensors, some useful information from two key works in this area have been summarised and compared in Table 2.4. It can be seen from the comparison that higher the frequency, the better the sensor resolution (GHz range has higher sensitivity than MHz and KHz).

Table 2.4: Comparison of different studies for frequency-based magnetic bead detection

	California Institute of Technology (Cal.Tech) 2009				Cal.Tech 2011	Bristol university
Inductor Diameter	250 µm	250 µm	250 µm	250 µm	110 µm	Oval Shape
Inductor Area (mm)2	0.049	0.049	0.049	0.049	0.0095	56.25
Bead Size (µm)	4.5	2.4	1	50 nm	4.5	2.8
Bead Volume $(\mu m)^3$	47.713	7.23	0.523	0.0000654	47.713	11.49
Sample Volume $(\mu m)^3$	47.713	7.23	0.523	0.0319152	47.713	1149000
Area/ Sample Volume	0.00102	0.0067	0.0936	0.007	0.000199	4.9×10^{-5}
Resonance frequency	928 MHz	928 MHz	928 MHz	1 GHz	1 GHz	529 KHz
Frequency Shift	[928 MHz/8.9 KHz]≈ 10.42×10^4	[928 MHz/2.4 KHz]≈ 38.6×10^4	[928 MHz/213 Hz]≈ 435×10^4	[928 MHz/2.8 KHz]≈ 33.14×10^4	[1 GHz/18 KHz]≈ 55.5×10^3	[529 KHz/3.5 Hz] ≈ 151×10^3

Although studies have been conducted to detect the magnetic labels, the review has found that the presented techniques are designed and applicable for immunoassay methods only. In their method the magnetic particles were attached to the antibody and magnetic detection performed after successful bonding of the antibody-antigen. As a result, those detectors were designed for immunoassay setup and may not be valid and suitable for molecular detection or nucleic acid test, which is the main aim of this research.

In the next chapter the introduction to the magnetism and magnetic beads is demonstrated, including the method for synthesising iron oxide particles and their characterization.

CHAPTER 3: **PREPARING MAGNETIC NANOPARTICLES USING MICROEMULSION**

3.1 Introduction

The detection of bio-molecular interaction in medical and biosensor research is of fundamental importance. Biological entities have non-magnetic nature, and most of the bio-molecules have zero magnetic susceptibility, thus magnetic particles are a very powerful candidate and an important source of labels for clinical diagnosis. Factors such as simplicity and rapidity, long-term stability, easy miniaturization and elimination of interference effect and noise from sample background make them a viable alternative method for labelling in molecular assays [76].

Magnetic particles are commercially available in a choice of sizes, magnetic properties and coatings; therefore, each has a specific fabrication method. These small particles have a polymeric or non-polymeric (silica) body, inside which is a single or multi-core of iron oxide nanoparticles. In the presence of external magnetic field, these cores help induce a net magnetic moment.

In order to understand the working principles of the magnetic biosensors that use magnetic particles as labels, it is necessary to first comprehend the fundamentals of the engaged phenomenon. Hence, the first section of this chapter gives a brief review of magnetic materials and the phenomenon of *superparamagnetism*. The second section introduces all of the magnetic particles used so far for this research. The final section focuses on explaining the different methods of synthesizing magnetic particles and describes in detail how the magnetic particles were synthesized for this project.

3.1.1 Magnetic material

Electric field and magnetic field are two different but interconnected phenomena. The magnetic field is produced by the influence of electrical current and magnetic material. The field lines have no end and are always in a closed loop. The magnetic force appears in the direction of the magnetic lines and causes the materials to align in their direction. Different materials have dissimilar reactions to the external magnetic field. This reaction is dependent on the spin orientation of the material at atomic level or the orbital electron motion. Therefore, based on the materials' reaction to the magnetic field, they are categorised as described below.

3.1.2 Diamagnetic material

Diamagnetism occurs in an atom without the net magnetic field, while the magnetic field produced by electron spin cancels out the magnetic field created by the orbital electron motion. Therefore, in

the presence of external magnetic field, the material induces the magnetic field in the opposite direction to the external field. These materials have no permanent magnetic moment and their magnetic permeability is less than the free space permeability ($\mu_0 = 4\pi\times10^{-7}$ H/m). Diamagnetism is the weak effect which exists latently in all materials (water, wood, copper, gold etc.) but it is negligible in some types of materials, such as paramagnetic and ferromagnetic [76].

3.1.3 Paramagnet material

Unlike diamagnetism, the two generated fields from orbital motion and electron spin do not countervail one another. These materials have permanent magnetic moment (dipoles) but they are randomly oriented and in the presence of external magnetic field these dipoles align with the applied field (due to a small torque being supplied to them), thus a net magnetic field is produced in the direction of applied field. These materials have$\mu \geq 1$, which means they are attracted by the external magnetic field. However in the absence of the applied field their magnetic moments change their orientation (due to the thermal agitation) and consequently the material cannot retain the magnetization and the magnetic properties. Materials such as magnesium, potassium and oxygen are examples of paramagnetic materials [77].

3.1.4 Ferromagnetic and ferrimagnetic materials

Similar to the paramagnetic material, ferromagnetic materials have permanent magnetic moment, but their moments are spontaneously aligned together, caused by the strong interaction and energy exchange between their neighbouring atomic moments (interatomic forces). These atoms align in parallel and form a *magnetic domain*. These domains have different shapes, directions and sizes (μm-cm). In the presence of external magnetic field, the domains in the direction of external field have a tendency to expand by utilizing other domains. Consequently, a strong internal moment will be generated and remain in the material, which cannot be cancelled even if the external field was removed. As a result, these materials show specific domain orientations based on each applied magnetic field, hence they have a memory; this is the phenomenon of hysteresis. The relationship between field strength and magnetization is shown in the hysteresis loop (H-M). Only a few materials are ferromagnetic, mainly iron, cobalt, nickel and some of their alloys.

In ferrimagnetic materials, the orientations of some atoms are antagonistic, thus the generated internal magnetic moment is less than ferromagnetic materials. The most important examples of these materials are ferrites, such as magnetite (Fe_3O_4) and maghemite (Fe_2O_3, γ-Fe_2O_3). Maghemite can be produced by the oxidation of magnetite at low temperature, at which its susceptibility reduces. They have similar structures but their electrical properties are different; maghemite is

chemically more stable than magnetite [78]. These materials lose their magnetic characteristics and magnetization at temperatures above Curie point.

3.2 Magnetic particles

Magnetic particles have been developed and widely used for different types of applications, such as drug delivery, nucleic acid purification and a variety of laboratory diagnostics. These particles have sizes ranging from a few nanometer up to micrometers based on their application [79-81]. Nanometer size particles are preferred for binding with biological entities and also as the biomolecular labels (by surface modification), due to their small and comparable size to biomolecules. On the other hand, external magnetic field can take a control over them and manipulate them for applications such as drug delivery [42,76].

In the event that the nanoparticles are ferromagnetic, the interparticle magnetostatic interaction and van der Waals interactions can cause the particles' agglomeration [42, 82]. The magnetostatic force depends on the thermal stability of magnetic moment and is normally stronger than van der Waals interactions. However, at room temperature this effect is negligible, and clustering of particles is led by van der Waals' force [82]. Therefore, to protect the nanoparticles against agglomeration, they ought to be dispersed in an appropriate liquid. The liquid can be either water or different types of oil, based on their synthesis method. In some cases surface modification and functionalization is also required which can be done via organic, inorganic or oxide materials (e.g. polymers, gold and silica) [81].

3.3 Superparamagnetism

Superparamagnetism happens within nanoparticles synthesised by ferromagnetic or ferrimagnetic materials. Theoretically, the magnetic properties and characteristics of these nanoparticles are strongly dependent on their sizes. In particles with sizes less than 500nm, the magnetic domain reduces and becomes a single domain (like a magnetic dipole); the domain wall will disappear and therefore magnetization changes occur due to electron spin only [81]. In the single domain nanoparticles, the uniform magnetization occurs at any field and the anisotropy energy is comparable with thermal energy. Thus the magnetic moments of the particles fluctuate randomly due to the thermal disturbance and as a result the net magnetic moment becomes zero in the absence of the external field and the particles demagnetize quickly. This behaviour is called superparamagnetism. The superparamagnetic materials behave similarly to the paramagnetic materials below Curie temperature [83]. Their difference is in the presence of external magnetic field, which lowers the strength of field is required for the superparamagnetic particles to reach the saturation level, and the magnetization is greater than the paramagnetic particles [81].

Superparamagnetic nanoparticles have less magnetic attraction toward each other in the presence of external magnetic field compared to the ferromagnetic particles, thus they will not aggregate. This performance is the necessity for biomedical application. Hence most of the nanoparticles are produced with superparamagnetic characteristic.

Below is the description of some of the fundamental magnetic properties of material:

- The intensity of external magnetic field is expressed by ***H*** with the unit of **(A/m)**

The magnetic dipole moment per unit volume or the average field strength caused by the magnetic moments (generates from electron spins) is the definition of *Internal Magnetization* ***M*** with the unit of **(A/m)**. This internal magnetization is induced by external field ***H***, thus there is a linear relationship between them which can be expressed as equation 3.1:

$$M = \chi_m H \qquad (3.1)$$

Where $\boldsymbol{\chi_m}$ is defined as *Magnetic Susceptibility* in isotropic media and it is dimensionless constant which indicates the magnetization level of a material in response to an external magnetic field.

- The density of *Magnetic Flux* ***B*** for free space is illustrated here as a linear function of magnetic field:

$$B = \mu_0 H \qquad (in\ Tesla\ (T)) \qquad (3.2)$$

$\boldsymbol{\mu_0}$: the permeability of free space ($\mu_0 = 4\pi \times 10^{-7}\ (N/A^2)$)

Considering the internal magnetisation of material ***M***, the actual relationship between ***B*** and ***H*** can be defined as:

$$B = \mu_0 (H + M) \qquad (3.3)$$

Therefore, both internal and external magnetizations are calculated for the magnetic flux density.

Consequently:

$$B = \mu_0 (H + \chi_m H) = \mu_0 H\ (1 + \chi_m) = \mu_0 \mu_r H = \mu H \qquad (3.4)$$

Where

$$\mu_r = 1 + \chi_m \qquad (3.5)$$

And

$$\mu = \mu_0 \mu_r \qquad (3.6)$$

$\boldsymbol{\mu}$ is *permeability* with the unit of Henry per meter (H/m) which can be defined as the ability of a material to become magnetized.

There are two other important parameters that arise only within ferromagnetic material: *Remanence* (***Br***) and *Coercivity* (***Hc***). After removal of external magnetic field (***H***=0) from the ferromagnetic material, specific amount of flux density remains on it ,which represents the Remanence, having the unit of tesla (**T**). For removing this flux density, the field strength is required to apply (*coerce*) to the material. Therefore permanent magnets have high *Coercivity* ($\boldsymbol{H_c}$). The unit of this quantity is **A/m**.

3.4 Commercial magnetic beads used in this research

Three different types of commercially available magnetic samples were chosen in this project, each of which has specific specifications. Their sizes range from nanometer to micrometer. The small ones (nm size) were chosen to test the sensor sensitivity and the larger ones (µm) were considered and tested with the idea that this sensor will be used in the future with the real biological sample, including nucleic acids and particles with large surface area, which are preferred for binding to the nucleic acid [80]. These particles are described in the following subsections.

3.4.1 Superparamagnetic beads from Cytodiagnostics

Superparamagnetic iron oxide nanoparticles are in water-soluble format and they are coated with a protective layer (carboxyl functional groups) for conjugation [105]. Although the manufacturer claimed six-month stability of particles in the solution, these particles unfortunately oxidized within a month, and the solution colour turned to light brown. On the other hand they oxidized quickly (within two minutes) with exposure to oxygen.

Superparamagnetic Nanoparticles (Magnetite Fe_3O_4)
Diameter: 10nm (+/- 1.5nm)
Concentration: 5mg/ml
Magnetization: >45 emu/g
Volume: 5ml
Formulation: Supplied in ddH2O
Single Bead Volume: 523.6e-19 g
Bead Mass: 2.7 attogram

Figure 3.1: Cytodiagnostics Beads

3.4.2 Magnetite powder (Fe_3O_4)

This powder sample was purchased from Inoxia Ltd., UK. Magnetite is a ferrimagnetic material with high density and good thermal conductivity. Figure 3.2 shows the TEM image of these Fe_3O_4 particles taken to show the actual size distribution. The particles' sizes vary from 1-50µm.

Synonyms: Iron(II,III) oxide, Fe_3O_4

Magnetite Powder
Diameter : 50µm
Magnetization: >45 emu/g

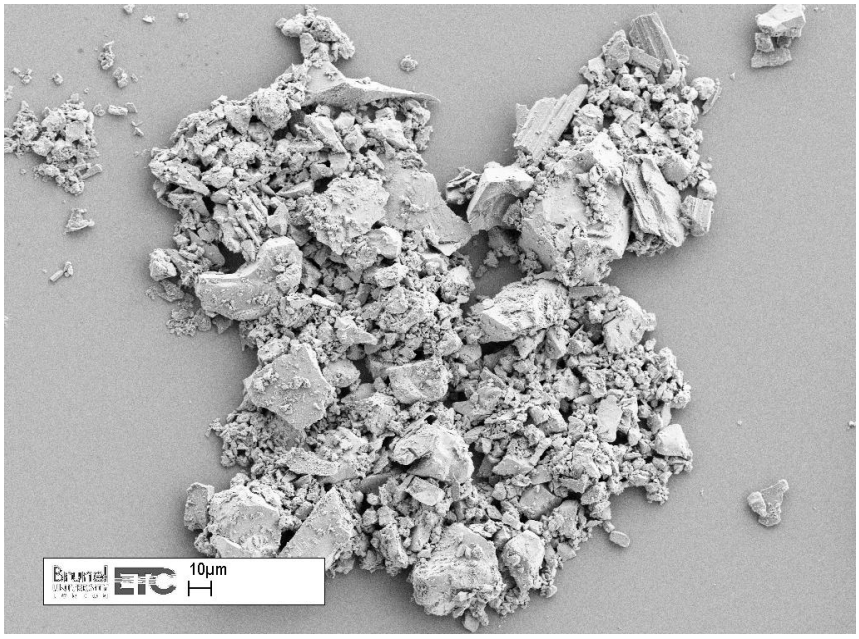

Figure 3.2: TEM image of magnetite powder

3.4.3 Magnetisable Agarose Beads (Scipac Ltd.)

These beads are kept in a viscous suspending medium (50% glycerol) and are stable for two years. The magnetic iron nanoparticles are impregnated into these beads. Figure 3.3 shows the TEM image of these beads. It was found that the particles range in size from 200nm up to 1µm. These particles have 4% agarose and were only used in the GMR sensor experiment (Chapter 6).

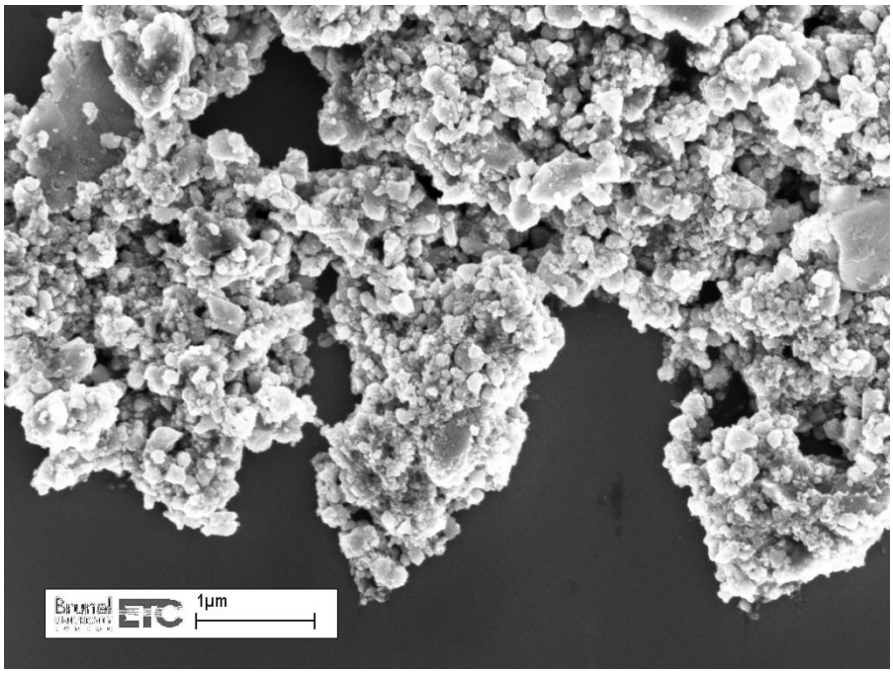

Figure 3.3: TEM image of magnetisable agarose beads

The above magnetic samples were tested by magnetic sensor and the results are presented in chapter 6.

3.5 Synthesising magnetic (iron) particles within microemulsions

Magnetic particles are widely used in several biomedical applications, such as magnetic biosensors, due to their unique characteristics and properties. They can be prepared by using iron, cobalt and nickel. Although all of these oxidize readily, iron oxide (such as magnetite) shows more stability and also biological compatibility compared to the other magnetic metals [84].

The iron oxide particles are commercially available through companies such as Dynabeads, Cytodiagnostics, Chemicell, Bangs Laboratories, Polysciences and many others. They can be ordered with specific coating (e.g. gold, silica and biotin) depending on the types of applications. However, the cost of buying them is high, especially when large amounts are required for experimental purposes. Therefore, synthesising them is of significant interest, while the preparation time is just a few hours and is much more cost-effective.

Within different types of these particles, superparamagnetic iron oxide nanoparticles (SPION) are attractive and useful because they are not retaining any magnetism in the absence of external magnetic field, and their exclusive chemical, physical and thermal properties make them the best candidate for applications such as MRI and cellular therapy. Synthesising iron oxide particles by chemical methods can be divided in two main categories: co-precipitation and microemulsions [85].

The co-precipitation method is simple but needs an oxygen-free environment. In this methodology synthesized particles are normally uniform with small sizes (< 100nm). The procedure can be done within single beaker, by adding the base (i.e. ammonium hydroxides) to the desirable amount of salt solution [84]. The salt solution (e.g. iron chlorides, iron nitrates or sulphates) can be Fe (II) or Fe (III) or a mixture of the two, with the ratio of Fe^{2+}/Fe^{3+} = 1/2 plus water. The existence of oxygen unbalances this ratio and deviation from it can influence on the magnetic property of the synthesized particles. As a result, some impurities such as γ-Fe_2O_3 and α-Fe_2O_3 will be present in the products, of which the latter is nonmagnetic. Therefore, the co-precipitation reaction needs to be done in the presence of nitrogen as a prevention of oxidation [86]. However, nitrogen can help to prevent aggregation of particles and it reduces the particles' size. This method is not without difficulty, because the shape of nanoparticles cannot be controlled and nitrogen is insufficient to prevent aggregation, consequently synthesized particles have to be coated with some type of surfactant [87].

Conversely, in the microemulsion method the particles' shape and morphology can be well controlled. This method can be defined as stable liquid mixtures of water in oil solutions, which also contains surfactant and sometimes co-surfactant (which both are amphiphilic). The surfactant helps prevention of particles' agglomeration and growth of the particles inside the microemulsion droplets by lowering the surface tension of liquids. However, surfactants can only reduce the oil-water interfacial tension by a specific amount and that is the reason of adding co-surfactant to the solutions [88]. On dispersal into immiscible solution of oil/water, surfactant molecules can form a variety of structures (equilibrium phases) by locating itself at the oil/water interface [79]. Figure 3.4 shows the most probable structures.

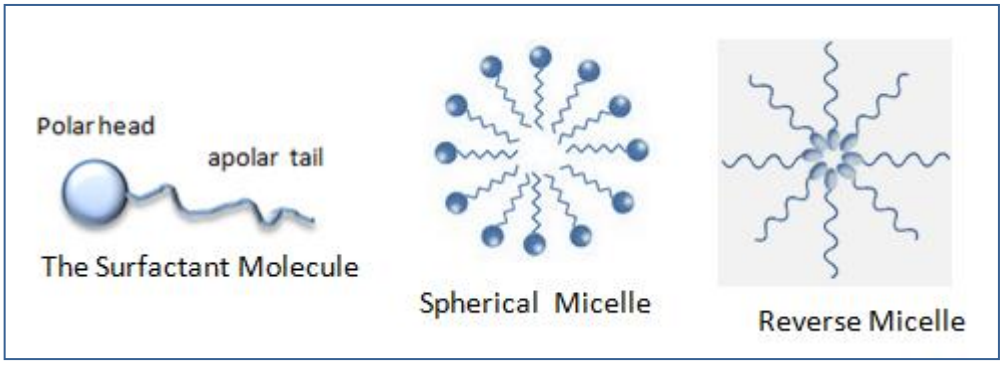

Figure 3.4: Schematic illustration of surfactant structures

Depending on the surfactant molecular structures, different types of microemulsions microstructures can be formed. Figure 3.5 shows the schematic of the most common microemulsion droplets.

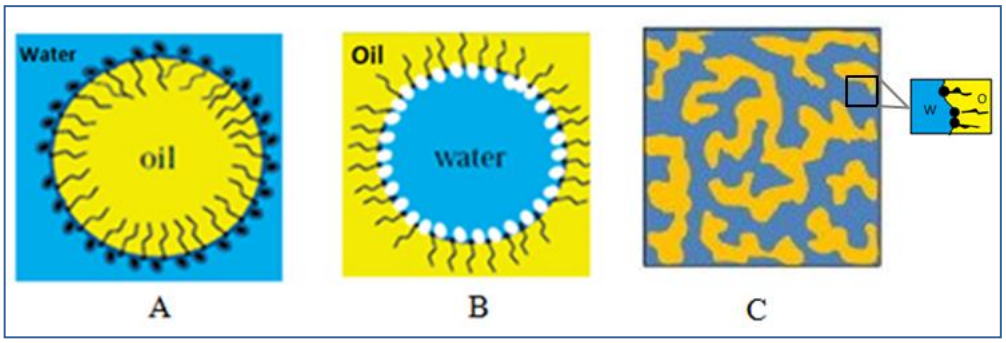

Figure 3.5: (a) Oil in water microemulsion (o/w), (b) Water in oil microemulsion (w/o), (c) Bicontinuous microemulsion

When the volume of water is low in the solutions, the existence of water in oil (w/o) microemulsion droplets are likely. Conversely, a higher volume of water results in o/w microemulsion; in the case of water and oil volume being equal, then bicontinuous microemulsion can result. The characterization of different microemulsion systems has been reviewed by Lawrence [79]. Kowgli et al synthesised metal particles within bicontinuous microemulsions and claimed that higher yields of particles can be produced in bicontinuous phase than in the w/o and o/w systems [89].

The microemulsion methodology is based on the Brownian motion for the reaction between two microemulsion solutions: a reducing agent (i.e. $NaBH_4$, etc) and salt solution or precursor (i.e. $FeCl_3$, $FeCl_2$ etc.). The reducing agent donates electrons to the other materials and chemically reduces them.

After choosing the right microemulsion reactants, the process of particles preparation is straightforward. Two microemulsion solutions should be prepared, one with metal salt and one with reducing agent. Mixing these two solutions results in nanoparticles' formation, and the reaction occurs very quickly [90]. Figure 3.6 illustrates the procedure of nanoparticle synthesises [90]. Depending on the parameters of four reactants (i.e. concentrations) used for preparing microemulsion solutions, particles' sizes, shapes, magnetic properties and heating effects will be different [91]. Some other external parameters such as pH and temperature also influence this reaction.

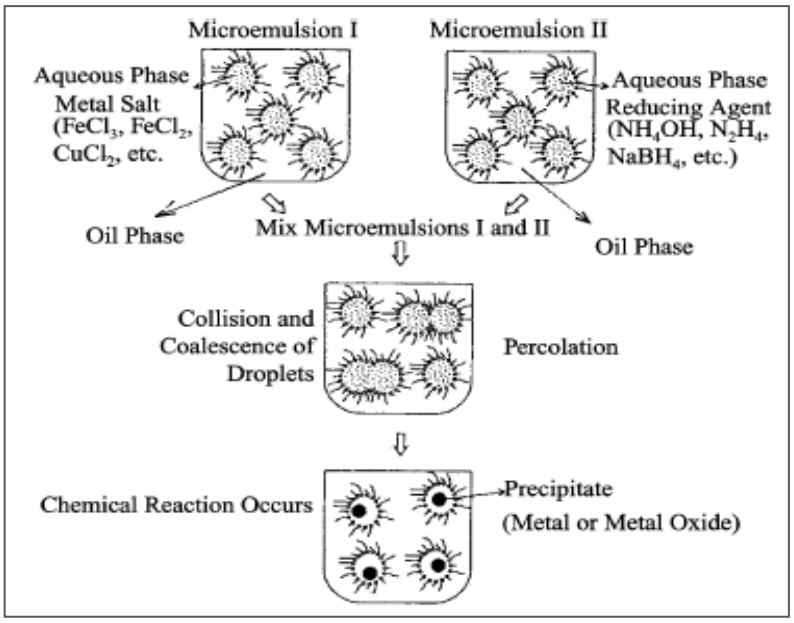

Figure 3.6: The procedure of metal particles synthesis by microemulsion method [89]

It was noted that w/o and o/w microemulsion methods have narrow size distribution of particles, with very low amount of aggregation [92]; the size is controllable, although yield of particles synthesized may be questionable and higher yields can be achieved using bicontinuous method.

The microemulsion system of interest in this research should contain iron or iron chloride as a salt or precursor. Different protocols for iron nanoparticle synthesis have been investigated in the literature, but most of them are elusive or the synthesized particles have iron core with the addition of a silica shell, because of biocompatibility issues. The main aim of the most protocols published each year is synthesizing particles for drug delivery and clinical diagnostics, thus biocompatibility is of primary importance; therefore, iron particles cannot offer those applications without surface functionalization and a biocompatible shell covering the iron core.

In this project the particles were tested with the magnetic sensor, thus magnetic properties such as high coercivity, superparamagnetism and high magnetic susceptibility are the only important characterizations. The particles were not kept for several months or tested *in vitro*, thus surface modification is not required here. Several authors have reported the synthesis of metal nanoparticles [79, 90, 92-94] but only few researchers have presented the protocols for the iron nanoparticles synthesis (Table 3.1). Some of the common surfactants and co-surfactants used in metal nanoparticle synthesis [95] are:

- Sodium bis (2-ethyhexyl) sulphosuccinate (AOT);
- Triton X100;
- Cetyltrimethylammonium bromide (cTAB);

- Amines, amine oxides;
- Alcohols;
- n-butanol; and
- Phosphates.

Table 3.1 shows some of the protocols used for synthesising iron nanoparticles. It can be seen that CTAB microemulsions seem to be the most commonly used system for synthesising iron nanoparticles. CTAB is a strongly charged positive ionic surfactant, which facilitates its rapid absorption into the iron nanoparticles [93].

Table 3.1: Protocols for iron nanoparticle synthesis

Microemulsion system	Precursor	Reducing agent	Size of particles produced	Additional comments	Reference
cTAB/n-butanol/ n-octane (weight % 12/1/44)	$FeCl_3$ (Iron chloride) [0.08M] (34%)	$NaBH_4$ (sodium borohydride) [0.2M] (34%)	40-200nm depending on flow rate	Particle size was varied by flow rate of $NaBH_4$; at 0.75ml/min particles were seen to grow to 200nm Spherical shape Ms = 168 (emu/g)	Zeng & Baker (2011)[95]
CTAB/n-butanol/ n-octane (12/1/44)	$FeCl_3$ [0.08M]	$NaBH_4$ [0.5M]	40	Spherical shape Flow rate (50 ml/min) Ms = 133 (emu/g)	Zeng & Baker, (2011)[95]
CTAB/n-butanol/ n-octane (1:4.1:11.7)	$FeCl_3$ (Iron chloride) [0.2M]	$NaBH_4$ [0.8M]	8-16nm	Iron core/Fe_3O_4 shell Particle size based on O/W ratio: Ratio 7: 1 = 8nm Ratio 2.5:1 = 16nm Fe_3O_4 shell thickness: 2-3nm	Zhang & Liao (2009) [93]
CTAB/ n-butanol/ n-octane Wt.% (12/10/44)	$FeCl_3$ [0.24M]	$NaBH_4$ [0.9M]	12-18 nm	Iron core/Fe_3O_4 shell Round and uniform particles, increasing water phase results in oval shape particles. Shell thickness: 2-3nm	Kimberly & Sung (2007)[96]
AOT/N-hexane	Deoxygenated Fe^{3+} and Fe^{2+} salts (molar ratio 2:1)	Sodium hydroxide	Less than 15nm	More uniform particles prepared by precipitation at lower temperatures in the presence of nitrogen gas	Gupta & Gupta (2005)[85]
AOT/N-heptane (W=10)	$FeCl_3$	$NaBH_4$	3.4nm		Capek (2004)[97]
CTAB/ Butanol/octane/water	Iron precursor (not stated) HAuCl4	Hydrazine	2.5nm thickness of shell	Gold and iron grown with complementary crystal structures	Capek (2004)[97]

3.6 Experimental material and method

Iron particles were synthesised through water-in-oil (w/o) microemulsion method. Iron nanoparticle has been chosen over iron oxide nanoparticles because of the higher saturation magnetization value (M_s) of iron. M_s indicates the maximum achievable magnetization value in response to a magnetic field. Iron has M_s > 210 emu/g while this value in iron oxide is 90 emu/g [95]. Iron particles were prepared using two similar flasks of microemulsion solution, each of which contained:

- A surfactant: 0.5M cetyl trimethyl ammonium bromide (CTAB) ≈ 0.2188g
- A co-surfactant: n-butanol = 1000µL
- An oil phase: n-octane = 4400µL
- And water phase including $FeCl_3$ (0.08M) and $NaBH_4$ (0.2M), each dissolved in 10ml of deionised water. The reduction of an aqueous iron chloride within $NaBH_4$ was performed in air.

For preparing the microemulsions, two flasks with similar combination of CTAB, n-butanol and n-octane were made, then 3400 ml of $FeCl_3$ solution was added to one of the microemulsion flask and 3400 ml of $NaBH_4$ was added to the second flask. As shown in Figure 3.7a, the flask with yellow colour contains iron chloride. After stirring and mixing in each flask, the solution containing $NaBH_4$ was added to the same volume of iron chloride flask (Figure 3.7b, c). The solution colour changed to dark brown within a minute. The microemulsion solution was then mixed by stirring (Figure. 3.7d). According to the regular contact and collisions of the reacting species in the solution, iron nanoparticles were precipitated within the micro-droplets of the solution [95]. The nanoparticles were then separated by permanent magnet (Figure 3.7e).

Different attempts were made for synthesising iron nanoparticle and the mentioned protocol was chosen from them because of its best outcome and result. Nanoparticles produced with this method stayed stable for several days with narrow size range distribution and uniform properties (physical and chemical).

Using different charged surfactants was conducted, such as Triton x-100 (non-ionic) and AOT, but the protocols were vague (Figure 3.8a). Another attempt was made by changing the molar concentration of surfactant (CTAB) and the reducing agent ($NaBH_4$). Table 3.2 shows some of the different procedure tried for producing nanoparticles. However in all cases the molar ratio between surfactants and oil phase remained constant; CTAB/n-butanol/n-octane: 12/1/44.

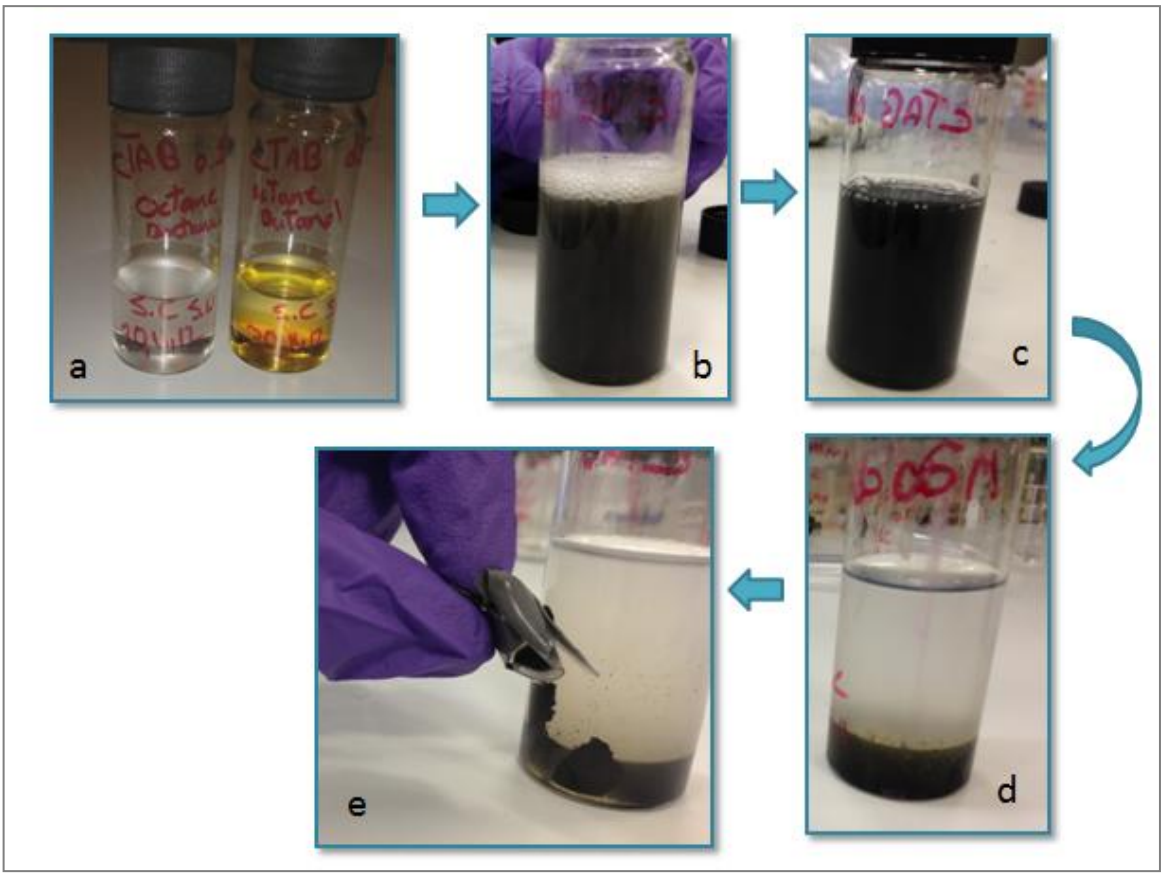

Figure 3.7: Preparing iron particles within w/o microemulsion system

Table 3.2: Iron nanoparticle preparation with different concentration of CTAB and $NaBH_4$

	Test 1		Test 2		Test 3	
Microemulsion solutions	I	II	I	II	I	II
Aqueous phase	0.08 M Fe_3O_4	0.1M $NaBH_4$	0.08 M Fe_3O_4	0.1M $NaBH_4$	0.08 M Fe_3O_4	1M $NaBH_4$
oil phase (Octane)	4400 µl	4400 µl	4400 µl	4400 µl	4400 µl	4400 µl
Surfactant (CTAB)	1 M	1 M	0.5 M	0.5 M	0.5 M	0.5 M
co-surfactant (n-Butanol)	1000 µl	1000 µl	1000 µl	1000 µl	1000 µl	1000 µl

The test 1 was done while the molar concentration of the CTAB and NaBH4 were 1 molar and 0.1 molar. The results show that the reactants were not solving completely (Figure 3.8b), the particles produced became oxidized quickly and the colour of solution became light brown within a day.

In test 2 the concentration of the CTAB was decreased to 0.5M. The solution stability was good and the reactants mixed together; however, non-uniform particle sizes were produced, which was due to the small concentration of the reducing agent, therefore in test 3 the molar concentration of the $NaBH_4$ was increased to 1M.

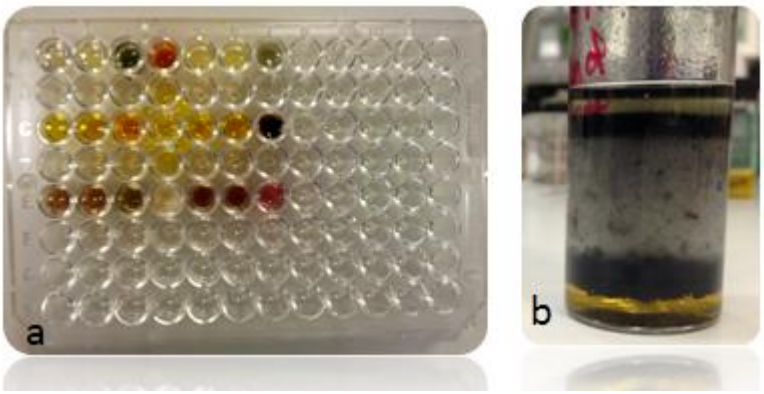

Figure 3.8: (a) Different surfactants tried for nanoparticles synthesis, (b) The microemulsion with 1M of CTAB (Test 1)

The outcome of microemulsion system in test 3 was the synthesis of iron particles with a very large size. Hence, between 0.1-1M of reducing agent, 0.5M and 0.2M was tried, which both showed excellent results, but according to the work done by Baker et al [95] with similar protocol, nanoparticles produced with 0.5M of reducing agent had a smaller value of magnetization (M_s), therefore NaBH4 with concentration of 0.2M was chosen as the best protocol for this project. The nanoparticles synthesised are superparamagnetic, which means that they are not magnetic without the presence of magnetic field, and they are not aggregate in the solution, thus they are likely to stay uniform.

The synthesized nanoparticles were characterized using Zygo white light interferometer for surface roughness measurement and transmission electron microscopy (TEM) for size distribution and shape (Figure 3.9). The Zygo device tests the nanoparticles through their depth and the average roughness of particles were about 40nm (Figure 3.9a). Preparation of the nanoparticles for this test was done by applying small amounts of sample on the silicon wafer and then placing the wafer under the interferometer. Unfortunately, the iron particles oxidized in contact with air, therefore an alternative way is to undergo the nanoparticles' separation under the nitrogen gas and minimise exposure to oxygen using desiccator. Figure 3.9b, c show the TEM images of particles. The size distribution is from 15-30nm. Figure 3.9b shows that the nanoparticles have a spherical shape with 4-5nm cTAB coating size.

Magnetic particles used in this work for detection are designed to exhibit superparamagnetic behaviour. After the exposure of external magnetic field, these particles were magnetised and experienced a net magnetic force. This force can be applied under the influence of two sources. The first and main source can be the result of only external magnetic field, called imposed force, which then the uniformity of the magnetic field is important factor.

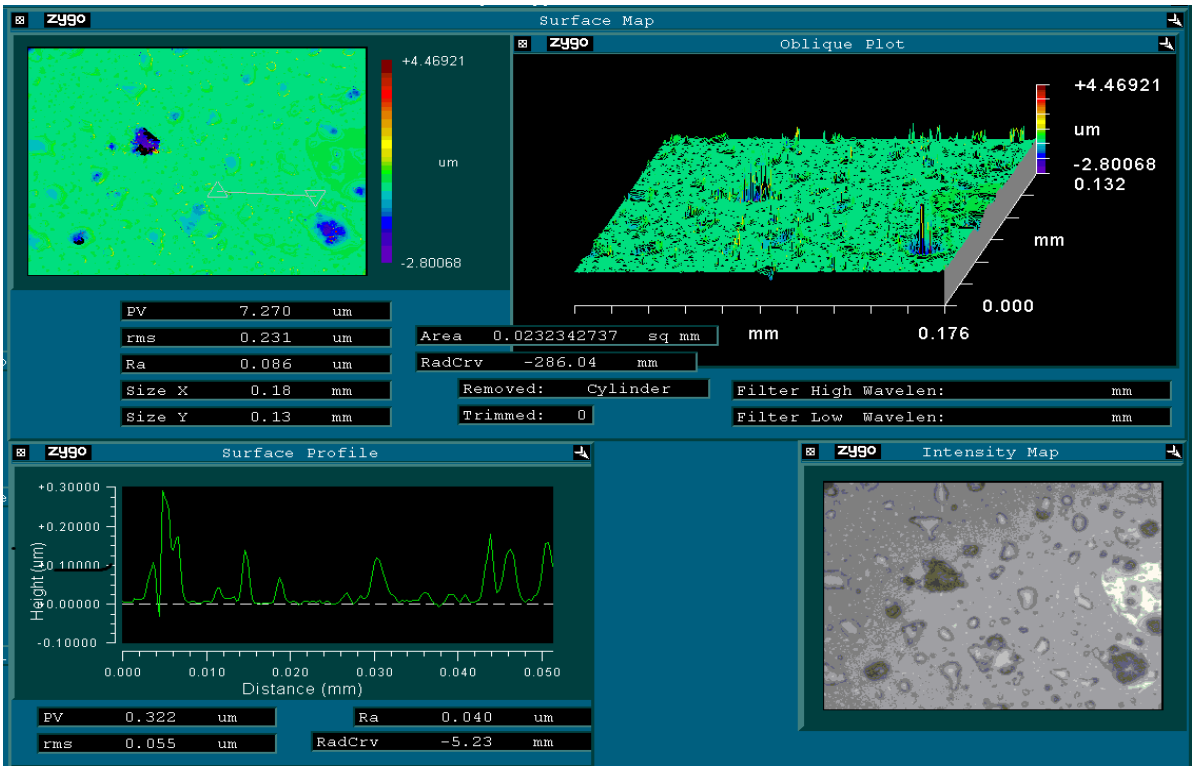

a

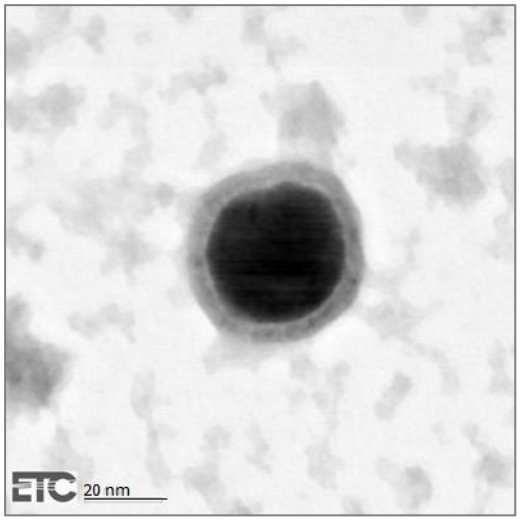

b

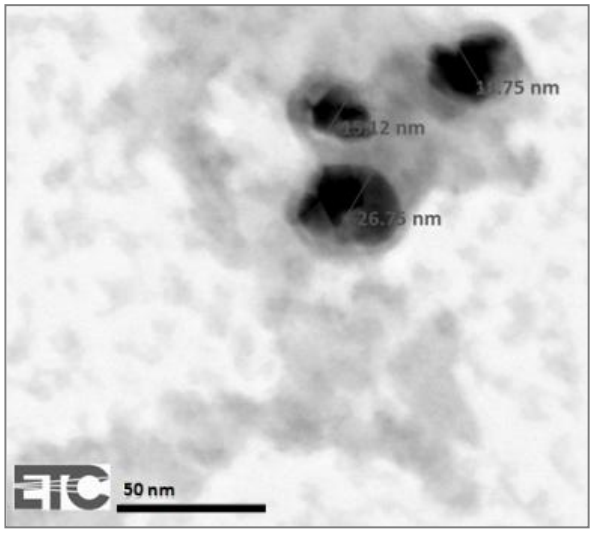

c

Figure 3.9: (a) The light interferometer images of iron nanoparticles with average size of nanoparticles: 40nm, (b) STEM image of single iron particles with cTAB coating, (c) TEM image of synthesized iron nanoparticles with size distribution of 15-27nm.

The second source is when magnetic particles are placed close to each other and the internal magnetic field of one particle induces the magnetic moment to the neighbouring particle. This type of force is called mutual particle [98]. The imposed field is stronger compared to the mutual effect and by distancing the particles this mutual effect decrease quickly.

3.7 Heating effect of magnetic nanoparticles

The magnetic property and heating efficiency of the magnetic particles under an AC applied field were investigated by Li et al in 2011 [99]. It was noted that the heat generation in nanoparticles is the results of relaxation loss and hysteresis loss and it also dependent on the particle size and the applied magnetic field intensity. They prepared different sizes of particles in the range of 8-103nm in an aqueous solution and then they studied the *in vitro* heating effect of the applied field on the particles. The external magnetic field had 100KHz frequency with two different strengths of AC magnetic field: 12mT and 30mT. They used five different sizes of nanoparticles: sample A with 8nm size is superparamagnetic, which means no remanence and coercivity; samples B, C and D are single domain, and ranged from 24, 36 and 65nm; and sample E was estimated to be 103nm. According to the superparamagnetic nature of sample A, there is no hysteresis loss for that sample, therefore the heat generated in this sample is mainly attributable to the relaxation loss. The results of the heating effect are illustrated as time-dependant temperature curves (Figure 3.10) and the samples were dispersed in agar phantoms.

Samples B and C are similar to the synthesized nanoparticles (with average size of 25nm). As illustrated in Figure 3.10a, the temperature increase (ΔT) of sample B at 50s is less than 10°C.

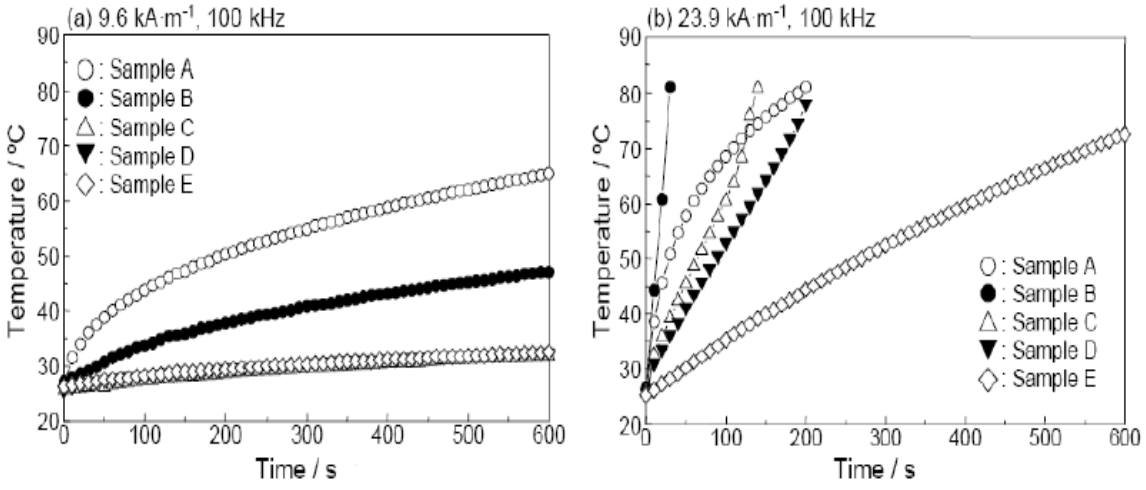

(a) Under applied AC magnetic field of 12mT (b) AC magnetic field of 30mT

Figure 3.10: Time-dependant temperature curve [99]

Kong et al [100] studied the effect of temperature on the magnetic properties of magnetite nanoparticles (Fe_3O_4) under the applied magnetic field of 1.2T (the nanoparticle sizes are not stated). Properties such as the saturation magnetization (M_S), remanence (M_R) and coercivity (H_C) were investigated. M_S for magnetite at room temperature (25°C= 298K) is 63.79 (emu/g). It was concluded that decreasing temperature can increase the above magnetic properties. Figure 3.11 shows the temperature dependant of M_S and M_R.

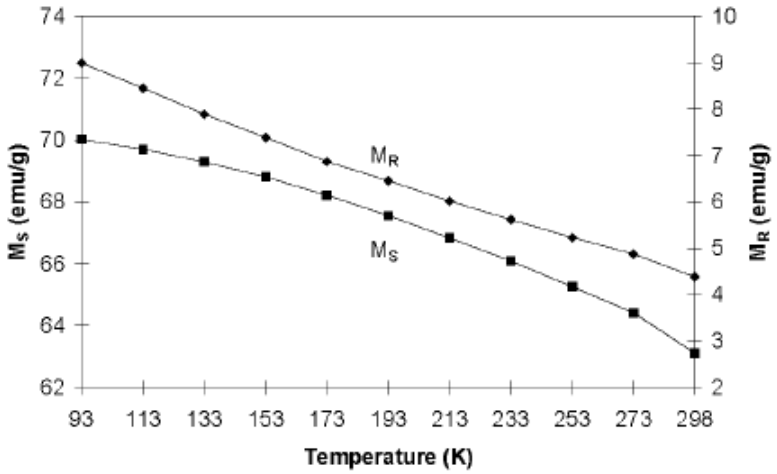

Figure 3.11: Effect of temperature on the saturation magnetization and remanence of the magnetite nanoparticles [100]

3.8 Summary

This chapter has introduced the magnetic materials and their characteristics. Three different types of commercially available magnetic particles used in this research were explained:

- Superparamagnetic beads from Cytodiagnostics;
- Magnetisable Agarose beads from Scipac Ltd.; and
- Magnetite (Fe_3O_4) powder.

These particles were tested with magnetic sensor and their test designs with results are presented in chapter 6. According to the requirements of this project, a large amount of particles were needed for experiments; therefore the most cost-effective method of synthesising iron nanoparticles was chosen to meet this requirement.

Iron nanoparticles were synthesised using the water in oil microemulsion method. Average particle sizes were 25nm with narrow size distribution. The synthesised iron particles have strong magnetic property and could easily be separated by magnetic field. These particles were produced several times during this project based on the CTAB/n-butanol/n-octane (molar ratio:12/1/44) microemulsion system using 0.2M of sodium borohydride as the reducing agent and 0.08M iron chloride as the precursor. The result of using these particles in the experiment for magnetic detection purposes are demonstrated in chapter 6. Detection of magnetic particles need high sensitivity sensor to magnetic fields below 1mT [81]. In the following chapter the design and working principles of magnetic sensor is presented.

CHAPTER 4: **SENSOR DESIGN, SIMULATION AND FABRICATION**

4.1 Introduction

This chapter is entirely dedicated to describing the design and characteristics of a DNA sensor using magnetic particles as a label. This sensor is based on a resonant coil for quantifying the magnetic nanoparticles. The concept for designing this sensor is derived by reviewing the literature (chapter 2) and it has been concluded that the most successful sensor design should be:

- Sensitive enough to detect the required number of beads based on each application;
- Able to accept an extensive diversity of sample types;
- Cost effective;
- Easy to automate, fabricate and mass produce.

Considering all of the above specifications; frequency-based sensors are the best candidate for MP detection, therefore the proposed sensor design in this research is frequency-based, consisting of an electronic circuit and the sensing element, the latter of which is the most important, comprising the air core coil. The size, shape, material, method of fabrication, number of turns and wire specification are the parameters that have a major impact on the MP detection. The principle of how this sensor works is illustrated in Figure 4.1. The magnetic sensor itself is shown in Figure 4.1a, which consists of the electronic circuits, including the coil as a sensing element in the resonance circuit. The detection chamber in which the nanoparticles are going to be placed is demonstrated in Figure 4.1b. The magnetic beads on top of the coil surface generate magnetic field in opposite direction to the coil magnetic field, therefore the sensor inductance will alter and output frequency of the system will change.

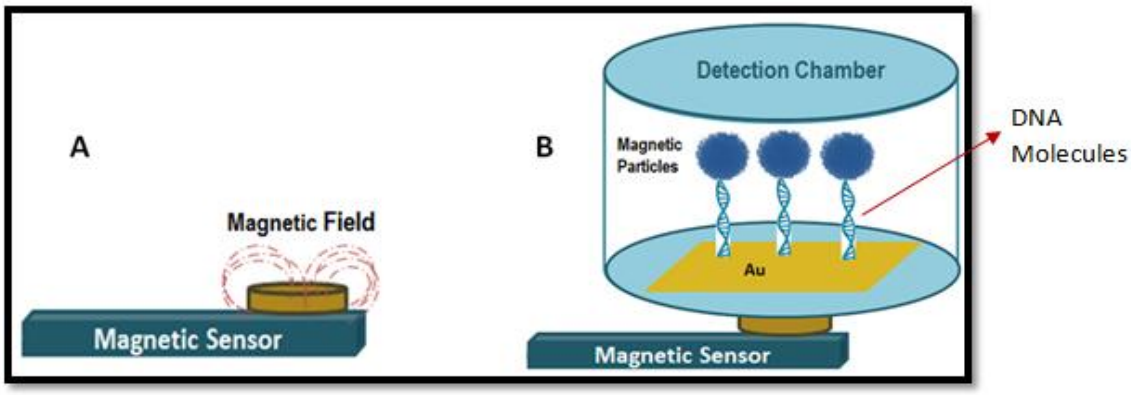

Figure 4.1: (a) The magnetic sensor, (b) How the proposed sensor works

The brief explanation of coil design with numerical calculation of coil inductance, the COMSOL simulation of coil, and the specific coil fabricated for use in the actual system is given in the following section, while the subsequent part of this chapter presents the description of the initial design of the sensor, which was based on Colpitts oscillator. The experimental results of this sensor with magnetic beads are also presented.

Due to the low sensitivity and specificity of the Colpitts oscillator sensor, a new system was designed based on tank oscillator in differential sensing scheme using phase lock loop (PLL). The design description of this sensor including its challenges is explained in the final portion of this chapter.

4.2 Coil design

In order to achieve the optimum design for the coil, different aspects of the inductor need to be considered, such as different models, sizes and shapes. There are many options available for designing the coil; it can be fabricated in a very small size with planar shape or in multilayer shape etc.; the fundamental criterion is that the design should be compatible with the system needs, thus the size should be in proportion and as small as the required mass of the beads required for detection. Similarly, the shape should be such that low power consumption is required to generate a sufficient magnetic field, as uniformly as possible, in which the sample can be treated equally while it is on the sensor.

On-chip inductors can be modelled via two different approaches: lumped circuit models [42, 110] and field solvers [42, 110-112], the latter of which is the most accurate method for calculation of Maxwell equation, but it is slow and requires significant computer memory. On the other hand, the complexity in the coil structure makes it an impractical solution. A lumped circuit model is more amenable for 3D Maxwell equations using spiral inductor. The inductor is replaced with equivalent resistance, inductance and parasitic capacitors in the lumped π model (Figure 4.2)

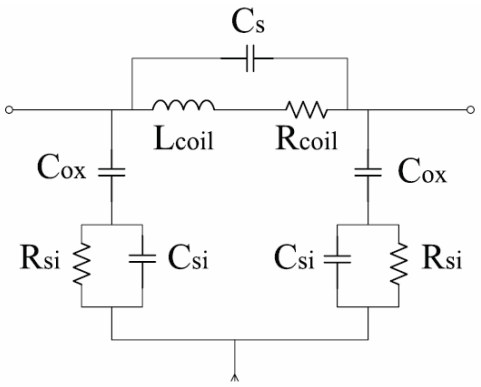

Figure 4.2: Lumped π model of spiral inductor [5]

The most widely used spiral inductors are in a form of square and circular [42] (Figure 4.3) and their parameters can be defined as follows:

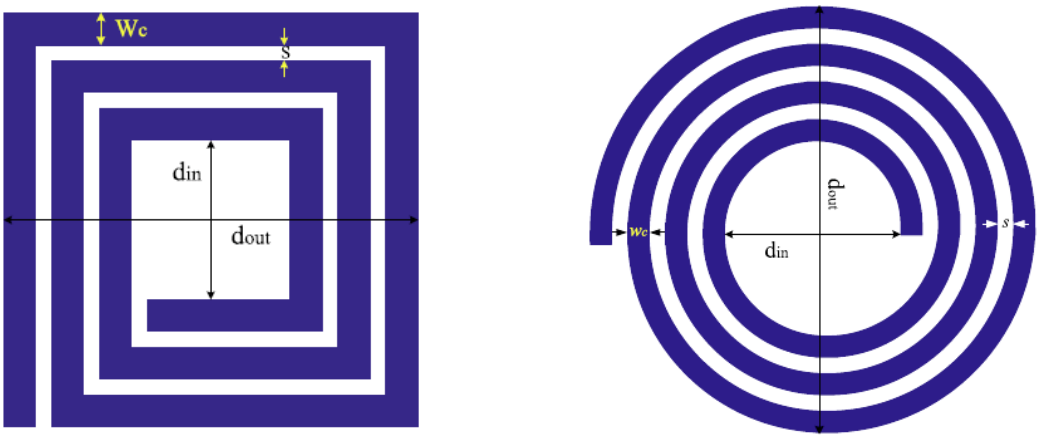

a b

Figure 4.3: Two dimensional view of a (a) Square spiral inductor, (b) Circular spiral coil

d_{out}	**Outer diameter of the coil**
d_{in}	Inner diameter of the coil
w_c	Conductor width
t_c	Conductor thickness
s	Distance between coil winding
d_{avg}	Average diameter of the coil = $((d_{out} + d_{in})/2)$
ρ	Fill Ratio = $((d_{out} - d_{in})/ (d_{out} + d_{in}))$

It was noted that in the frequency range below 1 GHz, the capacitive effects between the coil turns (windings) is negligible [113]. Even skin effect, which results in higher series resistance, is only effective at high frequency [111]. The coil selected for this research is air core, which is free of iron losses, and this is an important factor in high frequency (≈ up to 1GHz), because it can lead to higher Q factor, less distortion and better efficiency. The problem with the air coil is its low permeability core, which then requires a larger number of turns for the coil to obtain specific inductance, resulting in a larger coil. Larger coils have higher inter-winding capacitance and copper loss, but on the other hand, when using them in the high frequency, smaller inductance is required, which makes this air core less problematic.

Therefore, the most important parameter in the coil is its inductance, which has a significant impact in circuit design. Several expressions and equations have been proposed by different researchers [112-119], the majority of which are based on experiments, however due to the structural and

geometrical complexity and frequency dependence of the coil, none of those expressions are giving the exact value of inductance. Some of the methods available for calculating the inductance of spiral coil are explained below.

The following formula is presented in [118-119] for calculating the inductance of the planar spiral coil with different layout (Table 4.1):

$$L=[(\mu_0 N^2 D_{AVG} C_1)/2][\ln(C_2/\rho)+C_3\rho+C_4\rho^2)] \quad (4.1)$$

Where N is the number of turns; μ_0 is the vacuum permeability, $4\pi\times10^{-7}$; ρ is the fill ratio, D_{AVG} is the average diameter, $(D_{IN}+D_{OUT})/2$; and C_1~C_2 are factors depending on layout

Table 4.1: Values in Eq. 4.1

Layout	C_1	C_2	C_3	C_4
Square	1.27	2.07	0.18	0.13
Hexagonal	1.09	2.23	0	0.17
Octagonal	1.07	2.29	0	0.19
Circle	1	2.46	0	0.2

This formula exhibits a maximum 8% error depending on the ratio of s/w. while its accuracy worsens by larger ratio of ***s/w***.

Three equations are mentioned in [116]:

1. Grover method for planar circular coils is stated below where a is the mean diameter (m) and *P* is normalized radial thickness, depending on w/2a.

$$L = \frac{25\mu_o}{\pi} aPN^2 \quad (4.2)$$

2. Schieber method for circular coil:

$$L = 1.748\times10^{-5}\mu_o \pi R_o N^2 \quad (4.3)$$

3. Wheeler method: the maximum error for this formula is about 5% although some claimed the error of <20% [12]. C=w: winding thickness:

$$L = 31.33\mu_o N^2 \frac{a^2}{8a + 11c} \quad (4.4)$$

Each of the above equations can be used for inductance calculation of the spiral coil, but depending on the coil geometry they may show higher or lower error percentage, therefore considering the specification of each expression is essential before using them.

4.3 Planar coil COMSOL simulation

The previous subsection introduced different expressions for coil inductance calculations, which were able to give the correct approximation. However, studying magnetic parameters and behaviours in the circuit, such as magnetic flux density and electromagnetic power losses, requires intensive numerical computation using Maxwell's equations. Simulating the inductor with the Finite Element software can be beneficial and give the most accurate prediction and results.

Most of the inductor simulations done by different groups [42, 111, 120-121] were based on 2D simulators. The researchers avoided 3D simulation due to its complex calculation and the need to access large computer memory. In this research the 3D simulation of the spiral planar coils was performed with COMSOL multiphysic software (Finite Elements simulator).

The aim of these simulations is not only to assess the impact of geometrical factors on the magnetic flux density and inductance value; it also determines and shows how the magnetic field generated by the coil can impact on the MP detection.

Among diverse planar spirals, square winding is more alluring due to its simplicity of design [42]. In addition, circular windings have high quality factor, and thus they have been utilized broadly within RF circuit. In this work different types of planar coil were designed for detection purposes, and significant results were obtained, as described below.

- **Square Planar Coil Simulation**

In this section the simulation of a 3D structure of the planar square coil is presented. The micrometer-sized inductor was modelled based on the finite element method, with COMSOL AC DC Module with 5 numbers of turns (N), the latter of which was informed by previous literature [42, 111, 119-121], which found that coils with a small number of turns can produce sufficient magnetic field for magnetic bead detection. Although different values of N (<10) were modelled, the best result was achieved with N=5.

Another important issue for fabrication of micro coils was the effect of operating temperature. Change of inductance and resistance alters the output signal, and the value of both parameters depends on the temperature [122]. On the other hand, Joule heating, which depends on the resistance per unit length or the amount of current passing through the coil, should be considered in the design. If the inductor temperature increases to an undesirable value, the sensor could be of damage.

Copper was selected as a coil material for this simulation, due to its low DC resistivity and the electric conductivity of 5.998×10^7 (S/m). The coil is driven by 100mA DC current. Experimental evaluation in [123] shows that current above 150mA can be harmful to the system and biological samples on it. Although in this work different amounts of current were simulated, as shown in Figures 4.4 and 4.5, I=100mA was the best result in terms of magnetic field generation and also according to the background research of this project [123]. Therefore, the coil is driven by the 100mA DC current, which is the source for the computation of magnetic flux and magnetic energy. Accordingly the coil inductance is calculated based on the total magnetic energy using equation (4.5), where W_m is the total magnetic energy:

$$W_m = \frac{1}{2}LI^2 \Rightarrow L = \frac{2W_m}{I^2} \qquad (4.5)$$

This inductor is surrounded by the air (Figure 4.7b) and has an outer diameter of 40µm. Coil thickness (t_c), coil width ($w_{c)}$ and the space between the windings (s) are all set at 5µm.

Magnetic field distribution, magnetic flux density, magnetic energy density and many other parameters were simulated, and the results are shown in Figures 4.4-4.7 and Appendix 1, for the coil with five numbers of turns and the current of 100mA as a source. The electric potential of copper coil is around 20-110mV with the maximum value in the centre. Figures 4.4 and 4.5 show the magnetic flux density generated by the copper coil and with different current of 60mA and 200mA. The simulation results illustrated that the maximum magnetic field was achieved in the centre of the coil and it was changed from 20mT to 60mT by increasing the current from 60mA to 200mA. The results prove the direct relation between the generated magnetic field and the current passing through the coil. This relationship was demonstrated theoretically (Eq. 4.6) by the Biot-Savart law [124-125]. Thus the total magnetic field generated in the micro-coil is the sum of all small differential units of the coil (*dl*). The equation also shows that the smaller size of coil needs less current for generating specific magnetic field due to the inverse relation between *B* and *r* (displacement).

$$\vec{B} = \int d\vec{B} = \int \frac{\mu_0}{4\pi} \cdot \frac{I d\vec{l} \times \vec{\hat{r}}}{|r|^2} \qquad (4.6)$$

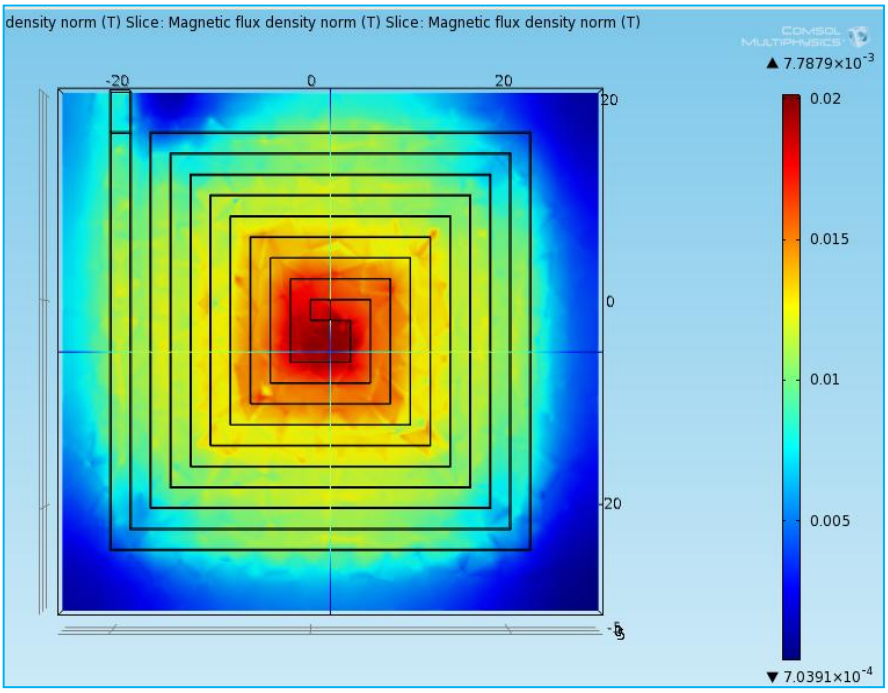

*Figure 4.4: Copper coil with **I= 60mA**, Magnetic flux density: **5 - 20mT***

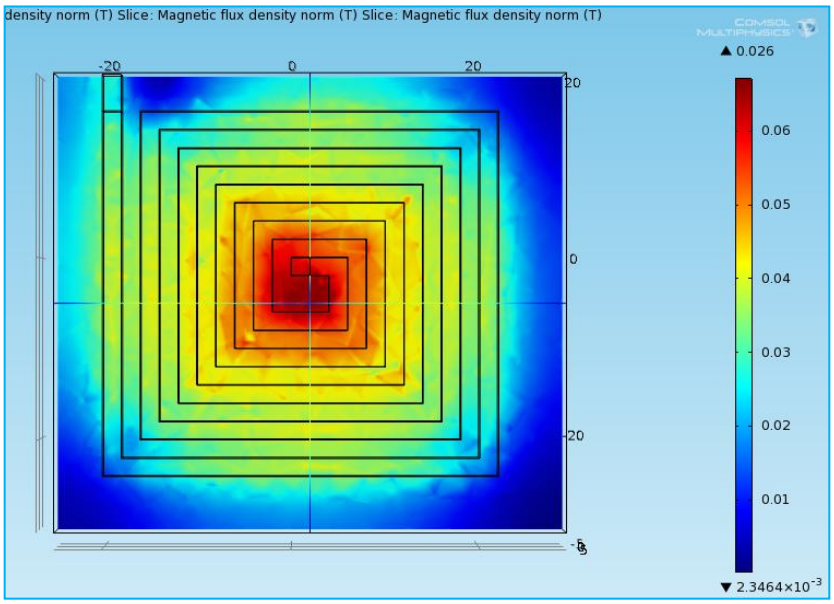

*Figure 4.5: Copper coil with **I= 200mA**, Magnetic flux density: **20 - 60mT***

Figure 4.7 presents the modelling results of copper coil with the current of 100mA. Figure 4.7a shows the computation of magnetic flux density and the way it is distributed. This exhibits the fact that the maximum magnetic flux density of 30mT was generated in the vicinity of the inductor centre and the field magnitude drops quickly by moving away from the centre. This is one of the disadvantages of using planar coil for magnetic bead detection, since this leads to the gathering and

clustering of magnetic beads in the coil centre only. Zheng et al [125] demonstrated the particles clustering in their work by means of simulation of beads and micro-coils within a microchannel. Their solution to overcome above problem is fabricating an array of small micro-coils instead of one large coil within the same area, which then leads to a bigger trapping area. Figure 4.7c shows the magnetic field distribution with the stream lines around the coil. A group of researchers in France [126] created the experimental model based on the coils in the size of 5×5µm and a current of 50mA to check the magnetic field distribution produced by the coil. Their experimental results show a good correlation with the simulation of magnetic field distribution on the coil [126] (Figure 4.6).

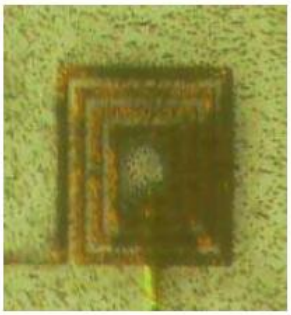

Figure 4.6: Real-time experiment for repartition of magnetic field around the coil

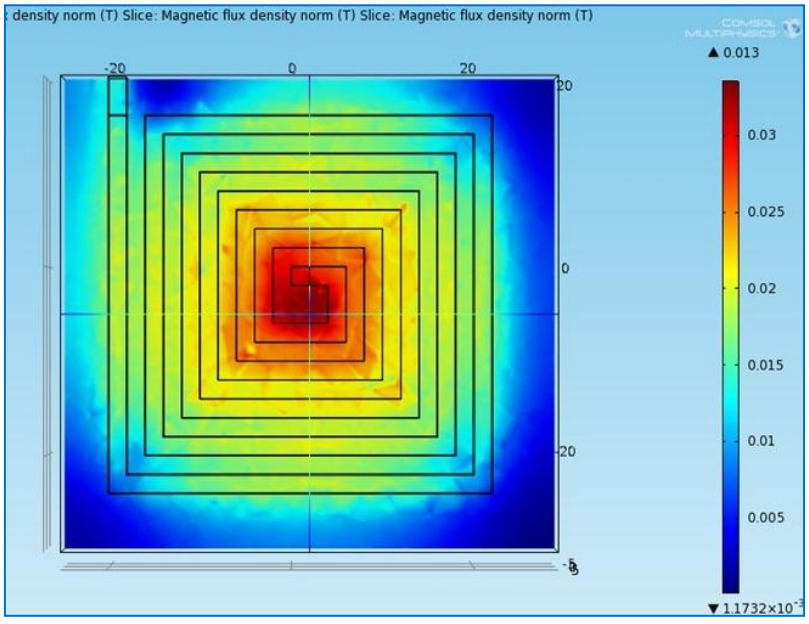

a

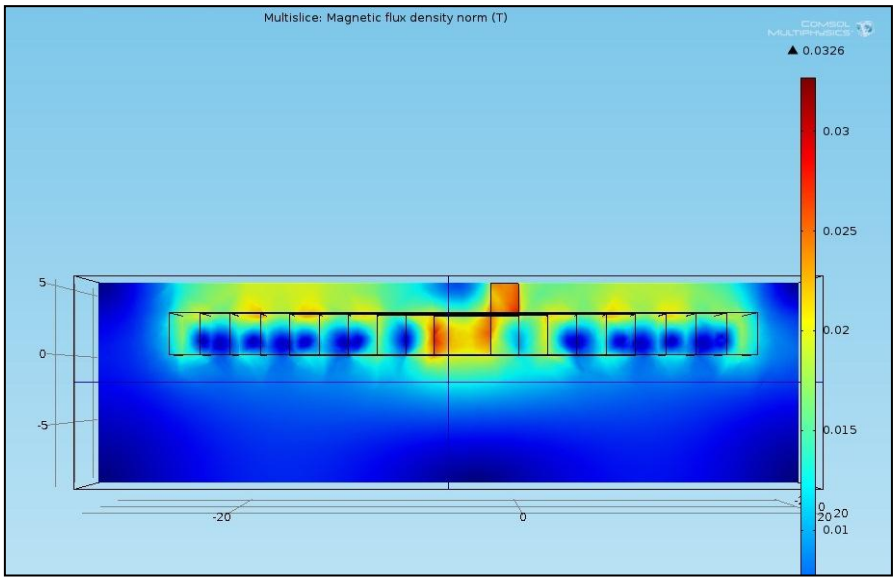

b

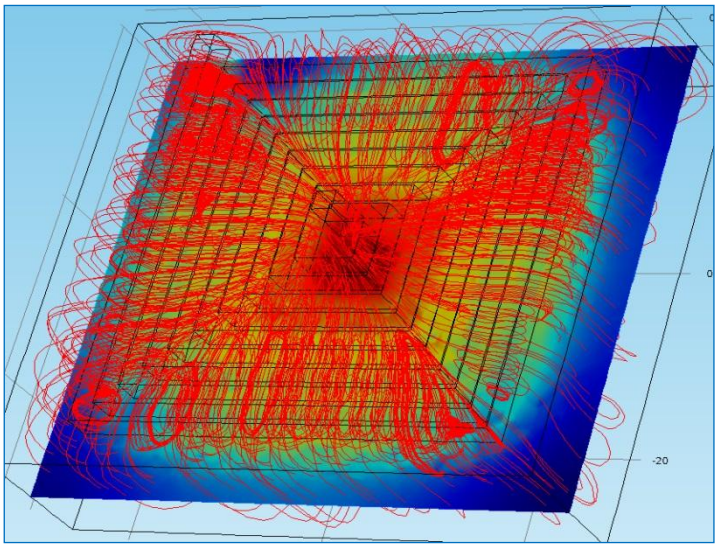

c

Figure 4.7: Copper coil with N=5, I= 100mA, Dout= 40µm, Inductance= ***0.235nH***
a Magnetic flux density norm: **10 - 30mT**, b Cross sectional view of the coil in room temperature, c Magnetic field distribution

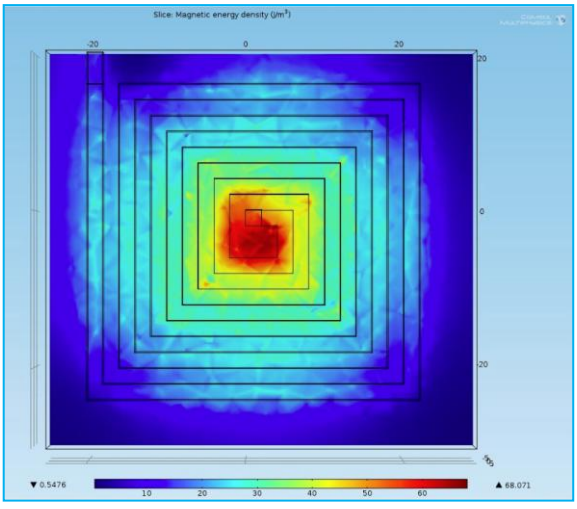

Figure 4.8: Copper coil, magnetic energy density; 10-60 (J/m^3)

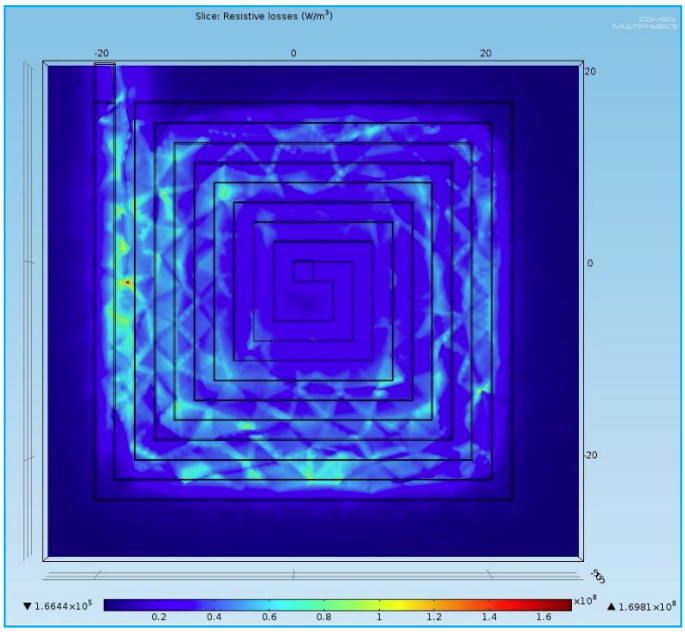

Figure 4.9: Copper coil (N=5, I= 100mA), resistive losses: 1.65×10^{5} - 1.69×10^{6} (W/m^{3})

Figures 4.8 and 4.9 show the magnetic energy density and resistive losses of the coil. Some other magnetic properties and features of the inductor were also simulated with copper, as presented in Appendix 1. (Resistive losses are high in some regions which is a result of different meshing in different areas.)

As demonstrated by the above results, the magnetic field is concentrated in the centre of the coil. On the other hand, the detection of the magnetic-field-dependence of the particles requires a homogenous field distribution. Therefore, in those applications, optimum detection with high sensitivity can be achieved if the coil size is comparable with the size of magnetic particles. Otherwise, the distribution of magnetic particles on the coil's active area could not have the uniform and similar effect on the inductance change of the inductor. Therefore the parameters such as sample volume and sample distribution play an important role in detection. On the other hand, shrinking down the coil size near to the magnetic bead volume can increase the joule heating effect by reducing the coil width [126], although less power and current is required to produce specific magnetic field within the smaller size coil.

- **Circular Planar Coil Simulation**

A similar approach was considered for simulating the circular spiral inductor. Regarding the simplicity and high quality factor of this type of coil, it has a wide application in RF circuit. The coil is simulated with copper material and surrounded in the air at room temperature. The outer diameter is 70µm, and the width, thickness and space between windings are 5µm. Figure 4.10 shows the generated magnetic flux density in the range of 10-60mT by 100mA of current. The

electric potential produced is 50mV greater than the square one (Figure 4.11b), and the inductance is 0.196nH, which is smaller than in the square coil, although the circular coil has a larger outer diameter.

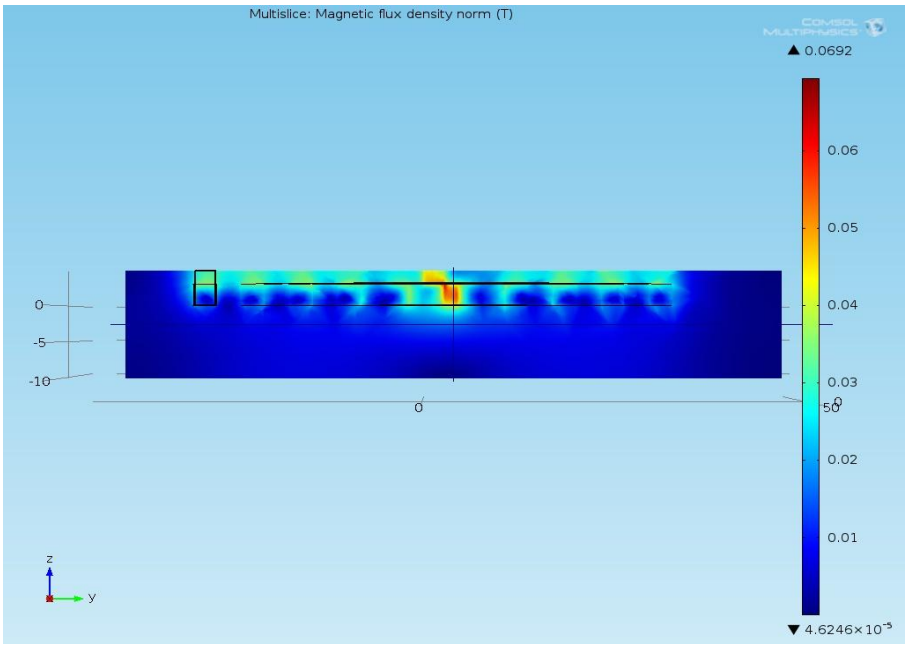

Figure 4.10: Circular spiral model I = 100mA, N = 5, magnetic flux density norm = 20 - 60mT

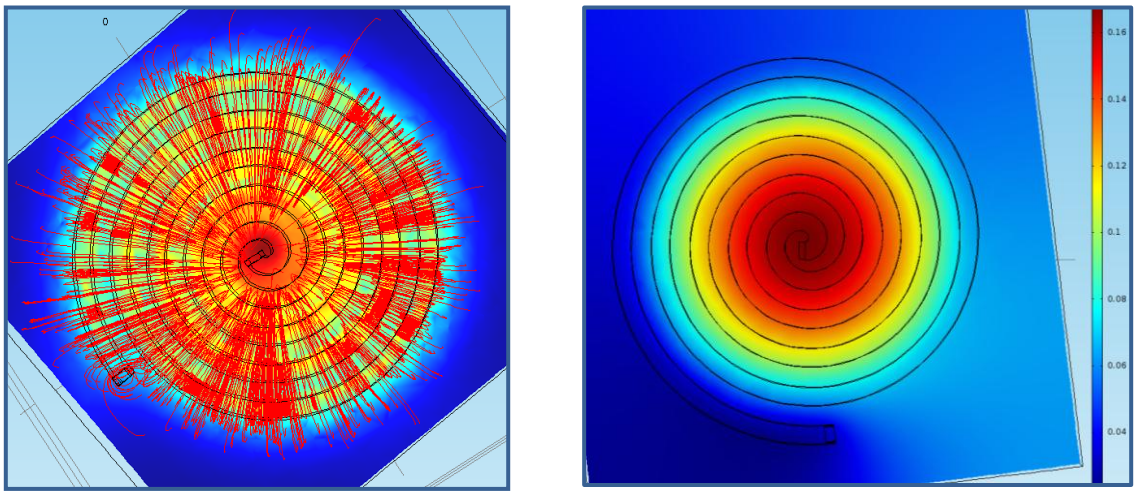

a b

Figure 4.11: (a) Flux distribution of circular inductor, (b) Maximum electric potential 160mV

4.4 Fabrication of planar coil sensor for DNA detection

The next step after modelling the inductor is fabrication. These coils have to be fabricated by photolithography. Figure 4.12 shows the proposed process flow of the fabrication of the magnetic DNA detection sensor.

According to the better heating effect of aluminium and its higher quality factor (Q) at higher frequencies [127], it was selected for the coil material (Appendix 2 shows the COMSOL simulation

result of aluminium coil). The coil needs to be fabricated on 100µm silicon wafer (whose eddy current effect is negligible by using it up to 3GHz frequency [127]). After adding 2µm of aluminium layer for etching the coil on top of the substrate, the epoxy-based photoresist SU-8 is added for metal insulation. At the end, because of the need for DNA attachment, the chromium and gold layer were chosen due to their biocompatibility properties. The best way of immobilizing target DNA on the sensor is via gold. By using a very thin layer of chromium, the gold layer can be attached to the sensor.

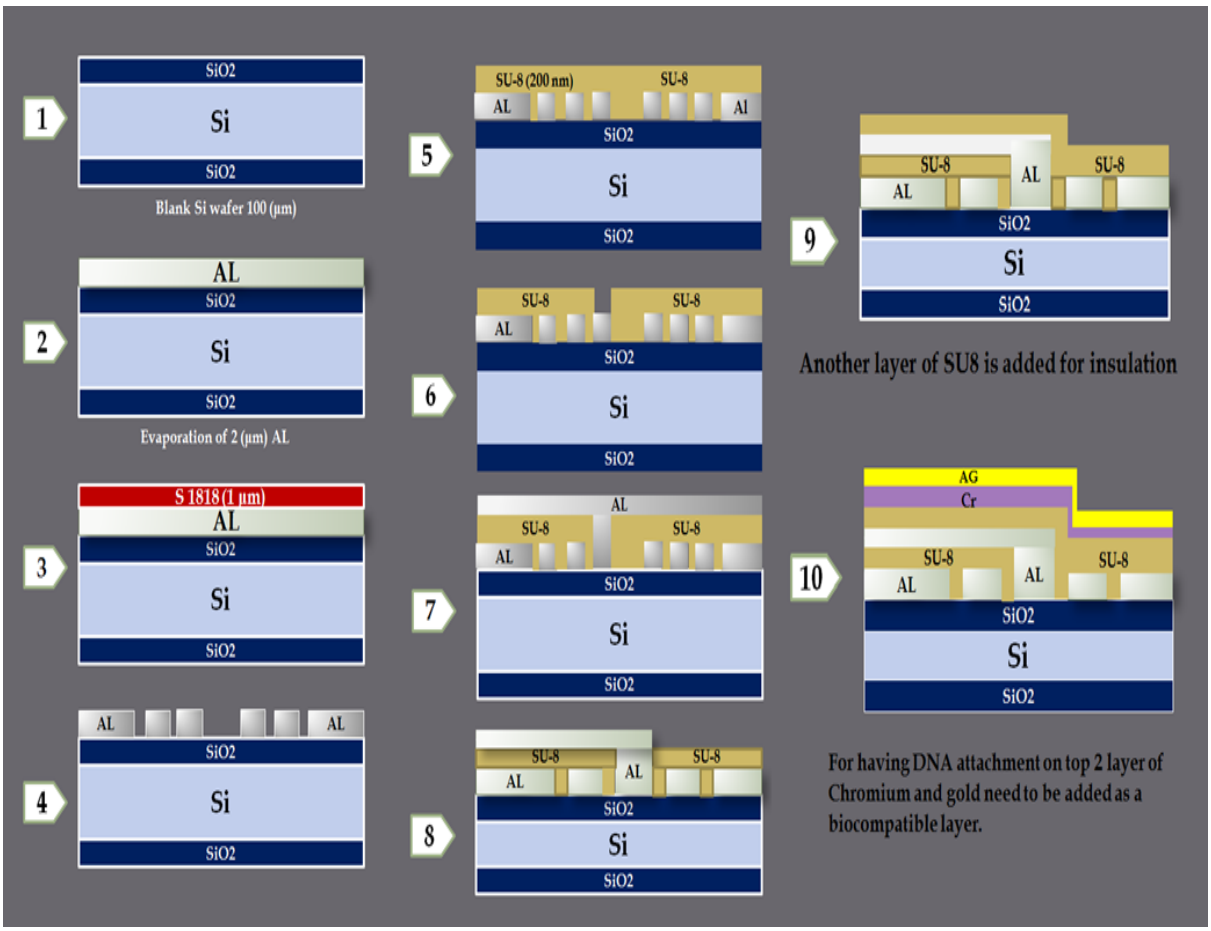

Figure 4.12: Proposed DNA detection sensor process flow

This fabrication method sounds promising although it requires access to the clean room and advanced micromachining equipment. On the other hand, the fabrication process is complex and extremely expensive, conflicting with the aim of this project to produce a low cost sensor. Consequently, an alternative type of inductor needs to be designed which can be fabricated in a more convenient and low-cost way.

Figure 4.13a, shows the fabricated coils, which consist of a PMMA or aluminium bobbins and copper wire. The bobbins specification are given in Table 4.1. The wire has circular cross-section of 100µm with gage 42 (SWG #42). These coils are manually wound with the device shown in Figure 4.14b, which is designed for precision winding of the coil with a specific number of turns.

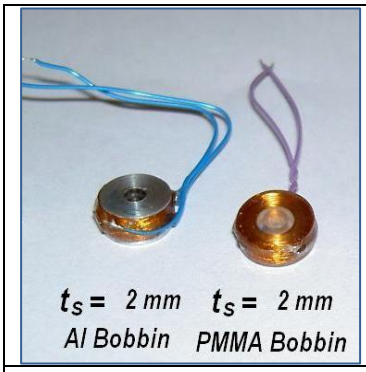

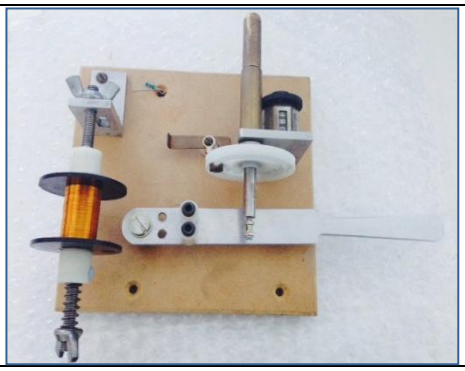

Figure 4.13: (a) Copper coil with aluminium and PMMA bobbin, (b) Coil winding machine

Table 4.2: Coils specifications

Coil Thickness (t_S)	2mm
Coil Outer Diameter (d_{out})	8mm
Winding Width (W_S)	2mm
Electric Resistance (R_S)	15.4Ω
Bobbin Cheek Thickness (t_{cheek})	500µm
Bobbin Material	Al/PMMA
Total Conductor Cross Section	2.83µm^2
Coil Inductance	0.5mH

This coil is used in the magnetic sensor as the sensing element in the following experiments of this project. It helps for polarising the magnetic beads and to cooperate with the stray field generated by the beads, which results in increased net local magnetic field and consequently changing the output signal of the sensor.

4.5 Colpitts oscillator

The first inductive-sensing experiment designed for this project was based on the Colpitts oscillator (Figure 4.14) with the fabricated coil as an inductor. Colpitts oscillator was selected because in this type of design the frequency of oscillation (Eq. 4.7) can be controlled by the LC resonant circuit. By introducing the magnetic particles to the coil, the inductance (L) of the coil will change due to the magnetic permeability of the particles. Consequently the output circuit frequency will change; this change is directly proportional to the number of magnetic particles applied to the sensor. Richardson et al [128] described this relationship with Eq. (4.8).

$$f = \frac{1}{(2\pi\sqrt{LC})} \qquad (4.7)$$

Where in this specific circuit: $C = \frac{C1 \times C2}{C1 + C2}$

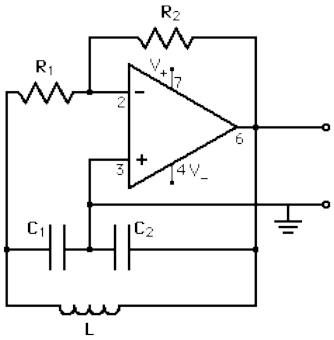

Figure 4.14: Colpitts oscillator

$$\boldsymbol{f_n = f_0\{1 - 1/2(k/L_0)n\}} \quad \textit{and} \quad k = \mu_p \mu_0 n^2 dA \qquad (4.8)$$

Where f_0 is the initial resonance frequency of the circuit and L_0 is the initial inductance of the inductor (before applying the magnetic particles). *K* is a constant depending on the following parameters:μ_0 is the permeability of a vacuum ($4\pi\times10^{-7}$ H/m);μ_p is the total effective relative permeability of the magnetic particles; *n* is the number of turns per unit length; and *d* is the length and *A* is the cross-sectional area of the coil

According to Eq. (4.8), increasing the number of particles causes linear decrease to the resonance frequency.

Based on the above concept, the experiment was designed using Colpitts oscillator. Resonance frequency of the circuit was 733kHz and coupling capacitors of 1nF and 100pF were used. Spice software was used for simulating the resonance circuit and obtaining the best components selection and frequency response. In this method of detection, while the electronic circuit was resonating at 733KHz, different amounts of magnetic beads were placed on a glass slide (as a substrate) and brought near to the coil. The output circuit frequency was measured by the frequency meter. Frequency shift was observed due to the presence of magnetic particles. These particles were placed in different distances from the coil. This sensor was tested with the permanent magnets as well and it shows maximum changes of 10KHz by attaching a permanent magnet (380mT) to the coil.

The circuit was tested with magnetic beads to check if the sensor is sensitive enough to detect any amount of beads. Afterwards, the same experiment was repeated using permanent magnets. The test was conducted by varying the distance of the permanent magnet from the coil and accordingly applying different magnetic fields to the coil. The results are presented in the following section.

4.6 Testing the resonance circuit with a permanent magnet

The intention of designing this sensor was to detect the presence of magnetic particles and thus determine the sensitivity of the Colpitts sensor. In this experiment different volume of magnetic

particles in the range of 0.1-10µl were introduced to the sensor while they were on the glass cover. The glass substrate also causes some frequency shift due to its iron content. Therefore the effect of the glass cover was investigated on the sensor resonance frequency. Figure 4.15 shows the diagram of the results while the sample (magnetic particles on the glass slide) was placed near to the coil (from 0-2cm distance) and the sensor output frequency was measured with the frequency meter. 0L of sample means only the glass slide without any magnetic particles on it. As illustrated, there is not much difference in the amount of frequency shift created with different amounts of sample. The Colpitts sensor was not able to distinguish between any selected amounts of magnetic beads and therefore it is not sensitive enough for magnetic beads detection purposes. Although those amounts of magnetic beads were small and very small changes of frequency shift were expected to achieve from the sensor thus detecting the small signal requires very stable and reliable system.

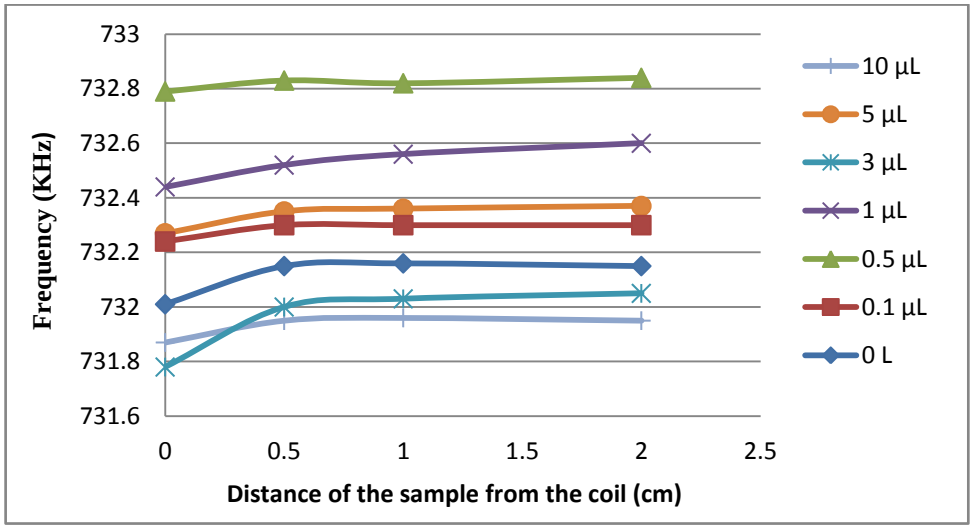

Figure 4.15: Frequency-shifts of different amount of magnetic beads in different distances

It was also concluded that the coil was mostly sensitive in the centre and on the connecting point of the wire, and the sensitivity was not uniform. The sensor was not stable over a short period of time, and frequency fluctuation makes the measurement difficult and imperfect. The reason of these fluctuations can be Miller effect (due to the parasitic capacitance between input and output terminal of an inverting voltage amplifier , the effective input capacitance is increased virtually, which is called Miller capacitance).

Since the sensor does not show any sensitivity to the magnetic particles, another test was designed to investigate the sensor behaviour and to proof the validity of the results provided by the first experiment. Therefore two permanent magnets with different strength of magnetic field were selected and used in the second experiment (Figure 4.16). The DC magnetometer shown in Figure 4.17 was used to validate the strength of magnetic field in each permanent magnet. This magnetometer (Alphalab, Inc.) has a universal Hall effect sensor and the resolution range of 1µT up

to 2 Tesla. The sensor used in this meter has 1.1mm thickness and 4.3mm width. The circular permanent magnet is bigger in size and generated magnetic field strength of 370mT at zero distance, while the small square one produced a field of 280mT.

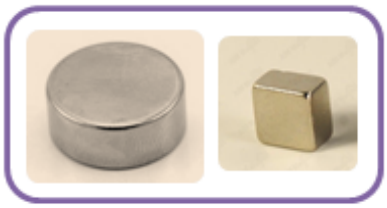

Figure 4.16: Circular and square neodymium (NdFeB) permanent magnets

Figure 4.17: The magnetometer used to measure the magnetic flux density of permanent magnets

The DC magnetometer sensor was kept in a range of distances (0-4 cm) from the permanent magnets to measure their magnetic field strength. Figure 4.18 illustrates the amount of generated magnetic field in each distance. It can be seen that by moving away about 0.5cm from the magnets, their magnetic field drops dramatically (290mT from the circular magnet and 244mT from the square). The closer view of diagram in shorter distances is demonstrated in Figure 4.18b.

After determining the amount of produced field by circular and square magnets in different distances, they were placed near the resonance circuit to evaluate the effect of various magnetic fields on the sensor output frequency.

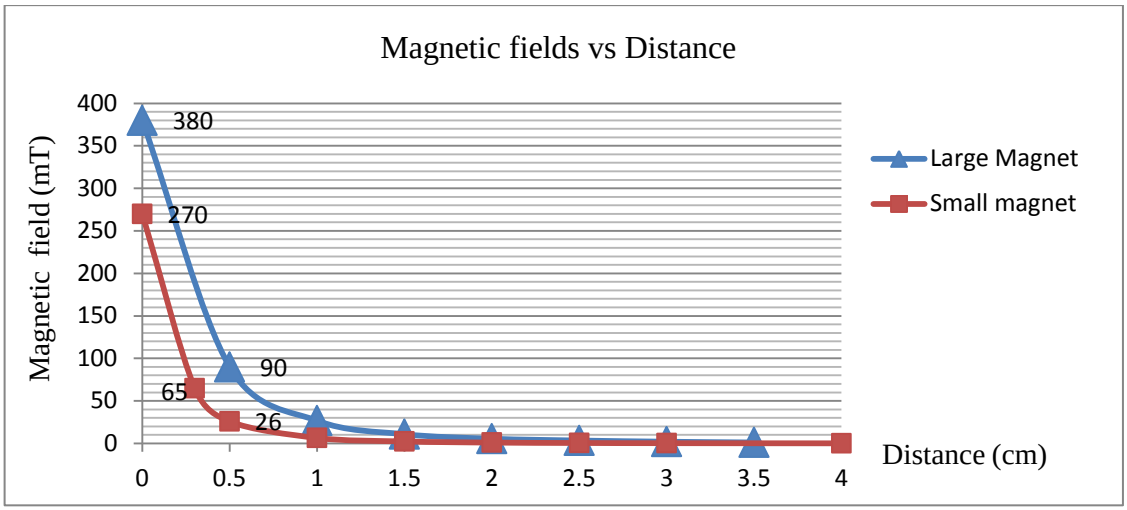

(a)

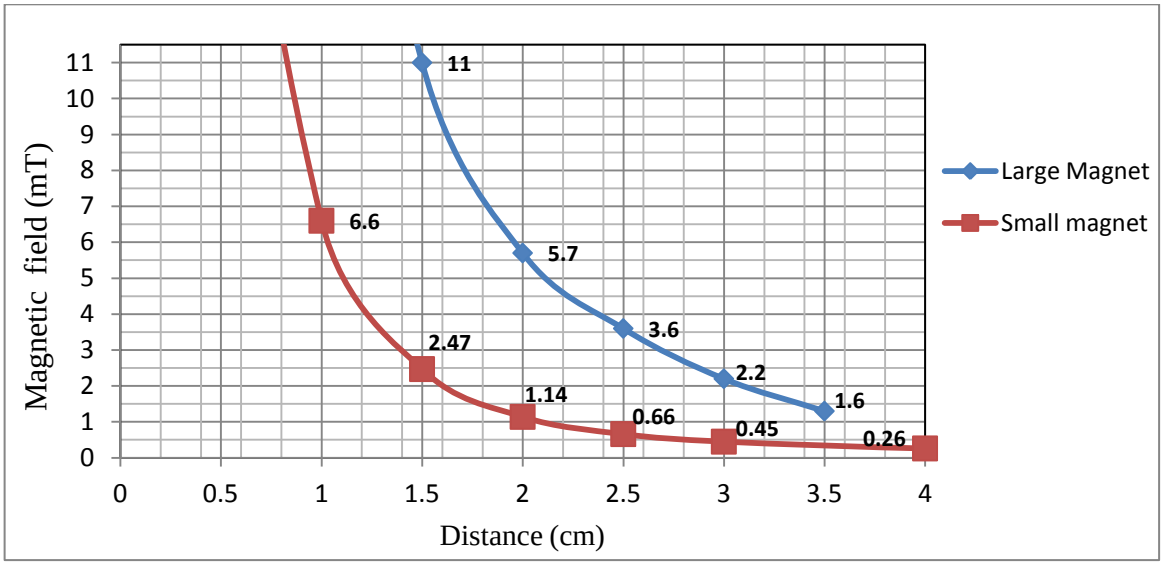

(b)

Figure 4.18: (a) Permanent magnets calibration with magnetometer, (b) Closer view of produced magnetic fields of magnet within 1-4 cm

The circular permanent magnet was placed near to the sensor while the coil was in the vertical position, and once while it was in the horizontal position, as shown in Figure 4.19. At that time the resonance frequency of the sensor was measured before and after applying the magnet. The amount of frequency shifts is plotted in Figure 4.20. According to the unstable output frequency (high frequency fluctuation), the test was repeated with several resonance frequencies.

The maximum frequency shift achieved while the magnets touched the coil completely or the coil had the smallest distance from the magnets. The maximum frequency shift obtained by applying the circular coil was 7.7kHz and the maximum frequency reduction of the sensor by the small square magnet was 4.2kHz, although by moving the magnets away from the coil the amount of frequency

shift reduced due to the decrease in the magnetic field. As a result, the diagram in Figure 4.20 is just the outcome of testing with the circular coil, which has a stronger field.

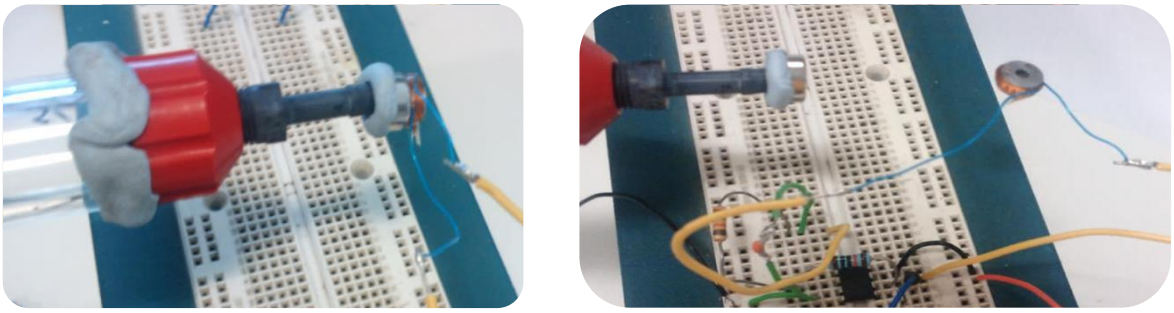

Figure 4.19: Permanent magnet in different position and distances from the coil

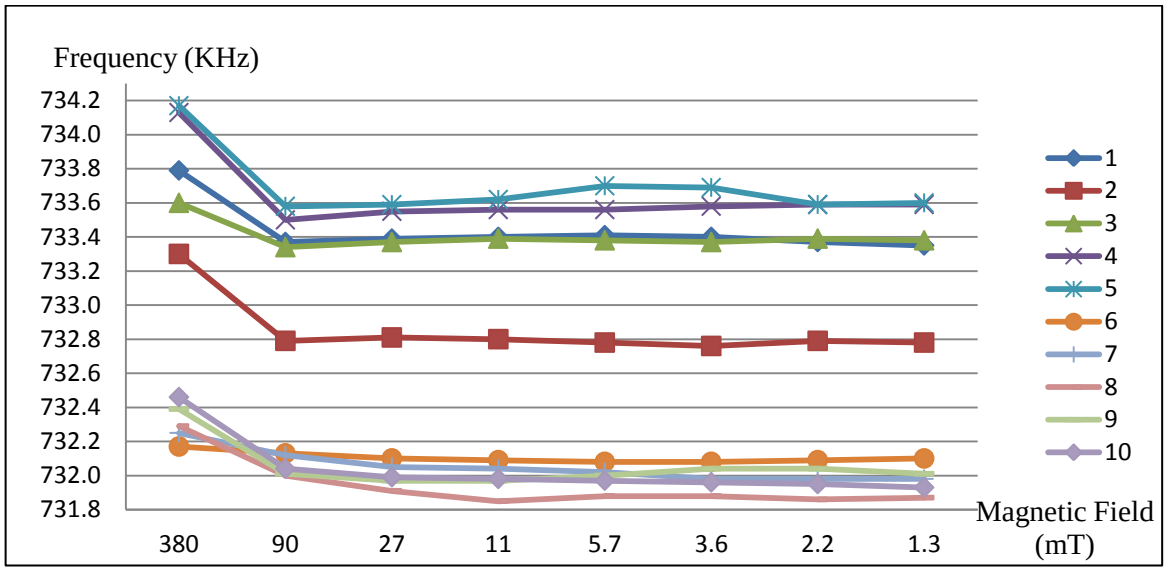

Figure 4.20: Frequency shift of the sensor in response to the circular magnet

Series 1-5: Magnet placed in the horizontal position towards the coil

Series 6-10: Magnet placed in the vertical position towards the coil

As illustrated in the diagram, placing the permanent magnet near to the coil in horizontal position created a higher frequency shift compared to the vertical position, which means that the inductor is more sensitive where the winding is located, and distribution of the field is not uniform. On the other hand, linear frequency changes were observed in both the vertical and horizontal positions. Another outcome of this experiment was discovering the minimum strength of magnetic field required for detection by this sensor. As shown by the graphs in Figure 4.20, the sensor response is detectable while the applied magnetic field is above 80-90mT. This is a strong field which is not expected to be produced by small amount of magnetic particles (µl), and thus is proof that why this sensor could not sense the magnetic particle samples. An experiment was performed and presented in chapter 6, Figure 6.2, to evaluate the amount of magnetic field produced by magnetic particles used in this experiment; the result shows that <1mT field is expected to be produced.

The proposed resonance circuit shows low sensitivity for detecting magnetic beads is still a big challenge. To overcome this problem a new sensor needs to be designed wherein the resonance frequency of the circuit is higher than 733kHz, as concluded from the literature review [42,50, 128-131]; increasing the resonance frequency will improve the sensor sensitivity (due the better Q factor of the system in higher frequency).

4.7 PLL-resonance circuit

According to the insensitive Colpitts oscillator sensor for magnetic detection, an alternative detection scheme with a new sensor was designed to overcome the previous problems.

It was noted from the literature review (that having differential sensing setup can help gain more accurate reading and measurement. This can be achieved by using two similar inputs in frequency domain whose phases can reveal their difference. Wang et al [50] and Richardson et al [128] both investigated the differential sensing design for detection applications. Their differential scheme is derived from the phase lock loop (PLL) concept, which sounds promising for comparing the phase of two signals and producing output voltage accordingly. Detecting the magnetic particles with the Colpitts oscillator was based on only one output signal which had high frequency fluctuation and precise measurement of small frequency changes was unreliable, however by using PLL, the output signal was compared with the reference signal and the frequency shift was measured based on the phase difference between the actual and reference signal. Based on this method, more accurate, precise and reliable signal measurement can be achieved. The suggested sensing scheme and circuit design is explained in more detail below, including an introduction to the PLL.

4.8 Design considerations

According to this project vision, this sensor will be used in diagnosing the pathogenic diseases by detecting the presence of magnetic particles attached to the DNA molecule. The sample input will be the large quantity (around 4mL). Therefore, more than millions DNA needs to be tagged with magnetic particles. Thus, there is no need to have a sensor able to detect a single bead, and a high number of beads will be available in the sample. The sensor should also be portable, accurate and fast to be a good replacement for the conventional clinical test.

Figure 4.21 shows the block diagram of the system, where the tank oscillator is used for generating the resonance frequency with the inductor as a sensing element of the magnetic particles. Two voltage comparators have been utilized as a differential scheme to compare the frequencies of the input signal from the oscillator and the input signal from feedback control.

The output signal of the oscillator will be the main input to the voltage comparator and the second input is from the output of PLL. These two signals will be applied to the comparators and from there to the PLL and then the phase detector inside the PLL will sense the phase shift between two signals and produce the voltage signal accordingly. In this way the PLL tries to keep these two input signals in the same phase within the specific frequency lock range, which can be set by some of the external components of the PLL. One of the most essential design considerations is choosing these components and determining the lock range. The components should be set in a way that the expected frequency shift caused by the magnetic particles must be within this lock range.

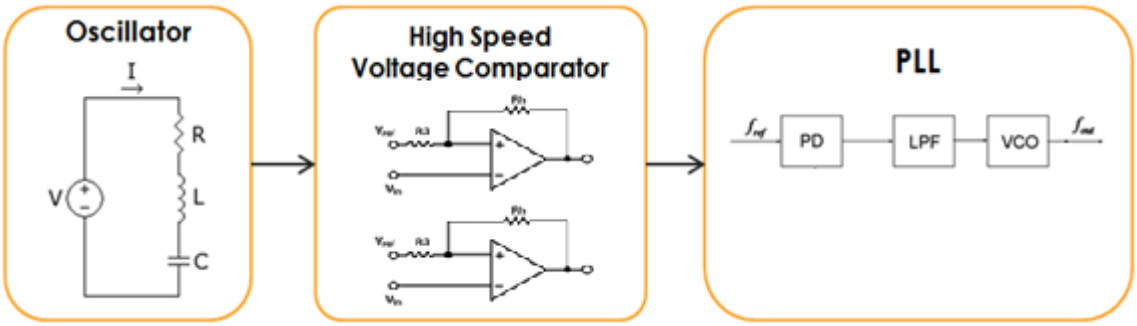

Figure 4.21: The resonance circuit block diagram

Another important issue in designing this sensor is the level of resonance frequency; higher value means better sensitivity and selectivity. However, higher frequency means smaller value of inductance and capacitance in the tank circuit, while there are some limitations to lowering those values according to the PCB design and fabrication and parameters such as parasitic effects, coupling capacitance and line resistance. On the other hand, lowering the inductance of coil can increase the resistive losses such as the skin effect, eddy current and hysteresis, all of which can decrease the quality factor and consequently reduce the sensitivity.

Considering all of the above issues, the PLL base sensor was designed and tested with magnetic particles; the sensor design is presented in the following section. The sensor calibration methods are presented in chapter 5 and the test results with magnetic particles are presented in chapter 6. For the start the brief overview to the PLL is given in the next section.

4.9 PLL frequency synthesizer fundamentals

Phase lock loop (PLL) is a kind of frequency control system in which the phase of a voltage controlled oscillator (VCO) is ruled by a feedback control. In the PLL one input is coming from the main reference source and another one is from the feedback. It is expected for both input signals to have similar frequencies. Thus, in the next step, the phase detector is located to compare the input signals and sense their phase difference and then generate a voltage in proportion to the phase shift.

This voltage signal will be applied to the loop filter for setting the dynamic characteristic of the PLL and accordingly controlling the VCO. In this research the MM74HCT4046 PLL IC was used, in which the centre frequency (f_0) can be designed up to 17MHz. This PLL has three sets of outputs wherein Phase Comparator II was selected for this research due to its sensitivity to only the positive edge of the signal. Some other unique specifications and technical notes can be found in Appendix 3.

4.10 Circuit design and analysis

According to the inability of the previous Colpitts sensor for detection of 10µl of magnetic particles and its instability, this new sensor is designed based on the differential sensing structure to create stable enough method for reliable measurement. In this design the LC circuit was kept with the fabricated coil as a sensing element and for generating the MHz range resonance frequency. The problem with the Colpitts circuit was that the detection was based on the measurement and fluctuation of only one signal, which was the circuit output frequency, and a lot of external parameters such as noise affect it. If there could be a reference signal beside the input signal by which the differences between these two could be measured to produce the final output signal for measurement, then a more stable system could be expected. As a result, the new stable sensor was devised using phase lock loop to stabilize the sensor output and control the frequency. The system resonance frequency (f_0) was set by the LC circuit and the PLL locks the VCO output frequency onto this f_0. Which means the VCO output frequency follows the LC circuit resonance frequency.

The input signal and reference signal of this sensor were taken from the red points 1 and 2 on Figure 4.22. The phase of these two voltage signals was then compared with the phase detector and an error signal was produced based on their phase difference. This error signal is a DC input for the VCO. At resonance, the impedance of LC circuit is completely resistive, therefore the phase of voltages across the resistor $\boldsymbol{R_c}$ (between point 1 and 2) is the same. Choosing the value for $\boldsymbol{R_c}$ is critical, because low values cause lower sensitivity in the phase detecting circuit, whereas high values can amplify the noise and interference, which means greater instability [64].

After applying the magnetic particles to the coil, this system will be unbalanced and new f_n will be produced based on Eq. (4.8), hence the VCO output frequency will be changed. Ultimately, the sensor output frequency was measured by a frequency meter from the VCO output signal.

The main input to the PLL, is the output signal of the LC oscillator, which determines the resonance frequency (f_r), which should be similar with the centre frequency (f_0) of the PLL lock range ($2f_L$),

as defined by the PLL components (R_1, R_2, C_1). The VCO centre frequency (f_0) is set by the R_1 and C_1. Indeed the lock range is controlled by R_1 and reducing this resistance can create wider frequency range. The offset frequency is set by R_2. It can be concluded from PLL IC application note that (Appendix 3):

$$F_{max} = f_0 + f_L \ , \ F_{min} = f_0 - f_L \qquad (4.9)$$

$$2f_L = F_{max} - F_{min} \qquad (4.10)$$

$$F_{offset} = = f_0 - 1.6 f_L \qquad (4.11)$$

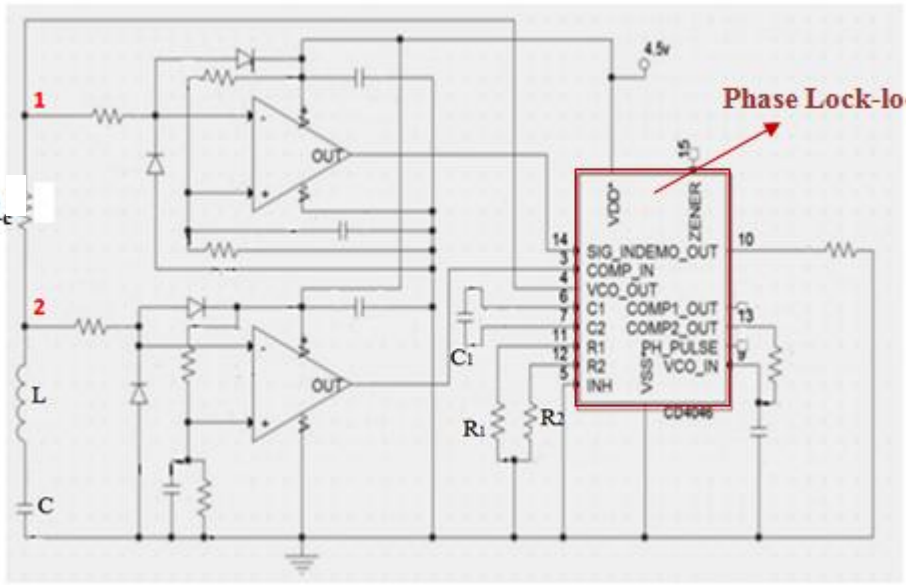

Figure 4.22: Circuit block diagram based on PLL

Understanding all of the above concepts and considering the formulae and design limitations, the sensor was designed based on the algorithm shown in Figure 4.23. At first the resonance frequency value needs to be selected by the mean of capacitor and inductance of the LC oscillator. Increasing frequency means smaller values of L and C (Eq. 4.7). For MHz range frequency, the coil inductance needs to be a few μH and the capacitor value should be a few pF. However, the value of capacitor cannot be below a specific value (20pF) due to the parasitic effect in the system caused by design limitations. Consequently, the coil must be fabricated in a way that could generates MHz range resonance frequency using the capacitor with more than 20pF capacitance; this combination also should make a satisfactory quality factor, Q. Different approaches were considered and examined for calculating the coil inductance, such as checking the coil inductance within a circuit experimentally in a range of frequencies, or theoretically by using equations and expressions available for calculating the multilayer inductance of an air core coil. As already mentioned the coil inductance is a frequency dependant parameter and there is no precise formula for calculating the

inductance theoretically, thus the best way is to fabricate the coil and test it within the circuit experimentally in different frequencies for evaluating its inductance.

Accordingly, a range of inductors were fabricated with different numbers of turns (50-300) and they were tested experimentally. After determining their inductance they were tested within the LC circuit with different capacitors to check if there is a LC combination that can produce resonance frequency in the range of 2-17MHz (the PLL maximum operating frequency). Only a few numbers of fabricated coils were useful for this purpose, and parameters such as small value of capacitor and parasitic effect limited this selection. The best results were achieved with two of the coils, one of them named the black coil with 85µH; and the other one the yellow coil, with 9.5µH inductance. These coils were used within the PLL resonance circuit.

At this critical point the PLL external components (R_1, R_2 and C_1) need to be chosen. The VCO operates correctly if its centre frequency f_0 is equal to the sensor resonance frequency. Although a lot of formulae and graphs are presented for selecting these components by the manufacturer, unfortunately they are not sufficient for designing this circuit, which is a complex process. This sensor design could not be completed without using other PLL manufacturer specifications and guidance. Some other rules and formulae were used [132] (Table 4.3) to improve the sensor stability significantly.

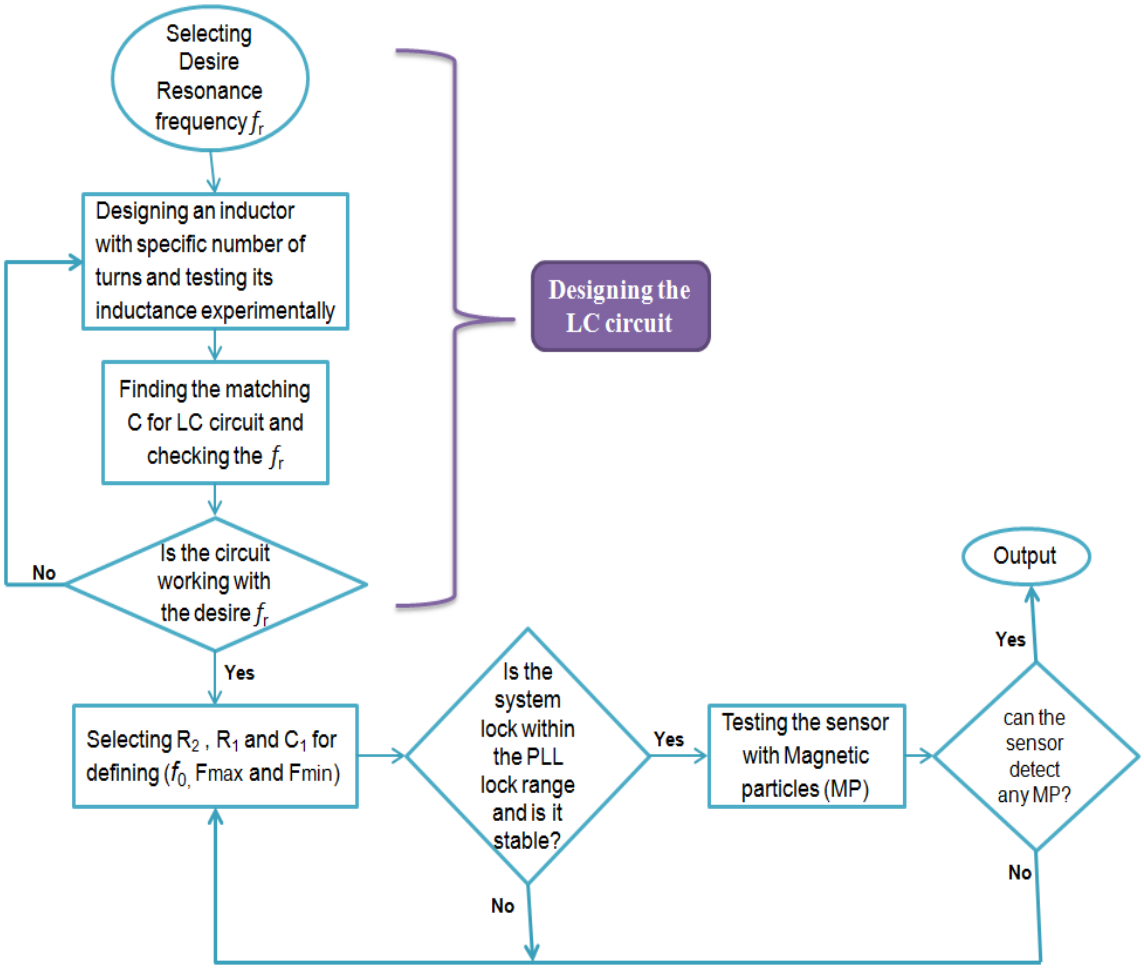

Figure 4.23: Magnetic sensor design algorithm

Table 4.3: 74HCT4046 PLL components formulae

$0.01 < \frac{R_2}{R_1} < 0.1$
If $F_{off} > 1MHz$ Then: $1 < R_2 < 12\ K\Omega$
$\frac{F_{max}}{F_{min}} < 1.1$

Different parameters affect the VCO (the most noise-sensitive part of PLL), which prevent it from following the input resonance frequency [133-134]. Most of the parameters in the circuit will influence the VCO changes and results in unstable system, not working in its specific frequency lock range. Different source of noises, such as electrical noise and interference, can cause phase and frequency fluctuation. Flicker noise and thermal noise can all change the circuit characteristics [135]. (The numerical calculation of signal to noise ratio is presented in chapter 5).

Accordingly, one of the challenging parts of the design was to check if the PLL and VCO are working in the intended lock range. Various experimental tests and theoretical estimations were performed to evaluate the sensor performance. Appendix 5 and Appendix 6 show some of the

sensor theoretical calculations undertaken based on the logarithmic equations derived from the diagrams in Appendix 4 (Eq. 4.12 and Eq. 4.13) and also the information from other sources. Each row of the tables in Appendix 5 and Appendix 6 represents set of components for one sensor design. The red colour values show that the design cannot be optimum based on that specific row parameters. The other rows of the tables which were theoretically satisfactory have been tested experimentally, which means more than 10 circuits were implemented based on the different components combinations, and the circuit has been checked in terms of locking the PLL in the right range of frequency, stability and sensitivity to the magnetic particles.

$$log(Y) = -0.87\, log(x) + 8.47 \qquad (4.12)$$

Where Y= f_{offset} (Hz) and x = C_1 (pF)

$$Log\ (Y) = -log(x) + 0.7782 \qquad (4.13)$$

Where Y=2 f_L and x =$R_1 \times C_1$

It has been found that the PLL capacitor (C_1=C_{PLL}) should be big enough to overcome the parasitic effect of LC circuit, and a capacitor below 120pF is required to push the system out of lock. Another finding was that choosing a bigger capacitor in the LC circuit results in larger frequency shift during detection, therefore for achieving higher resonance frequency and better detection resolution, choosing low inductance coil with larger capacitor is recommended. In addition, there is a wide variety of components values and combinations which can be used for designing this sensor (some of which are illustrated in Appendices 5 & 6), and in many of them the circuit is working fine and the PLL can lock in frequency range easily, but the problem with those circuits is their low stability, which is an important factor for magnetic particle detection, wherein the frequency shift might be just few hertz due to the small size of the particles and their low permeability.

After all of those considerations and theoretical calculations, small numbers of coils were fabricated with different numbers of turns (50-300). Each was placed into the circuit and tested with different resonance frequencies and couples of PLL resistors and capacitors.

The best results achieved with three circuit design, after calibrating the sensor (chapter 5), which two of them is based on using the black coil (85µH) and therefore those circuits are called *black coil circuits*, and the other one is the *yellow coil circuit* based on using the yellow coil (9.5µH). The sensor circuit was designed as described in the following subsections.

4.10.1 *Black coil circuits*

The black coil used in this sensor has an inductance of ***85µH*** with inductor resistance (R_C) of 5Ω. Two similar circuits were designed based on this coil just differing in the capacitor values and they are as follows:

1. The LC circuit capacitor is C_r = 39pf and the selected PLL Components are: $R_1 = R_2 = 10$ kΩ and C_1 = 390pf. This sensor is resonating at ***2.7MHz*** frequency.
2. The LC circuit capacitor is C_r = 47pf and the selected PLL Components are: $R_1 = R_2 = 10$ kΩ and C_1 = 270pf. This sensor is resonating at ***2.46MHz*** frequency.

These sensors have stable output and they are sensitive enough to detect small amount of magnetic particles. The sensor's calibration was done with different methods presented in chapter 5, including the signal to noise ratio (S/N) calculation. The results of the experiment with magnetic particles are presented in chapter 6.

4.10.2 *Yellow coil circuit*

The yellow coil fabricated for this circuit has 100 numbers of turns, which results in inductance of ***9.5µH*** at resonance frequency of ***7.2MHz.*** The LC circuit capacitor is Cr = 47pF and the selected PLL components are: R_1= 56 kΩ, R_2= 4.7 kΩ and C_1= 270pf. This sensor has stable output and it is sensitive enough to detect small amounts of magnetic particles (6µL of 10nm magnetic beads equivalent to 30µg magnetite powder). The sensor calibration methods are presented in chapter 5, including the (S/N) calculation. The results of the experiment with magnetic particles are presented in chapter 6.

The experimental set up of above circuits and the way they were calibrated for magnetic detection are fully explained in chapter 5.

4.11 Summary

This chapter explains the sensor design from initial plans up to final design version, exploring the steps taken by the author to find the optimum design for the magnetic bead detection sensor. The first attempt and intention was to design the inductive-based sensing technique using the spiral coil. Some of the methods for calculating and designing coil inductance were presented, and COMSOL simulation was performed for designing the planar inductor in circular and square forms with different materials. Due to the complexity in fabrication and also low quality factor of these types of

coil compared to conventional air wounded coils, they have not been fabricated and therefore an air core inductor was produced using PMMA bobbins (Figure 4.13a).

The first sensor was designed based on the inductor and Colpitts oscillator, which (due to the high frequency fluctuation and unstable nature of this system) did not show any sensitivity to the magnetic particles. Thus the circuit design was replaced with the differential sensing method based on using phase lock loop and RLC circuit. The fundamentals of phase lock loop and design considerations were presented. Complexities of designing a stable and sensitive sensor were discussed and the appropriate solutions for overcoming the issues with the most effective circuit designs were considered. The black and yellow circuits were introduced as the best candidates for magnetic particles' detection with the resonance frequency of 2.7 and *7.2MHz*. The experimental set up, the sensor calibration and characterization are presented in Chapter 5.

CHAPTER 5: **EXPERIMENTAL SETUP AND CALIBRATION**

5.1 Introduction and setup

In the previous section the sensor design, analysis and specification was discussed and the best frequency range based on the PLL components and system stability was selected for magnetic bead detection. In this chapter the experimental setup and the sensor calibration (with its limitations and challenges) are explained. Although theory rarely matches practical testing entirely, the system needs to be tested for validation.

The experimental set-up used for the magnetic bead sensor is shown in Figures 5.1 and 5.2. The sensor was designed based on the PLL and LC oscillator with an air core coil as a sensing element. The electronic circuit board designed with a ground plate (Figure 5.1 (a)) as a continuous ground on the bottom layer for noise dissipation. Having it can reduce the conducted noise by lowering the impedance of all ground connections and also acts as a shield for electromagnetic interference and radio-frequency interference (EMI/RFI).

The circuit board was placed inside the diecast enclosure with a fitting lid to reduce the frequency fluctuation. Because this sensor is performing at high frequency (MHz) using just ground plate, it cannot completely screen EMI/RFI effects. The diecast box and the coil were designed in such a way that the coil remains outside the box for magnetic beads' detection.

A jig was designed for the elimination of hand effect on the circuit and for holding the sample (magnetic particles on a substrate) on top of the coil; it was also used to adjust the distance of the sample from the coil surface (Figure 5.1 (b)). The diecast box was located inside the Faraday cage to achieve more stable results by reducing the effect of environmental conditions such as air cooling and heating, humidity, dust and electromagnetic radiation (Figure 5.2).

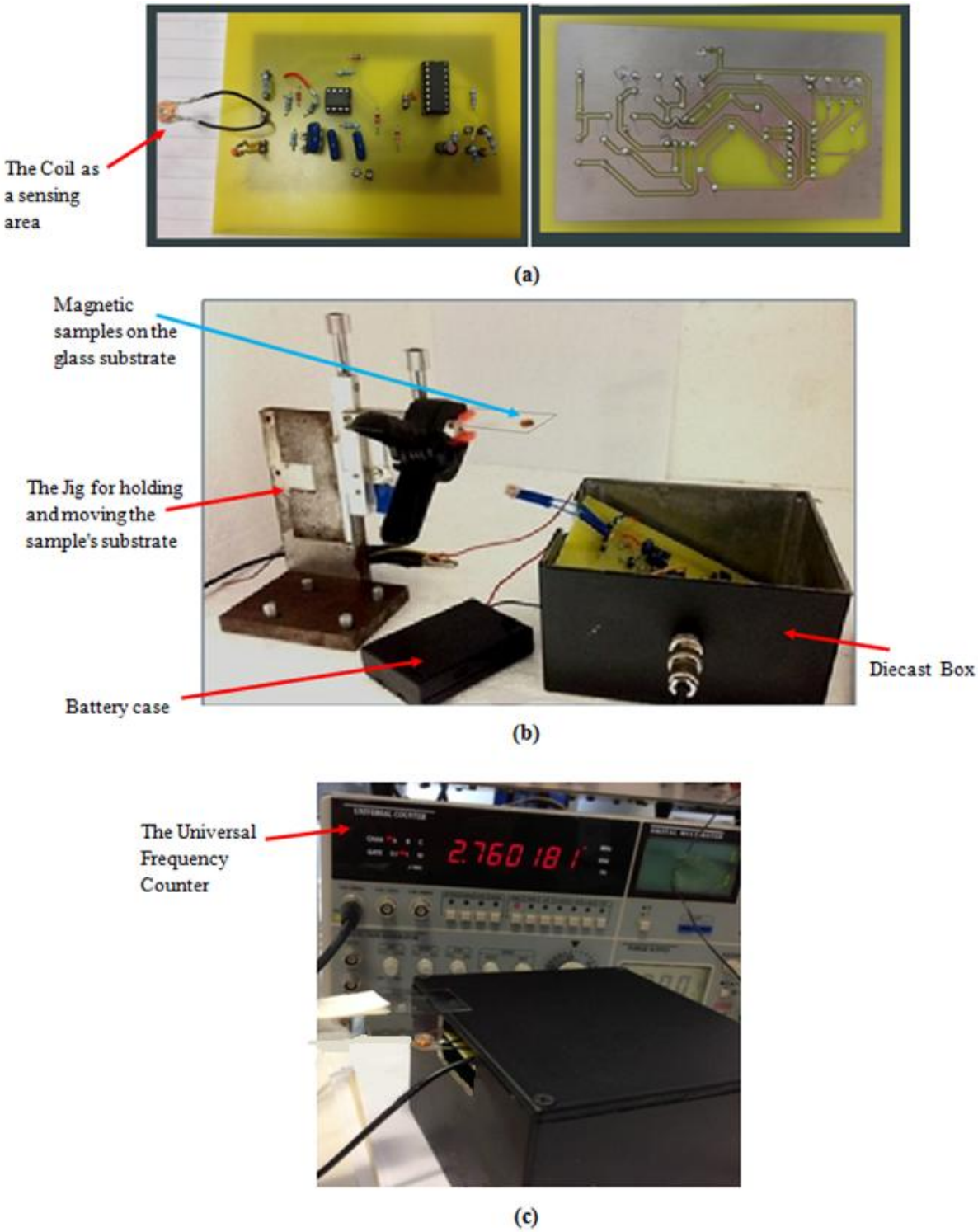

Figure 5.1: Experimental setup of the magnetic sensor (a) PCB board of the sensor (b) The jig and the circuit inside the diecast box, (c) The sensor with frequency meter for output measurement

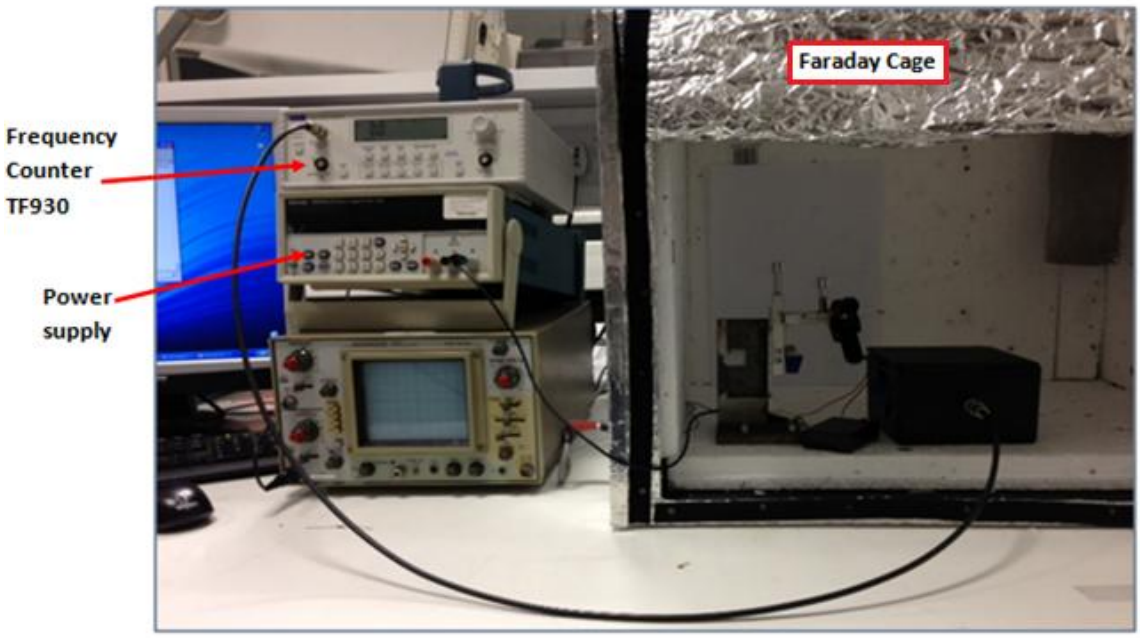

Figure 5.2: Complete system setup including the Faraday cage and frequency meter TF930

Figure 5.1 (c) shows the initial setup for the system in which the experiments were run using universal frequency meter at 2.7MHz. In this counter recording the output results were done manually in each 10 seconds, consequently a lot of time was spent on calibrating the sensor with the universal frequency meter and a series of results were taken, which are presented in chapter 6. The main problems with this setup were that recording the data manually was difficult, with a high chance of making mistakes, and very long measurement time was needed. Therefore, the new setup was introduced based on using Faraday cage for more stability and the new frequency counter (TF930).

As illustrated in Figure 5.2, the sensor is connected to the frequency counter (TF930) (with 9 digits resolution after 10s) for output frequency measurement, and this counter is connected to the computer via a USB interface for recoding the results. In this setup the sensor circuit board was kept inside the diecast enclosure with a closed lid, but the coil is out of the box for detection (one of the reasons for using s Faraday cage). The jig was fitted in the distance from the coil, which does not (by itself) have any influence on the circuit; it was only used for holding and adjusting the sample substrate on top of the coil. This entire system was located inside the Faraday cage and all were grounded properly.

Most of the equipment used for this research can be summarized as:

- Pipette for measuring sample liquid down to 0.1µL
- Frequency counter: universal counter

This counter can show the output frequency in 1 sec, 10 sec or 100 second gate, which means the frequency sampling is taking place in those intervals. There is no computer interface for this counter and thus all the measurements and readings were recorded manually. Therefore, for having reliable results, each experiment was run several times. According to the time consumable process of working with this meter and due to the chance of errors in recording the data, this counter was replaced with the more accurate one TF930.

- Frequency counter: TF930 (0-3GHz) Counter from TTi

This meter uses a reciprocal counting technique and it has high resolution. Setting the measurement time to 1sec, 8 digits of answer are generated and measurement time of 10sec, results in 9 digits output [140]. TF930 is a programmable counter, able to record all its data on the computer via serial port and USB interface, which makes the tests much easier and more accurate. The natural noise level of this counter is about 20Hz and the selected sampling time for most of the experiments was 10 sec.

- The weight scale: Denver Instrument M-220D with sensitivity of 0.01mg
- Power supply: Tektronix PWS2721 (0-72 v, 1.5 A)

The power supply was replaced by battery after a while. The glass cover slip was used as a substrate for magnetic particles to hold the samples on top of the coil. Below is some of the Chemical composition of the cover slip:

- Silicon dioxide (SiO2) =70%-73%
- Ferric oxide (Fe_2O_3) =0.08%-0.14%
- Aluminium oxide (Al2O3) =1.0%-2.0%
- Calcium oxide (CaO) =7%-12%
- MgO=1.0-4.5, etc.

As illustrated, a small percentage of ferric oxide was used in the glass cover, which could alter the coil inductance and consequently output frequency changes, therefore the effect of cover glass without any magnetic particle on its surface needs to be investigated prior to the magnetic bead test.

5.2 Sensor calibration

Calibration is an important and critical part of designing any system. Without calibration the system performance is unreliable and this can affect the results. The proposed sensor in this research includes an LC oscillator, which is supposed to produce a stable output frequency based on its LC

components (according to the Equation 4.7). Since in this detector the presence of magnetic particles is identified by the difference between the sensor output frequency and the sensor resonance frequency, the output of VCO was monitored as the sensor output signal. This signal represents the value of frequency and it is expected to be continuously stable. *Stability* is the main specification of this sensor, which indicates how well the sensor can produce the same frequency over a given period of time. LC oscillator and voltage controlled oscillator (VCO) in the sensor are both very sensitive to the environmental changes and noise such as temperature and phase noise. Even turning the sensor on and off can invalidate the calibration, thus the sensor was recalibrated for every single test.

Another important specification of the sensor and its oscillators is how close the produced frequency is to the expected resonance frequency (calculated by Equation 4.7); in other words, the accuracy of the sensor. The difference between the actual frequency and the expected resonance frequency is called frequency offset. This offset value will fluctuate within the limit and the range of frequencies (upper and lower), which indicates the noise level of sensor [141]. The sensor output frequency fluctuates within the specific noise level. One system can be very accurate but not stable, and vice versa. To better understand these specifications, Figure 5.3 illustrates the relationship between stability and accuracy, wherein f_c is the expected resonance frequency [141].

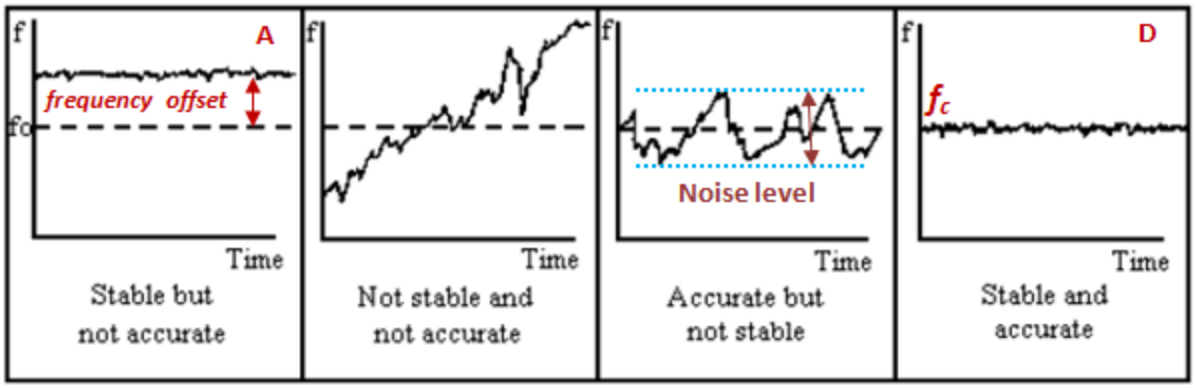

Figure 5.3: Definition of frequency accuracy and stability

The aim of calibration for this sensor is to understand the behaviour of the system and to discover the sensor specification in terms of stability. This sensor can be reliable and sensitive if its output signal performance is similar to that shown in Figure 5.3 (D), however the performance such as Figure 5.3 (A) can be practical and acceptable for the magnetic particle detection application if the fluctuation limits (noise level) is similar and independent from the frequency offset for one specific resonance frequency.

Another specification which affects the performance of the sensor is the long-term stability or the slow drift of the output frequency during a specific time (minutes, hours). Frequency stability depends on the stability of the components (e.g. L and C) utilized as a part of the oscillator circuit. Factors such as temperature changes can cause the inductor and the capacitor values to change. Shielding the coil can protect it from ambient temperature changes, although the air wound inductor used in this sensor is the best design for temperature stability. On the other hand, changing the temperature can alter the temperature coefficient of the components used in the circuit and accordingly change their values. A variant supply voltage can also change the output frequency. These are causes of a frequency drift in the oscillator. The following section explains these specifications in detail.

The frequency fluctuation of the output signal sometimes can be described by phase noise [142]. The random noise in the oscillator can result in phase perturbations and consequently frequency shift in the oscillator output. This random noise can cause by flicker noise, shot noise or thermal noise [142-145].

By the sensor calibration, the maximum value of the output frequency fluctuation and frequency drift should be determined and recognised precisely. Accordingly, the frequency shift occurs due to the presence of magnetic particles, which should be above those values. Therefore, accurate identification of the noise level and frequency drift in specific times is of high importance, since these distinguish between the different causes of the output frequency fluctuation, identifying whether it is due to random drift or the presence of magnetic particles. As a result, the system needs to be calibrated and all of its specifications should be revealed clearly. The following sections contribute towards this subject while the circuit has been tested against different situations (time period, temperature, humidity).

In the following section the parameters influencing the frequency signal are presented.

5.2.1 Factors affecting the sensor performance

The magnetic sensor performance is highly dependent on its oscillators' performance (the LC oscillator and the PLL oscillator, VCO). There are several characteristics inside the sensor and some environmental factors, which together must be considered in selecting the best circuit for magnetic particle detection.

One of the sensor characteristics is the operating frequency. The oscillators operating above 100 KHz have lower frequency stability compared to those working below this range. The frequency stability is dependent on the quality factor (Q) of the resonant circuit, the components used in the

circuit and the load impedance. Changing the load of an oscillator will cause a phase shift, which results in a change in the oscillating frequency. Some of these factors have been discussed in the previous section and also in chapter 4 for selecting the right components values.

In this research the effect of some of the mentioned noise sources has been investigated experimentally. All the experiments conducted for this thesis took place at room temperature, however the temperature was not stable and constant all the time, and during the day it fluctuated, sometimes by up to 5°C. The series of experiments was done in the lab, monitoring the temperature to discover if there is any relationship between sensor natural fluctuation and temperature changes. For example, in one of the experiments the temperature was 20°C before turning on the system, but after applying the voltage, a 1°C increase occurred. During three-hour testing the temperature was increased by about 3.5°C inside the coil. Temperature was gradually increased over time by about 0.5°C each half an hour. There was no significant frequency shift due to the ambient temperature changes in short time periods, but increasing temperature gradually caused the frequency reduction. The calibration experiments are very time-consuming, normally taking up to six hours per day, during which time there will be heating effects inside the circuit which can naturally change the frequency gradually. Figure 5.5 shows this graduate frequency shift which can be the result of heating effect.

The effect of electric shock caused by lightning or any electronic noise was also investigated. These noise sources can produce the frequency shift for tens of seconds and then the system will come back to its previous value quickly. Figure 5.4 shows an example of these sorts of tests. The sharp jump on the graph occurred due to turning on the electronic device (Vortex mixer) and because of the electrical shock. After a minute the system tries to come back to its previous value, but the mixer is still on and working, therefore the centre frequency shifts. To avoid some of these issues, the power supply of the sensor was replaced with a battery.

Another important factor is the humidity. The tests were conducted in different days to investigate this effect. It can be concluded from the results that humidity up to 60% did not influence on the sensor, but above this the system became unstable, with more frequency fluctuation. It was also stated in [146] that the best performance of electronic components can be achieved with relative humidity between 45% and 55%.

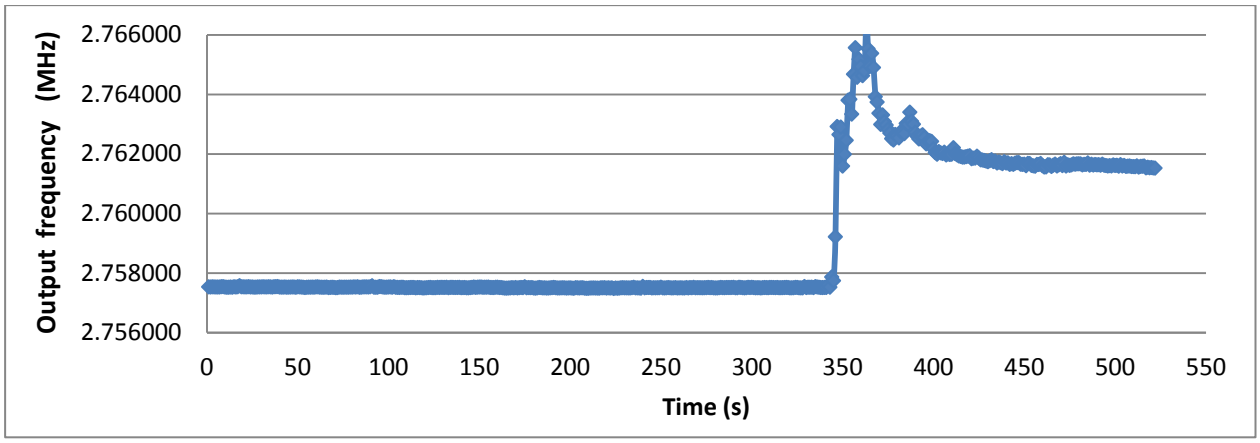

Figure 5.4: Effect of electric shock on the output signal

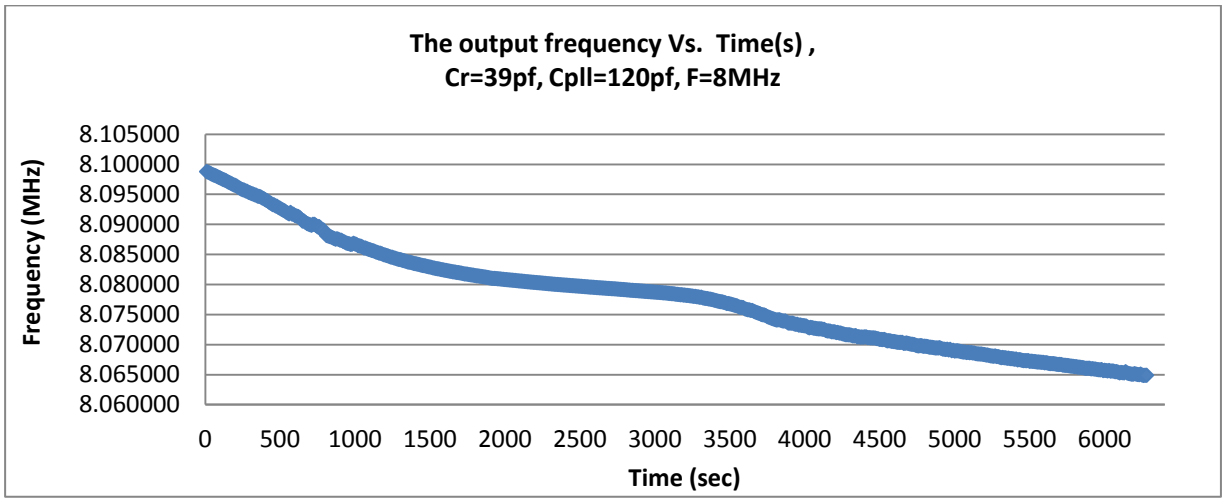

Figure 5.5: The circuit behaviour during $1\frac{1}{2}$ hour

It is also essential to consider the heating effect of the circuit components. The inductor is one of the most sensitive components to temperature changes, especially in inductive sensing, in which everything is measured based on the inductance variation. Temperature change can alter the wire resistivity and therefore change the conductive skin depth and also the eddy current distribution, which in turn can affect the mutual inductance between the winding. All of these can result in frequency change. This effect has more influence when the magnetic samples are placed on the coil, and as a result more frequency reduction and higher frequency shift is achieved by keeping the sample on the coil. Figure 5.6 illustrates the change in the coil inductance due to the temperature changes for different frequency [147]. Copper was used as a conductive target for sensing. It can be seen that higher frequency caused more inductance change by increasing the temperature.

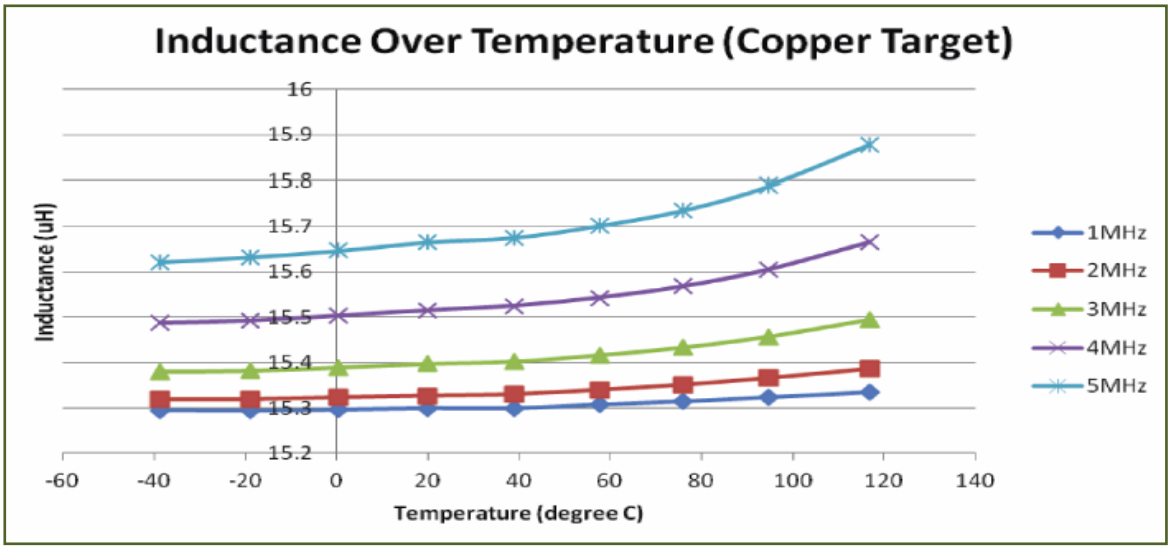

Figure 5.6: Inductance of a coil as a function of temperature across frequency

5.2.2 Effect of PLL capacitor

As discussed in chapter 4, there are three effective components on the PLL that can control the circuit (R_1, R_2 and C_1). These can keep the output frequency within the lock range and also can affect the value of resonance frequency (f_0) by changing the load impedance of the LC oscillator. The capacitor $C_{1,}$ beside the LC oscillator circuit can change the resonance frequency and define the centre frequency.

Figure 5.7 demonstrates the sensor output signal corresponding to the PLL capacitor. It can be seen that having the same LC oscillator parameter but not the same PLL capacitor can result in the different centre frequency and also the different output signal variations. (As an example in the sensor with Cpll=150 pf , the system cannot lock in the defined frequency range).

Figure 5.8 shows another example in this case, in which the PLL capacitor results in various centre frequency. Although the sensors look stable, the stability appears after a long time (>400 s). They also did not show good sensitivity to the presence of magnetic beads. This sensor was tested within the different range of resonance frequency (2 - 9MHz) in order to find the components combinations that result in the smallest natural fluctuation and more stable and reliable sensor. Figures 5.9 and 5.10 are examples of the experiments performed in different centre frequency.

The resonance frequency of 6.5MHz was obtained in Figure 5.9, but the frequency fluctuation is high, which means the circuit design is not perfect; one reason for this is that the chosen capacitors cannot balance the circuit impedance. Another instable sensor is shown in Figure 5.10, in which the low S/N ratio compared to the other stable circuit confirms its weak performance (as discussed in

the following section). Low Q factor, very long settling time and high output variation can cause an unstable and insensitive sensor for magnetic beads detection.

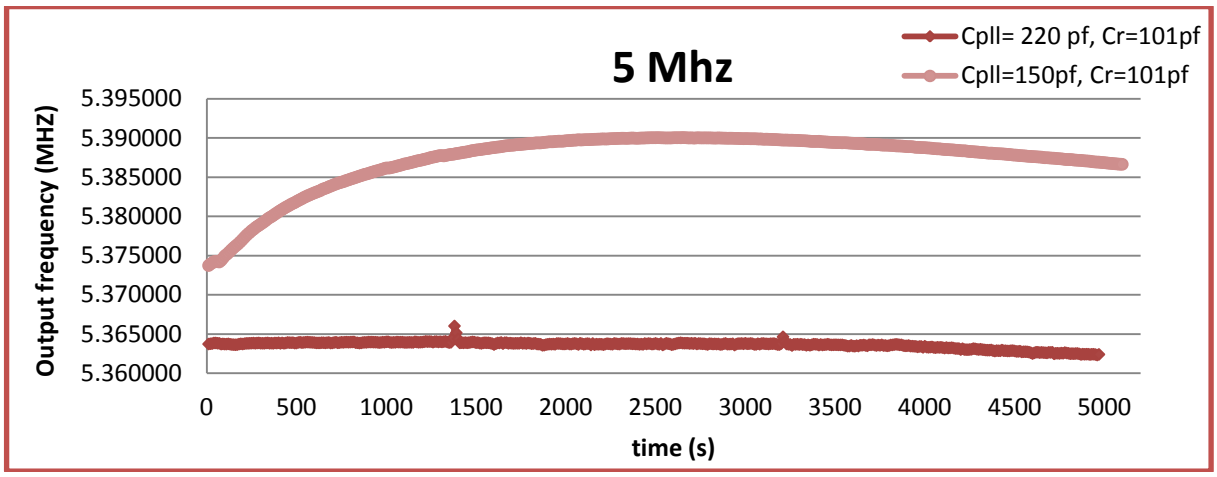

Figure 5.7: Different centre frequency in accordance of the different value of PLL capacitor, $C_{PLL}=C_1$

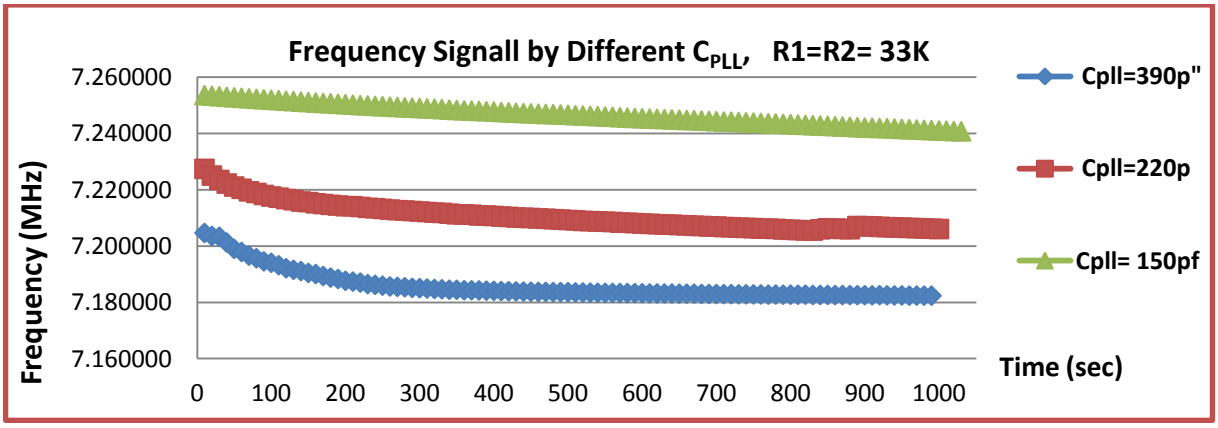

Figure 5.8: Calibration the sensors with different f_0

Among the different circuit designs calibrated three circuit design show more stability with higher sensitivity to the presence of magnetic particles. These circuits are as follows:

- The Black coil circuit with f= 2.4MHz
- The Black coil circuit with f= 2.7MHz
- The Yellow coil circuit with f= 7.2MHz

These circuits were introduced in chapter 4 and their calibration results are presented in the following sections.

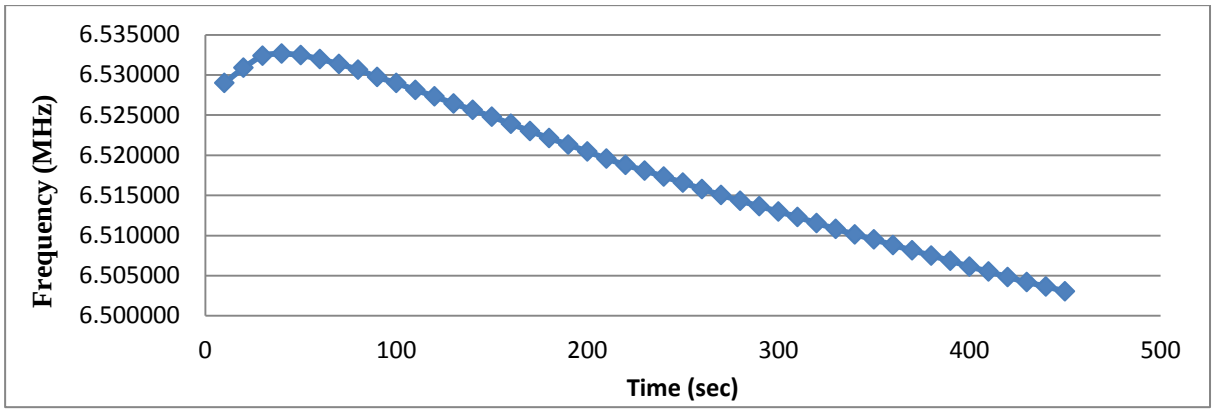

Figure 5.9: An unstable output signal at f=6.5MHz with C_{PLL}= 270 pf

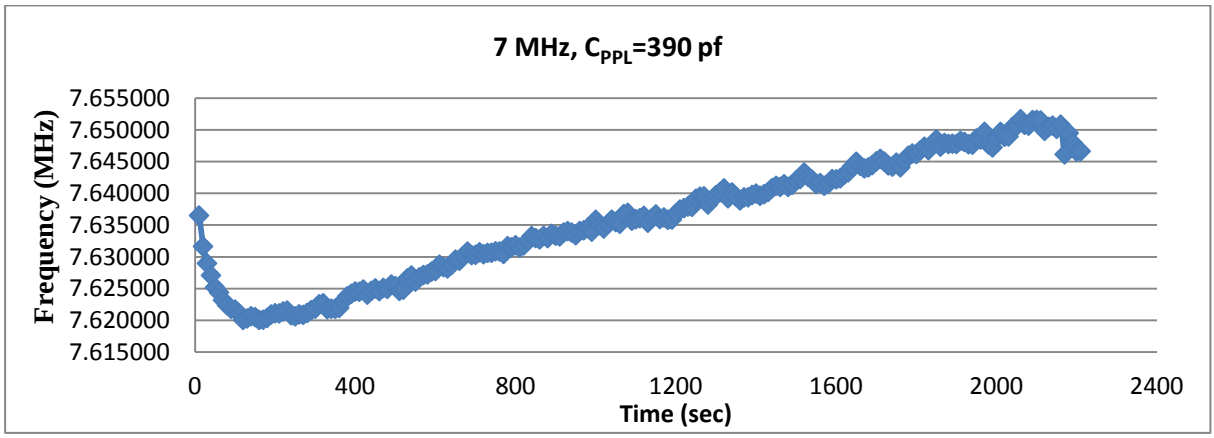

Figure 5.10: An unstable sensor with C_{PLL}= 390 pf , S/N= 35153

5.3 Calibration for the Black coil circuit

As mentioned previously, there were two types of frequency counters used in these experiments: the universal counter and the TF930 meter. The Black coil circuit (chapter 4) with the resonance frequency of 2.7MHz was tested and calibrated with two different frequency counters mentioned earlier and the results are presented in the following sections.

5.3.1 Calibration using the universal frequency counter

One of the main factors in measuring the signal is the time interval chosen for measurement representation. In this counter average frequency can be measured over time intervals of 1 sec, 10 sec and 100 seconds, producing different results for each interval. The results shown in the following section are based on the 10 sec. interval.

The output signal was monitored in different time duration. Figure 5.11 shows the first 10 minutes of the circuit start up in which each point on the graph is the representation of one 10 sec reading of the counter.

The maximum variation experienced during ten minutes output signal was about 445Hz. The fluctuations represented in the output are not in the sinusoidal form or periodic, they mostly look like random drift. To find out the answer, the frequency components of a signal need to be investigated.

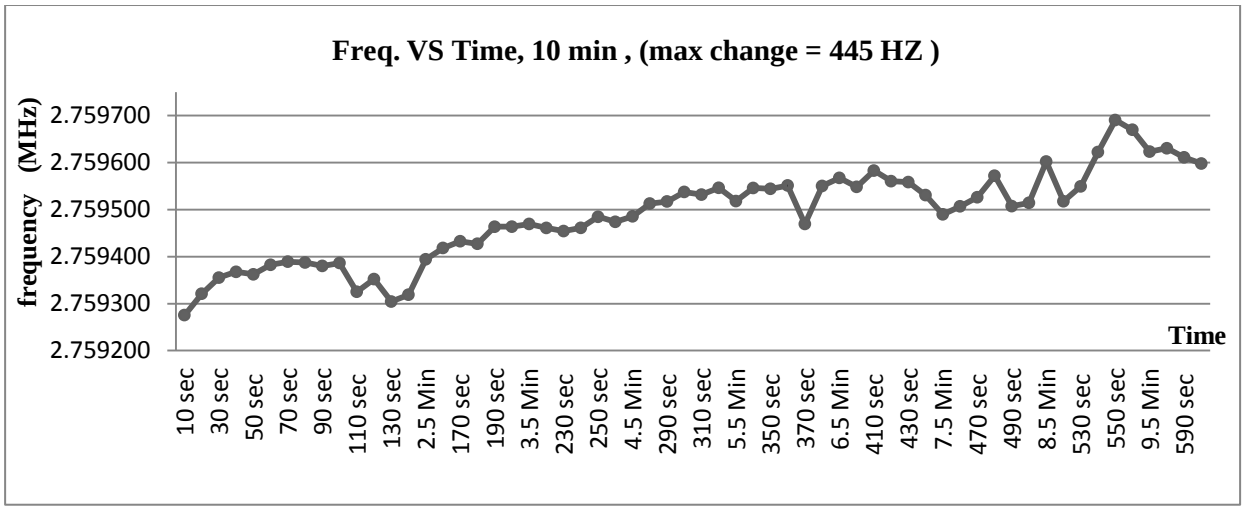

Figure 5.11: 10 minutes measurement of the output frequency with 10 sec time intervals

Fourier transform of the data (the sensor output **frequency** signal) was calculated to understand the frequency of the data and to discover the signal to noise ratio. Figure 5.12 illustrates the results calculated for three different samples. Each sample is the sensor output signal (VCO) taken within the specific time duration, which in Figure 5.12 (A) represents the 20 minutes test, Figure 5.12 (B) represents the 10 minutes and (C) represents the 5 minutes test.

In all samples, Figure number 1 shows the DC component of the frequency amplitude (the DC component is simply the average value of the signal) and Figure number 2 shows the noise variation. Comparing the amplitude of DC component which is about 331 (Figure 5.12 A (1)) to the average amplitude of noise (Figure 5.12 A (2)) that is about 0.001, the signal to noise ratio can be calculated and because the noise amplitude is so small, therefore the S/N is very large number and thus the noise is negligible in this sensor. Similar approach was considered for the other signals (Figure 5.12 B and C) and noise was very small. The signal to noise ratio (S/N) calculation for Figure 5.12 is as shown below:

- **A**: $S/N = 331/0.001 = 331\times10^3$
- **B**: $S/N = 151.7/0.00025 = 606\times10^3$
- **C**: $S/N = 82.76/0.0002 = 413\times10^3$

The S/N value for most of the samples tested was similar and the amplitude of DC component was much larger than the noise signal. As a result, the noise can be neglected from the calculation. Thus it can be concluded that the sensor output fluctuations are due to the frequency drift. The amount of this drift needs to be considered accurately during the magnetic beads detection test. Therefore the output signal was monitored several times with different time periods (20, 10, 5 and 3 minutes) to find out the sensor behaviour.

Figures 5.13 and 5.14 illustrate the frequency variation of the sensor output signal resonating at 2.7MHz in 10 minutes and 5 minutes period. Each line in the graphs represents the first few minutes of the signal after turning on the sensor. These lines were chosen randomly from the experiments done in different days and time. Comparing these two figures, the amount of frequency drift in the signals monitored for 10 minutes are more than the signals monitored for 5 minutes duration. The maximum frequency shift in Figure 5.13 is 426Hz while this value in Figure 5.14 is 190Hz. Therefore, the natural fluctuation of the sensor during 5 minutes is 190Hz.

This sensor was tested with the magnetic beads prior to the calibration to find out how long it takes for the frequency to drop due to the presence of magnetic particles. These particles were placed on the cover glass and brought in proximity of the coil. The same process was repeated with the cover glass without any magnetite powder on it. The result of this test is illustrated in Figure 5.15. The cover glass did not make any changes to the output signal, while the magnetite powder causes the frequency to drop more than 1kHz. On the other hand, the frequency reductions due to the magnetite samples occurred straight away (within 10 seconds), which means the effect of sample can be detected with the sensor in few seconds. It can also be concluded from Figure 5.15 that, by leaving the particles on the sensor, the frequency reduction increased continuously. This phenomenon can be described by the heating effect of magnetic particles (chapter 3, section3.7). Experiments with magnetic sample were repeated with this sensor setup to discover the sensor sensitivity and the smallest detectable amount of particles. The results of these tests are illustrated in chapter 6.

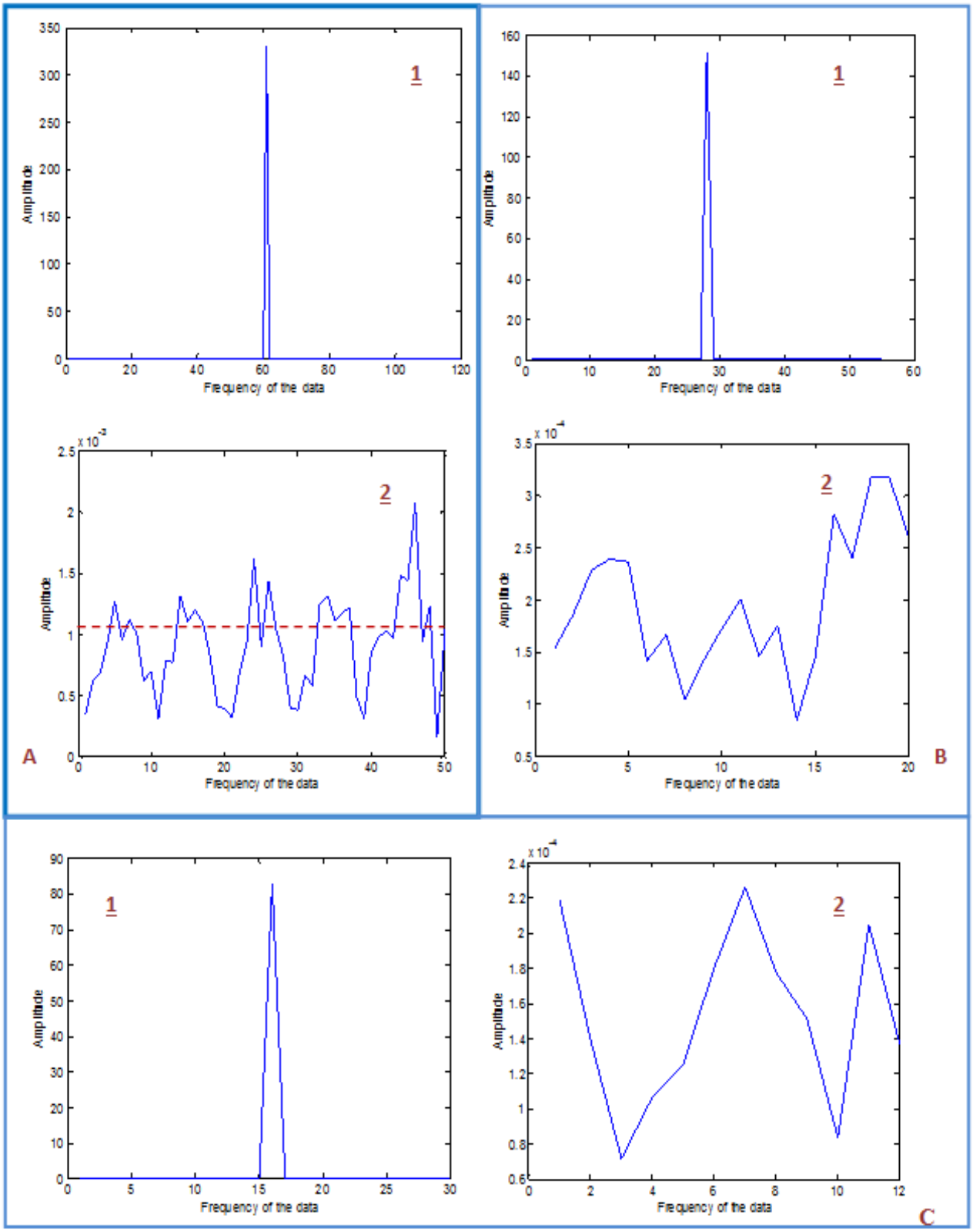

Figure 5.12: Fourier transform of the sensor output frequency signal

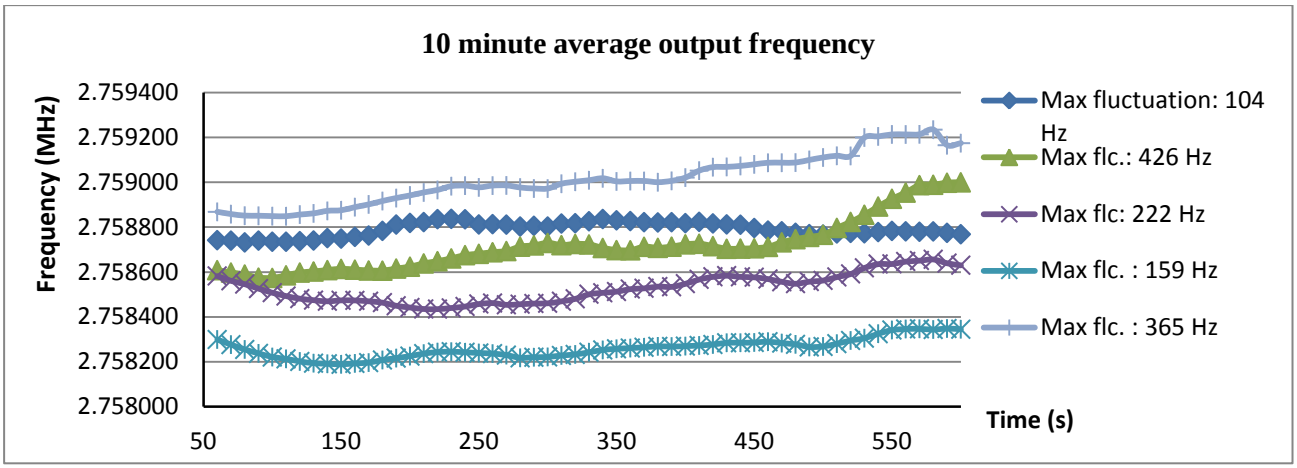

Figure 5.13: Measurement of the output frequency in 10 minutes (flc: fluctuation)

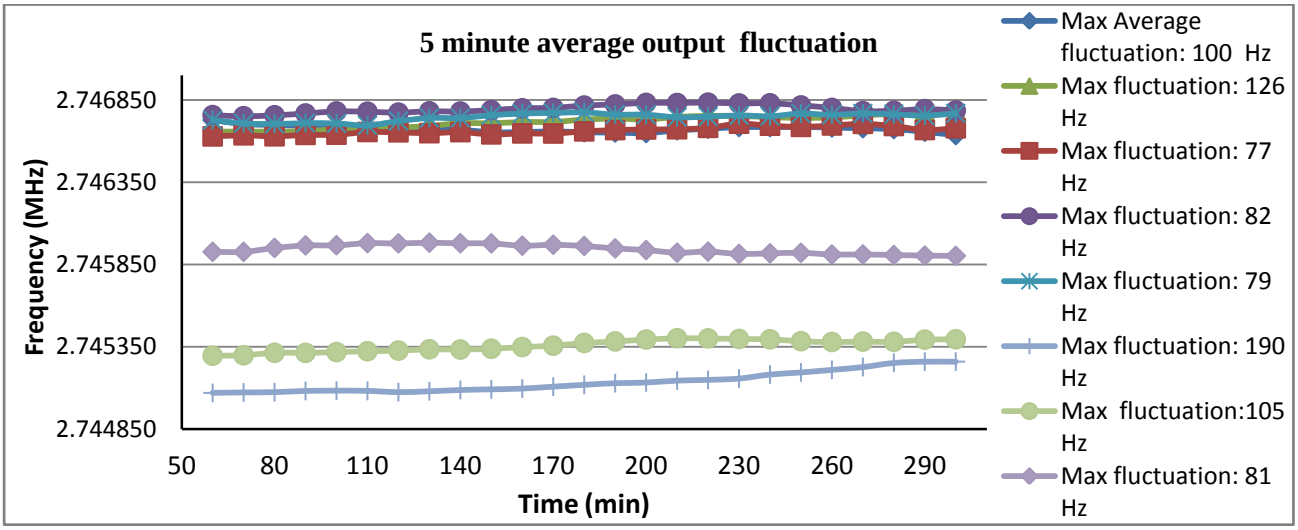

Figure 5.14: Measurement of the output frequency in 5 minutes

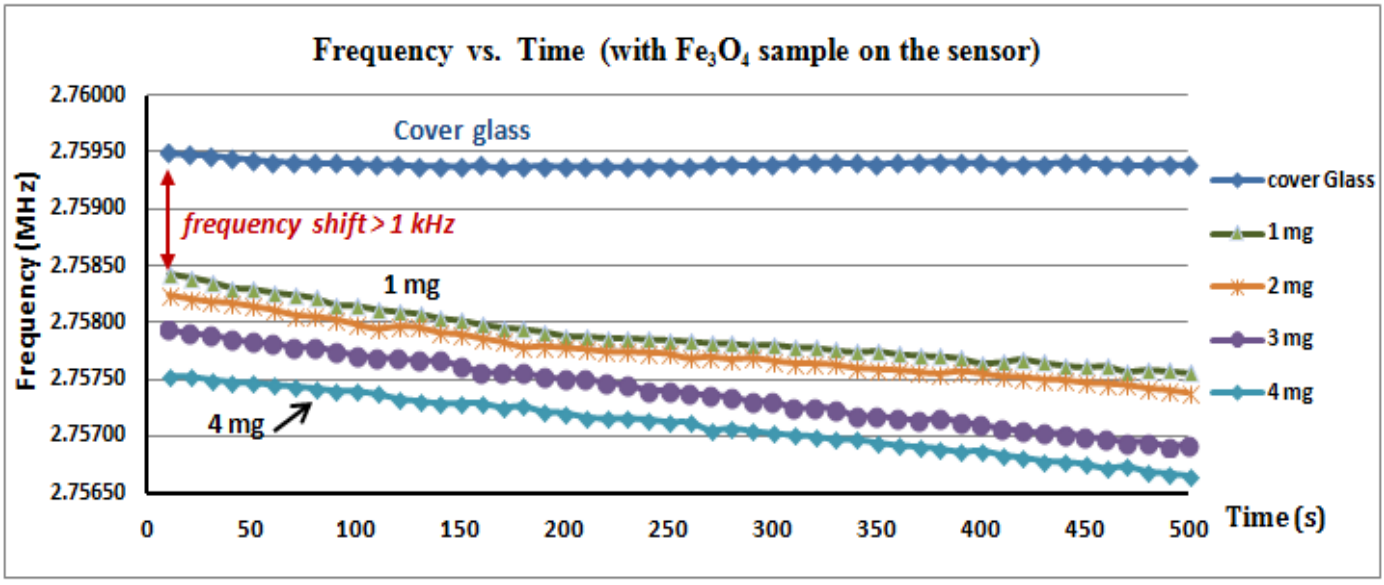

Figure 5.15: Measurement of the output frequency with magnetite sample on the Black coil

As mentioned earlier, the magnetic samples can be detected in less than a minute. Therefore, characterizing the sensor for 3 minutes can cover the maximum frequency drift of the sensor during the sample detection. For that reason the diagram were made such as Figure 5.15 while the output was monitored for 3 minutes and the maximum frequency shift achieved was below 170Hz.

As a result, the natural fluctuation (frequency drift) of the Black coil sensor monitoring with the universal counter was considered **170Hz**. This value needs to be considered while calculating the amount of frequency shift as a result of any magnetic samples. This amount of frequency fluctuation was done during three minutes and as a result the sensor *frequency Drift* can be defined as : Max frequency fluctuation per second (Hz/sec).

This value for this sensor is: 170/180= **0.94** (Hz/s)

The lower the frequency drift value, the better the system stability.

5.3.2 Calibration using the TF930 frequency counter

A similar approach to that described in the previous section was used to calibrate the Black coil circuit using the TF930 frequency counter. However, using this counter the signal measurements were recorded automatically at both 1 and 10 second time intervals (the settling time of the sensor is 2s). This counter is more precise and accurate compared to the universal one, and its manufacturer application notes state that 20Hz random fluctuation needs to be considered as its natural fluctuation.

Two sensors in the range of 2-3MHz frequency, both using Black coil with inductance of 85µH (chapter 4), were tested with this counter. The sensors were calibrated by monitoring the output signal in different time periods. Although the sensor was tested while it was continuously on for hours, because the detection of magnetic particles occurs in less than 30 seconds, long-term stability is not of interest. Therefore, the graphs presented here are a sample of the tests used to check the short-term stability (<5 min).

Figure 5.16 illustrates a sample of the output measurement (with 1 second time interval) for the circuit oscillating at 2.7MHz. The graphs demonstrate the output frequency of the sensor since it is turned on for 1 minutes. It shows no more than 50Hz fluctuation at each line.

Figure 5.17 shows the similar measurement done within a 5 minutes from start-up of the sensor oscillating at 2.4MHz. This sensor shows more stability compared to the previous sensor (2.7MHz), while it has maximum fluctuation of 45Hz in 5 minutes.

The signal to noise ratio (S/N) calculation for these sensors was done by the similar method explained based on Fourier transform. This is a sample of measurement for this sensor:

$S/N = 827.91/0.0012 = 689\times10^3$

Which shows the small noise signal is negligible.

The maximum output fluctuation calculated for the 2.7MHz resonance frequency sensor is about 70Hz, and for the sensor resonating at 2.46MHz it is 50Hz. Consequently these amounts of frequency fluctuation were happened during two and five minutes and therefore, the sensor *frequency drift* **is**:

For the sensor oscillating at 2.7MHz: 70/120= **0.58** (Hz/s)

And for the sensor oscillating at 2.4MHz: 50/300= **0.16** (Hz/s)

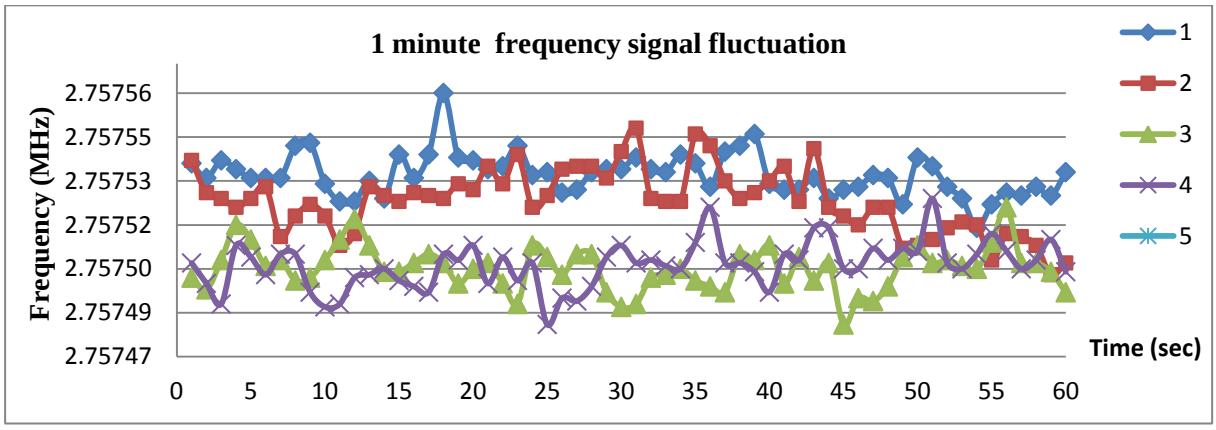

Figure 5.16: Measurement of output frequency signal during 1 minute (time interval=1 sec.).

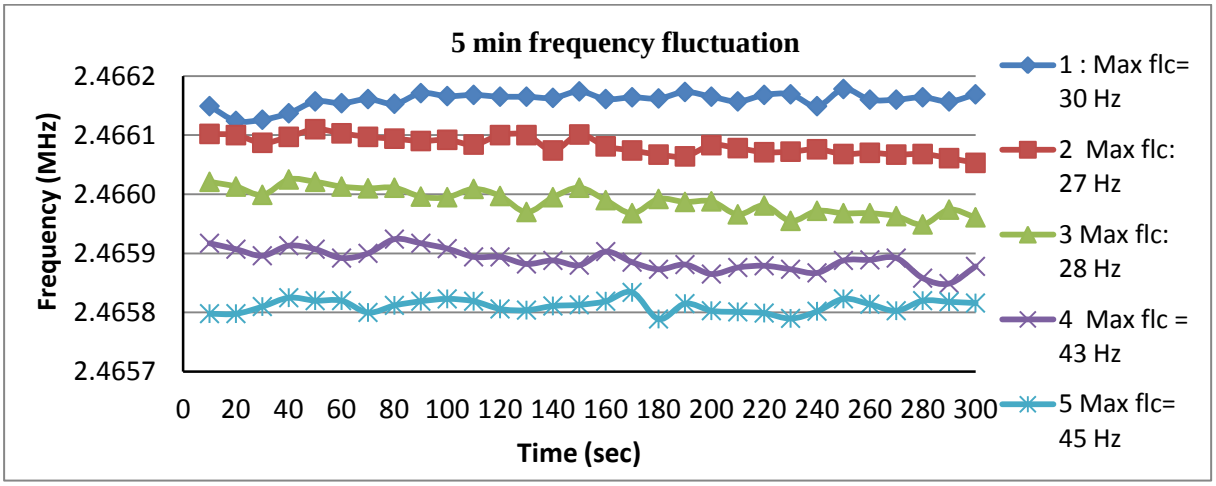

Figure 5.17: Measurement of output frequency signal during 5 minute (time interval=10 sec.).

5.4 Calibration for the Yellow coil circuit

The Yellow coil circuit is oscillating at 7.2MHz. Calibration of the sensor was done as for the Black coil circuits by measuring the signal in 10 sec. time intervals. Figure 5.18 illustrates the amplitude of frequency fluctuations for several tests. It can be seen that the maximum frequency shift achieved was below 100Hz. The duration of sampling and calculating the frequency difference was 30 seconds, which means waiting for three readings from the counter. 30 seconds timing was allocated for measurement after running experiments with magnetic particles. The results showed that the presence of magnetic beads on the sensor was sensed in the first 10 seconds, with the beads placed on top of the coil, and the frequency shift appears on the output signal immediately (such as Figure 5.15). The sampling time interval of the frequency counter was 10 sec, however for reliable detection 1 minute frequency fluctuation was considered to define the natural fluctuation of the system, which was 200Hz. Figure 5.19 demonstrates the fft analysis of the frequency signal for calculating the S/N ratio. The noise amplitude is very small comparing to the signal amplitude and therefore the S/N ratio is very large number. Although the S/N ratio of the Black circuit (2.7MHz) is higher than this circuit.

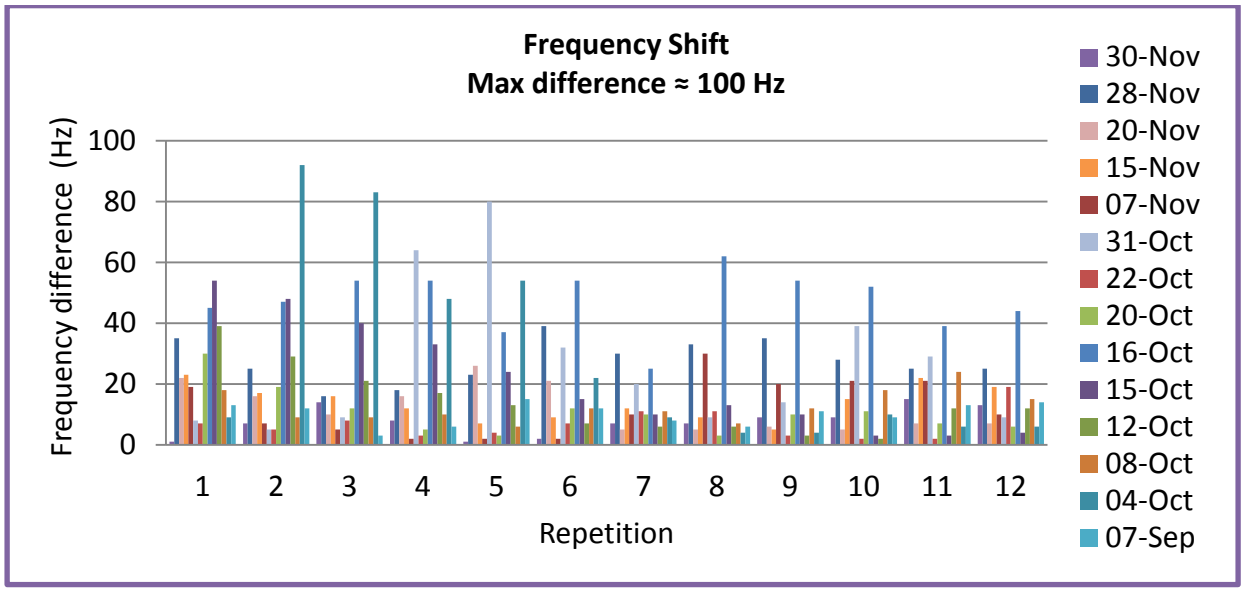

Figure 5.18: 30 sec frequency variations (duration: 140 s)

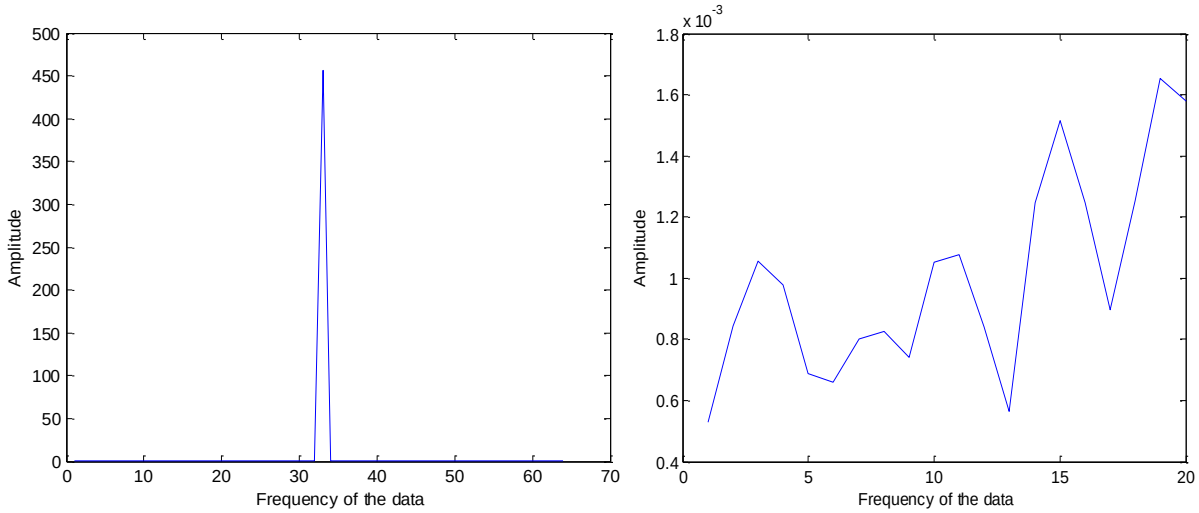

Figure 5.19: Signal to noise ratio (S/N) calculation - S/N = 456.31/0.0018 = 253×10^3

As a result, the natural fluctuation of the Yellow coil sensor was considered to be 200Hz. This amount of frequency fluctuation was done during one minute and as a result the sensor *frequency Drift* is: 200/60= **3.3** (Hz/s)

Which is large number comparing to the previous sensor. This illustrates that increasing the frequency can affect the system stability. And higher the frequency, lower the stability.

5.5 Sample positioning

This section emphasises the magnetic particles' distribution on the glass cover, which results in different output signals. In reality, the particles' positions take place randomly, and it is necessary to study effect of randomly distributed magnetic particles on the signal.

Figure 5.20 shows some of the common positions different types of particles assume after application on the coil. Liquid samples are more likely to spread over a larger area (depending on the volume of the sample) or they easily form the shape of the magnetic field distribution line. Powder samples tend to stay close together and form the heap structure.

The particle magnetic field and the coil magnetic field and inductance all vary with the location of magnetic particles. Furthermore, inter-particle interaction may differ based on their position. Consequently, the output frequency signal varies depends on the particle position.

The maximum frequency shift was achieved when the particles stay towards a sensor centre. Due mainly to the concentration of the magnetic field in the centre of the sensor, the magnetic particles generate a larger field, which in turn, creates a larger frequency shift.

In summary, due to the sensor dependence on the particle location, is best for the magnetic samples to be located close to the coil centre and not near to the sensor edges for reliable signal detection. In this way the random distribution of particles cannot influence the sensor signal significantly if the particles are placed close to the centre of the coil.

In other words, it is better to have the sensing area as small as the mass or density of the particles to be detected. The higher the ratio of (Particles Density/Sensing Area), the better signal quantification and thus the more sensitive and reliable the sensor.

The experiments conducted with magnetic particles in chapter 6 demonstrate the effect of particle positioning on the sensor.

5.6 Summary

In this chapter the experimental setup was introduced and the sensor calibration, with its limitations and challenges, was explained. The effect of different parameters on the sensor output frequency was discussed (e.g. ambient temperature, PLL circuit components, humidity etc.).

Calibration results reveal the best circuit designs for magnetic particle detection with high S/N ratio and the maximum output signal fluctuation in few minutes. The results are presented in Table 5.1. Sensors numbers 1 to 3 were designed using Black coil and sensor number 4 was designed based on the Yellow coil. Although similar components were used for sensors 2 and 3, the experimental setup and circuit platform was different. Sensor number 3 was tested via the universal frequency counter, which identified the highest output fluctuation. However, the Faraday cage was not used during the experiment with that sensor, which is another reason for having higher fluctuation.

These sensors were all tested with different types of magnetic particles. Their test setup and outcomes are presented in the next chapter.

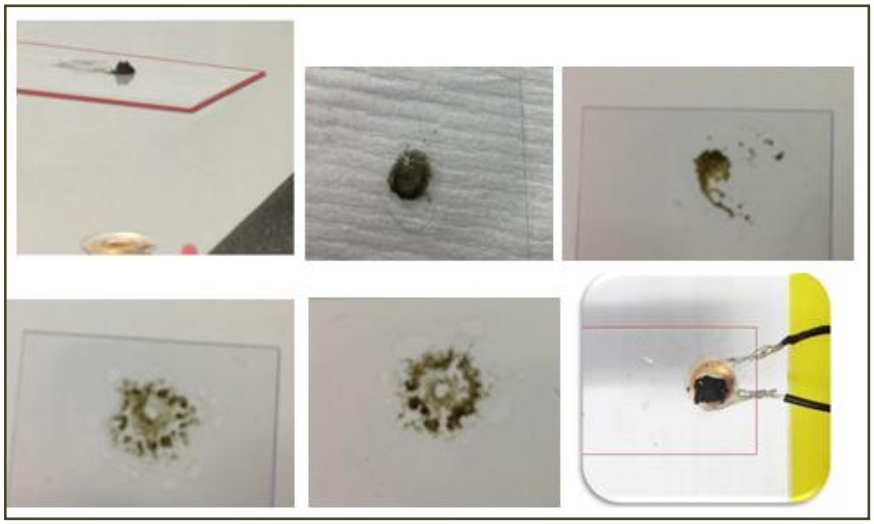

Figure 5.20: Magnetic particles position on the coil

		Resonance Circuit		Phase Lock Loop Circuit			Max Fluctuation (Hz)	S/N Ratio	Frequency Drift (Hz/sec)
	Resonance Frequency	L (µH)	Cr (pf)	R_1 (KΩ)	R_2 (KΩ)	C_1 (pf)			
1	2.4MHz	85	47	10	10	270	50	689×10^3	0.166
2	2.7MHz	85	39	10	10	390	90	580×10^3	0.58
3	2.7MHz	85	39	10	10	390	170	331×10^3	0.98
4	7.2MHz	9.5	47	56	4.7	270	200	253×10^3	3.3

Table 5.1: Magnetic sensors circuit specification

CHAPTER 6: **EXPERIMENTS WITH MAGNETIC PARTICLES**

6.1 Introduction

In the previous chapters, the PLL-based sensor was introduced and designed for magnetic bead detection purposes. The circuit frequency range is calibrated for 2MHz and 7MHz (chapter 5). According to the environmental issues (e.g. temperature, humidity) and the effects of different circuit components and measurement equipment (e.g. frequency counter), the sensor output has frequency drift and fluctuations. As mentioned earlier, the main purpose of this project is to produce a sensor able to detect the presence and quantity of magnetic particles, therefore after designing and calibrating the circuits described in chapters 4 and 5, this chapter is entirely dedicated to perform the experiments with actual magnetic samples.

Different types of magnetic samples (in terms of size and permeability) were tested using the sensor and each sample was tested several times in different time periods. The required time for the sensor to detect the presence of the magnetic particles is a few seconds, and according to the sensor calibration in chapter 5 the sensor output was measured 30 seconds after applying the magnetic sample to calculate the frequency shift. Another important factor for these types of detection is the sample substrate, which has to be selected carefully due to its influence on the output signal, especially if there is any chemical property (e.g. iron) that can influence the sensor output. The substrates should not have any magnetic permeability, which may mask the sensor output due to the presence of the particles.

In these experiments, four different types of samples were used, three of them in solution: Cytodiagnostics magnetic nanoparticles, agarose magnetic beads and synthesized magnetic particles. One of them consisted of pure iron oxide in a dry state: magnetite powder (Fe_3O_4), as explained in chapter 3.

Below are the sample substrates selected for these experiments;

- Microscope cover glass cover (24×50mm 100PSC 0.13mm thick)
- The filter paper from Whatman, Grade 1
- The acetate paper

The glass substrates chosen because of their small width which is similar to the most microfluidic channel (100µm); this will be the future sample substrates for this sensor. On the other hand its structure is firm and its surface is highly resistant to most chemicals, which helps to hold the sample

without spreading or absorbing it. Its transparent material facilitates sample positioning on the coil surface area. However, small percentages of the iron material inside the glass cover alter the coil inductance and consequently reduce the sensor detection resolution. Therefore, two more paper-based substrates were used which were able to overcome the frequency reduction issue of the glass cover, but they had some other problems such as very soft structure or liquid sample absorption, which resulted in the conclusion that they were not better options than the cover glass. The experiments performed based on different substrates are presented in this chapter.

6.2 Early experiment with GMR sensor

As described in chapter 2, the GMR sensor is designed to sense magnetic field strength and it is highly sensitive to the small field; it gives a rapid electronic readout under low magnetic field (nT) at room temperature. It can be used as a DC field sensor because it directly detects magnetic field, not the variation of the field strength; therefore, magnetic beads' magnetic fields cause a GMR sensor resistance change, and thus variation in the sensor current and consequently the output voltage signal difference.

The GMR sensor chosen for this experiment is from NVE Corporation, as described in chapter 2. In this method of detection, the substrate (on which the magnetic particles have been placed on its surface) is positioned above the GMR sensor. The sensor active area should be as small as the total surface area of MNPs (magnetic nano particles) that can be detected to achieve high sensitivity. The sample distance from the surface of the sensor active area has a major impact on the detection limit; this distance should be kept as short as possible (nm).

The sensor has a planar square shape and is only able to sense magnetic fields in the range of (0mT-15mT). Figure 6.1 shows the output voltage signal behaviour to the applied magnetic field [148]. The slop of each line indicates the sensor sensitivity to the magnetic field. Thus the sensitivity of this sensor can be defined by differential output voltage in millivolts per applied magnetic field in mT ($\frac{\Delta V\ (mv)}{H\ (mT)}$).

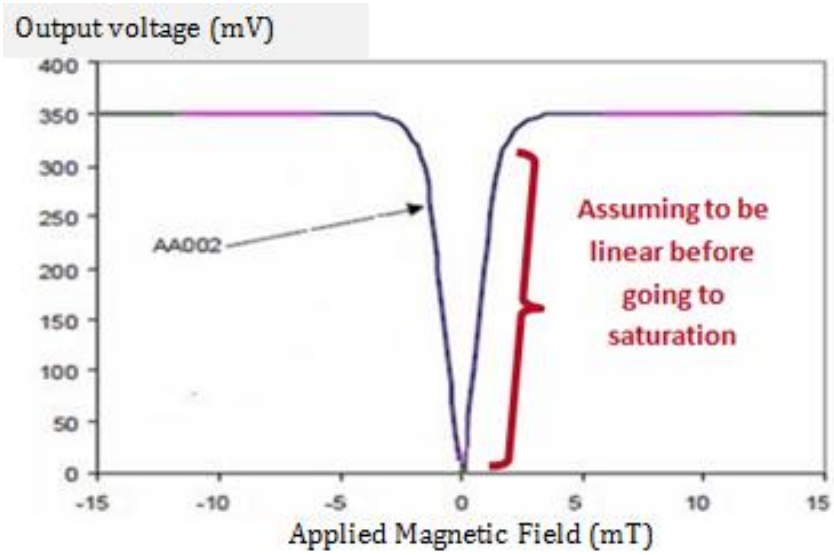

Figure 6.1: GMR sensor sensitivity to the magnetic field, Sensor AA002 which used in this research work;

It has been assumed that the diagram is linear before the sensor goes to the saturation.

The only way of sensing the agarose magnetic beads with GMR sensor is to magnetize them first with a permanent magnet. The magnetization was done by passing the beads placed on the glass substrate over a permanent magnet. The permanent magnets used in this experiment are the same as those described in chapter 4 for the oscillator experiment (i.e. large circular magnets with field strength of 380 mT).

For choosing the best sensor according to the detection requirement, a small amounts of agarose beads were magnetized with the permanent magnets, and the generated magnetic field from the beads is illustrated in Figure 6.2. This measurement is done using a Hall effect sensor magnetometer, as described in chapter 4, and the sensor is covered by a protective rubber whose thickness is accurately measured (T_r=500µm). The magnetic beads are placed on the cover glass with of thickness of 130µm, therefore the actual distance of the sensor from the magnetized beads was 630µm.

As shown in Figure 6.2, the magnetic field generated by the beads is small (below 1 mT), therefore the GMR sensor with the smallest field strength sensitivity was chosen for this experiment, which is AA002-02.

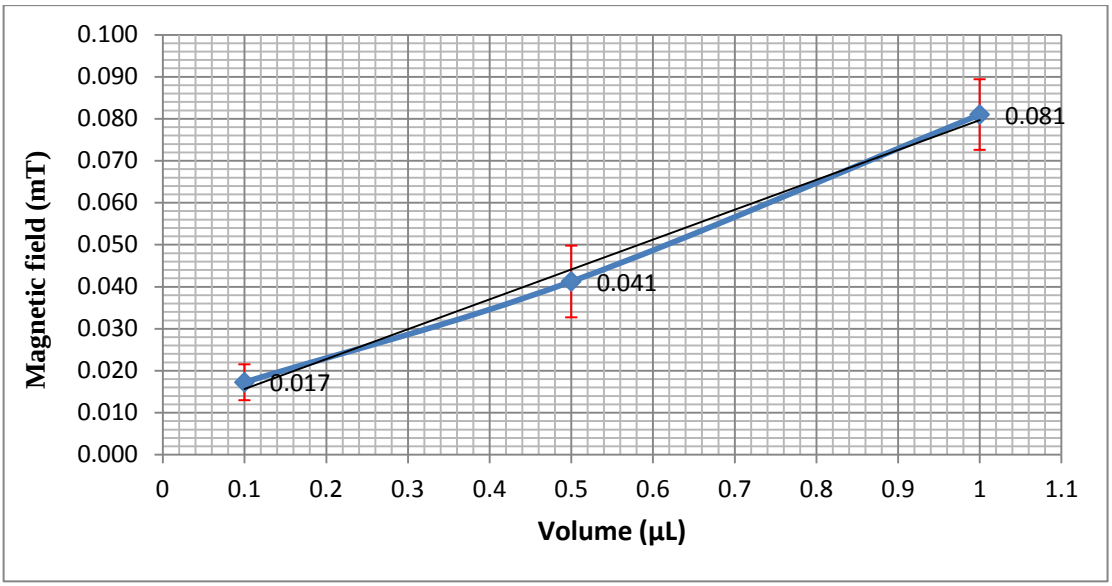

Figure 6.2: Field strength of magnetized beads with permanent magnet in different volume

The GMR sensor AA002 (chapter 2) is like an all-purpose magnetometer, which in this experiment is tested with different amounts of magnetized beads (superparamagnetic agarose beads, as explained in chapter 3) on cover glass and gold slides substrates. The AA002 shows good sensitivity using 1 micro-litre of magnetized beads. The output signal of GMR sensor is proportional to the strength of the magnetic field applied to the sensor.

The GMR sensor used in this study is associated with an op-amp circuit (based on TL081 JFET-input operational amplifier) for magnetic bead detection. The 10 volts voltage is supplied to the circuit and output signal measured without any sample or external magnetic field is 2.4 V. Appendix 7 shows the circuit diagram of the sensor.

At first the sensor is tested with permanent magnets, and a circular magnet is placed close to the sensor. The output changes are shown in Figure 6.3. as a result of the strong magnetic field generated by this magnet (380mT at zero distance), the sensor saturated at 3.9V (even while the magnet is located few cm away from the sensor). This magnet is placed in different distances and positions from the GMR sensor, and according to the sensitivity axis of the sensor, small positional changes can cause corresponding changes in the output, therefore all the samples in this test should be placed in the same position or line in the planar axis to the sensor. Due to the strong magnetic field of the circular magnet, it was replaced with a smaller square permanent magnet, which has 270mT field strength if the magnetometer sensor touches it. The same experiment is repeated with the small magnet placed at different distances (5.6-10cm) from the GMR sensor. To discover what strength of field the small magnet can produce to varying distances, the magnetometer is placed at different distances from the small square magnet to produce the results shown in Figure 6.4. The permanent magnet generates 0.16 mT (16 Gauss) magnetic field, while the GMR sensor is about

5.5cm away from it. Using the GMR sensor, the same magnet is placed at different distances from the sensor.

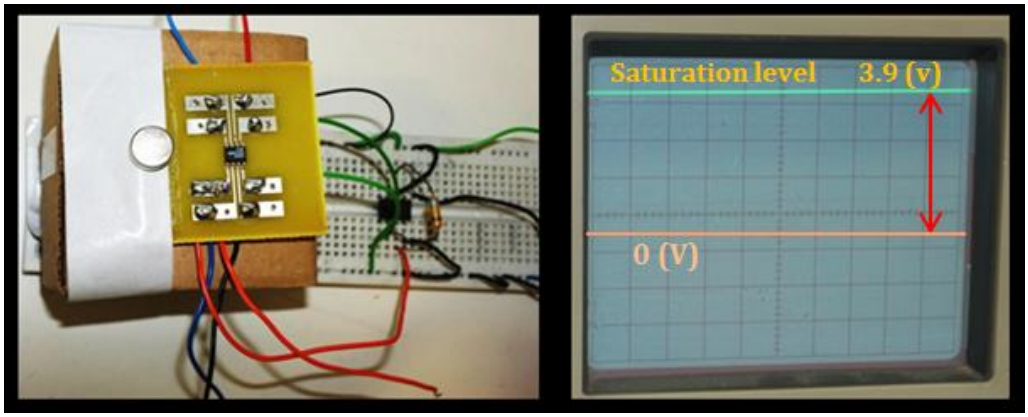

Figure 6.3: Sensory output with circular permanent magnet

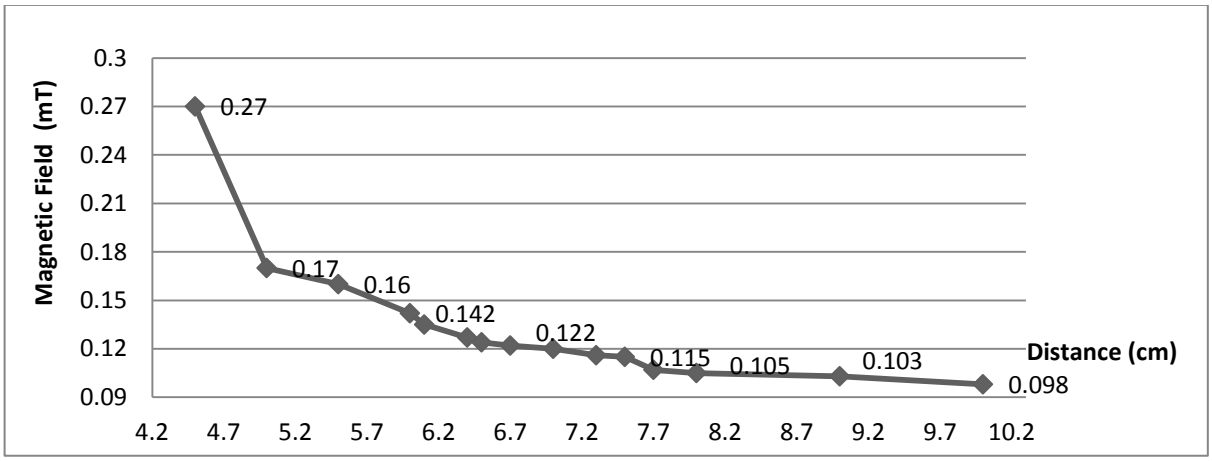

Figure 6.4: Magnetic field strength of square permanent magnet at different distances from the magnetometer (1G = 0.1mT)

Figure 6.5 shows these experimental results; when a magnetic field strength of 0.098-0.27 mT is applied to the GMR sensor by the permanent magnet (placed at different distances), its output signal differs from 100 to 1520 mV. Linear trend line on Figure 6.5 (a and b) has been allocated to show the estimation of sensitivity of the sensor, as mentioned earlier with regard to Figure 6.1, the slope of the diagram indicates the sensor sensitivity.

Figure 6.5 (a) shows the voltage difference (ΔV = output voltage without the magnet - output voltage after placing the magnet near the sensor) by applying 0.1-0.27 mT magnetic field. The output voltage increases to 4V by the 1520mV change using 0.27mT field strength (small magnet in 4.5cm distance) and the sensor approaches the saturation level. It can be seen on the diagram that ΔV drops significantly below 1.2 Gauss of magnetic field; this means that placing the sensor more than 7cm away from the source of the field may not give accurate measurements, thus this part (< 0.12 mT) can be eliminated for sensitivity calculation. According to Figure 6.5 (b), the sensor

should behave linearly before saturation, therefore considering only the linear part of the graph at Figure 6.5 (a) (magnetic field ≥0.12 mT), the system can be plotted again on Figure 6.5 (b). The linear trend line shows the slope of ≈ 564, which indicates the GMR sensitivity to the magnetic field.

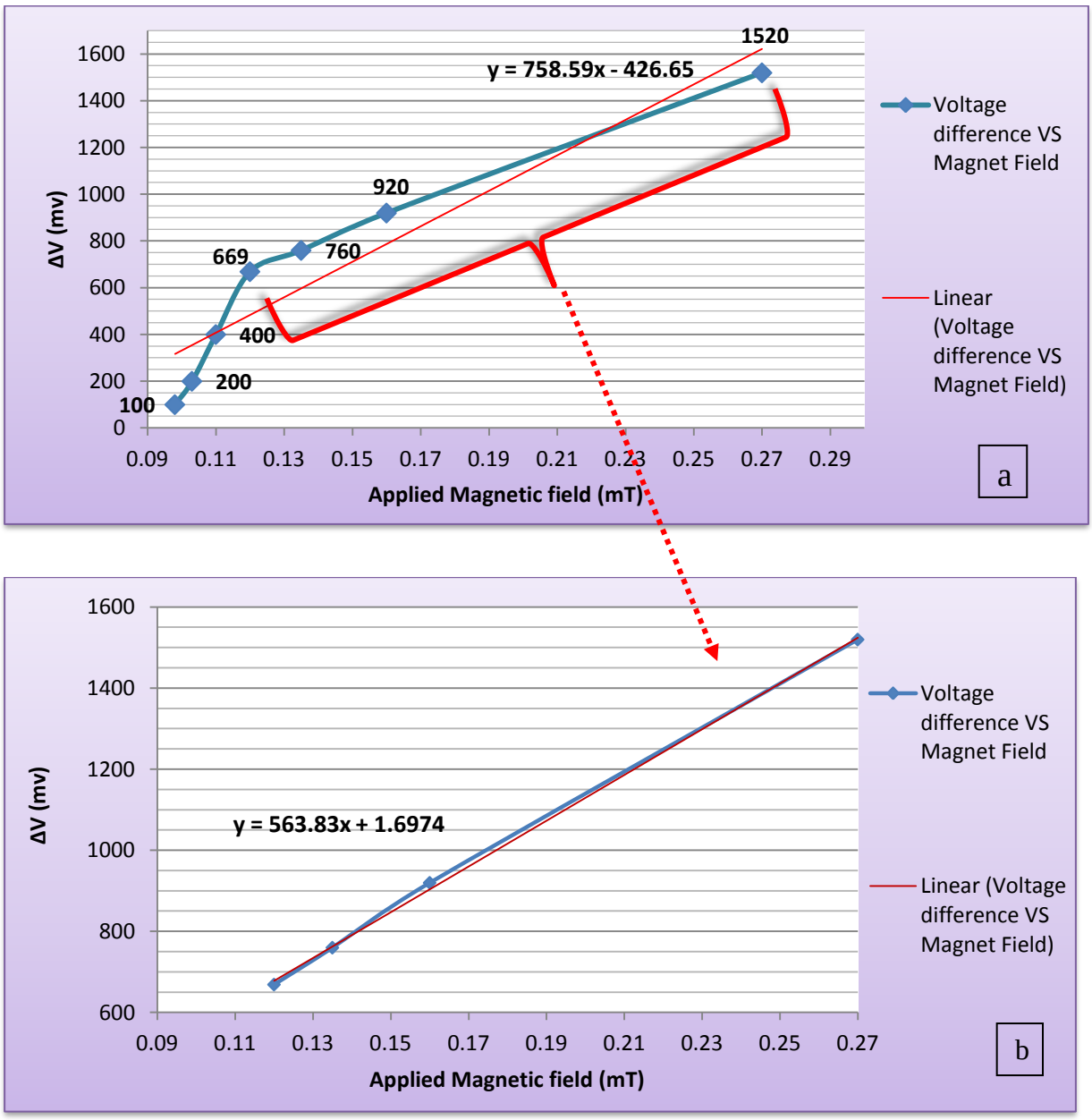

Figure 6.5: GMR sensor characteristic under the small permanent magnet exposure, (a) ΔV versus magnetic field of 0.098-0.27, (b) Exposure of field between 0.12-0.27mT

In Figure 6.6 the output signal (V+ΔV) is plotted in the presence of small permanent magnet, which is going to saturation after the output reaches 3.92mV. This plot is provided in comparison with AA002 sensor characteristic diagram on Figure 6.1.

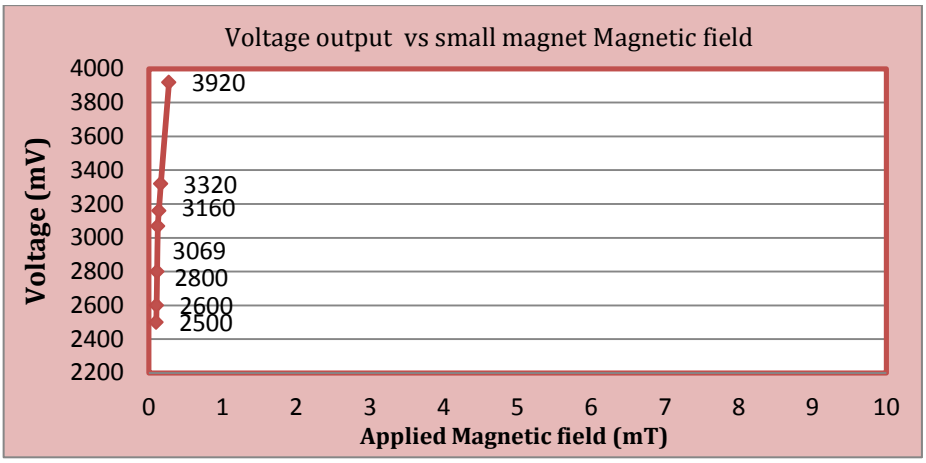

Figure 6.6: GMR sensor output under the small permanent magnet exposure

The actual aim of this experiment was to see if it is possible to detect different amounts of magnetized beads with the GMR Sensor. Therefore for this purpose different amounts of beads were placed on a gold substrate on top of the glass cover slip for easier handling and this sample was located at several distances from the sensor (Figure 6.7) to check if the GMR sensor is able to sense the small magnetic field generated by magnetic beads. Gold substrate was chosen because if in the future a DNA sample needs to be added then gold is one of the best substrates by which DNA can be immobilized via Thiol linker [149].

This test starts by magnetising 1µL of Agarose magnetic beads and then transporting them to the vicinity of the sensor. The beads are kept in the solution; after applying them on the substrate, within a few minutes (7-10 min) they are dried out. This experiment is tested for both dry beads and the beads in solution and they are sensed by GMR soon after magnetization. The sensor shows good sensitivity to 1µL of sample thus smaller amounts of beads were applied to check the sensitivity. The results of this experiment are illustrated in Figure 6.8 with dried magnetic beads and beads in solution.

In Figure 6.8 (a) the beads are positioned 1mm away from the sensor and in Figure 6.8 (b) they are 5mm distant. It should be mentioned that the cover glass used contains 0.08-0.14% ferric oxide (Fe_2O_3) according to the manufacturer's details, and it was seen that bringing the cover glass with the gold slide without any sample on near the sensor by hand has some effect on the output voltage, which is 100mv reduction and this amount has been subtracted from the values labelled on the diagrams (ΔV) in Figure 6.8. The labelled values represent the voltage difference calculated as shown below:

ΔV = (GMR output voltage without any sample or substrate) - (GMR output voltage after applying magnetic beads) - (glass + hand effect ≈ 100mv).

Figure 6.7: Magnetic beads on gold substrate applied to the GMR sensor

Although the magnetic field produced by the beads is small (< 0.2mT), the output voltage changes are considerable. Comparing the results of the two diagrams in Figure 6.8, it can be seen that dried beads exert more influence on the sensor than beads in solution for the sample volume smaller than 1 uL, which can be explained by the mutual particle-particle effect, whereby the particles in dried state are placed closer together than in liquid state when the beads are in motion. When the amount of beads increases above 1µL, non-uniform distribution of dried particles can be seen on the cover slip, in which the beads are spread at distances from each other and away from the sensor's sensitivity axis, therefore the magnetic moment produced by neighbouring particles is reduced compared to the smaller volume of the sample. Thus ΔV is smaller for the larger volume of dried beads (more details about magnetic particles' behaviour is explained in chapter 3).

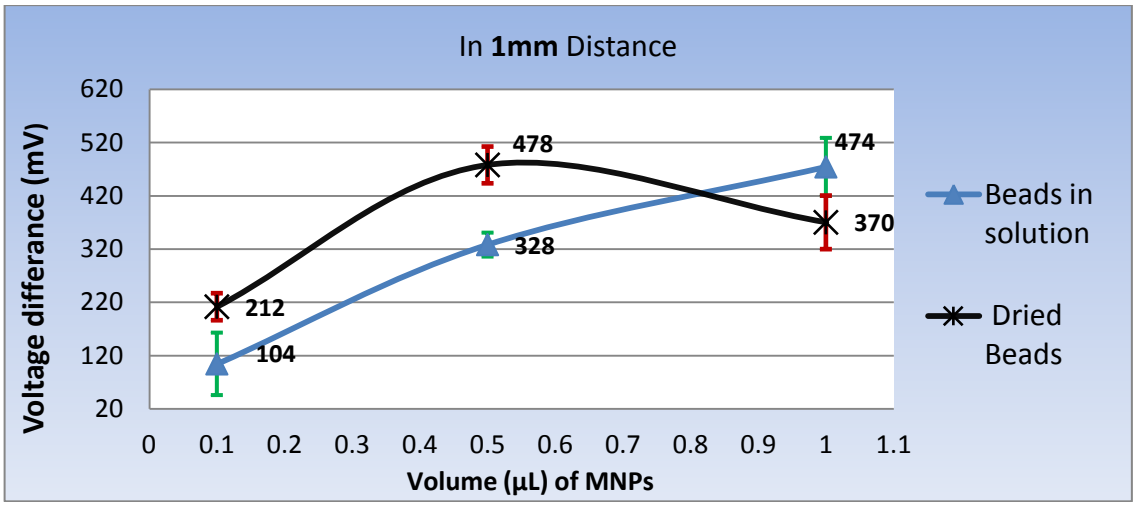

(a)

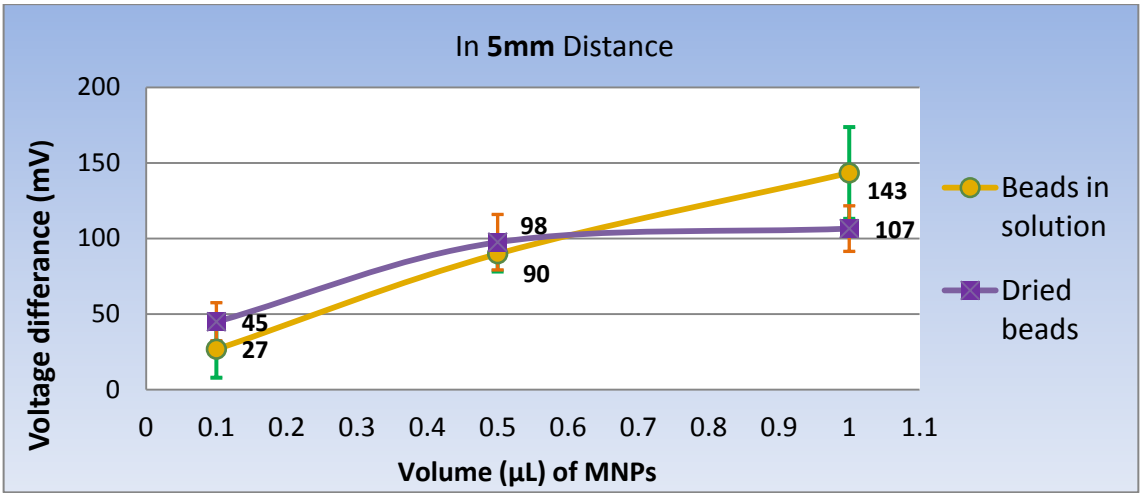

(b)

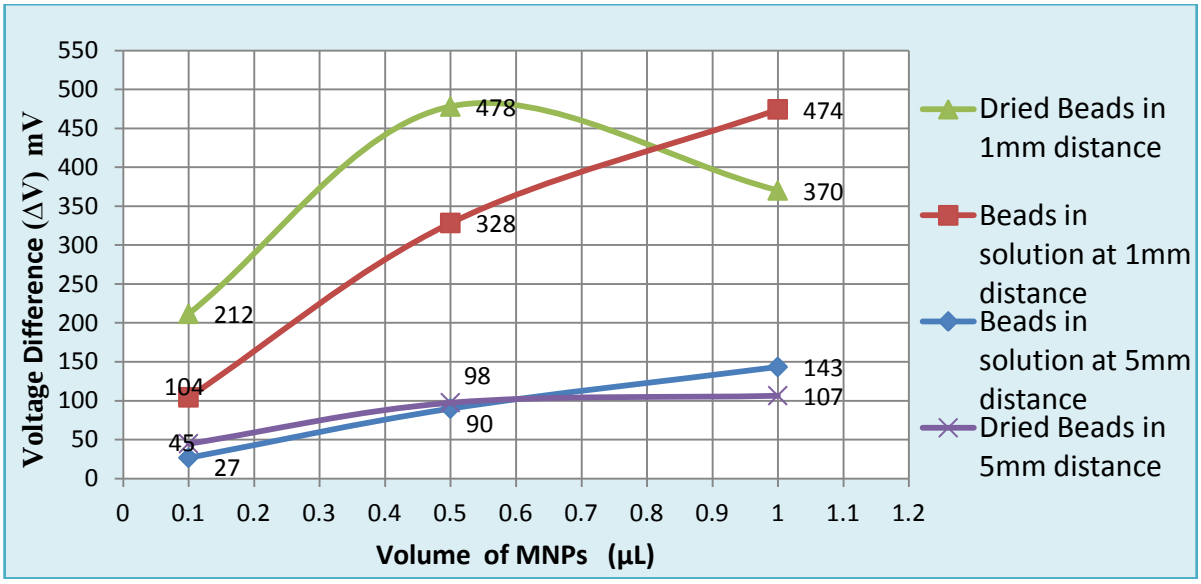

(c)

Figure 6.8: (a) Different volumes of MNPs in solution and dried state tested on GMR sensor with only 1mm distance from it, (b) MNPs tested on GMR sensor with 5mm distance, (c) Both diagrams together

The difference between Figure 6.8 (a) and (b) is the distance at which the sample has been placed from the GMR sensor. The labelled values clearly indicate that by moving the sample away from the sensor, ΔV reduces dramatically. The cover glass and hand movement effect in this case (5mm from the sensor) is about 20mv, which has already been deduced from the presented values.

Considering the sensor sensitivity diagram (Figure 6.1) and the previous experiment with permanent magnet and GMR (Figure 6.2), it has been mentioned that assuming the result diagram is linear then the sensor sensitivity is the slope of the line. Using the equation shown in Figure 6.5 (b), we can calculate how much ΔV is expected when different amounts of sample (specific magnetic field strength) are placed on the sensor (with 4.5-10 cm distance from the sensor).

$$Y = 563.83X + 1.6974; \qquad (6.1)$$

Where,

Y= Voltage difference (mv) = ΔV and X= Applied magnetic field

Therefore, for validating the experiments done with the magnetic beads (Figure 6.8), the amount of magnetic field generated by them is substituted in the Equation 6.1 and the result is as follows:

Table 6.1: Expected voltage difference for sample (Eq. 6.1)

Magnetic field (G)	0.8	0.4	0.17
Calculated ΔV (mv)	453	230	98
Actual ΔV (mv)	474	328	104

Table 6.1 shows the expected voltage difference for the magnetic bead sample regarding Equation 6.1. As presented, the voltage difference calculated for magnetic beads is quite similar to the actual results of beads in suspension while they are 1mm away from the sensor. Therefore we can claim that sensor sensitivity is about 564 (V/T).

In summary, the GMR sensor experiment is sensitive enough to detect the minimum required mass of the magnetic beads (0.1µL), and the output signal is large but unfortunately it cannot quantify the amount of beads exactly. GMR sensor can only detect the presence of the magnetic field, therefore the extra step of magnetizing beads is added to this process. For a small hand-held instrument, a quick sample in-answer out approach is optimal to minimize the number of steps. The circuit should also be designed so that it is sensitive only to magnetic properties, like conventional metal detectors; thus by using a tiny circuit board containing a small coil, the aim is achievable.

In the following sections the results of the magnetic particles detection experiments with the phase lock loop-resonance sensor on different substrates is presented. All the samples used have been explained in detail in chapter 3.

6.3 Experiments with Fe3O4 magnetite powder

After designing (chapter 4) and calibrating (chapter 5) the resonance sensor, the first test conducted with the sample was based on magnetite powder (Fe_3O_4). Initially, 4mg of the powder was placed on the glass substrate on top of the coil and output changes were recorded. As the output difference was large and 4mg was also a large amount of beads, the rest of the tests were continued with smaller masses of the particles down to the sensor limitation of detection (sensor resolution).

As mentioned in chapter 5, the early frequency counter used for this research was the universal counter, which was not able to connect to the PC to record its data, therefore the measurement was recorded manually every 10 seconds. The first part of the following results is in regard to using this counter at low frequency.

The series of the presented experiment in this section (6.3) are in the following order:

- Black coil circuit test with the universal counter at 2.7MHz resonance frequency.
- Black coil circuit test with TF930 frequency counter at 2.4- 2.7MHz resonance frequency.
- Yellow coil circuit test with TF930 frequency counter at 7.2MHz resonance frequency.

This experiment starts with using the Black coil (85µH) in the LC circuit (chapter 4) at 2.75MHz. Different amounts of sample were tried using this sensor, but according to the limitations created by the high inductance coil in the circuit, and the need for higher frequency, this coil was replaced with the Yellow coil (9.5µH) and the tests were repeated from 2.4MHz up to 7.2MHz frequency. According to the literature, detecting smaller amounts of beads is possible in high frequency (e.g. for single bead of micrometre size, GHz range frequency is required [38]). Furthermore, comparing different research works, it can be concluded that detection of smaller size in addition to lower amounts of magnetic particles is possible by increasing the frequency (chapter 2).

The principle of the experiment presented can be seen in Figure 6.9 [32]. The coil generates the magnetic field, which polarizes the magnetic particles present as close as possible to the sensor surface on the glass substrate; the result is that the total magnetic energy increases, which leads to an increase in the coil inductance, thus the oscillation frequency experiences down-shift.

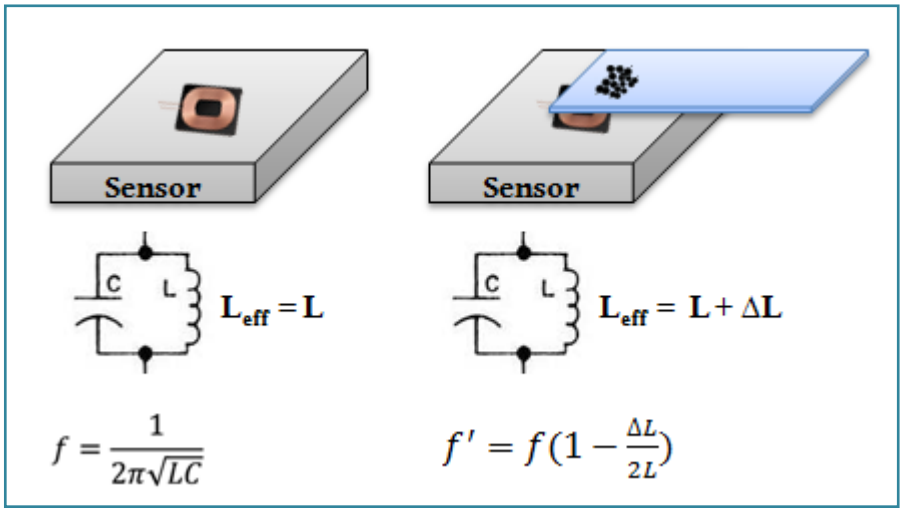

Figure 6.9: Magnetic sensor scheme

6.3.1 Black coil circuit test with the universal counter at 2.7MHz resonance frequency

Experiments were conducted based on the cover glass substrate for different frequencies. In each test a specific amount of Fe_3O_4 powder was placed on top of the glass and applied to the sensor. At first the glass substrate was positioned at different distances from the sensor but the results showed that at distances greater than 1mm, the sensitivity reduces radically. If this type of sensor is to be used in microfluidic applications, the sample needs to be as close as possible to the sensor (a fewμm away), due to the microfluidic channel thickness, which is normally about 100μm, thus the results presented here are for tests when the glass substrate is positioned on the sensor and therefore the samples are about 130μm above from the sensor (based on the cover glass thickness).

Figure 6.10 illustrates how the output frequency differs for samples of 1-4 mg magnetite. The mass of 1, 2, 3 and 4mg was used and the maximum average changes of 1742Hz are achieved after about 40 seconds of leaving the sample on the sensor.

This experiment was repeated many times in different conditions, and because the measurement for these tests is not always the same, the error bar was added to show the fluctuation between tests (the results table can be found in Appendix 8). Smaller masses of the sample (below 1 mg) were also tried but the sensor was not sensitive enough to differentiate the mass, thus there is a large error bar for them (Figure 6.11 (b) & Appendix 8).

Although this sensor can sense the presence of magnetic particles for very small masses, it cannot distinguish the amount of samples precisely. As shown in chapter 5, the natural fluctuation of this sensor with the universal counter is about 170Hz. Figure 6.10 shows the sensor behaviour for samples of 1-4mg.

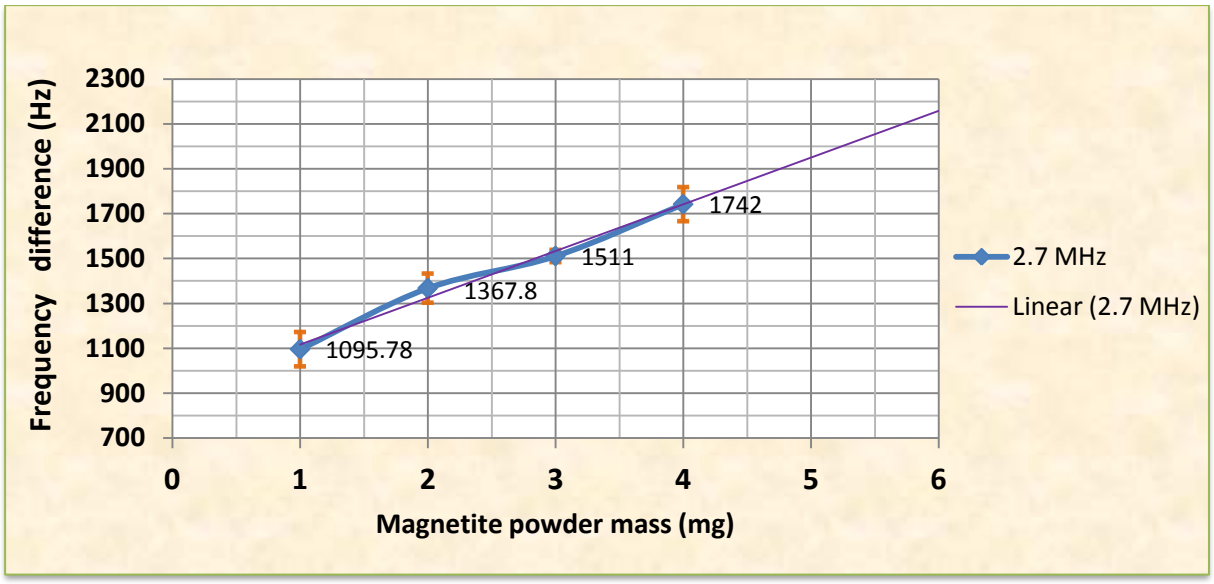

Figure 6.10: Frequency shift Vs. Magnetite mass; the sample is 0.13mm away from the sensor using the universal frequency meter on the Black coil circuit

Another example of above tests is illustrated in Figure 6.11 (a) with a difference in the way of detecting. In Figure 6.10 the sample was placed on the sensor (0.13mm above the sensor) for only 40 seconds and then the measurement was taken and the sample was removed. This method was repeated for all of the samples, but in Figure 6.11 (a) the sample was first located 3cm above the sensor and kept there for 40 seconds for the output frequency measurement, then the sample position changed to 2cm above the sensor and again remained there for 40 seconds. This process continued for the distances of 1cm, 0.5 cm and 0cm (which means the sample was placed exactly on the sensor with the glass substrate thickness ≈ 0.13 mm).

In this way the magnetic powder is kept near the sensor surface for a longer time than in the test shown in Figure 6.10. As illustrated in Figure 6.11(a), the maximum output frequency changes at zero distance (0cm) is 2798Hz based on 4mg of sample, however this value at the same distance in Figure 6.10 is 1742Hz. This difference is regarding to the time duration in which the sample was kept on the sensor. In the first test (Figure 6.10) the sample was kept over the sensor for 40 seconds, while in the second one (Figure 6.11) it was kept over the sensor for 3.5 minutes. The results show that keeping the sample on the sensor for a longer time can result in larger frequency shift (due to the heating effect of the particles and coil, as described in chapters 3 and 5); an example of this test is demonstrated in the next section.

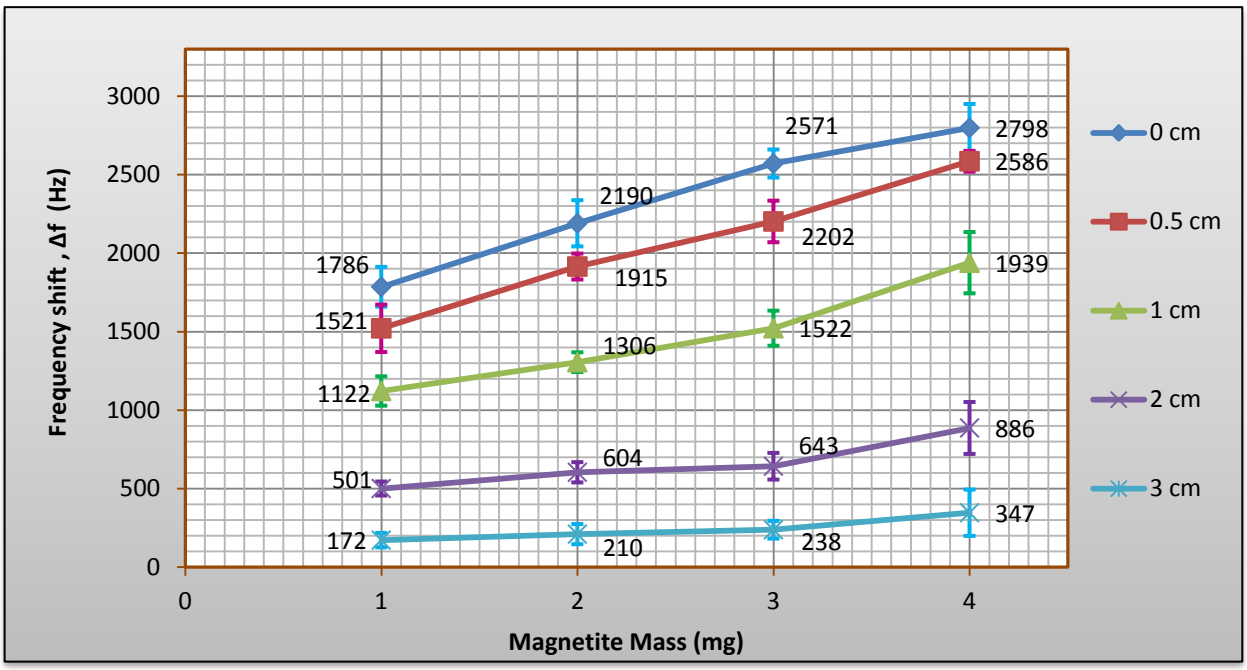

(a)

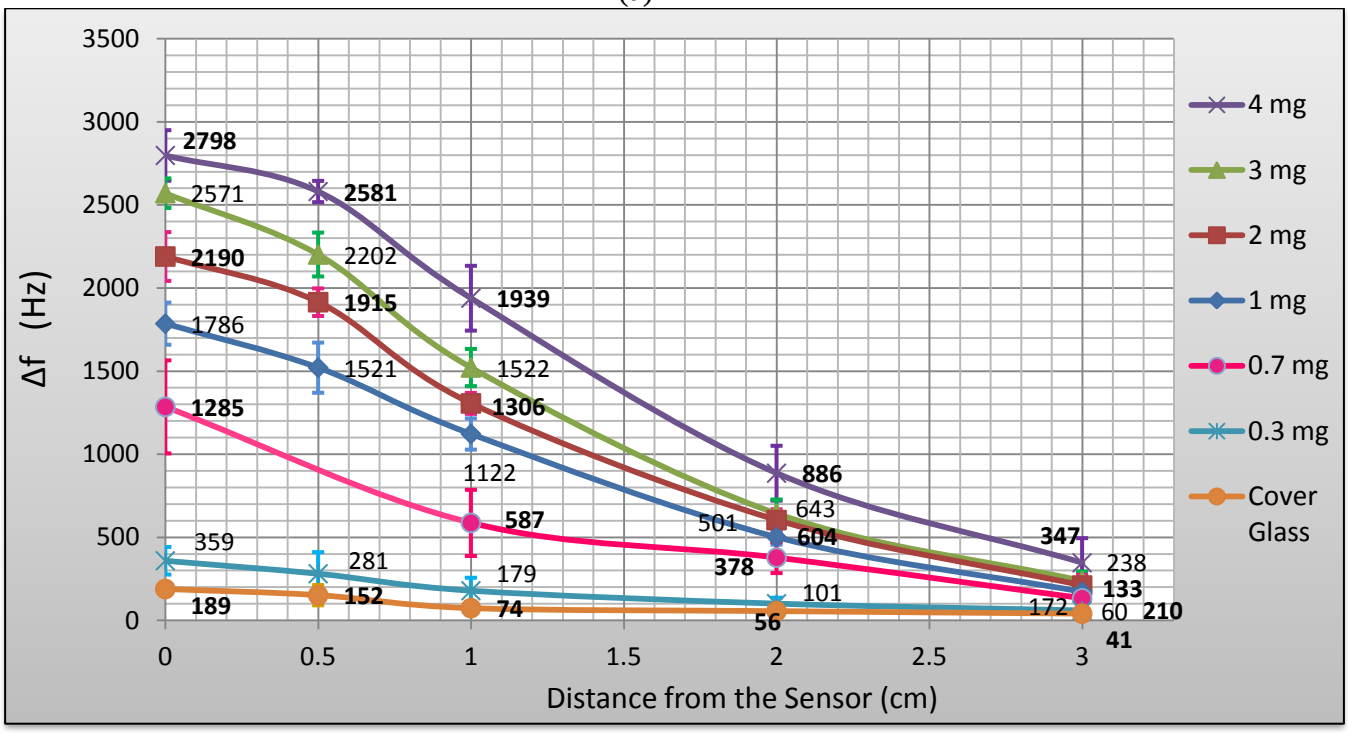

(b)

Figure 6.11: (a) Δf versus mass of magnetic powder in different distances, (b) Frequency shift versus distance between the sample and the sensor surface for cover glass and samples of 0.3-4mg

- Effect of magnetic sample distance from the sensor on sensitivity (Figure 6.11, b)

The experiment described in this section was conducted to investigate the effect of distance between the sensor and the sample. Regarding the total magnetic energy around the coil, the further the sample is from the coil, the less it will be magnetically coupled, therefore a smaller change of inductance occurs. Thus, the magnetic field measurement is position-dependant; by staying close to the sensor surface, larger amounts of inductance change can be produced. A series of tests was

carried out based on different amounts of sample to demonstrate this idea, and the results illustrated in Figure 6.11 confirm that the maximum frequency shift can be achieved when the sample is placed as close as possible to the sensor (0.13mm). It also shows that there is a nonlinear relationship between the distance and Δf.

6.3.2 Black coil circuit test with TF930 frequency counter at 2.7MHz resonance frequency

In this section experiments are with the same Black inductor (L=85µH) as in the previous section. The only difference is that the universal counter has been replaced with the TF930 frequency counter. As explained in chapter 5, this counter is more accurate and the data were uploaded to the computer automatically. The reading was done in each 10 seconds (according to the circuit low pass filter and settling time; it takes about 2 seconds for the output signal to settle, much shorter than the 10s frequency reading). From turning the sensor on, the counter transfers the measurement data to the computer every 10 seconds, and at the end of each test (each of which normally takes a few hours), the series of measurements are recorded and ready for analysis. Two examples of these measurements are presented in Appendices 9 and 10.

According to the sensor calibration (chapter 5), the maximum output fluctuation for this sensor is 70Hz for an overall time of 2 minutes (the detection of magnetic particles happens in less than 30 seconds). This means that 70Hz fluctuation in the output signal should be considered as the limit of measurements. On the other hand, for calculating the exact effect of magnetic particles on the sensor and to find out how much the output frequency signal will be changed by different amounts of particles, the impact of the substrate needs to be considered as well. For example, using a cover glass containing 0.14% ferric oxide can cause specific frequency shift depending on the circuit resonance frequency. Table 6.2 shows the value of frequency shift caused by cover glass at 2.7MHz after leaving the glass on top of the sensor for 30 seconds, 1 minute and 2 minutes. Each value in the table is calculated using moving average method within 30 seconds of applying the sample. After repeating the test ten times, the average of all values can be determined in the last row of Table 6.2.

Figure 6.12 shows one of the tests. It is evident that the output frequency changes by applying different samples to it. The masses of magnetite powder tested in this experiment were 90µg, 300µg, 480µg, 700µg, 1.24mg and 1.62mg. The output frequency measurements are presented in Appendix 9.

As illustrated in Figure 6.12, different amounts of samples were applied and kept on the sensor for about 2 minutes and then removed, after which the system continued to work without any sample

for about 3 minutes, then another amount of sample was placed on the sensor and the same process continued. The first sample applied was 1.62mg of magnetite powder, which caused the biggest frequency changes of about 1196Hz (including glass cover effect and output natural variation).

This sample remained on the sensor for 2 minutes and caused the continuous frequency reduction (the gold arrow in Figure 6.12) and was then removed, thus the output signal shifted up somewhere near its previous level (before applying the sample), and the sensor was working without sample for 3 minutes until the 1.24mg of magnetite was applied, and the output was reduced by 922Hz. This process was repeated for other amounts of magnetite until the sensor resolution level was about 90µg. It should be noted that the frequency after removing the sample does not revert to exactly the same level at which it started (see the black dashed line on the Figure 6.12), and over time this difference level increases due to the natural system fluctuation, as explained and illustrated in chapter 5 (regarding calibration).

Figure 6.12 shows the output frequency variation for different amounts of beads, but for having more accurate results to find out the sensor detection limitation this test was repeated several times with the same amount of samples. The frequency changes of each sample were calculated and analysed, achieving the results presented in Figure 6.13 and Table 6.3. The way of calculating the frequency variation after placing the sample (for example, 1.24mg magnetite) was to wait for 30 seconds while the counter was measuring the output and recording it each 10 seconds, then calculate the average value of frequency difference in the previous 40 seconds to give one value of changes for a specific sample (1.24mg). By repeating this test for 1.24mg magnetite about 10 times, ten numbers are available, which shows how the sensor output changes regarding that specific sample.

Figure 6.13 shows the amount of Δf versus the mass of magnetite powder. In these experiments, the glass cover plate was used as a substrate. The value illustrated on the zero mass (207) is the effect of glass cover only without any sample on top of it. As mentioned earlier, the iron content (Fe_2O_3) of cover glasses can alter the sensor inductance.

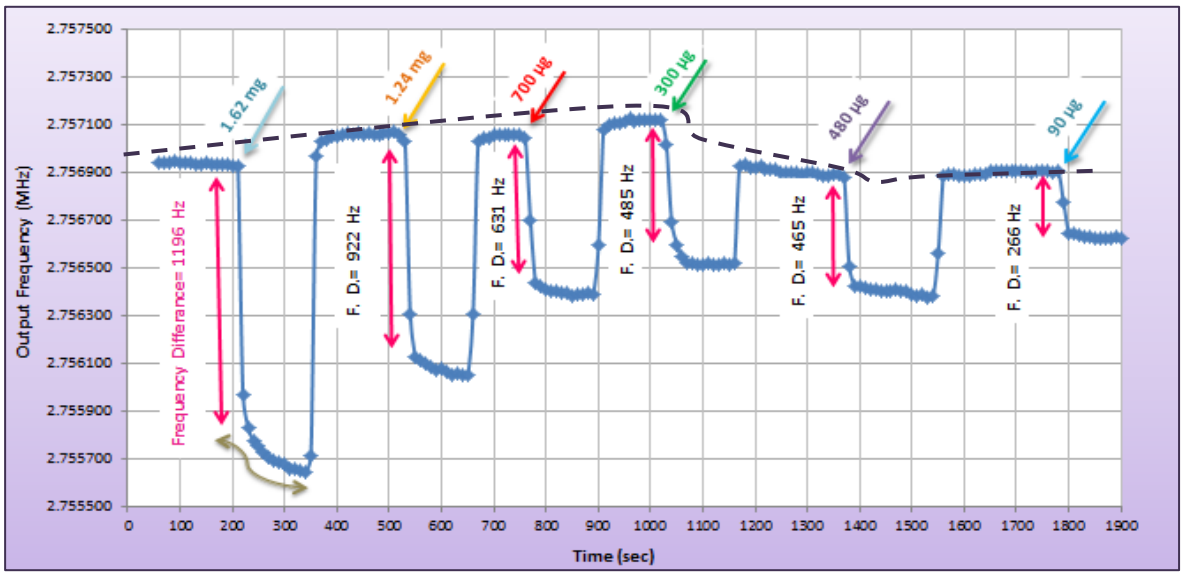

Figure 6.12: The output frequency signal behaviour in presence of different amounts of magnetite powder

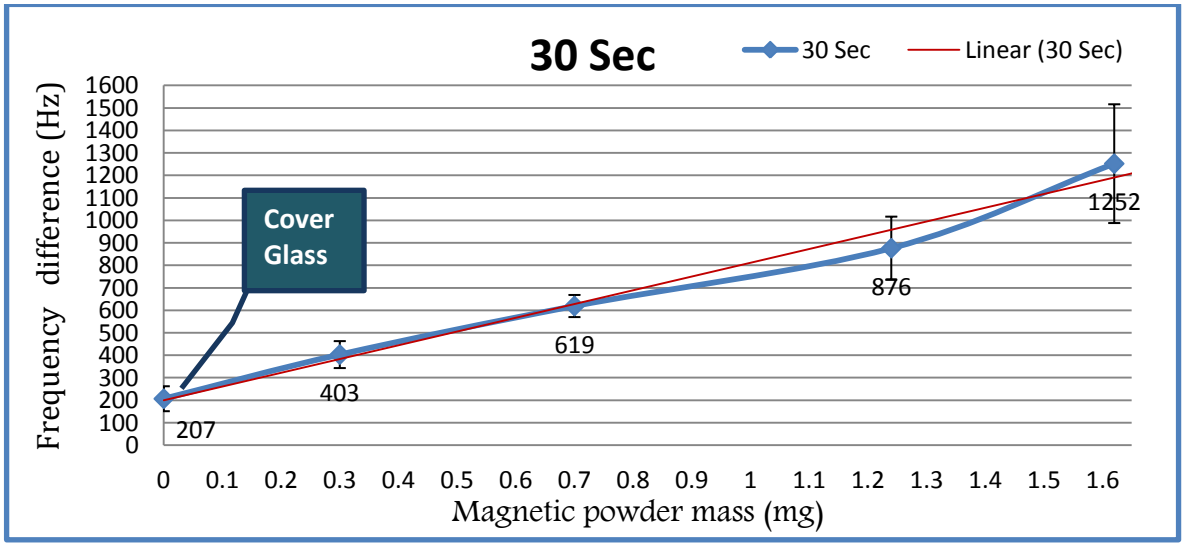

Figure 6.13: The output variation of the Black coil circuit at 2.7MHz resonance frequency with TF930 counter

Table 6.2: Results table of frequency shift caused by magnetite powder in different times

	30 sec.					1 min					2 min				
	1.62 mg	1.24 mg	700 µg	300 µg	Cover glass	1.62 mg	1.24 mg	700 µg	300 µg	Cover glass	1.62 mg	1.24 mg	700 µg	300 µg	Cover glass
Δf	1070	880	563	484	245	1135	921	612	485	257	1310	962	652	558	249
	1172	693	620	464	214	1264	778	631	383	276	1364	842	694	494	285
	1125	1083	674	439	292	1220	1104	732	465	342	1304	1148	764	503	368
	1803	1038	568	347	204	1845	1054	734	340	227	1970	1079	763	434	250
	1089	820	617	283	88	1261	903	667	374	147	1416	1016	734	437	235
	1132	714	651	374	208	1523	810	610	497	224	1346	918	655	564	253
	1357	910	550	386	234	1204	867	623	379	197	1517	945	684	445	330
	1042	720	687	443	197	1754	1094	654	458	251	1620	1028	715	538	215
	1097	890	665	391	236	1174	974	642	415	278	1473	1131	652	426	223
	1637	1016	597	421	151	1272	775	645	387	270	1338	873	681	450	314
STND	*264*	*140*	*49*	*60*	*55*	*252*	*125*	*45*	*54*	*53*	*204*	*105*	*43*	*54*	*50*
Ave.	*1252*	*876*	*619*	*403*	*207*	*1365*	*928*	*655*	*418*	*247*	*1466*	*994*	*699*	*485*	*272*

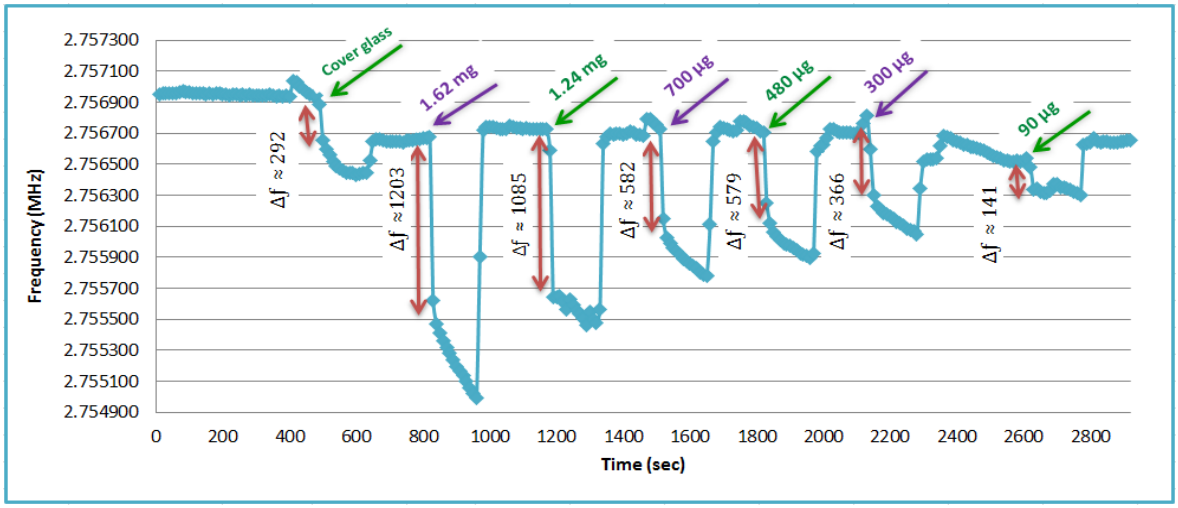

Figure 6.14: The sensor output signal during the introduction of different amount of magnetite sample

Another example of the above test is presented in Figure 6.14 as a full continuous measurement done by introducing different samples consecutively in descending order. First, the cover glass without sample was applied and then removed after a few minutes, letting the output signal return to its baseline before applying 1.62mg magnetite powder at 830 sec then removing it. This process was continued for the different samples in this order: 1.24mg, 700µg, 480µg, 300µg and 90µg; the latter of which is believed to be the detection limit regarding the value of Δf=366 compared to the average value of Δf=207 for introducing the glass cover without the sample. Therefore this sensor can detect the sample of 90µg but it has problem for distinguishing the exact amount of beads after this level.

The output reading of this test (Figure 6.14) is presented in Appendix 10. The experiments described above show that the magnetic field generated from the coil is strong enough not only to sense the presence of magnetic beads without getting saturated but also to differentiate between the variable amounts of beads.

All samples were kept on the sensor for about 30 seconds and then removed (Figure 6.13), but the question arises of what would happen if they stayed on the sensor for a minute or more. This is illustrated in Figure 6.16, where the sample was kept on the sensor for 1 and 2 minutes. All the experiments in this research work indicate that the output frequency signal decreases during the longer time of keeping the sample on the coil. The pink arrows in Figure 6.15 show examples of this behaviour, which can also be found in Figures 6.12 and 6.14. This means that after applying the sample and having frequency reduction for a certain amount within the first 30 seconds, the output does not settle with its natural frequency; rather it keeps decreasing until the sample is removed.

The best explanation for this phenomenon is the heating effect of the inductor and magnetic nanoparticles. After placing the cover glass on the inductor, its temperature increases and the coil gets warmer; the temperature can change the inductance in different ways, such as changing the coupling coefficients between different layers of the coil or changing the wire resistivity, and consequently the current distribution in the coil. The heat effect on the inductor is described in chapter 5; it which causes the output frequency to decrease either without the sample or while the sample is on the sensor, but the difference is in the rate of the reduction (greater reduction occurs in the presence of sample and in a shorter time). As shown in chapter 5, the output signal is gradually decreasing over time (Figure 5.5), and depending on the resonance frequency of the sensor, the reduction rate is different. The same behaviour is happening while the sample is on the sensor, but placing the sample near to the sensor increases the rate radically. Figure 6.15 shows the maximum frequency reduction while the sample is on the sensor and after the major frequency jump once the sample is applied.

Table 6.3 shows the average value of these kinds of reduction in different time duration wherein the sample is on the sensor. It can be seen from the table that the frequency reduction is higher when the amount of sample is larger. It also shows the frequency reduction with cover glass only, which is small compared to the other columns (where the sample is on the sensor). As a result the magnetic nanoparticles influence the frequency reduction and they can cause more heating on the coil. It should be considered that magnetic nanoparticles can get warm as well, which then leads to increased magnetic moment of the particle, and consequently of the overall magnetic field, which results in coil induction increase and output frequency decrease. Therefore, by applying an external magnetic field to the magnetite powder for a longer time, the frequency shift (Δf) increases between 5 to 8% for each Δt=30 sec (keeping the samples on the coil for 30 sec more) (according to the Figures 6.13 and 6.16). The magnetic particles' heating effect has been explained in chapter 3.

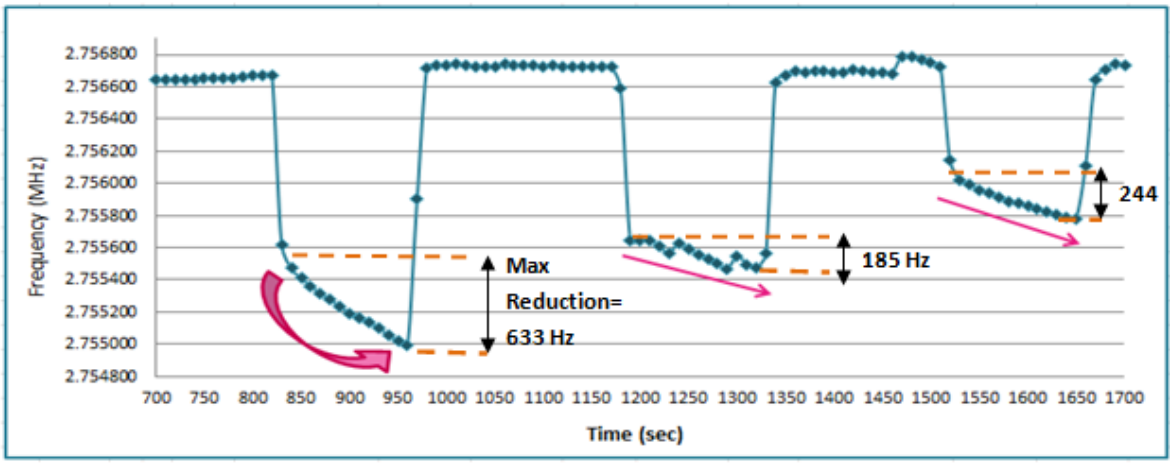

Figure 6.15: Output frequency signal in presence of magnetite sample and illustration of frequency reduction during the time that sample is on the sensor

Table 6.3: Maximum frequency reduction in presence of sample at 2.7MHz resonance frequency

	Magnetite Powder (Fe_3O_4)					Cover glass only	
Duration Time (Sec)	1.62 mg	1.24 mg	700 µg	480 µg	300 µg		
130	559	326	270	266	156	91	Maximum Frequency Reduction (Hz)
140	668	416	282	297	219	96	
150	760	472	300	310	234	100	

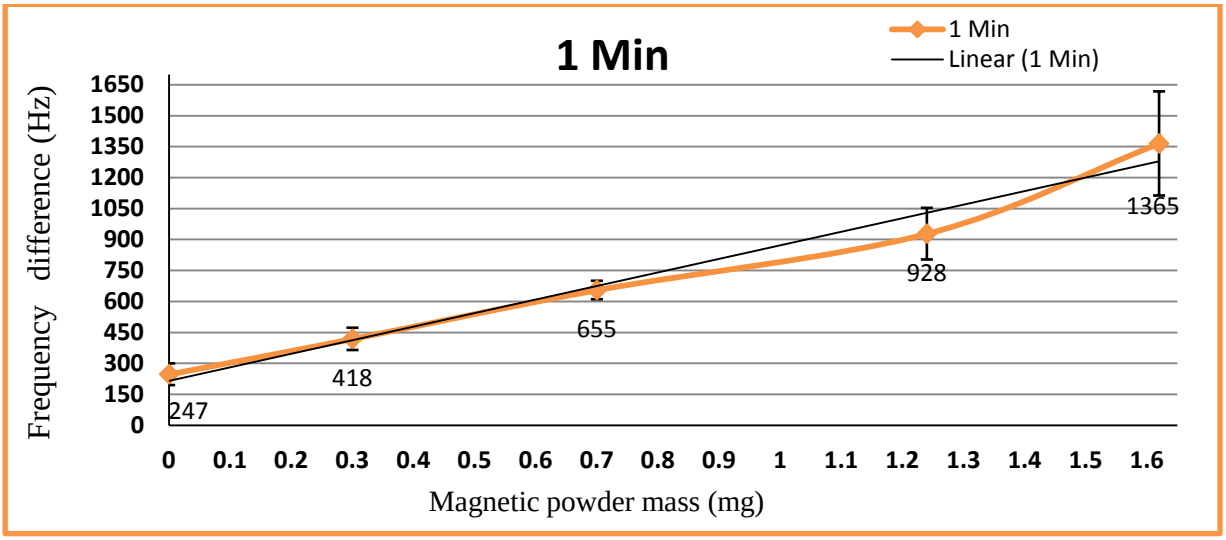

(a)

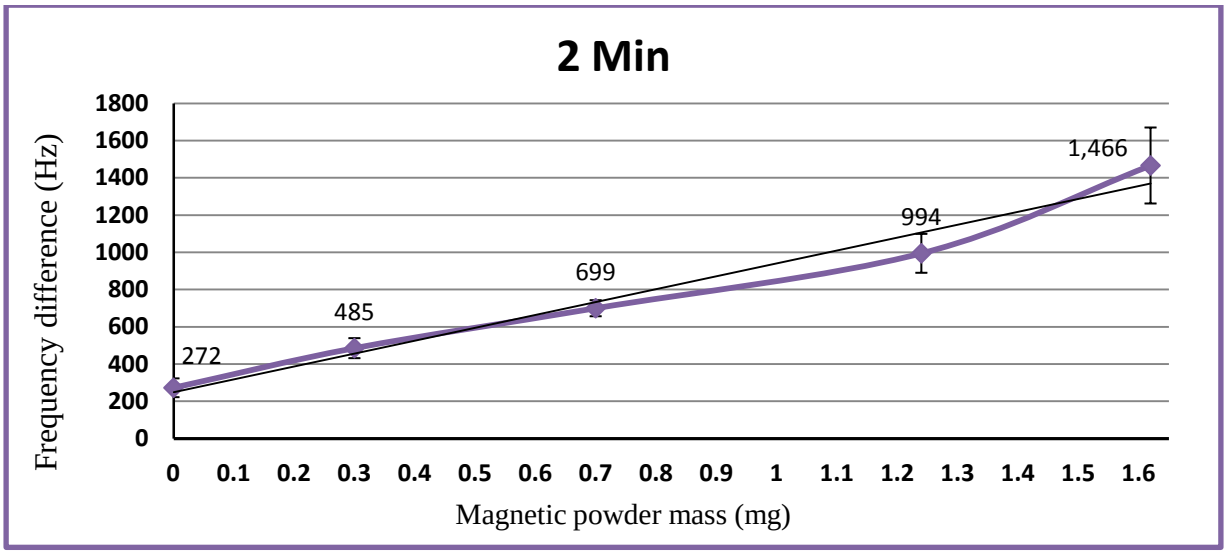

(b)

Figure 6.16: The output variation of the Black coil circuit at 2.7MHz resonance frequency, (a) 1 minute of keeping the sample on the coil surface, (b) keeping the sample for 2 minutes

Although by keeping the sample for longer time a higher output signal difference can be achieved, the purpose of this test is to sense the presence of magnetic particles, which can be done after the first 30 seconds of applying them. Comparing the results of Figure 6.13 with those of Figure 6.16, it can be seen that the error bars are smaller when the sample is kept for a longer time, therefore if the quantity of the sample is important then this way can achieve better sensitivity (Table 6.3).

To check the stability and repeatability of the sensor system, another PCB board was constructed with the same circuit design like a Black circuit (explained in chapters 4 and 5) by using the Black coil (85µH). The previous Black circuit sensor was resonating at 2.7MHz with the fluctuation of 70Hz (chapter 5). This new sensor is showing better stability while resonating at 2.4MHz (fluctuation level=50Hz). Although the circuit design and the coil itself were both the same as the previous system, the test platform and components are all new, and also the different capacitors were used in the LC and PLL circuit: Cr=47pf and C_{PLL}=270pf, which results in 2.4MHz resonance frequency. The new sensor design output response to the magnetite sample has been plotted in Figure 6.17. The comparison between these two centre frequencies at 2.7MHz and 2.4MHz is presented in Figure 6.18. The Δf for the similar mass of magnetite powder was higher in the sensor with 2.4MHz resonance, because this sensor has more stable performance than the other one oscillating at 2.7MHz (chapter 5).

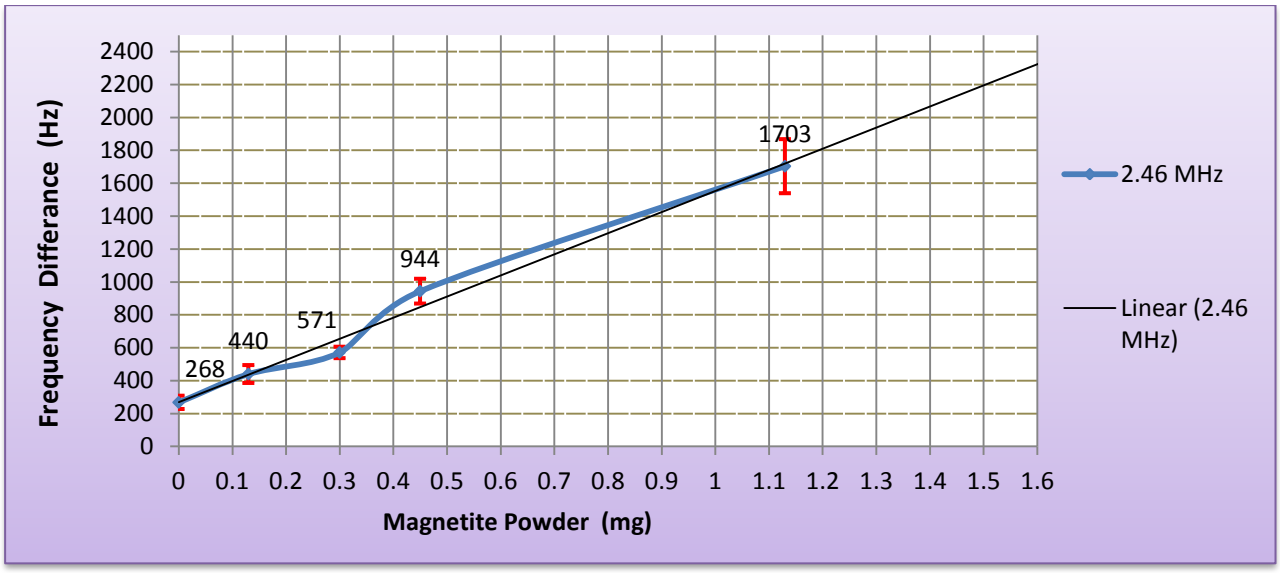

Figure 6.17: Output difference at 2.46MHz from the Yellow coil circuit

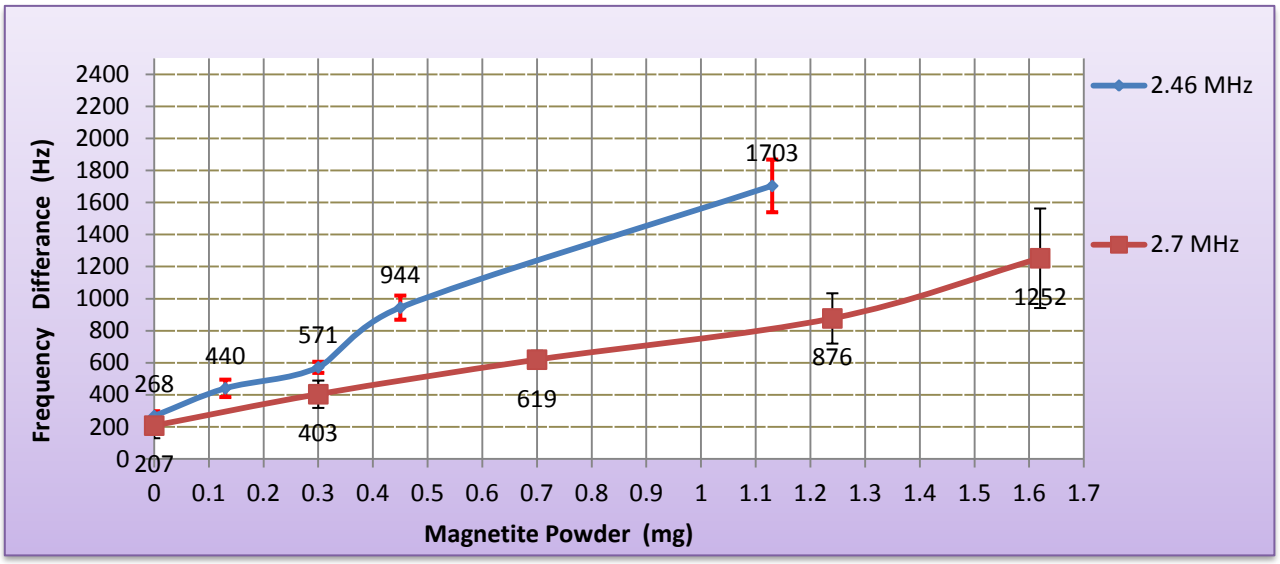

Figure 6.18: Frequency difference in presence of magnetic beads at two resonance frequencies

6.3.3 Yellow coil circuit test at 7.2MHz resonance frequency

Here the same experiments described in the previous section were carried out, but the circuit was replaced with the Yellow coil circuit (chapter 4) utilizing the coil with much smaller inductance (9.5µH) which can lead to the higher resonance frequency (up to 7.2MHz) and this helps to check if the higher frequency correspond to better sensitivity.

During the last several years many researchers have tried to make a handheld device able to translate the presence of magnetic particles to an electrical signal, and they covered a range of frequencies in kHz and GHz (chapter 2). It is understood that lower frequency reduces the detection resolution [38,46,150-151]. As shown in chapter 2, in the kHz range of resonance frequency, at least millions of beads needed for the sensor to detect them, and a single magnetic particle can be

detected if the resonance frequency is in GHz, but none of the above research work is based on the MHz range, which is the emphasis of this thesis, and also the effect of different resonance frequencies on the detection technique has not been studied yet.

The design of the Yellow circuit for 7.2MHz was explained in chapter 4. Using the coil with about 9.5µH inductance and capacitor of 47pf in the tank oscillator as a sensor core can generate resonance frequency of about 7.2MHz (considering the effect of PLL component on the resonance frequency). Using this value in the circuit and testing it with magnetite powder, typical sensor responses are plotted in Figure 6.19. The results table of these tests is presented in Table 6.4, showing the frequency shift of each sample and average value of results. The experimental set up for this system is the same as previous systems mentioned in chapter 5.

As can be seen, the cover glass without sample results in a frequency shift of approximately 782Hz, and the smallest mass of particles which can be detected quantitatively and qualitatively by Yellow coil circuit is around 130µg; this is larger than 90µg at 2.7MHz, due to the higher natural fluctuation at 7MHz and also higher frequency shift in presence of cover glass without any sample on it, which limits the sensor resolution. Although the resolution of the devices used for these measurements in the laboratory is not more than 0.1mg, the error bar on the graphs also shows that it is not easy for the sensor to distinguish between the small amount of sample (<300µg). The maximum natural fluctuation of the sensor with this centre frequency is about 200Hz. This value is higher compared to the system resonating at 2.7MHz (natural fluctuation=70Hz) due to more noise and frequency drift in higher resonance frequency (chapter 5).

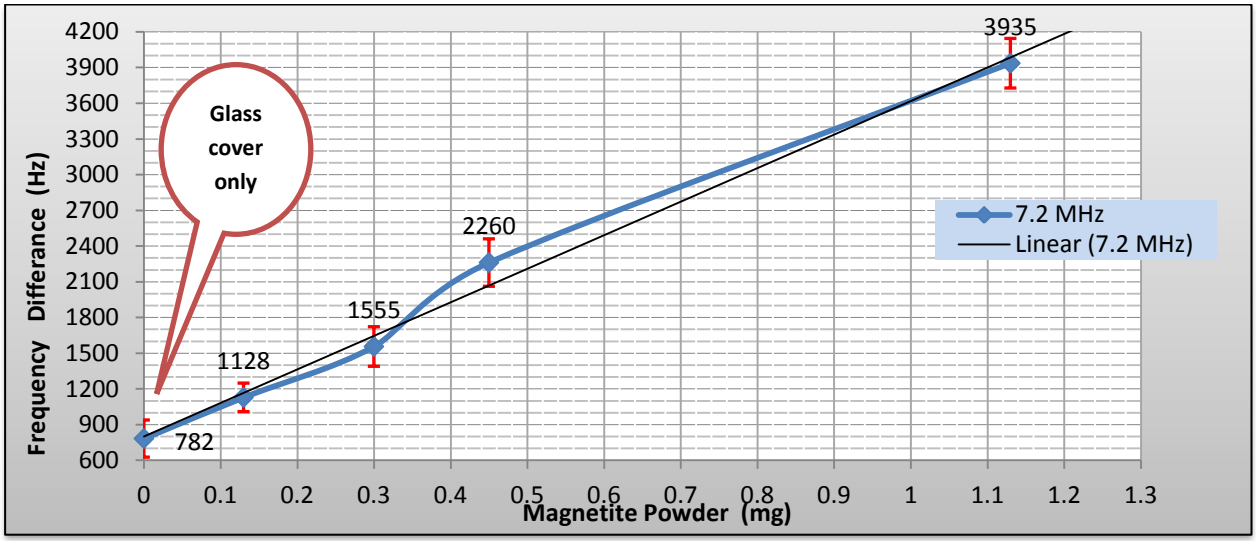

Figure 6.19: Sensor frequency shift for different mass of magnetite sample (7.2MHz centre frequency)

Table 6.4: Average values of frequency shifts caused by magnetite powder on the sensor with 7.2MHz centre frequency

7.2 MHZ	1.13 mg	450 ug	300 µg	130 µg	Cover glass
Frequency shift (Hz)	4200	2180	1528	1087	715
	3927	2688	1422	1242	712
	4100	2075	1293	1191	640
	3817	2430	1700	1040	890
	3616	2100	1540	1079	680
	4072	2349	1802	1134	963
	3915	2253	1755	1325	1066
	4119	2143	1488	912	759
	3651	2126	1470	1143	610
STDEV	208.23	199.35	166.22	119.64	156.18
Ave.	3935	2260	1555	1128	782

Comparing the response of the sensor at 7.2MHz frequency with the response at 2.4MHz resonance frequency (Figure 6.20) (in both, the exact amount of sample was tested), it can be seen how much increase in frequency shift has happened for each sample by changing the sensor centre frequency from 2.4 to 7.2MHz (Figure 6.19), starting from 219% (more than double) in the largest amount of sample (1.13 mg of magnetite powder). In this diagram the effect of cover glass has been subtracted from the frequency shift of each sample, thus the label numbers show the exact effect of each amount of sample presented by the output signal.

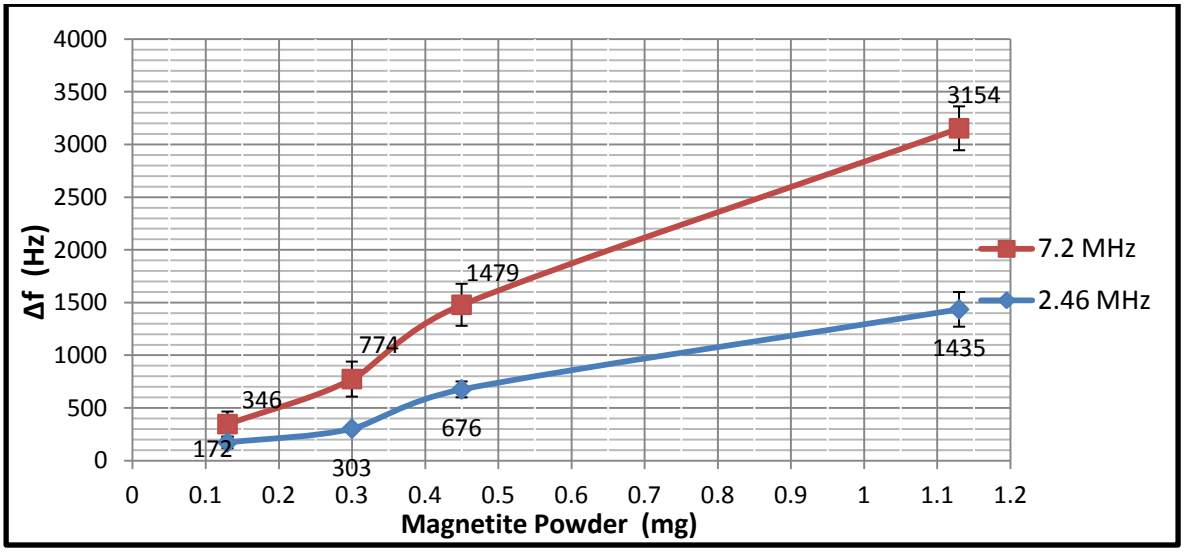

Figure 6.20: Comparison of sensor response to the magnetite powder sample at two level of centre frequencies; 2.46MHz and 7.2MHz

It has to be mentioned that although the frequency shift (Δf) for magnetic particle detection is higher in the system with high resonance frequency compared to the system with low resonance frequency, the larger natural fluctuation (200Hz) in high frequency (7.2MHz) limits the readout of

the sensor, and therefore the sensor sensitivity may not be better than low resonance sensor (2.4MHz).

6.4 Testing with other substrates (Acetate & Whatman paper)

All of the above tests were conducted using glass cover slip as a sample substrate. They were used mostly because of the easy handling, especially in the case of powder sample in which a firm substrate was required for holding it. On the other hand, the cover glass contains a small percentage of ferric oxide in its chemical structure, which leads to frequency shift (268Hz at f =2.43MHz and 782Hz at f = 7.2MHz) when applied on the sensor and thus gives a baseline shift for the detection. Right now the detection limit for 7.2MHz sensor is 130µg of magnetite powder, which gives about 1.1kHz shift to the output, but if we want to measure the smaller amount of sample (<130µg), the frequency shift consequently reduces to between 782-1100Hz (glass cover shift- 130µg sample); unfortunately this is the error bar range for the cover glass, therefore a smaller amount of sample cannot be tested, because the shift will conflict with the glass cover effect on the output.

Reducing the effect of substrates on the output can produce more room available for smaller amounts of sample to be detected. These issues motivated the idea of trying other substrates to eliminate the substrate effect from the sensor. For this purpose, acetate and Whatman 1 filter paper were examined. The manufacturers do not mention how much or if there is any amount of iron inside the acetate sheet, but the full details about the filter paper are as follows:

Figure 6.21: Whatman filter paper

As can be seen, a very small mass of iron is used for each filter paper. A series of tests were run to measure the influence of paper on the sensor and then the results were compared with the glass effect, as plotted in Figure 6.22. The figure shows the test run about seven times; in each iteration the glass cover is first placed on the sensor without any magnetic particle on it and then it is removed after a few minutes, then the Whatman paper is positioned on the sensor. This procedure is repeated seven times to plot Figure 6.22.

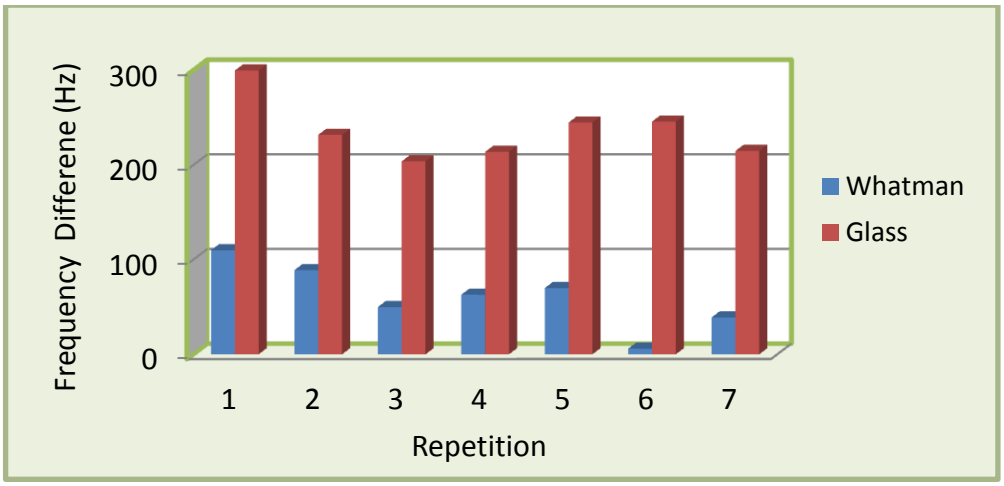

Figure 6.22: measuring and comparing the output changes between glass and paper substrate

As illustrated, the glass cover causes approximately 200Hz more difference in the output signal. This means the amount of frequency variation caused by the paper substrate is lower than the natural drift of the sensor, and it can be neglected. However, the important issue with using paper is difficulty in sample handling. For powder samples a firm substrate is required to avoid the powder spreading around during the test. Unfortunately, because of the soft and flexible structure of the paper, this cannot be achieved. Conversely, liquid samples are absorbed by the paper instantly, and instead of gathering in one small point they spread over the paper. As mentioned in chapter 5, sample positioning plays an important role in detection, and if the sample spreads in a way that becomes larger than the coil active area, it is likely that sensor could not detect the entire amount of sample quantitatively. Another problem with the paper is that it is lightweight and cannot easily be placed on top of the coil properly when offered to the other substrate (where the jig clipper can keep them in position). Thus, using paper substrate was unsuccessful for this detection application. For the acetate sheet, although the amount of iron it contains is unknown, the experiment shows that positioning this sheet on the coil can influence the inductance and change the output signal slightly. The result of this experiment as an average is presented in Table 6.5.

	Δf (Hz)	
F (MHz)	Cover glass	Acetate
7.2	782	448
2.4	268	87

(a)

	7.2 MHz		2.4 MHz	
	Cover glass	Acetate	Cover glass	Acetate
Δf (Hz)	715	400	266	99
	712	394	227	110
	640	560	326	83
	890	375	280	72
	680	346	274	64
	963	523	198	76
	1066	474	253	102
	759	514	320	81
	610	442	267	95
STDV	156	74	40	15
Ave.	782	448	268	87

(b)

Table 6.5: (a) Total average of the frequency shift, (b) Result table of the test

Although the frequency shift caused by the acetate is smaller than the glass, the sample handling for magnetite powder is still a problem, because acetate is also flexible; applying very small pressure to it changes the position of the sample. Therefore, using acetate with liquid sample was tried out, as described in the following section.

6.5 Experiments with synthesized magnetic particles on resonance-PLL circuit with acetate substrate

Considering the aim of this project, which is designing the sensor for point of care diagnostics, it is expected that this device is going to be tested with the samples in the liquid states, therefore it is important to examine this sensor with the iron oxide nanoparticles in the solution. According to chapter 3, in which synthesizing of magnetic nanoparticles was explained, this section is entirely dedicated to testing the sensor with those samples. The experiment was carried out in both 7.2MHz and 2.4MHz resonance frequencies; the only consideration is that iron oxide particles will oxidize soon and the test is not repeatable for the same sample, although it is repeatable for the same amount of sample. This means that, for example, detecting 1µl of nanoparticles (average size of each nanoparticle ≈ 25nm) should be repeated several times, but each time the new sample with 1µl of nanoparticles should be prepared, thus for eight times detection, eight samples of 1µl need to be prepared prior to the test. Thus, all of the tests in this section were undertaken with fresh samples.

The sensor response for different volumes of the sample in different frequencies is plotted in the Figure 6.34. The first value illustrated on the zero point of the X axis shows the frequency shift of acetate substrate without any sample on it.

The output frequency variation without any sample and substrate according to the calibration method for 7.2MHz circuit (described in chapter 5) was about 200Hz, which is a baseline for detection. The frequency difference (Δf) shown in the Y axis of the diagrams shows the difference between the circuit resonance frequency and the sensor output while the sample is on the coil. After applying the sample on the sensor, the value of output is not recorded immediately; 30 seconds is allocated for keeping the samples on top of the sensor before recording the sensor output, which means the magnetic beads were kept on the coil at least 30-40 seconds before the reading was taken.

Figure 6.23 presents the sensor response to the beads at 7.2MHz and 2.4MHz centre frequency. Sample positioning in the liquid state is much more variable and different from the magnetite powder. Here the liquid takes a circular shape like a coil shape or it can be completely different and uncontrollable (as described regarding sample positioning in chapter 5). Therefore, it should be considered that in some cases of these tests the sample may be larger than the coil diameter, getting out of its active area and consequently resulting in non-accurate detection. It happens rarely that the same volume of sample (especially for larger amount) results in exactly the same output signal difference due to the sample shape during preparation. This explains the large error bar on each point in the following illustrations.

Another point needs to be made regarding the fresh sample usage in each test. Because the nanoparticles are inside the solution, pipetting the same volume of liquid each time does not guarantee a similar sample concentration to the previous pipette; the amount of iron nanoparticles can differ for the same volume of liquid in each test.

Beside the sample concentration error, the pipette itself is volumetric equipment with its own margin of error; it was noted that for 25cm^3 pipette the percentage error is about 0.24%. The smaller the value measured, the greater the percentage error.

Therefore, all of the tests here are based on the assumption that the sample concentration is the same at a similar sample volume, and pipetting is done in the right way, preventing the error, although the error bars in the graphs show tolerance.

Another reason for large error bars in this section is due to the higher frequency fluctuation in high frequency (as discussed in chapter 5 regarding calibration).

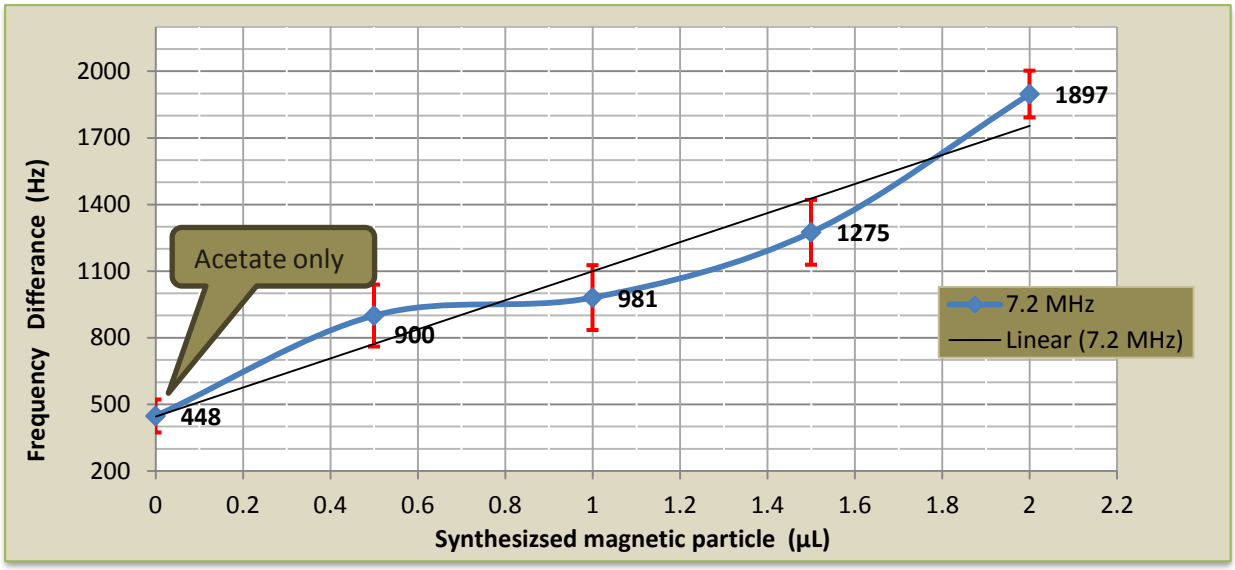

(a)

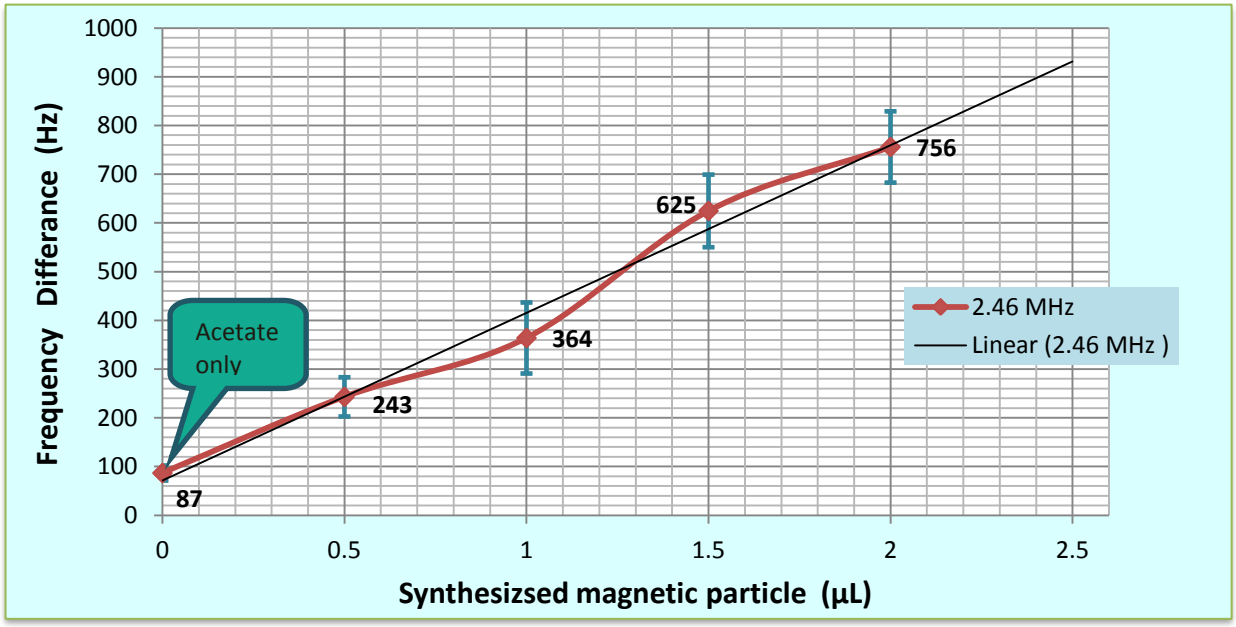

(b)

	7.2 MHZ					2.4 MHZ				
	30 sec Acetate	0.5 µL SNp	1 µL SNp	1.5 µL SNp	2 µL SNp	30 sec Acetate	0.5 µL SNp	1 µL SNp	1.5 µL SNp	2 µL SNp
Frequency shift (Hz)	400	654	1266	1380	1780	99	300	322	541	660
	394	1102	1073	1122	2014	110	229	267	652	743
	560	782	986	1016	1898	83	214	496	557	664
	375	870	835	1436	1837	72	312	328	710	790
	346	1015	1107	1319	1952	64	229	367	720	843
	523	960	824	1442	2044	76	195	430	552	772
	474	956	948	1328	1775	102	257	405	673	687
	514	782	930	1253	1983	81	245	378	672	856
	442	976	857	1176	1792	95	208	284	548	791
STDEV	74.32	139.55	146.04	145.93	105.43	15.37	40.27	72.92	74.52	73.16
Average	448	900	981	1275	1897	87	243	364	625	756

(c)

Figure 6.23: Output signal difference at (a) Resonance frequency = 7.2MHz, (b) f= 2.46MHz, (c) Result table

Similar to Figure 6.23 for synthesized beads, Figure 6.24 shows the comparison of frequency shift for synthesized beads, excluding the acetate substrate effect the label values are the actual frequency shift from the resonance frequency value.

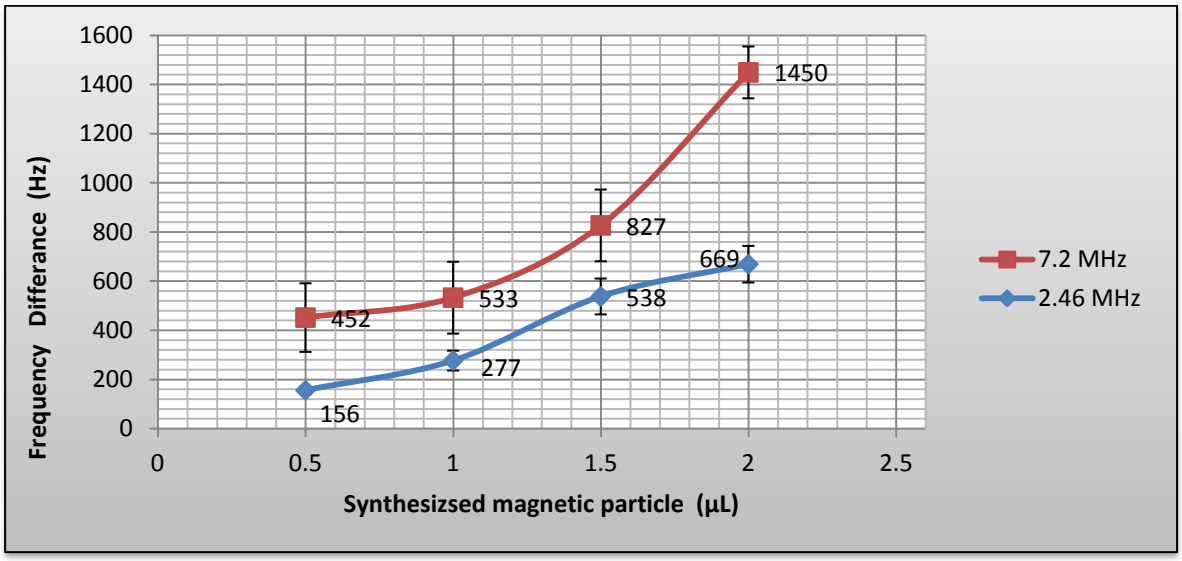

Figure 6.24: Sensor output changes for the same sample volume but at two different levels of Frequencies (2.46MHz and 7.2MHz)

6.6 Experiments with Fe_3O_4 in solution (Cytodiagnostic beads)

In most of the published research for magnetic particle detection [38, 46, 150-151], specific types of magnetic micro-particle have been used that are well characterized by their manufacturers; the most famous is Dynabeads [152]. Numerous papers have been published using these types of beads for their detection purposes.

According to the previous section describing the testing of the synthesized magnetic particles, it could be useful to test the sensor with a commercial type of Fe_3O_4 sample as well and then compare it with our synthesized beads.

Hence the Cytodiagnostic beads were chosen, which have the same chemical properties as the synthesised magnetic particle (chapter 3) but which are smaller in size. The sample specification is as follows:

- 10nm iron-oxide superparamagnetic nanoparticles (magnetite, Fe_3O_4)
- Concentration: 5mg/ml

According to the size and concentration, the equivalent amount of sample with magnetite powder mass can be calculated:

- 10µl of Cytodiagnostic beads = 50µg Fe_3O_4 powder
- 6µl of Cytodiagnostic beads = 30µg Fe_3O_4 powder

However, using Cytodiagnostic beads, which are a diluted Fe_3O_4, it is possible to test the sensor with smaller amounts of sample. Figure 6.25 presents the sensor response and frequency shift per small micro litre of beads using Whatman paper substrate. This experiment was done with 2.7MHz resonance frequency.

Considering the natural fluctuation and drift of the TF930 frequency counter used for these measurements (20Hz), it is wise to consider 10µL of iron oxide as the limitation and resolution of the detection. Therefore, the sensor resolution can change to 50µg of iron-oxide powder compared to section 6.3.3, which was around 130µg; this indicates an improvement in the detection resolution of about 40%.

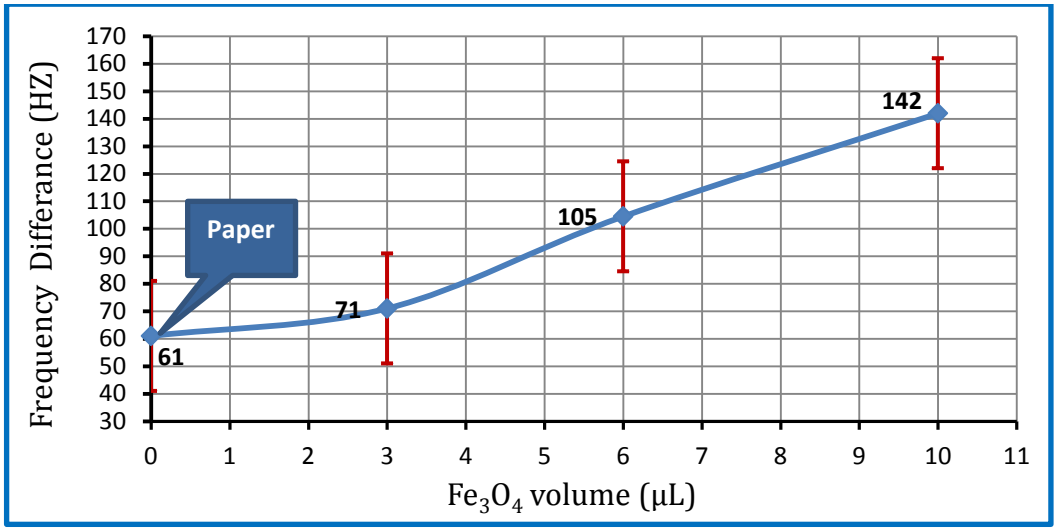

Figure 6.25: 30 second reading based on Whatman 1 substrate and Cytodiagnostic beads

The only problem with the Cytodiagnostics beads is that they oxidize quite quickly. Although the manufacturer claims six months before complete oxidization, unfortunately these samples oxidized during the first few weeks and their solution changed colour to light brown (complete oxidation; Figure 6.26). The experiments run with these beads are not repeatable, because after positioning the small amount of beads on the substrate, the beads became oxidized in air after a few minutes, thus the tests had to be run quite quickly, otherwise some of the particles would became light brown due to oxidization; as explained in chapter 3, oxidization changes the entire chemical properties of the sample and magnetite (Fe_3O_4) converts to maghemite Fe_2O_3, with less iron content.

Figure 6.26: Oxidized iron particles

6.7 Summary

In this chapter two types of sensors have been tested with real magnetic samples in different conditions. The GMR sensor shows good sensitivity to 0.1µL of the magnetic agarose beads, which have high concentration and sensitivity of about 564 (mV/mT), but the magnetic beads should be magnetized prior to the test. A PLL-resonance circuit was examined with three different types of samples in dried and liquid states.

It has been shown that by having a higher resonance frequency, a better sensitivity can be achieved and accordingly higher Δf per µL or µg of sample is guaranteed. However the higher the resonance frequency, the more natural fluctuation of the system; this somehow limits the detection of small amounts of sample and therefore reduces the sensor resolution. The effect of sensor distance with the sample has been investigated. Having simple calculation as a comparison between the amount of sample used with the number of magnetic particles of Fe_3O_4, (density: 5.17 g/cm^3), we can state the following estimations.

- Magnetite powder sample

Assuming that each particle diameter is about 50µm and the mass of interest is about 50µg (sensor sensitivity), then each bead volume is 6.5 ×10^{-5} mm^3 and 50µg of powder gives the volume of 10^{-2} mm^3, subsequently this volume of sample consists of about 153 beads.

- Synthesized magnetic particles

According to the TEM images and measurements (chapter 3), our synthesized particle has an average diameter of 25nm. Considering the bead volume 8.18123E-15 mm^3, it can be estimated that this sensor is able to detect 120E+10 beads.

In summary, this research shows:

At higher resonance frequency (GHz), the sensor is able to detect smaller mass or volume of magnetic particles, which means higher detection resolution. Comparing the results of magnetic detection in 7.2 MHz resonance frequency with the 2.4MHz, it can be concluded that 4MHz increase in the resonance frequency can increase the amount of frequency shift; the larger output signal difference is achieved in the presence of sample at higher frequency comparing to the lower frequency, however, the sensor with better stability has better detection resolution and sensitivity.

For the similar amount of samples, the size of nanoparticles play important role in detection. The sample which consists of smaller size particles can be heated up sooner (chapter 3) and therefore results in higher frequency shift in the sensor output. As a result the sensor is able to detect smaller amount of specific sample with smaller size. As an example this sensor was able to detect 130ug of magnetite powder (with particle size of 50ug) and on the other hand it was able to detect 50ug of iron-oxide particles while each bead diameter was 10nm.

Sample distance from the sensor and the substrate thickness has a major impact on the sensitivity; the shorter the distance, the higher the sensitivity.

Temperature is affecting the circuit in the long run, but during the detection period, which only takes few minutes, this effect shows up as a frequency fluctuation.

Although this sensor is able to detect the presence of magnetic particles, but for increasing the sensitivity and lowering the amount of detectable particles, a more stable system is required. One of the factors which will affect the sensitivity is the inductor. A different coil design with higher quality factor and smaller size might overcome this issue. A coil design with a uniform magnetic field distribution is preferred.

Another factor which should be considered is using a technique for suppressing the frequency drift. Although Faraday shield and diecast box were used for reducing the ground-effect of frequency shift, they are not applicable in the hand-held device.

The magnetic particles were oxidizing quickly during the test, and fresh samples should be prepared prior to each single test. This decreases the system accuracy, because the same test should be run with different samples of the same amount. Due to the small size of the sample, it was unlikely that measuring equipment (pipette and scale) gave the exact amount each time. The similar amount of sample may vary in two different substrates. Sample preparation was time-consuming and troublesome; using microfluidic chamber and conducting the test inside the chamber can help to keep the sample in the liquid state and prevent exposure to oxygen.

CHAPTER 7: **Conclusions and future work**

7.1 Conclusion

In this study the inductor-based sensor was designed to detect the presence of magnetic particles. Literature concerning the field of magnetic biosensor was critically reviewed, focusing on the inductive and frequency-based sensing scheme. A wide variety of sensors have been already employed for the detection of magnetic particles, but there is a high demand for the rapid, sensitive and accurate multiplex detection in which different types of samples can be tested simultaneously and the sensor can be used for molecular diagnostics. All of these specifications can be achieved by inductive sensing method.

There are varieties of detection methods available in which magnetic particles are utilized as labels. The amount of beads for detection is based on each application purposes. In this study the aim was to detect pathogenic DNA, thus the sample input size is large.

Development of the magnetic sensor was achieved by investigating and designing different sensors. Among the designed platforms, the PLL-resonance sensor was found to have the best sensitivity and stability while it was resonating at 2MHz and 7 MHz frequency.

This sensor design is such that different types of magnetic samples can be detected with it, as long as the sample has magnetic permeability. The magnetic sensor is optimized by fabrication of low inductance coil whereby the output signal fluctuates due to the presence of a small volume of magnetic particles, which can create significantly large frequency shift (>200 Hz). This signal can be easily detected and measured with readily available, low-cost equipment.

The sensor was designed using LC circuit as a source of oscillation. Several air core multilayer coils were fabricated with different specifications (such as number of turns, bobbins material, coil width) and they were implemented in the sensor circuit. The desire to attain a sensor with the highest feasible resonance frequency with very stable performance requires a low inductance coil and capacitor with low value. Although the value of capacitor cannot be chosen below 20pf due to the effect of parasitic capacitance on the sensor, higher frequency can only be obtained by using low inductance coil. On the other hand, this leads to the higher quality factor for the resonance circuit, which ultimately results in better sensitivity.

To optimize the design, the sensor calibration was completed and the limitations, challenges, signal to noise ratio and sensor stability were described. The ultimate limit on any magnetic sensor is noise. The sources for the noise can be inherent (from within the sensor, such as thermal noise or

flicker noise) or from external sources picked up by the sensor (for instance electrical noise or magnetic field from unwanted resources). As a result, the effect of ambient temperature, PLL circuit components (resistors and capacitor), humidity and electrical noise were considered and discussed on the sensor output frequency. Signal to ratio was calculated through the Fourier transform to expose the effect of noise (white noise). The results show that S/N ratio is a large number for this sensor (>235000). However, the frequency stability was not 100% perfect due to the presence of frequency drift. The value of capacitor and inductor in the LC circuit determines the resonance or centre frequency (f_0 or f_r). After setting this frequency for the oscillator, the sensor could not be maintained throughout and the output frequency signal kept changing randomly. On the other hand, detecting the small amount of magnetic particles required a very stable system able to detect very small frequency shift. As a result, the best sensor design needs to be obtained and calibrated to maintain the most stable performance with the minimum output frequency fluctuation.

The design and optimization process of the sensor was as follows:

- ✓ At first, the sensor was designed based on the LC oscillator and phase lock loop. The fabricated inductors were tested within the circuit with different capacitors. The successful oscillator should create the output resonance frequency as close as possible to the intended frequency with the minimum frequency offset.
- ✓ There should be a balance between the RLC circuit and the PLL circuit (in terms of impedance). The PLL circuit components should be selected such that the output signal remains stable and the output frequency changes should be within the defined frequency lock range by the PLL.
- ✓ The outcome sensor from above consideration should be a stable sensor with maximum S/N ratio and minimum output frequency drift.

With these provisos, the sensor could be tested with the actual magnetic particles sample, subject to the following considerations:

- ➢ Is the sensor sensitive enough to detect the presence of magnetic particles in its vicinity?
- ➢ How much frequency shift can be achieved for different amount of magnetic samples?
- ➢ Is the sensor capable of distinguishing between different amounts of magnetic particles?

To be acceptable, the sensor design had to meet these conditions. Focus was then given to designing a similar sensor at higher frequency to increase the detection limit, otherwise the whole process was repeated to discover the optimized circuit design.

Calibration results reveal the best sensor circuit for magnetic particle detection with high S/N ratio and the minimum output fluctuation during the detection period. The most excellent sensor performance accomplished using two different inductors; one with 85μH (Black coil) and one with 9.5μH (Yellow coil) for producing higher resonance frequency. Table 7.1 illustrates the best circuits' designs. The first two sensors (2.4MHz and 2.7MHz) were designed using Black coil and the 7.2MHz sensor was designed based on the Yellow coil. It can be seen that increasing the S/N ratio is inversely proportional to the decreasing of the frequency drift.

Table 7.1: Magnetic sensor specifications

Resonance Frequency (f_0)	Resonance Circuit		Phase Lock Loop Circuit			S/N Ratio	Frequency Drift (Hz/sec)
	L (μH)	Cr (pf)	R_1 (KΩ)	R_2 (KΩ)	C_1 (pf)		
2.4 MHz	85	47	10	10	270	689×10^3	0.166
2.7 MHz	85	39	10	10	390	580×10^3	0.58
7.2 MHz	9.5	47	56	4.7	270	253×10^3	3.3

These sensors were all tested with diverse types of magnetic particles as samples. The samples were different in size, material and physical state. Besides commercially available iron oxide particles, the iron nanoparticles were specially synthesized in this research based on this project's aim and requirements through water in oil microemulsion method and with the size distribution of 15-27nm in spherical/circular shape. They have strong magnetic properties and were produced based on the CTAB/n-butanol/n-octane microemulsion system using sodium borohydride as the reducing agent and iron chloride as the precursor.

The sensor sensitivity to different amounts of iron-oxide particles was examined and the results are presented in Table 7.2. Sensors number 2 and 3 are using different frequency counters and experimental setups (as described in chapters 4 and 5); it can be seen that sensor number 3 has higher frequency drift and less sensitivity.

Sensor number	Resonance frequency	Frequency drift (Hz/sec)	Detection limit (sensor resolution)	Frequency shift (Hz) (including substrate effect) (Hz)	Substrate effect (Hz)	Sensitivity (Hz)
1	2.4 MHz	0.166	130 µg magnetite powder	440	268	172
			0.5µL of 25nm beads	243	87	156
2	2.7 MHz	0.58	300 µg Magnetite powder	403	207	196
			10µL of 10nm beads = 50µg iron-oxide particles	142	61	81
3	2.7 MHz	0.94	1 mg magnetite powder	1100	300	800
4	7.2 MHz	3.3	130 µg magnetite powder	1128	782	346
			1µL of 25nm beads	981	448	533

Table 7.2: Sensitivity and detection resolution of resonance magnetic sensor

The maximum resonance frequency used in this work was 7.2 MHz and the detection resolution of 50µg iron oxide magnetic particles was achieved for the bead diameter of 10nm. The sensor sensitivity to the synthesized magnetic nanoparticles with the average diameter of 25nm was 0.5µL.

According to literature, at higher resonance frequency (GHz), the sensor is able to detect smaller mass or volume of magnetic particles (few number of beads), which means higher detection resolution. This research shows that increasing the resonance frequency for about 4MHz can cause the larger output signal difference in the presence of magnetic particles; however, the sensor stability is the most important factor for determining the detection resolution and sensitivity.

The sensor sensitivity is better if the sensor can detect smaller amount of magnetic sample. The results of this research demonstrate that while the sample is consists of smaller size particles, the sensor can detect the lower amount of sample. This is due to heating effect of nanoparticles (chapter 3). Sample distance from the sensor has a major impact on the sensitivity; the shorter the distance, the higher the sensitivity.

Temperature is affecting the circuit during the detection period, which only takes few minutes; this effect shows up as a frequency fluctuation.

7.2 Future work

This sensor has specific frequency drift, which limits its detection resolution. Detection of smaller amounts of magnetic particles would be possible by implementing a more stable system. Applying the following suggestions can improve the sensor performance and extend this research in order to make the hand-held and portable sensor:

- Integrating the sensor with microfluidic technology can help for having precise sample preparation and positioning. Preventing the iron oxide particles from oxygen exposure results in more accurate and reliable detection.
- Implementation of on-chip frequency counter can result in a handheld device
- Fabrication of on-chip inductor can improve the sensor sensitivity (e.g. the proposed sensor shown in Figure 4.12). Although the coil used in this research is magnetically very efficient and has higher quality factor than the planar coil, the air core planar spiral inductor is preferable for a lower resistance, smaller surface area and good temperature performance. As illustrated by the COMSOL simulation, the magnetic field is more concentrated in the middle of the coil. Using an inductor with a smaller surface area (smaller outer dimensions) will make it more likely for the sample to be placed near the coil centre, resulting in increased sensor sensitivity.
- Surface functionalization of the synthesized iron nanoparticles with the appropriate chemical methodology can stabilize the nanoparticles in the solution under a variety of processing situations for DNA attachment, and thus can prepare the system to be tested within molecular assay.

Biological tests with DNA sample can be performed to assess the capability and reliability of this sensor to be used in diagnostic application. Therefore, this sensor can be developed to sense the occurrence of DNA hybridization, whereby the biomolecules can be tagged with magnetic particles.

The above suggestions can lead to very high sensitivity magnetic particles' detection, however the desired sensitivity should be determined first according to the application requirement. Otherwise an expensive system could be designed with single particle sensitivity.

7.2.1 DNA immobilization

This work could be extended to test a DNA sample tagged to the magnetic particles on the sensor. This first requires immobilisation of DNA on the sample substrate. The surface chemistry of the sample substrates should be chosen to ensure effective immobilisation. The sensor surface can be easily coated with a gold layer via chromium (as proposed earlier in chapter 4, and shown in Figure 4.12). Nucleotides can be attached to the gold layer via a covalent Thiol linker.

As DNA hybridization is the fundamental principle for most of the biosensors in molecular detection, a study should be conducted to investigate the factors influencing DNA hybridization efficiency, which is depends on:

- Probe immobilization

- Probe density
- Conformation of the DNA strands
- Interaction of various strands of DNA with gold
- Effect of heating
- Effect of electrostatic filed

Considering the above suggestions, these design principles can be used to develop a detection sensor for higher frequency, with better sensor resolution and sensitivity.

Bibliography

1) Jenny G.ransson, Teresa Zardn Gmez De La Torre, Mattias Strmberg, “Sensitive Detection of Bacterial DNA by Magnetic Nanoparticle’’, *Anal. Chem.* 2010
2) Clarissa Lui , "Nucleic Acid-based Detection of Bacterial Pathogens Using Integrated Microfluidic Platform Systems", *Sensors* 2009, ISSN 1424-8220
3) C.D. Chin S.Y. Chin T. Laksanasopin S. , "Low-Cost Microdevices for Point-of-Care Testing", Chapter 1, Springer-Verlag Berlin Heidelberg 2013
4) Steven F. Buchsbaum, "Integrated Microfluidic Platforms Toward Point of Care Pathogenic Nucleic Acid Detection", University of California, Santa Barbara 2010
5) Shahzi S. Iqbal, Michael W. Mayo, "A review of molecular recognition technologies for detection of biological threat agents"
6) Berg J., Tymoczko J. and Stryer L. [2002] Biochemistry. W. H. Freeman and Company ISBN 0-7167-4955-6
7) Ghosh A, Bansal M [2003]. "A glossary of DNA structures from A to Z". Acta Crystallogr D 59
8) Abbreviations and Symbols for Nucleic Acids, Polynucleotides and their Constituents IUPAC-IUB Commission on Biochemical Nomenclature [CBN]. Retrieved 03 January 2006.
9) PMID 12657780. J Clin Microbiol. 2003 Oct; 41[10]:4542-50.Molecular detection and identification of influenza viruses by oligonucleotide microarray hybridization. Sengupta S, Onodera K, Lai A, Melcher U. Source Department of Biochemistry and Molecular Biology, Oklahoma State University, Stillwater, Oklahoma 74078, USA
10) J.A. Land, J.E.A.M. Van Bergen et al , “Epidemiology of Chlamydia trachomatis infection in women and the cost-effectiveness of screening” Human Reproduction Update, Vol.16, No.2 pp. 189–204, 2010
11) J. Tüdos, G. A. J. Besselink, and R. B. M. Schasfoort, “Trends in miniaturized total analysis systems for point-of-care testing in clinical chemistry,” Lab on a Chip, 2001.
12) Pascal Craw and Wamadeva Balachandran , "Isothermal nucleic acid amplification technologies for point-of-care diagnostics: a critical review" , March 2012
13) D. Mark, S. Haeberle, G. Roth, F. Von Stetten, and R. Zengerle, “Microfluidic lab-on-a-chip platforms: requirements, characteristics and applications,” Chemical Society Reviews, vol. 39, no. 3, pp. 1153–1182, 2010.
14) Birkhahn, R. H., Haines, E., Wen, W., Reddy, L., Briggs, W. M., & Datillo, P. a. The American journal of emergency medicine, 2011, 29[3], 304-8.
15) Figeys, D. & Pinto, D. 2000, "Lab-on-a-chip: A revolution in biological and medical sciences", *Analytical Chemistry*, vol. 72, no. 9.
16) Lab on Chip; Available at: www.gene-quantification.de/lab-on-chip [Retrieved, 30/09/2011]

17) P. Yager, G. J. Domingo, and J. Gerdes, “Point-of-care diagnostics for global health,” Annual Review of Biomedical Engineering, 2008.
18) C. D. Chin, V. Linder, and S. K. Sia, “Lab-on-a-chip devices for global health: past studies and future opportunities,” Lab on a Chip, 2007.
19) Mapping the landscape of diagnostics for sexually, Key Findings and Recommendations. World Health Organisation 2004 Source, Available at : www.who.int/std_diagnostics
20) Angelika Niemz, Tanya M. Ferguson and David S. Boyle, "Point-of-care nucleic acid testing for infectious diseases" 2011 , Elsevier Ltd
21) Dayong Yang, Michael J. Campolongo, "Novel DNA materials and their applications" 2010 WIREs Nanomedicine and Nanobiotechnology
22) Watson JD, Crick FHC. "Molecular structure of nucleic acids - A Structure for deoxyribose nucleic acid", Nature 1953
23) M Curreli, F N Ishikawa, Fumiaki N Ishikawa, M E Thompson, Richard J Cote, Chongwu Zhou, Mark E Thompson; “Real-Time, Label-Free Detection of Biological Entities Using Nanowire-Based FETs” IEEE Transactions on Nanotechnology, Nov. 2008
24) Michael W. Pfaffl , The Gene Quantification, Available at: www.gene-quantification.de
25) John Waswa, Joseph Irudayaraj, Chitrita DebRoy; “Direct detection of E. Coli O157:H7 in selected food systems by a Surface Plasmon resonance biosensor” 2005 Swiss Society of Food Science and Technology
26) Y. Amano and Q. Cheng, “Detection of influenza virus: traditional approaches and development of biosensors,” Anal. Bioanalysis Chemistry,2004
27) P. Tallury, A. Malhotra, L. M Byrne and S. Santra, “Nano bioimaging and sensing of infectious diseases” Advanced Drug Delivery review, 2009
28) C. Fournier-Wirth and J. Coste, “Nanotechnologies for pathogen detection: Future alternatives?” Biologicals 2009
29) H. M.E. Azzazy, M. M.h. Mansour, “In vitro diagnostic prospects of nanoparticles” Clinical Chimica Acta 2008
30) Minghui Yang, Kim E. Sapsford, Nikolay Sergeev, “Meeting current public health needs: Optical biosensors for pathogen detection and analysis” National Cancer Institute, Rockville, 2009
31) Tim Damrow, Brent Hagemeyer, Hassan Ismail, Ryan Oldham “Optical, Electrochemical, and Magnetic DNA Biosensors – An Overview “ ,2009 Northern Illinois University, USA
32) Shuming Nie, Richard N. Zare, “Optical Detection of Single Molecules” Annual Review of Biophysics and Biomolecular Structure, 1997
33) T Gregory Drummond, Michael G Hill & Jacquelin K Barton, “ Electrochemical DNA sensors” Nature Biotechnology 2003
34) Joseph Wang, "Review, Electrochemical detection for microscale analytical systems" 2002 Elsevier Science

35) Umasankar Yogeswaran and Shen-Ming Chen, " A Review on the Electrochemical Sensors and Biosensors Composed of Nanowires as Sensing Material" Sensors 2008

36) Mir M, Homs A, Samitier J., "Integrated electrochemical DNA biosensors for lab-on-a-chip devices" Electrophoresis, 2009

37) "STJ-001**,** TMR Magnetic field Microsensor [Bare Die] " Micro Magnetics sensible solutions www.micromagnetics.com

38) Hua Wang, Shohei Kosai, Constantine Sideris, and Ali Hajimiri, 'An Ultrasensitive CMOS Magnetic Biosensor Array with Correlated Double Counting Noise Suppression' California Institute of Technology,2010

39) Jenny G.ransson, Teresa Zardn Gmez De La Torre, M attias Strmberg, "Multiplex Detection of DNA Sequences using the Volume-Amplified Magnetic Nanobead Detection Assay" Uppsala University, 2009

40) Daniel L. Graham1, Hugo A. Ferreira1, and Paulo P. Freitas, " Magnetoresistive-based biosensors and biochips" TRENDS in Biotechnology Vol.22 No.9 September 2004

41) Christel LA, Petersen K, McMillan W, Northrup MA, 1999 Rapid, automated nucleic acid probe assays using silicon microstructures for nucleic acid concentration. J Biomech Eng. 1999

42) Shan X. Wang and Guanxiong Li, "Advances in Giant Magnetoresistance Biosensors with Magnetic Nanoparticle Tags: Review and Outlook" IEEE TRANSACTIONS ON MAGNETICS, VOL. 44, NO. 7, JULY 2008

43) Christine Berggren Kriz, Kajsa Rådevik and Dario Kriz, 'Magnetic Permeability Measurements in Bioanalysis and Biosensors', Anal. Chem. 1996

44) Detection of a single magnetic Micro-bead using a miniaturized hall sensor, 2002

45) G Li, "Model and Experiment of Detecting Multiple Magnetic nanoparticles by spin valve sensor", 2004

46) Weifeng Shen, "In situ detection of single micron sized magnetic beads" (Tunnel junction MTJ), 2005

47) Marius Volmer and Marioara Avram, "Electrical characterization of magnetoresistive sensors based on AMR and GMR effects used for lab-on-a-chip applications" Rev.Adv.Mater.Sci. 15(2007) 220-224

48) Jeong Dae Suh, Sang Don Jung, and Myung Ae Chung "Spin Valve Ring Sensors for Superparamagnetic Bead Detections" Electronics & Telecommunications Research Institute, Daejeon , Korea, IEEE 2009

49) P P Freitas, R Ferreira, S Cardoso and F Cardoso, "Magnetoresistive sensors", J. Phys.: Condens. Matter 19 , 2007

50) Shu-Jen Han**,** and Shan Wang**,** IBM T.J. Watson Research center , Yorktown Heights, NY, Stanford University, "Magnetic Nanotechnology for Biodetection" 2010

51) Ripka, P. “Magnetic Sensors and Magnetometers”, Artech House Publishers: Boston, UK, 2001

52) K. Skucha, P. Liu, M. Megens, J. Kim and B. Boser, “A compact Hall-effect sensor array for the detection and imaging of single magnetic beads in biomedical assays”, 2011 IEEE

53) NVE Corporation, GMR Sensors Data Book

54) Gooneratne, Chinthaka P.; Giouroudi, Ioanna; Liang, Cai; Kosel, Jurgen; , "A giant magnetoresistance ring-sensor based microsystem for magnetic bead manipulation and detection," Journal of Applied Physics, vol.109, no.7, Apr 2011

55) J Feng, Y Q Wang, F Q Li, H P Shi and X Chen, “Detection of magnetic microbeads and Ferrofuid with giant magnetoresistance sensors”, IOP science 2011

56) Shu-Jen Han, Heng Yu, Boris Murmann, Nader Pourmand, Shan X. Wang, ‘A High-Density Magnetoresistive Biosensor Array with Drift-Compensation Mechanism’ , Stanford University, Stanford, CA 2007

57) Xu, L.; Yu, H.; Akhras, M.S.; Han, S.-J; Pourmand, N.; Wang, S.X., “Giant magnetoresistive biochip for DNA detection and HPV genotyping”. Biosensors & Bioelectronics, 2008

58) Kirstin Kriz a,b, Janin Gehrke a, Dario Kriz, ‘Advancements toward magneto immunoassays’ Biosensors & Bioelectronics 13 (1998)

59) P.I. Nikitin, P.M. Nikitin, M. Torno, H. Chen, and A. Rosengart , "Quantitative real-time in vivo detection of magnetic nanoparticles by their nonlinear magnetization" , Journal of applied Physics 103, 07A304, 2008

60) Petr I. Nikitina, Petr M. Vetoshkob, Tatiana I. Ksenevich, ‘New type of biosensor based on magnetic nanoparticle detection’ Journal of Magnetism and Magnetic Materials 311 (2007)

61) Maxim P.Nikitin, PetrM.Vetoshko, NikolaiA.Brusentsov, PetrI.Nikitin ‘Highly sensitive room-temperature method of non-invasive in vivo detection of magnetic nanoparticles’ Journal of Magnetism and Magnetic Materials 321 (2009)

62) Julie Richardson, Andrew Hill, Richard Luxton, Peter Hawkins, ‘A novel measuring system for the determination of paramagnetic particle labels for use in magneto-immunoassays’ Biosensors & Bioelectronics 16 (2001),University of the West of England, Bristol, UK

63) J Richardson et al, “The use of coated paramagnetic particles as a physical label in a magneto-immunoassay” , Biosensors & Bioelectronics 16 , 2001

64) Peter Hawkins, Richard Luxton, “Paramagnetic Particle detection” Bristol, GB , 2007

65) Hua Wang, Yan Chen, Arjang Hassibi, Axel Scherer, Ali Hajimiri , "A Frequency-Shift CMOS Magnetic Biosensor Array with Single-Bead Sensitivity and No External Magnet" California Institute of Technology, Pasadena, CA ,2009 IEEE International Solid-State Circuits Conference

66) Hua Wang, Alborz Mahdavi, David A. Tirrelld and Ali Hajimiri, 'A magnetic cell-based sensor' Lab on a Chip 2010

67) Hua Wang, Constantine Sideris, and Ali Hajimiri, 'A Frequency-Shift based CMOS Magnetic Biosensor with Spatially Uniform Sensor Transducer Gain' Department of Electrical Engineering, California Institute of Technology, Pasadena, CA, 91125, USA, 2010

68) Bruno Andò, Salvatore Baglio, Angela Beninato, Vincenzo Marletta, "Development integrated inductive sensors for magnetic immunoassay in 'lab on chip' devices" , University of Catania, Italy 2009

69) "The Discovery of Giant Magnetoresistance" Scientific Background on the Nobel Prize in Physics 2007, the Royal Swedish Academy of Sciences

70) Sayyed Mohamad Azimi, "Numerical Investigation of a Magnetic Sensor for DNA Hybridization Detection Using Planar Coupled Inductor with Spiral Windings" MPhil Thesis, Brunel University, 2007

71) Sayyed M. Azimi, M. Bahmanyar, M. Zolgharni, W. Balachandran, " An Inductance-based Sensor for DNA Hybridization Detection" 2007 IEEE

72) Melzer, M.; Karnaushenko, D.; Makarov, D. R.; Mei, Y.F.; Schmidt, O.G. Et al, " Elastic magnetic sensor with isotropic sensitivity for in-flow detection of magnetic objects". RSC Advances 2012

73) GMR Sensors Data Book, NVE GMR catalogue, 2003

74) C.R. Tamanaha, S.P. Mulvaney, J.C. Rife, L.J. Whitman, 'Magnetic labelling, detection, and system integration' Naval Research Laboratory, Washington, DC 20375-5342, USA, 2008

75) Charles D. Rakes, 'Metal-detecting circuit II' , Poptronics 2001

76) Kirstin Kriz a,b, Janin Gehrke a, Dario Kriz, "Advancements toward magneto immunoassays", Biosensors & Bioelectronics 13 (1998)

77) Hayt, W.H., Buck, J.A., "Engineering Electromagnetics", *McGraw Hill*, 6th edition, pp. 288-297, 2001

78) C.J. Serna and M.P. Morales, "MAGHEMITE (γ-Fe2O3): a versatile magnetic colloidal material" Surface and Colloid Science, Vol. 17, Chap. 2, pp. 27-81

79) M. Jayne Lawrence, Gareth D. Rees, “Microemulsion-based media as novel drug delivery systems” Advanced Drug Delivery Reviews 45 , 2000

80) Sonja Berensmeier, “Magnetic particles for the separation and purification of nucleic acids” Appl Microbiol Biotechnology (2006)

81) Ioanna Giouroudi and Franz Keplinger “Microfluidic Biosensing Systems Using Magnetic Nanoparticles”, International Journal of Molecular Sciences, ISSN 1422-0067, 2013

82) R. K. Zheng, Hongwei Gu et al, “ Self-assembly and self-orientation of truncated nano-octahedra of magnetite ” Department of Chemistry, The Hong Kong University of Science and Technology

83) S. M. Azimi, “Magnetic Bead-based DNA Extraction and Purification Microfluidic Chip” PhD Thesis, Brunel University, 2010

84) N D Kandpal et al, “Co precipitation method of synthesis and characterization of iron oxide nanoparticles ”, Journal of Scientific and Industrial Research, Vol. 73, 2014

85) Gupta A and Gupta M, “ Synthesis and surface engineering of iron oxide nanoparticles for biomedical applications”, Biomaterials 26, 3995-4021, 2005

86) Hossein Eivari, Abbas Rahdar, “Some Properties of Iron Oxide Nanoparticles Synthesized in n Different Conditions” , Vol (3), WAP journal 2013

87) Maria Cristina Mascolo, Yongbing Pei et al, “Room Temperature Co-Precipitation Synthesis of Magnetite Nanoparticles in a Large pH Window with Different Bases” Materials, 2013

88) D. Langevin , “Micelles and Microemulsions” , Annual Review, Phys. Chem. 1992

89) Kowgli K, Lafont U, Rappolt M and Koper G, “Uniform metal nanoparticles produced at high yild in dense microemulsions”, Journal of Colloid and Interface Science 372, 2012

90) I. Capek, “Preparation of metal nanoparticles in water-in-oil (w/o) microemulsions ”, Advances in Colloid and Interface Science , 2004

91) A. Drmota1, M. Drofenik, J. Koselj et al, “Microemulsion Method for Synthesis of Magnetic Oxide Nanoparticles” Faculty of Chemistry and Chemical Engineering, Slovenia 2012 www.intechopen.com

92) Aleksandr Marinin, “ Synthesis and characterization of superparamagnetic iron oxide nanoparticles coated with silica” Master thesis, Royal Institute of Technology, Stockholm, 2012

93) G. Zhang, Y. Liao, I. Baker, " Surface engineering of core/shell iron/iron oxide nanoparticles from microemulsions for hyperthermia" Materials Science and Engineering C, 2009

94) W. Wu, Q. He, Ch. Jiang, " Magnetic Iron Oxide Nanoparticles: Synthesis and Surface Functionalization Strategies" Nanoscale Res Lett, 2008

95) Zeng Q and Baker I, Patent; "Iron/iron oxide nanoparticle and use thereof"; PUB NO: US 2011/0104073 A1, 2011

96) K. Sung, "Synthesis and Magnetic Heating of Iron Core/Iron Oxide Shell Nanoparticles", Center for Nanomaterials Research at Dartmouth, 2007

97) Capek I, "Preparation of metal nanoparticles in water-in-oil (w/o) microemulsions", Advances in Colloid and Interface Science 110,49–74, 2004

98) Jones, T.B., "Electromechanics of Particles", Cambridge University Press, New York, 1995, USA

99) Z. Li, M. Kawashita et al, "Effect of Particle Size of Magnetite Nanoparticles on Heat Generating Ability under Alternating Magnetic Field", Bioceramics Development and Applications, Vol. 1, 2011

100) I. Kong, S.H. Ahmad, M.H. Abdullah, A. Yusoff, "The Effect Of Temperature On Magnetic Behavior Of Magnetite Nanoparticles And Its Nanocomposites" Nanoscience and Nanotechnology, 2008

101) Schmitt, R., "Electromagnetics Explained", *Newnes-Elsevier science*, USA, pp. 51-73, 2002

102) Sorensen, C.M., "Nanoscale Materials in Chemistry", John Wiley and Sons, Inc., New York, 2001, pp. 169.

103) Mikkelsen, C.I., "Magnetic Separation and Hydrodynamic Interactions in Microfluidic Systems". Ph.D. Thesis, Technical University of Denmark,2005

104) Jackson, J.D., "Classical Electrodynamics, *John Wiley & Sons Ltd*, 3rd Ed., New York, USA 1998

105) Cytodiagnostics, Nanotechnology products,(10nm Iron Oxide Magnetic Nanoparticles), www.cytodiagnostics.com

106) Sanchez-Dominguez M, Aubery C, Solans C, Chapter 9, "New Trends on the Synthesis of Inorganic Nanoparticles using Microemulsions as confined Reactions Media", Smart Nanoparticles Technology

107) Moulik S, Paul B, "Structure, dynamics and transport properties of microemulsions", Advances in colloid and interface science 78, 1998

108) Zhong C, Wang L and Luo J, Patent, “Method of forming iron oxide core metal shell nanoparticles”; Patent No; US 7,829,140 B1,2010

109) Zeng Q, Baker I, Loudis A and Liao Y, “Fe/Fe oxide nanocomposite particles with large specific absorption rate for hyperthermia”, Applied physics letters, 90, 2007

110) E.Haddad, Ch. Martin et al “Modeling, Fabrication, and Characterization of Planar Inductors on YIG Substrates” hal-00672240, version 1 - 20 Feb 2012

111) Sayyed Mohamad Azimi, “Numerical Investigation of a Magnetic Sensor for DNA Hybridization Detection Using Planar Coupled Inductor with Spiral Windings” MPhil Thesis, Brunel University, 2007

112) A. M. Niknejad and R. G. Meyer, “Analysis and optimization of monolithic inductors and transformers for RF IC's”, IEEE Journal of Solid-State Circuits, 1998

113) J. R. Long and M. A. Copeland, “The modeling, characterization, and design of monolithic inductors for silicon RF IC's”, IEEE Journal of Solid-State Circuits, 1997

114) C. P. Yue, S. S. Wong, “Physical modeling of spiral inductors on silicon”. IEEE Trans. Electron Dev., 2000.

115) “Multilayer air-cored coils” , Electronics world ,pg 752-753 September 1997

116) L. Kin Yun, T. Tian Swee, “A Rapid Inductance Estimation Technique By Frequency Manipulation” Latest Trends in Circuits, Control and Signal Processing

117) Marc Thompson, “Inductance calculation techniques ” Power Control and Intelligent Motion, Dec.1999

118) Tuan Huu Bui, “Design and Optimization of a 10nH Square-Spiral Inductor for Si RF Ics.” Master Thesis, University of North Carolina 1999

119) J Zhao, “A new calculation for designing multilayer planar spiral inductors” PULSE 2010

120) S. Mohan, M. Hershenson et al “Simple Accurate Expressions for planar spiral inductances”, IEEE Journal of solid-state circuits, VOL. 34, NO. 10, October 1999

121) John Long, “Monolithic Transformers for Silicon RF IC Design”, IEEE Journal of solid-state circuits, VOL. 35, NO.9, Sep. 2000

122) E.Haddad, Ch. MArtin et al “Micro-Fabrication of Planar Inductors for High Frequency DC-DC Power Converters” Advanced Magnetic Materials, Dr. Leszek Malkinski (Ed.), ISBN: 978-953-51-0637-1, InTech 2012

123) Evgeny Fomin “LDC1000 Temperature Compensation” Texas Instruments, SNAA212–September 2013

124) Kováč D., Cand.Sc., Prof. Ocilka M.,“CALCULATING OF INDUCTANCE OF SPIRAL COIL USING COMSOL MULTIPHYSICS” 2012

125) Arunava Santra, Niladri Chakraborty and Ranjan Ganguly “Analytical evaluation of magnetic field by planar micro-electromagnet spirals for MEMS Applications” Journal of Micromechanics and Microengineering, 2009

126) Y. Zheng, S. Bekhiche et al, “Planar Microcoils Array Applied to Magnetic Beads Based Lab-on-chip for high throughput applications” 2011 IEEE

127) Ch. Escriba, R. Fulcrand, Ph.Artillan, et al “Trapping Biological Species in a Lab-on-Chip Microsystem: Micro Inductor Optimization Design and SU8 Process”, Design Methodologies for SoC and SiP, 313, Springer, pp.81-96, 2010, IFIP Advances in Information and Communication Technology, 978-3-642-12266-8, 2014

128) C. Patrick Yue and S. Simon Wong, “Physical Modeling of Spiral Inductors on Silicon”, IEEE Transactions on Electron Devices, VOL. 47, NO. 3, MARCH 2000

129) J. Richardson et al “A novel measuring system for the determination of paramagnetic particle labels for use in magneto-immunoassays”, Biosensors & Bioelectronics 16 (2001) 1127–1132

130) Kirstin Kriz a,b, Janin Gehrke a, Dario Kriz, ‘Advancements toward magneto immunoassays’ Biosensors & Bioelectronics 13 (1998)

131) J Richardson et al, “The use of coated paramagnetic particles as a physical label in a magneto-immunoassay” , Biosensors & Bioelectronics 16 , 2001

132) MM74HC4046 CMOS Phase Lock Loop, FAIRCHILD SEMICONDUCTOR

133) Payam Heydary, “Analysis of the PLL Jitter Due to Power/Ground and Substrate Noise” IEEE TRANSACTIONS ON CIRCUITS AND SYSTEMS 2004

134) Bob Kelly “How to debug a PLL frequency synthesizer” Next Generation Wireless 200

135) Ali Hajimiri, Thomas H. Lee, “A General Theory of Phase Noise in Electrical Oscillators” IEEE JOURNAL OF SOLID-STATE CIRCUITS, VOL. 33, NO. 2, FEBRUARY 1998

136) Philips Semiconductors, 74HC/HCT4046A Phase-locked-loop with VCO

137) CMOS Phase-Locked-Loop Applications Using the CD54/74HC/HCT4046A and CD54/74HC/HCT7046A, Texas Instruments, September 2002

138) J. M. Barnett, Patrick Wraith et al “An Inexpensive, Fast and Sensitive Quantitative Lateral Flow Magneto-Immunoassay for Total Prostate Specific Antigen” Biosensors 2014

139) M. Azimi, “Magnetic Bead-based DNA Extraction and Purification Microfluidic Chip” PHD Thesis 2010, Brunel University, UK

140) TF930 , 3GHz UNIVERSAL COUNTER, INSTRUCTION MANUAL

141) An Introduction to Frequency Calibrations, NIST Frequency Measurement and Analysis System
142) 1/f Noise Characteristics Influencing Phase Noise, California Eastern Laboratories
143) VCO Phase noise, MINI CIRCUIT, 1999
144) R. J. Betancourt-Zamora and Thomas H. Lee, “LOW PHASE NOISE CMOS RING OSCILLATOR VCOs FOR FREQUENCY SYNTHESIS” Stanford University
145) S. Yoon, “LC-tank CMOS Voltage-Controlled Oscillators using High Quality Inductors Embedded in Advanced Packaging Technologies” 2004 PhD Thesis, Georgia Institute of Technology
146) R. Ciprian, B. Lehman, “Modeling Effects of Relative Humidity, Moisture, and Extreme Environmental Conditions on Power Electronic Performance” 2009 IEEE
147) Evgeny Fomin “LDC1000 Temperature Compensation” Texas Instruments, SNAA212–September 2013
148) NVE Corporation, GMR Sensors Data Book
149) Immobilization of DNA onto Gold and Dehybridization of Surface-Bound DNA on Glass, , Northwestern University, 2010
150) Detection of a single magnetic Micro-bead using a miniaturized hall sensor, 2002
151) G Li, "Model and Experiment of Detecting Multiple Magnetic nanoparticles by spin valve sensor", 2004
152) Life Technologies, www.lifetechnologies.com/uk
153) Zaitsev Dmitry D., 'Glossary of Nanotechnology and related terms', www.eng.thesaurus.rusnano.com

Appendix 1

COMSOL Simulation of copper coil

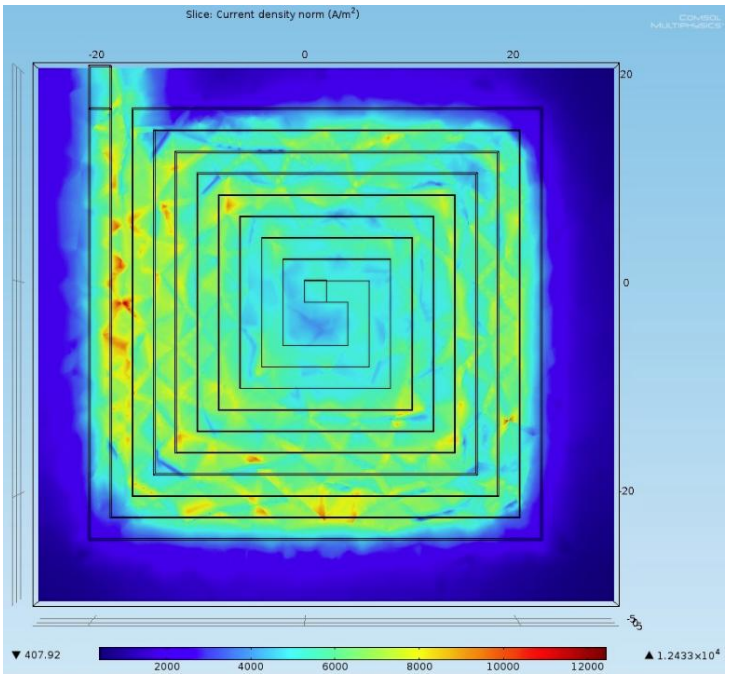

Copper coil (N=5, I= 100mA), current density norm: 2000 - 10000 (A/m^2)

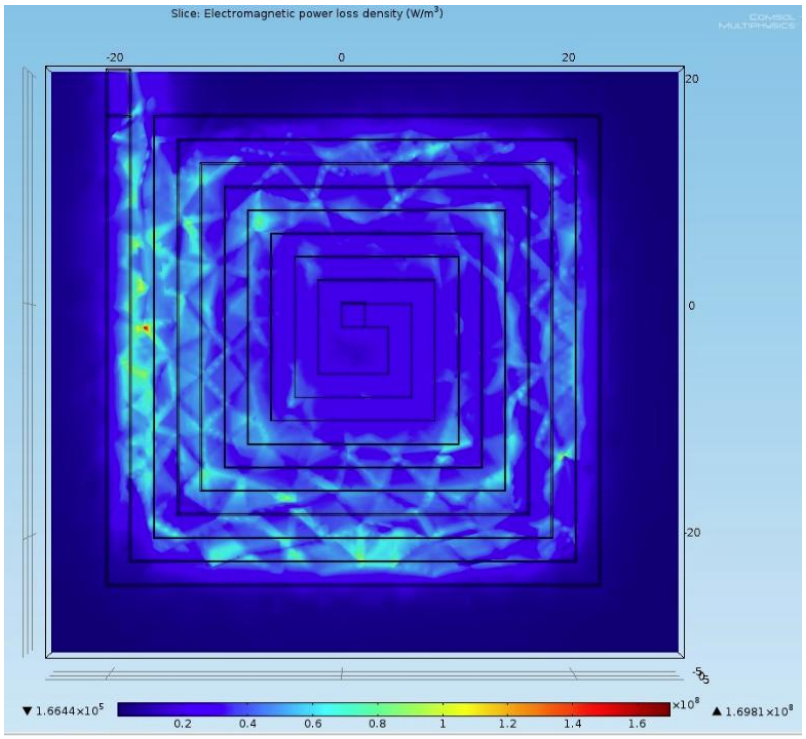

Copper, (N=5, I= 100mA), electromagnetic power loss density: 1.6×10^5 - 1.7×10^8(W/m^3)

Appendix 2

COMSOL Simulation of Aluminium Coil (N=5, I=100mA)

The following figure illustrates the magnetic flux density lines and the electrical voltage of the coil using aluminium alloy (due to its heat efficiency) instead of copper, the coil structure, size and conditions are all the same as before. The magnetic flux is generated with the maximum of 30mT in the centre similar to the copper coil and the coil inductance is evaluated as 0.23nH. The electrical voltage on the aluminium coil is between 60-180mV, which is higher than the copper one, but the magnetic field distribution is more uniform and stronger on the copper inductor.

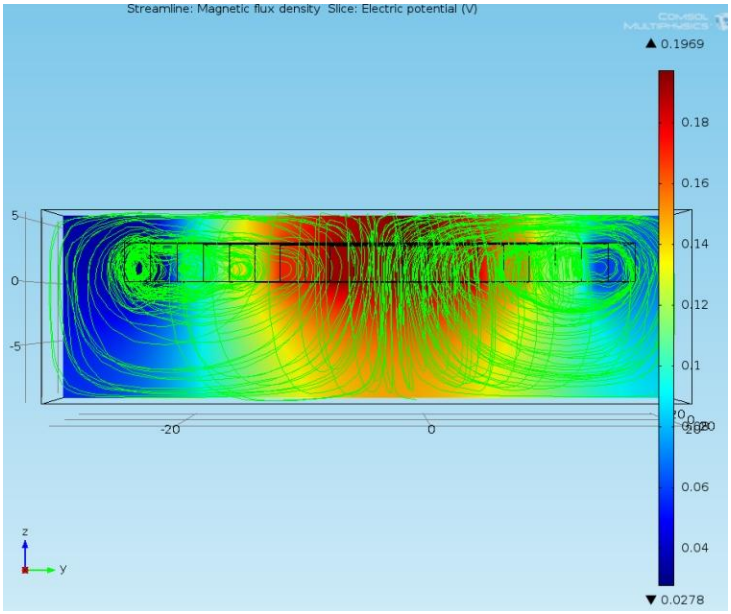

Aluminium coil with N=5 and **I= 100mA**, electric voltage: 60-180 mv including streamlines of magnetic flux density norm: **5 - 30mT**

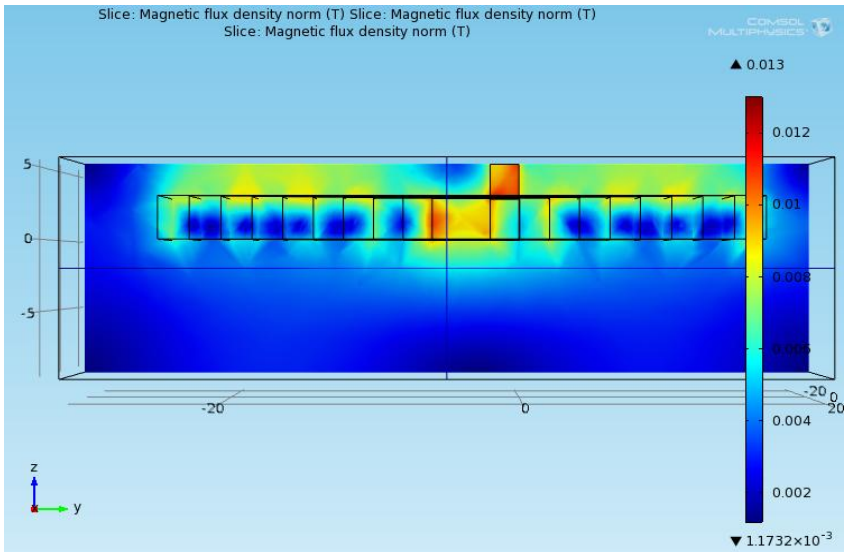

Aluminium coil: Cross sectional view of the aluminium coil in room temperature, N=5, I=0.1 A

Appendix 2

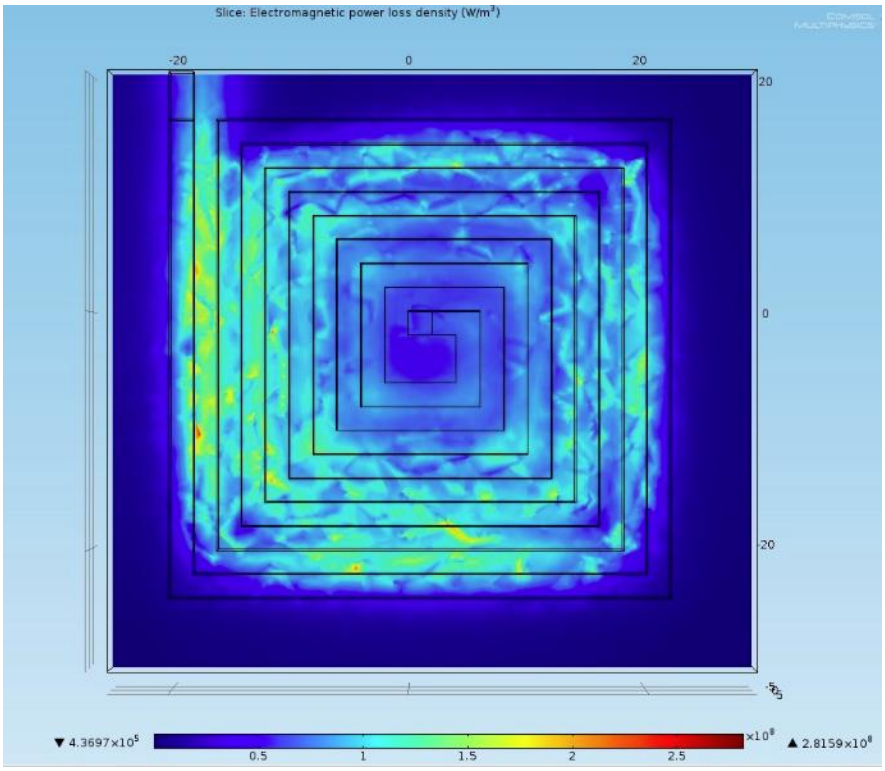

Aluminium coil (N=5, I= 100mA), electromagnetic power loss density: 4.4×10^{5} - 2.8×10^{8}(W/m^{3})

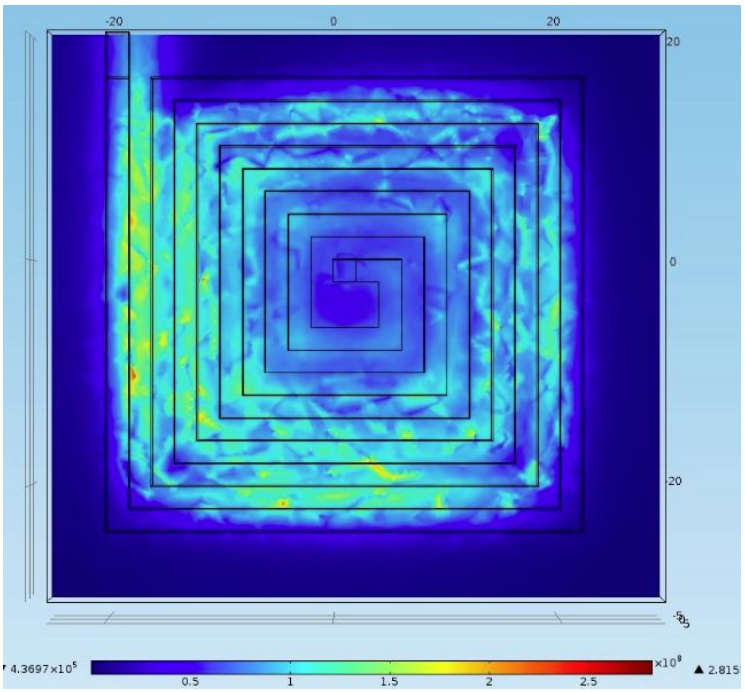

Aluminium coil (N=5, I= 100mA), resistive loss density: 4.4×10^{5} - 2.8×10^{8}(W/m^{3})

Appendix 2

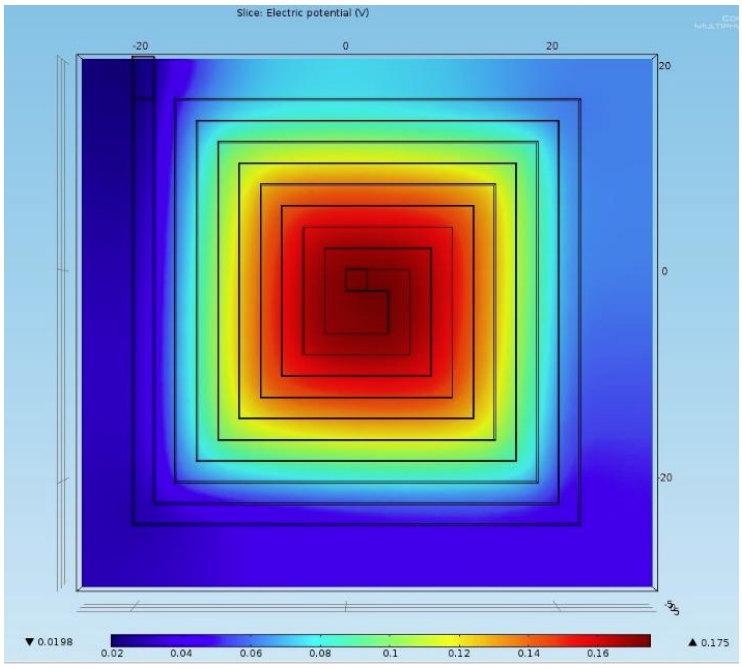

Aluminium coil: Electric potential: 20- 160mV

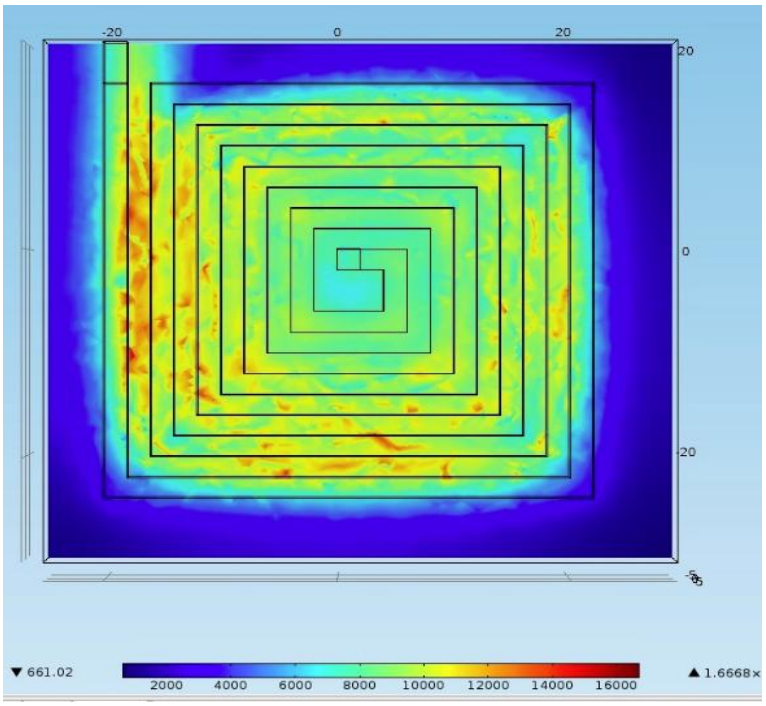

Aluminium coil: Current density norm: 6000 - 16000

Appendix 3

Phase Lock Loop (PLL) MM74HCT4046A [136]

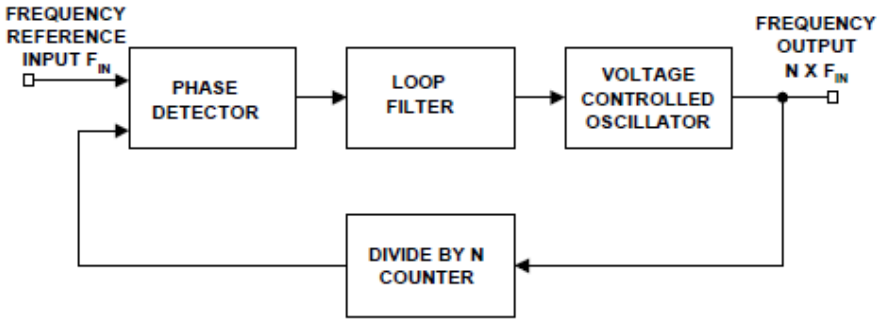

(a)

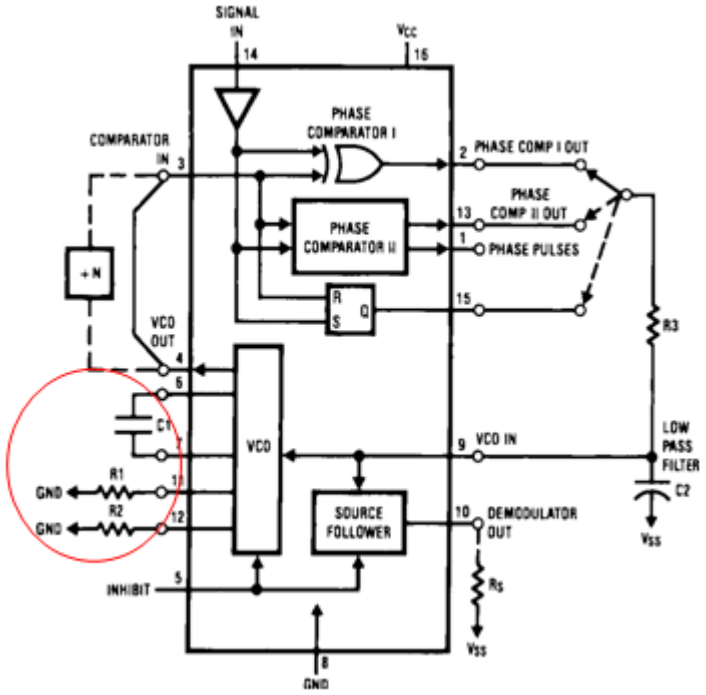

(b)

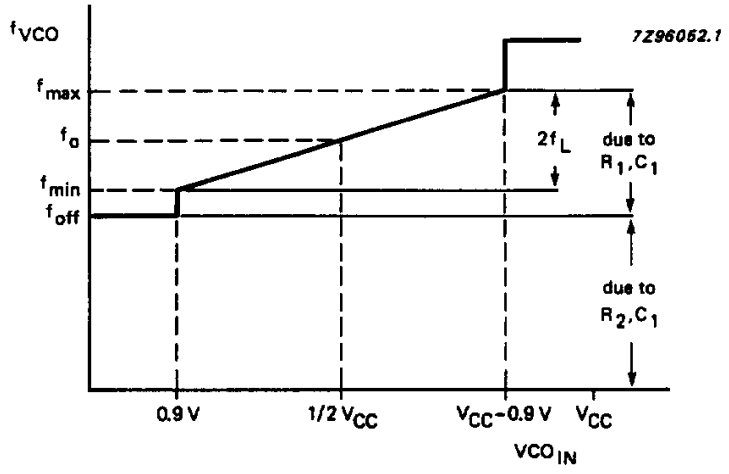

(c)

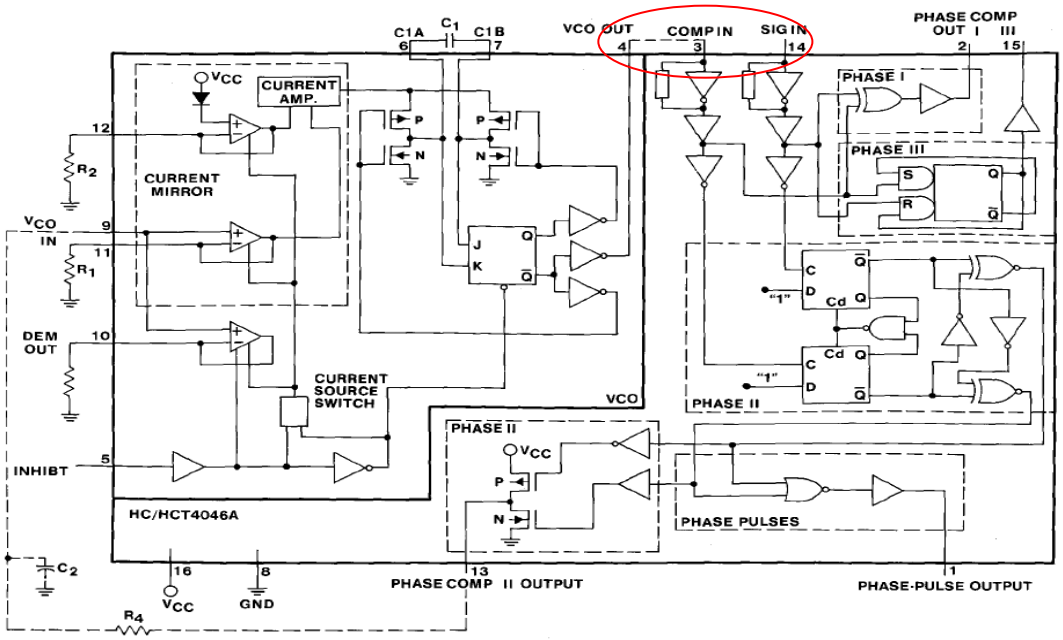

(d)

a PLL block diagram, b block diagram of PLL with phase Comparator II [136], c VCO frequency characteristics without offset (f_0 = centre frequency), d HCT4046A functional block diagram [140-141]

Phase Comparator II

According to the PLL IC 74HC/HCT4046A Data sheet [140]

This detector consists of two flip-flops and some gating logic, a three-state output and phase comparator pulse output (PCP_{OUT}), as shown in the Figure b and d. This comparator acts only on the positive edges of the input signals and is thus independent of signal duty cycle.

Phase comparator II operates in such a way as to force the PLL into lock with zero phase difference between the VCO output and the signal input positive waveform edges.

When the PLL is out of lock the VCO will be running either slower or faster than the signal input. If it is running slower, the phase detector will see more signals rising edges, so the output of the phase comparator will be HIGH most of the time, raising the VCO's frequency. Conversely, if the VCO is running faster the signal the output of the detector will be LOW most of the time, and the VCO's output frequency will decrease. While the PLL is locked the output of phase comparator II (PCP_{OUT}) is HIGH. This output can be used to determine when the PLL is in the locked condition.

This detector was selected due to unique characteristics such as:

The PLL lock range ($2f_L$) is the same as the frequency capture range ($2f_C$) and it is independent of the PLL low-pass filter characteristics.

The frequency capture range (2fc) is defined as the frequency range of input signals on which the PLL will lock if it was initially out-of-lock. The frequency lock range (2fL) is defined as the frequency range of input signals on which the loop will stay locked if it was initially in lock.

There is no initial phase difference between two input signals (SIG_{IN} and $COMP_{IN}$).

The PLL lock range (VCO's operating frequency) is determined with the three external components (R_1, R_2, and C_1) shown in the red circle in the image. Choosing the right value for these components is one of the challenges for designing this circuit as there are lots of limitations which needs to be considered. Some of these rules are illustrated in Table 1.

Fig. 4.24 provides logarithmic graphs for characterizing and selecting the PLL parameters for a specific centre frequency. These are the most significant diagrams for calibrating and controlling the circuit by defining and setting the values for PLL components, which leads to determining the frequency lock range.

3 KΩ < R1,R2 < 300 KΩ
(R1 | | R2) > 2.7 KΩ
R1,R2 >10 KΩ
C1 > 100 pF

Table 1

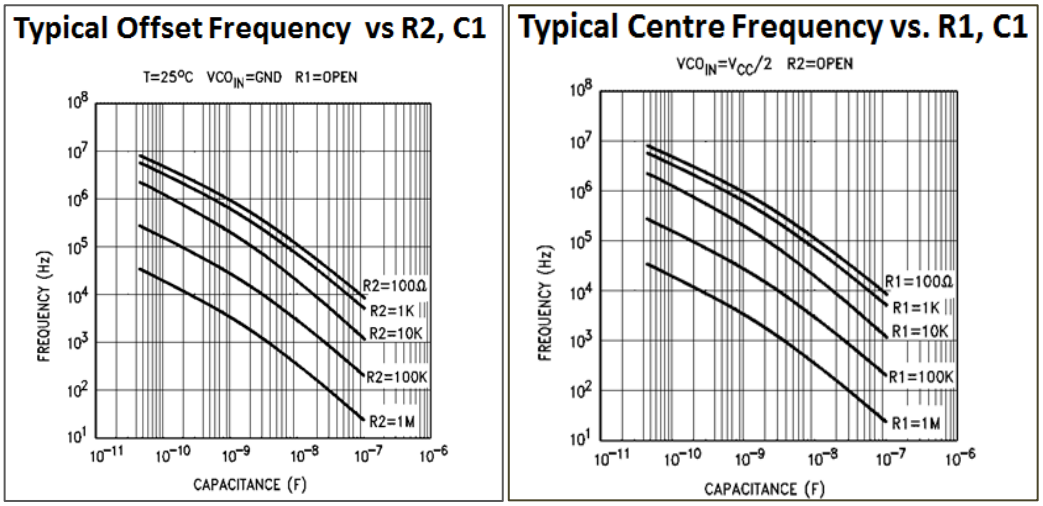

PLL IC characterization [139]

Appendix 4

Diagrams for obtaning the PLL components [141]

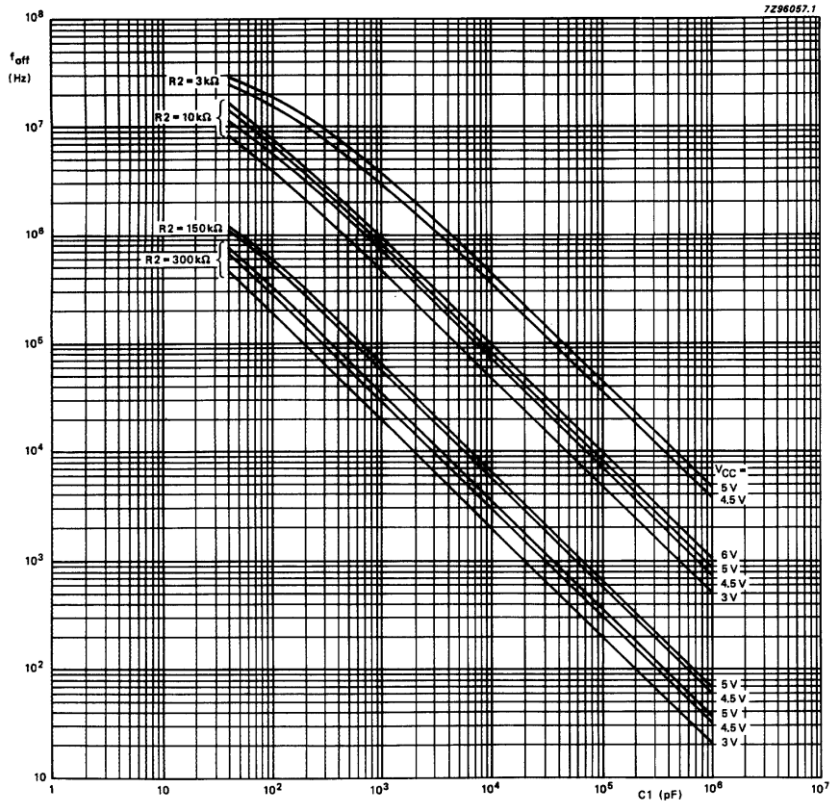

f_{offset} vs. C_1

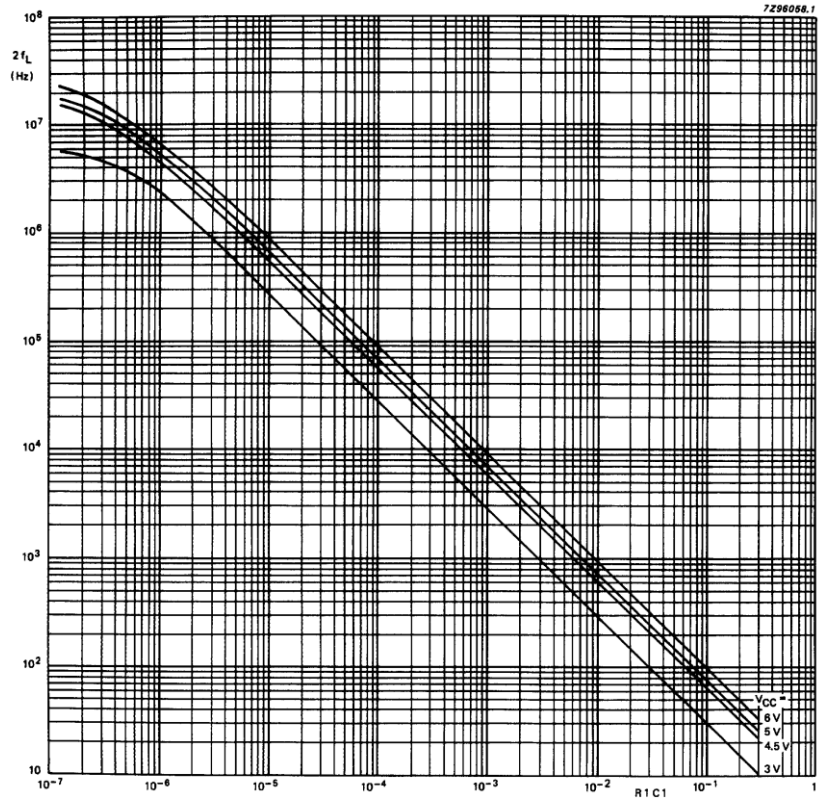

$2f_L$ vs. $R_1.C_1$

Appendix 5

PLL-resonance Circuit Measurements

Lock Range Measurment

Fo (MHz)	FL (MHz)	Foffset (MHz)	C1*R1	If R2 =3 KΩ		If R2 =10 KΩ		Rule 1: (R1 II R2) > 2.7 KΩ		Rule 2: 3 < (R1 + R2)< 300 KΩ		Q Factor
				C1 (pF) >100	R1 (KΩ)	C1 (pF) >100	R1 (KΩ)	R2 =3 KΩ	R2 =10 KΩ	R2 =3 KΩ	R2 =10 KΩ	
7.5	0.5	6.7	5.89E-06	340	17	80	74	2.56	8.80	20.30	83.60	7.50
7.5	0.4	6.86	7.36E-06	330	22	78	95	2.64	9.04	25.32	104.51	9.37
7.5	0.3	7.02	9.81E-06	320	31	76	129	2.73	9.28	33.69	139.35	12.50
7.5	0.2	7.18	1.47E-05	310	47	74	199	2.82	9.52	50.44	209.06	18.75
7.5	0.1	7.34	2.94E-05	301	98	72	408	2.91	9.76	100.72	418.22	37.50
7.4	0.7	6.28	4.21E-06	371	11	86	49	2.37	8.30	14.33	58.85	5.29
7.4	0.5	6.6	5.89E-06	347	17	81	72	2.55	8.79	19.95	82.36	7.40
7.4	0.3	6.92	9.81E-06	326	30	77	127	2.73	9.27	33.10	137.26	12.33
7.4	0.2	7.08	1.47E-05	316	47	75	196	2.82	9.51	49.56	205.92	18.50
7.2	**0.196**	**6.8864**	**1.5E-05**	**328**	**46**	**78**	**194**	**2.82**	**9.51**	**48.78**	**203.71**	**18.37**
5.09	0.41	4.434	7.18E-06	592	12	128	56	2.41	8.49	15.14	66.15	6.21
5.36	0.4	4.72	7.36E-06	544	14	119	62	2.46	8.61	16.53	71.79	6.70
5.36	0.3	4.88	9.81E-06	520	19	115	86	2.59	8.95	21.86	95.57	8.93
5.36	0.2	5.04	1.47E-05	498	30	111	133	2.72	9.30	32.54	143.15	13.40
5.09	0.1	4.93	2.94E-05	513	57	113	260	2.85	9.63	60.36	269.70	25.45
8.06	0.8	6.78	3.68E-06	335	11	79	47	2.36	8.23	13.98	56.63	5.04
8.06	0.5	7.26	5.89E-06	306	19	73	81	2.60	8.90	22.26	90.63	8.06
8.06	0.3	7.58	9.81E-06	289	34	70	141	2.76	9.34	37.01	151.14	13.43
5.472	0.5	4.672	5.89E-06	552	11	121	49	2.34	8.30	13.68	58.86	5.47
5.472	0.4	4.832	7.36E-06	527	14	116	63	2.47	8.64	16.96	73.46	6.84
5.472	0.3	4.992	9.81E-06	505	19	112	88	2.60	8.98	22.44	97.81	9.12
5.472	0.2	5.152	1.47E-05	484	30	108	137	2.73	9.32	33.42	146.52	13.68
5.472	0.1	5.312	2.94E-05	464	63	104	283	2.86	9.66	66.39	292.69	27.36
2.75	0.7	1.63	4.21E-06	2258	2	399	11	1.15	5.13	4.86	20.55	1.96
2.75	0.6	1.79	4.91E-06	1992	2	358	14	1.35	5.78	5.46	23.69	2.29
2.75	0.5	1.95	5.89E-06	1777	3	325	18	1.57	6.44	6.31	28.10	2.75
2.75	0.4	2.11	7.36E-06	1599	5	297	25	1.82	7.12	7.60	34.75	3.44
2.75	0.3	2.27	9.81E-06	1450	7	274	36	2.08	7.82	9.77	45.86	4.58
2.75	0.2	2.43	1.47E-05	1323	11	253	58	2.36	8.53	14.12	68.12	6.87
2.75	0.1	2.59	2.94E-05	1215	24	236	125	2.67	9.26	27.23	134.97	13.75

PLL components selection based on the known resonance frequency and the given frequency lock range
Each row represents one sensor design (F_0= Center frequency, F_L= Half of frequency lock range)

Appendix 6

PLL-resonance Circuit Measurements

Reverse Lock Range Measurment

C_r (F)	F_o (MHz)	C1 (pF)	R1 (KΩ)	R2 (KΩ)	C1*R1	F_L (MHz)	F_{offset} (MHz)	Fmax/Fmin	Rule 1: (R1 II R2) > 2.7 KΩ	Rule 2: 3 < (R1 + R2) < 300 KΩ	Rule 3: R2/R1 <0.1	Q= f0/(f2 – f1)	Q=(1/R)×√L/C
4.7E-11	7.5	101	56	10	5.656E-06	**0.530**	6.652	1.152	8.48	66.00	0.18	7.07	4.38
4.7E-11	7.5	120	47	10	0.00000564	**0.532**	6.649	1.153	8.25	57.00	0.21	7.05	4.38
4.7E-11	7.5	150	39	10	0.00000585	**0.513**	6.680	1.147	7.96	49.00	0.26	7.32	4.38
4.7E-11	7.5	220	33	10	0.00000726	**0.413**	6.839	1.117	7.67	43.00	0.30	9.08	4.38
4.7E-11	7.5	270	10	10	0.0000027	**1.111**	5.723	1.348	5.00	20.00	1.00	3.38	4.38
4.7E-11	7.5	390	10	10	0.0000039	**0.769**	6.270	1.228	5.00	20.00	1.00	4.88	4.38
4.7E-11	7.5	470	10	10	0.0000047	**0.638**	6.479	1.186	5.00	20.00	1.00	5.88	4.38
4.7E-11	7.5	560	10	10	0.0000056	**0.536**	6.643	1.154	5.00	20.00	1.00	7.00	4.38
4.7E-11	7.3	220	89	3	0.00001958	**0.153**	7.055	1.043	2.90	92.00	0.03	23.83	4.38
4.7E-11	7.3	220	56	3	0.00001232	**0.243**	6.911	1.069	2.85	59.00	0.05	14.99	4.38
4.7E-11	7.5	270	50	3	0.0000135	**0.222**	7.145	1.061	2.83	53.00	0.06	16.88	4.38
4.7E-11	7.5	390	33	5.6	0.00001287	**0.233**	7.127	1.064	4.79	38.60	0.17	16.09	4.38
4.7E-11	7.5	470	47	4.7	0.00002209	**0.136**	7.283	1.037	4.27	51.70	0.10	27.62	4.38
4.7E-11	7.5	470	39	4.7	0.00001833	**0.164**	7.238	1.045	4.19	43.70	0.12	22.92	4.38
4.5E-11	7.5	470	10	5.6	0.0000047	**0.638**	6.479	1.186	3.59	15.60	0.56	5.88	4.47
4.5E-11	7.5	470	5.6	5.6	2.632E-06	**1.139**	5.677	1.358	2.80	11.20	1.00	3.29	4.47
4.5E-11	7.4	470	10	10	0.0000047	0.638	6.379	1.189	5.00	20.00	1.00	5.80	4.47
4.5E-11	7.4	470	10	5	0.0000047	**0.638**	6.379	1.189	3.33	15.00	0.50	5.80	4.47
4.5E-11	7.5	390	20	5.6	0.0000078	0.384	6.885	1.108	4.38	25.60	0.28	9.75	4.47
4.5E-11	7.2	390	33	10	0.00001287	**0.233**	6.827	1.067	7.67	43.00	0.30	15.45	4.47
4.5E-11	7.4	390	33	33	0.00001287	**0.233**	7.027	1.065	16.50	66.00	1.00	15.88	4.47
4.5E-11	7.2	220	33	33	0.00000726	**0.413**	6.539	1.122	16.50	66.00	1.00	8.72	4.47
4.5E-11	7.2	156	33	33	5.148E-06	**0.583**	6.268	1.176	16.50	66.00	1.00	6.18	4.47
4.5E-11	7.18	390	33	3	0.00001287	**0.233**	6.807	1.067	2.75	36.00	0.09	15.41	4.47
4.5E-11	7.18	220	33	3	0.00000726	**0.413**	6.519	1.122	2.75	36.00	0.09	8.69	4.47
4.5E-11	7.18	390	33	5.6	0.00001287	**0.233**	6.807	1.067	4.79	38.60	0.17	15.41	4.47
4.5E-11	7.18	220	33	5.6	0.00000726	**0.413**	6.519	1.122	4.79	38.60	0.17	8.69	4.47
4.5E-11	7.18	150	33	5.6	0.00000495	**0.606**	6.211	1.184	4.79	38.60	0.17	5.93	4.47
4.5E-11	7.15	220	56	5.6	0.00001232	**0.243**	6.761	1.070	5.09	61.60	0.10	14.69	4.47
4.5E-11	7.15	150	56	5.6	0.0000084	**0.357**	6.579	1.105	5.09	61.60	0.10	10.01	4.47
4.7E-11	7.2	270	56	4.7	0.00001512	0.198	6.883	1.057	4.34	60.70	0.08	18.15	4.38
8.2E-11	5.2	220	56	5.6	0.00001232	**0.243**	4.811	1.098	5.09	61.60	0.10	10.68	3.31
8.2E-11	5.2	390	56	5.6	0.00002184	**0.137**	4.980	1.054	5.09	61.60	0.10	18.93	3.31
8.2E-11	5.2	390	56	4.7	0.00002184	**0.137**	4.980	1.054	4.34	60.70	0.08	18.93	3.31
1.01E-10	5.2	220	56	4.7	0.00001232	0.243	4.811	1.098	4.34	60.70	0.08	10.68	2.99
1.01E-10	5.2	270	56	4.7	0.00001512	0.198	4.883	1.079	4.34	60.70	0.08	13.11	2.99
1.01E-10	5.2	270	56	4.3	0.00001512	0.198	4.883	1.079	3.99	60.30	0.08	13.11	2.99
1.01E-10	5.2	250	56	4.7	0.000014	0.214	4.857	1.086	4.34	60.70	0.08	12.14	2.99
4.7E-11	7.1	220	56	4.7	0.00001232	0.2434	6.710525	1.071	4.34	60.70	0.08	14.58	4.38
4.7E-11	7.1	270	56	4.3	0.00001512	0.198	6.783	1.057	3.99	60.30	0.08	17.90	4.38

Determining sensor parameters (f_0, F_{offset}, Q) and predicting the successful design based on the reverse frequency measurement, giving the PLL components first

Appendix 7

GMR sensor circuit diagram

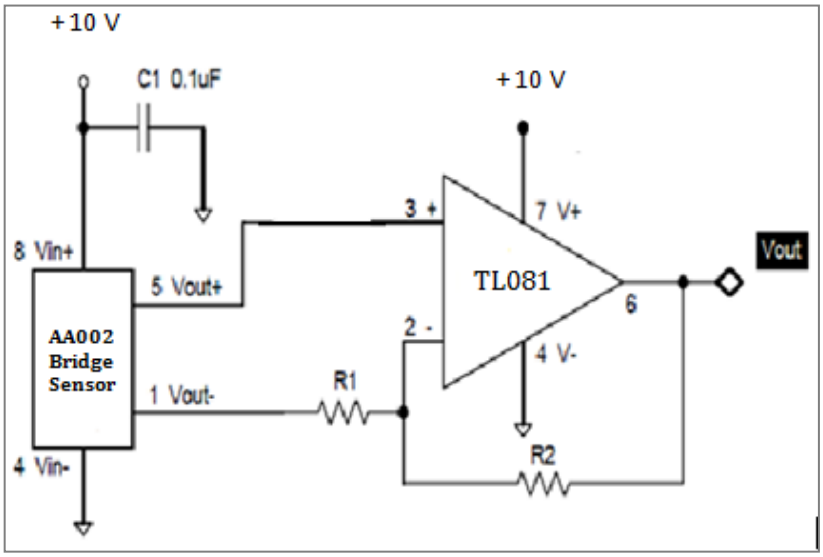

Appendix 8

Result table of Magnetite test with 2.7 MHz circuit

1 mg at 0.13 mm distance		
Actual	Measured	Difference (Hz)
2.756660	2.755345	1065
2.756620	2.755150	1220
2.756455	2.755190	1015
2.756510	2.755155	1105
2.756380	2.755056	1074
2.756240	2.755190	1050
2.756263	2.755119	1144
2.756210	2.755007	1203
2.756194	2.755057	1137
	STND	69.43
	Average	1112.54

2 mg at 0.13 mm distance		
Actual	Measured	Difference (Hz)
2.756690	2.755136	1304
2.756520	2.754830	1440
2.756440	2.754800	1390
2.756390	2.754730	1410
2.756395	2.754850	1295
2.756345	2.754999	1346
2.756275	2.754991	1284
2.756289	2.754882	1407
2.756214	2.754768	1446
	STND	63.24
	Average	1369.11

3 mg at 0.13 mm distance		
Actual	Measured	Difference (Hz)
2.756600	2.754819	1531
2.756540	2.754800	1490
2.756544	2.754820	1474
2.756420	2.754645	1525
2.756465	2.754680	1535
2.756392	2.754863	1529
2.756410	2.754941	1469
2.756318	2.754882	1436
2.756257	2.754694	1563
	STND	27.30
	Average	1505.78

4 mg at 0.13 mm distance		
Actual	Measured	Difference (Hz)
2.756500	2.754500	1750
2.756530	2.754630	1650
2.756530	2.754600	1680
2.756420	2.754350	1820
2.756440	2.754380	1810
2.756465	2.754781	1684
2.756370	2.754637	1733
2.756328	2.754576	1752
2.756330	2.754526	1804
	STND	61.71
	Average	1742.56

Result table of figure 6.10 with universal frequency counter

Distance (cm)	0 cm							0.5 cm						1 cm						
Magnetite (mg)	0	0.3	0.7	1	2	3	4	Glass	0.3 mg	1 mg	2 mg	3 mg	4 mg	Glass	0.3	0.7	1 mg	2 mg	3 mg	4 mg
Δf (Hz)	189	375	1703	1905	2306	2658	2737	100	412	1500	1816	2231	2569	40	206	538	1205	1260	1391	1862
	187	393	903	1915	2331	2689	3055	203	152	1686	1911	2233	2722	22	254	238	1165	1329	1530	2111
	200	271	1253	1928	2179	2612	2746	230	124	1670	2010	2312	2536	60	286	657	1170	1250	1700	1765
	237	262	1125	1781	2201	2530	2654	136	374	1700	2000	2389	2511	80	197	489	1198	1353	1554	1815
	164	500	1624	1800	2361	2437	2811	40	401	1330	1836	2266	2581	120	187	450	1010	1420	1624	2300
	176	380	1425	1581	2052	2564	2663	150	360	1350	1950	2049	2617	100	52	695	980	1276	1390	2063
	190	275	1036	1680	1927	2613	3006	161	112	1410	1815	1996	2538	78	89	852	1200	1232	1430	1820
	168	412	1212	1696	2165	2465	2714	194	315	1524	1980	2140	2610	94	164	780	1047	1324	1557	1778
Average	189	359	1285	1786	2190	2571	2798	152	281	1521	1915	2202	2586	74	179	587	1122	1306	1522	1939
STDV	23	83	280	127	147	89	152	61	130	151	83	132	66	32	78	199	94	63	112	195

Distance (cm)	2 cm							3 cm						
Magnetite (mg)	Glass	0.3 mg	0.7	1 mg	2 mg	3 mg	4 mg	Glass	0.3 mg	0.7	1 mg	2 mg	3 mg	4 mg
Δf (Hz)	20	165	332	515	704	780	912	40	124	192	250	160	230	580
	70	85	320	478	562	589	1254	18	12	162	177	190	186	574
	56	98	410	536	647	713	948	70	56	142	212	149	192	236
	48	62	245	510	663	697	802	30	38	102	127	163	292	244
	55	79	550	486	500	526	721	14	84	212	182	305	316	289
	81	143	346	440	583	580	805	27	62	98	173	307	190	220
	43	105	451	460	575	590	784	76	43	75	105	176	195	350
	78	68	368	580	598	665	865	51	58	83	150	231	304	279
Average	56	101	378	501	604	643	886	41	60	133	172	210	238	347
STDV	20	36	93	45	65	85	165	23	33	52	46	64	57	148

Result table of figure 6.11 (b), Based on TF930 frequency meter

Appendix 9

Black Circuit (inductor) test with TF930 frequency counter at 2.7 MHz (Fig. 6.12)

Time (Sec)	Actual Reading Output frequency (MHz)	f_x	Frequency Number	Δf (10 sec)	
10	2.756948487e+6Hz	2.756948	2.756948		
20	2.756948463e+6Hz	2.756948	2.756948		
30	2.756948473e+6Hz	2.756948	2.756948		
40	2.756944161e+6Hz	2.756944	2.756944		
50	2.756943589e+6Hz	2.756943	2.756943		
60	2.756938891e+6Hz	2.756938	2.756938		
70	2.756938520e+6Hz	2.756938	2.756938		
80	2.756943757e+6Hz	2.756943	2.756943		
90	2.756946598e+6Hz	2.756946	2.756946		
100	2.756940896e+6Hz	2.756940	2.756940		
110	2.756938002e+6Hz	2.756938	2.756938		
120	2.756940019e+6Hz	2.756940	2.756940		
130	2.756936254e+6Hz	2.756936	2.756936		
140	2.756934013e+6Hz	2.756934	2.756934		
150	2.756943600e+6Hz	2.756943	2.756943		
160	2.756936946e+6Hz	2.756936	2.756936		
170	2.756937678e+6Hz	2.756937	2.756937		
180	2.756935546e+6Hz	2.756935	2.756935		
190	2.756937876e+6Hz	2.756937	2.756937		
200	2.756928488e+6Hz	2.756928	2.756928	1.62 mg added	
210	2.756929011e+6Hz	2.756929	2.756929		
220	2.755967525e+6Hz	2.755967	2.755967	962	
230	2.755832946e+6Hz	2.755832	2.755832	1097	
240	2.755777554e+6Hz	2.755777	2.755777	1152	
250	2.755753893e+6Hz	2.755753	2.755753	1176	1 min Ave.
260	2.755727652e+6Hz	2.755727	2.755727	1202	
270	2.755707819e+6Hz	2.755707	2.755707	1222	1196
280	2.755696663e+6Hz	2.755696	2.755696	1233	
290	2.755688261e+6Hz	2.755688	2.755688	1241	
300	2.755680446e+6Hz	2.755680	2.755680	1249	
310	2.755659942e+6Hz	2.755659	2.755659	1270	
320	2.755656870e+6Hz	2.755656	2.755656	1273	
330	2.755650617e+6Hz	2.755650	2.755650	1279	
340	2.755645927e+6Hz	2.755645	2.755645	1284	
350	2.755712176e+6Hz	2.755712	2.755712	1217	
360	2.756966551e+6Hz	2.756966	2.756966		
370	2.757028267e+6Hz	2.757028	2.757028		

Time (Sec)	Actual Reading Output frequency (MHz)	f_x	Frequency Number	Δf (10 sec)	
380	2.757037950e+6Hz	2.757037	2.757037		
390	2.757053879e+6Hz	2.757053	2.757053		
400	2.757054345e+6Hz	2.757054	2.757054		
410	2.757057492e+6Hz	2.757057	2.757057		
420	2.757063173e+6Hz	2.757063	2.757063		
430	2.757058740e+6Hz	2.757058	2.757058		
440	2.757063476e+6Hz	2.757063	2.757063		
450	2.757061445e+6Hz	2.757061	2.757061		
460	2.757067372e+6Hz	2.757067	2.757067		
470	2.757059512e+6Hz	2.757059	2.757059		
480	2.757061568e+6Hz	2.757061	2.757061		
490	2.757065270e+6Hz	2.757065	2.757065		
500	2.757063235e+6Hz	2.757063	2.757063		
510	2.757069716e+6Hz	2.757069	2.757069		
520	2.757060080e+6Hz	2.757060	2.757060	1.24 mg added	
530	2.757033909e+6Hz	2.757033	2.757033		
540	2.756303984e+6Hz	2.756303	2.756303	757	
550	2.756128819e+6Hz	2.756128	2.756128	932	
560	2.756110017e+6Hz	2.756110	2.756110	950	
570	2.756100990e+6Hz	2.756100	2.756100	933	
580	2.756089464e+6Hz	2.756089	2.756089	971	1 min Ave.
590	2.756074691e+6Hz	2.756074	2.756074	986	
600	2.756076038e+6Hz	2.756076	2.756076	984	921.5
610	2.756063315e+6Hz	2.756063	2.756063	997	
620	2.756053054e+6Hz	2.756053	2.756053	1007	
630	2.756056305e+6Hz	2.756056	2.756056	1004	
640	2.756048420e+6Hz	2.756048	2.756048	1012	
650	2.756048096e+6Hz	2.756048	2.756048	1012	
660	2.756306517e+6Hz	2.756306	2.756306		
670	2.757028372e+6Hz	2.757028	2.757028		
680	2.757042732e+6Hz	2.757042	2.757042		
690	2.757041991e+6Hz	2.757041	2.757041		
700	2.757055745e+6Hz	2.757055	2.757055		
710	2.757055335e+6Hz	2.757055	2.757055		
720	2.757058783e+6Hz	2.757058	2.757058		
730	2.757055038e+6Hz	2.757055	2.757055		
740	2.757059678e+6Hz	2.757059	2.757059		

Appendix 9

Time (Sec)	Actual Reading Output frequency (MHz)	f_x	Frequency Number	Δf	
750	2.757058683e+6Hz	2.757058	2.757058		
760	2.757042015e+6Hz	2.757042	2.757042	700 µg added	
770	2.756700839e+6Hz	2.756700	2.756700		
780	2.756434680e+6Hz	2.756434	2.756434	608	
790	2.756423736e+6Hz	2.756423	2.756423	619	1 min Ave.
800	2.756408600e+6Hz	2.756408	2.756408	634	
810	2.756402767e+6Hz	2.756402	2.756402	640	631
820	2.756401865e+6Hz	2.756401	2.756401	641	
830	2.756397950e+6Hz	2.756397	2.756397	645	
840	2.756397520e+6Hz	2.756397	2.756397	645	
850	2.756385089e+6Hz	2.756385	2.756385	657	
860	2.756387401e+6Hz	2.756387	2.756387	655	
870	2.756389563e+6Hz	2.756389	2.756389	653	
880	2.756397215e+6Hz	2.756397	2.756397	645	
890	2.756390346e+6Hz	2.756390	2.756390	652	
900	2.756593531e+6Hz	2.756593	2.756593		
910	2.757081238e+6Hz	2.757081	2.757081		
920	2.757097246e+6Hz	2.757097	2.757097		
930	2.757107475e+6Hz	2.757107	2.757107		
940	2.757109023e+6Hz	2.757109	2.757109		
950	2.757115694e+6Hz	2.757115	2.757115		
960	2.757124373e+6Hz	2.757124	2.757124		
970	2.757115740e+6Hz	2.757115	2.757115		
980	2.757119227e+6Hz	2.757119	2.757119		
990	2.757120079e+6Hz	2.757120	2.757120		
1000	2.757122276e+6Hz	2.757122	2.757122		
1010	2.757119585e+6Hz	2.757119	2.757119		
1020	2.757123495e+6Hz	2.757123	2.757123		
1030	2.757020187e+6Hz	2.757020	2.757020	300 µg added	
1040	2.756695057e+6Hz	2.756695	2.756695		
1050	2.756599393e+6Hz	2.756599	2.756599	421	
1060	2.756545442e+6Hz	2.756545	2.756545	475	
1070	2.756522143e+6Hz	2.756522	2.756522	498	
1080	2.756520153e+6Hz	2.756520	2.756520	500	
1090	2.756514406e+6Hz	2.756514	2.756514	506	
1100	2.756510593e+6Hz	2.756510	2.756510	510	1 min Ave.
1110	2.756518034e+6Hz	2.756518	2.756518	502	
1120	2.756515337e+6Hz	2.756515	2.756515	505	485
1130	2.756512639e+6Hz	2.756512	2.756512	508	

Time (Sec)	Actual Reading Output frequency (MHz)	f_x	Frequency Number	Δf	
1140	2.756519651e+6Hz	2.756519	2.756519	501	
1150	2.756514716e+6Hz	2.756514	2.756514	506	
1160	2.756520119e+6Hz	2.756520	2.756520	500	
1170	2.756929391e+6Hz	2.756929	2.756929		
1180	2.756931782e+6Hz	2.756931	2.756931		
1190	2.756922436e+6Hz	2.756922	2.756922		
1200	2.756919757e+6Hz	2.756919	2.756919		
1210	2.756928875e+6Hz	2.756928	2.756928		
1220	2.756914443e+6Hz	2.756914	2.756914		
1230	2.756910585e+6Hz	2.756910	2.756910		
1240	2.756911279e+6Hz	2.756911	2.756911		
1250	2.756899763e+6Hz	2.756899	2.756899		
1260	2.756902441e+6Hz	2.756902	2.756902		
1270	2.756901290e+6Hz	2.756901	2.756901		
1280	2.756899001e+6Hz	2.756899	2.756899		
1290	2.756894646e+6Hz	2.756894	2.756894		
1300	2.756898763e+6Hz	2.756898	2.756898		
1310	2.756896152e+6Hz	2.756896	2.756896		
1320	2.756894720e+6Hz	2.756894	2.756894		
1330	2.756886462e+6Hz	2.756886	2.756886		
1340	2.756887150e+6Hz	2.756887	2.756887		
1350	2.756892758e+6Hz	2.756892	2.756892		
1360	2.756892174e+6Hz	2.756892	2.756892		
1370	2.756878773e+6Hz	2.756878	2.756878	480 µg added	
1380	2.756506280e+6Hz	2.756506	2.756506		
1390	2.756427163e+6Hz	2.756427	2.756427	451	
1400	2.756423546e+6Hz	2.756423	2.756423	455	
1410	2.756416227e+6Hz	2.756416	2.756416	462	
1420	2.756410481e+6Hz	2.756410	2.756410	468	
1430	2.756413876e+6Hz	2.756413	2.756413	465	
1440	2.756404015e+6Hz	2.756404	2.756404	474	
1450	2.756405449e+6Hz	2.756405	2.756405	473	1 min Ave.
1460	2.756405477e+6Hz	2.756405	2.756405	473	
1470	2.756409645e+6Hz	2.756409	2.756409	469	465
1480	2.756402581e+6Hz	2.756402	2.756402	476	
1490	2.756401803e+6Hz	2.756401	2.756401	477	
1500	2.756392288e+6Hz	2.756392	2.756392	486	
1510	2.756385923e+6Hz	2.756385	2.756385	493	
1520	2.756387155e+6Hz	2.756387	2.756387	491	

Appendix 9

Time (Sec)	Actual Reading Output frequency (MHz)	f_x	Frequency Number	Δf	
1530	2.756377733e+6Hz	2.756377	2.756377	501	
1540	2.756381354e+6Hz	2.756381	2.756381	497	
1550	2.756560432e+6Hz	2.756560	2.756560		
1560	2.756885901e+6Hz	2.756885	2.756885		
1570	2.756892389e+6Hz	2.756892	2.756892		
1580	2.756895159e+6Hz	2.756895	2.756895		
1590	2.756885807e+6Hz	2.756885	2.756885		
1600	2.756885708e+6Hz	2.756885	2.756885		
1610	2.756888860e+6Hz	2.756888	2.756888		
1620	2.756894519e+6Hz	2.756894	2.756894		
1630	2.756893345e+6Hz	2.756893	2.756893		
1640	2.756894051e+6Hz	2.756894	2.756894		
1650	2.756907166e+6Hz	2.756907	2.756907		
1660	2.756906397e+6Hz	2.756906	2.756906		
1670	2.756904416e+6Hz	2.756904	2.756904		
1680	2.756906570e+6Hz	2.756906	2.756906		
1690	2.756907043e+6Hz	2.756907	2.756907		
1700	2.756906033e+6Hz	2.756906	2.756906		
1710	2.756905914e+6Hz	2.756905	2.756905		
1720	2.756908923e+6Hz	2.756908	2.756908		
1730	2.756902638e+6Hz	2.756902	2.756902		
1740	2.756905989e+6Hz	2.756905	2.756905		
1750	2.756905100e+6Hz	2.756905	2.756905		
1760	2.756908819e+6Hz	2.756908	2.756908		
1770	2.756900757e+6Hz	2.756900	2.756900		
1780	2.756903699e+6Hz	2.756903	2.756903	90 µg added	
1790	2.756775127e+6Hz	2.756775	2.756775		
1800	2.756646343e+6Hz	2.756646	2.756646	257	
1810	2.756645675e+6Hz	2.756645	2.756645	258	
1820	2.756638052e+6Hz	2.756638	2.756638	265	
1830	2.756633496e+6Hz	2.756633	2.756633	270	
1840	2.756631664e+6Hz	2.756631	2.756631	272	1 min Ave.
1850	2.756624374e+6Hz	2.756624	2.756624	279	
1860	2.756624878e+6Hz	2.756624	2.756624	279	266.83
1870	2.756623752e+6Hz	2.756623	2.756623	280	
1880	2.756626710e+6Hz	2.756626	2.756626	277	
1890	2.756632421e+6Hz	2.756632	2.756632	271	
1900	2.756625714e+6Hz	2.756625	2.756625	278	
1910	2.756623502e+6Hz	2.756623	2.756623	280	

Time (Sec)	Actual Reading Output frequency (MHz)	f_x	Frequency Number	Δf
1920	2.756614483e+6Hz	2.756614	2.756614	289
1930	2.756617577e+6Hz	2.756617	2.756617	286
1940	2.756615436e+6Hz	2.756615	2.756615	288
1950	2.756610558e+6Hz	2.756610	2.756610	293
1960	2.756609761e+6Hz	2.756609	2.756609	294
1970	2.756602264e+6Hz	2.756602	2.756602	301
1980	2.756604082e+6Hz	2.756604	2.756604	299
1990	2.756600870e+6Hz	2.756600	2.756600	303
2000	2.756600623e+6Hz	2.756600	2.756600	

The third Column (f_x) is the function for changing the output reading format (2nd Column) to number and the 4th column is the output frequency in the number format with 6 digits.

The last column is the frequency difference between output without sample and the output after applying the sample. It means that each value in this column is the difference between the number besides it (in column 3) and the number before sample addition in the same column.

Appendix 10

Black Circuit (inductor) test with TF930 frequency counter at 2.7 MHz (Fig. 6.14)

Time (Sec)	Actual Reading Output frequency (MHz)	f_x	Frequency Number
10	2.756953916e+6Hz	2.756953	2.756953
20	2.756956258e+6Hz	2.756956	2.756956
30	2.756960749e+6Hz	2.756960	2.756960
40	2.756961623e+6Hz	2.756961	2.756961
50	2.756956818e+6Hz	2.756956	2.756956
60	2.756957827e+6Hz	2.756957	2.756957
70	2.756968288e+6Hz	2.756968	2.756968
80	2.756969655e+6Hz	2.756969	2.756969
90	2.756964340e+6Hz	2.756964	2.756964
100	2.756964660e+6Hz	2.756964	2.756964
110	2.756960695e+6Hz	2.756960	2.756960
120	2.756957085e+6Hz	2.756957	2.756957
130	2.756957098e+6Hz	2.756957	2.756957
140	2.756956136e+6Hz	2.756956	2.756956
150	2.756953302e+6Hz	2.756953	2.756953
160	2.756955430e+6Hz	2.756955	2.756955
170	2.756953109e+6Hz	2.756953	2.756953
180	2.756956116e+6Hz	2.756956	2.756956
190	2.756954637e+6Hz	2.756954	2.756954
200	2.756950311e+6Hz	2.756950	2.756950
210	2.756950722e+6Hz	2.756950	2.756950
220	2.756942827e+6Hz	2.756942	2.756942
230	2.756953580e+6Hz	2.756953	2.756953
240	2.756947482e+6Hz	2.756947	2.756947
250	2.756943032e+6Hz	2.756943	2.756943
260	2.756950132e+6Hz	2.756950	2.756950
270	2.756946073e+6Hz	2.756946	2.756946
280	2.756950397e+6Hz	2.756950	2.756950
290	2.756946320e+6Hz	2.756946	2.756946
300	2.756944624e+6Hz	2.756944	2.756944
310	2.756946864e+6Hz	2.756946	2.756946
320	2.756941551e+6Hz	2.756941	2.756941
330	2.756942951e+6Hz	2.756942	2.756942
340	2.756951159e+6Hz	2.756951	2.756951
350	2.756942259e+6Hz	2.756942	2.756942
360	2.756935375e+6Hz	2.756935	2.756935
370	2.756942761e+6Hz	2.756942	2.756942
380	2.756938041e+6Hz	2.756938	2.756938

Time (Sec)	Actual Reading Output frequency (MHz)	f_x	Frequency Number	Δf (30 sec)
390	2.756940981e+6Hz	2.756940	2.756940	
400	2.756937918e+6Hz	2.756937	2.756937	
410	2.757040000e+6Hz	2.757040	2.757040	
420	2.757031666e+6Hz	2.757031	2.757031	
430	2.757003893e+6Hz	2.757003	2.757003	
440	2.756983994e+6Hz	2.756983	2.756983	
450	2.756965160e+6Hz	2.756965	2.756965	
460	2.756953907e+6Hz	2.756953	2.756953	
470	2.756942997e+6Hz	2.756942	2.756942	
480	2.756943278e+6Hz	2.756943	2.756943	**Cover Glass added**
490	2.756887463e+6Hz	2.756887	2.756887	
500	2.756651487e+6Hz	2.756651	2.756651	
510	2.756595083e+6Hz	2.756595	2.756595	292
520	2.756557941e+6Hz	2.756557	2.756557	94
530	2.756514056e+6Hz	2.756514	2.756514	81
540	2.756490679e+6Hz	2.756490	2.756490	67
550	2.756473905e+6Hz	2.756473	2.756473	41
560	2.756459607e+6Hz	2.756459	2.756459	31
570	2.756447235e+6Hz	2.756447	2.756447	26
580	2.756445255e+6Hz	2.756445	2.756445	14
590	2.756442965e+6Hz	2.756442	2.756442	5
600	2.756433042e+6Hz	2.756433	2.756433	12
610	2.756440062e+6Hz	2.756440	2.756440	
620	2.756443351e+6Hz	2.756443	2.756443	
630	2.756448053e+6Hz	2.756448	2.756448	
640	2.756527409e+6Hz	2.756527	2.756527	
650	2.756646704e+6Hz	2.756646	2.756646	
660	2.756659623e+6Hz	2.756659	2.756659	
670	2.756659928e+6Hz	2.756659	2.756659	
680	2.756651162e+6Hz	2.756651	2.756651	
690	2.756645555e+6Hz	2.756645	2.756645	
700	2.756644423e+6Hz	2.756644	2.756644	
710	2.756647462e+6Hz	2.756647	2.756647	
720	2.756647608e+6Hz	2.756647	2.756647	
730	2.756645089e+6Hz	2.756645	2.756645	
740	2.756642691e+6Hz	2.756642	2.756642	
750	2.756651081e+6Hz	2.756651	2.756651	
760	2.756651826e+6Hz	2.756651	2.756651	

Appendix 10

Time (Sec)	Actual Reading Output frequency (MHz)	f_x	Frequency Number	Δf (30 sec)
770	2.756654507e+6Hz	2.756654	2.756654	
780	2.756658411e+6Hz	2.756658	2.756658	
790	2.756661712e+6Hz	2.756661	2.756661	
800	2.756670057e+6Hz	2.756670	2.756670	
810	2.756671000e+6Hz	2.756671	2.756671	**1.62 mg**
820	2.756675997e+6Hz	2.756675	2.756675	
830	2.755623288e+6Hz	2.755623	2.755623	1203
840	2.755472878e+6Hz	2.755472	2.755472	211
850	2.755412229e+6Hz	2.755412	2.755412	110
860	2.755362412e+6Hz	2.755362	2.755362	98
870	2.755314039e+6Hz	2.755314	2.755314	84
880	2.755278208e+6Hz	2.755278	2.755278	79
890	2.755235639e+6Hz	2.755235	2.755235	83
900	2.755195282e+6Hz	2.755195	2.755195	69
910	2.755166595e+6Hz	2.755166	2.755166	58
920	2.755137443e+6Hz	2.755137	2.755137	64
930	2.755102695e+6Hz	2.755102	2.755102	77
940	2.755060527e+6Hz	2.755060	2.755060	84
950	2.755018378e+6Hz	2.755018	2.755018	70
960	2.754990408e+6Hz	2.754990	2.754990	913
970	2.755903476e+6Hz	2.755903	2.755903	
980	2.756720351e+6Hz	2.756720	2.756720	
990	2.756739165e+6Hz	2.756739	2.756739	
1000	2.756738359e+6Hz	2.756738	2.756738	
1010	2.756741455e+6Hz	2.756741	2.756741	
1020	2.756735099e+6Hz	2.756735	2.756735	
1030	2.756728017e+6Hz	2.756728	2.756728	
1040	2.756728296e+6Hz	2.756728	2.756728	
1050	2.756729441e+6Hz	2.756729	2.756729	
1060	2.756747751e+6Hz	2.756747	2.756747	
1070	2.756739182e+6Hz	2.756739	2.756739	
1080	2.756734104e+6Hz	2.756734	2.756734	
1090	2.756733265e+6Hz	2.756733	2.756733	
1100	2.756729805e+6Hz	2.756729	2.756729	
1110	2.756731197e+6Hz	2.756731	2.756731	
1120	2.756727598e+6Hz	2.756727	2.756727	
1130	2.756727926e+6Hz	2.756727	2.756727	
1140	2.756729240e+6Hz	2.756729	2.756729	

Time (Sec)	Actual Reading Output frequency (MHz)	f_x	Frequency Number	Δf
1150	2.756726870e+6Hz	2.756726	2.756726	
1160	2.756724039e+6Hz	2.756724	2.756724	**1.24 mg**
1170	2.756727337e+6Hz	2.756727	2.756727	
1180	2.756591326e+6Hz	2.756591	2.756591	1085
1190	2.755642912e+6Hz	2.755642	2.755642	949
1200	2.755642736e+6Hz	2.755642	2.755642	6
1210	2.755648530e+6Hz	2.755648	2.755648	37
1220	2.755611226e+6Hz	2.755611	2.755611	83
1230	2.755565553e+6Hz	2.755565	2.755565	65
1240	2.755630375e+6Hz	2.755630	2.755630	65
1250	2.755592358e+6Hz	2.755592	2.755592	71
1260	2.755559322e+6Hz	2.755559	2.755559	59
1270	2.755533893e+6Hz	2.755533	2.755533	
1280	2.755504721e+6Hz	2.755504	2.755504	
1290	2.755463195e+6Hz	2.755463	2.755463	
1300	2.755550418e+6Hz	2.755550	2.755550	
1310	2.755498167e+6Hz	2.755498	2.755498	
1320	2.755475364e+6Hz	2.755475	2.755475	
1330	2.755565235e+6Hz	2.755565	2.755565	
1340	2.756632109e+6Hz	2.756632	2.756632	
1350	2.756675953e+6Hz	2.756675	2.756675	
1360	2.756698393e+6Hz	2.756698	2.756698	
1370	2.756693863e+6Hz	2.756693	2.756693	
1380	2.756699283e+6Hz	2.756699	2.756699	
1390	2.756699415e+6Hz	2.756699	2.756699	
1400	2.756691359e+6Hz	2.756691	2.756691	
1410	2.756694953e+6Hz	2.756694	2.756694	
1420	2.756710959e+6Hz	2.756710	2.756710	
1430	2.756701874e+6Hz	2.756701	2.756701	
1440	2.756692119e+6Hz	2.756692	2.756692	
1450	2.756688236e+6Hz	2.756688	2.756688	
1460	2.756683628e+6Hz	2.756683	2.756683	
1470	2.756791909e+6Hz	2.756791	2.756791	
1480	2.756791000e+6Hz	2.756791	2.756791	
1490	2.756767728e+6Hz	2.756767	2.756767	
1500	2.756753170e+6Hz	2.756753	2.756753	**700 µg Added**
1510	2.756728191e+6Hz	2.756728	2.756728	
1520	2.756146810e+6Hz	2.756146	2.756146	582

Appendix 10

Time (Sec)	Actual Reading Output frequency (MHz)	f_x	Frequency Number	Δf (30 sec)
1530	2.756022884e+6Hz	2.756022	2.756022	30
1540	2.755992751e+6Hz	2.755992	2.755992	61
1550	2.755961730e+6Hz	2.755961	2.755961	55
1560	2.755937021e+6Hz	2.755937	2.755937	43
1570	2.755918966e+6Hz	2.755918	2.755918	46
1580	2.755891071e+6Hz	2.755891	2.755891	42
1590	2.755876006e+6Hz	2.755876	2.755876	29
1600	2.755862312e+6Hz	2.755862	2.755862	31
1610	2.755845030e+6Hz	2.755845	2.755845	34
1620	2.755828354e+6Hz	2.755828	2.755828	42
1630	2.755803827e+6Hz	2.755803	2.755803	43
1640	2.755785615e+6Hz	2.755785	2.755785	25
1650	2.755778646e+6Hz	2.755778	2.755778	
1660	2.756111356e+6Hz	2.756111	2.756111	
1670	2.756650864e+6Hz	2.756650	2.756650	
1680	2.756707866e+6Hz	2.756707	2.756707	
1690	2.756741541e+6Hz	2.756741	2.756741	
1700	2.756734089e+6Hz	2.756734	2.756734	
1710	2.756727897e+6Hz	2.756727	2.756727	
1720	2.756716309e+6Hz	2.756716	2.756716	
1730	2.756709072e+6Hz	2.756709	2.756709	
1740	2.756718421e+6Hz	2.756718	2.756718	
1750	2.756774600e+6Hz	2.756774	2.756774	
1760	2.756779495e+6Hz	2.756779	2.756779	
1770	2.756767664e+6Hz	2.756767	2.756767	
1780	2.756751383e+6Hz	2.756751	2.756751	
1790	2.756740552e+6Hz	2.756740	2.756740	
1800	2.756731064e+6Hz	2.756731	2.756731	
1810	2.756710637e+6Hz	2.756710	2.756710	**480 µg Added**
1820	2.756701084e+6Hz	2.756701	2.756701	
1830	2.756247723e+6Hz	2.756247	2.756247	579
1840	2.756122984e+6Hz	2.756122	2.756122	183
1850	2.756064590e+6Hz	2.756064	2.756064	88
1860	2.756034872e+6Hz	2.756034	2.756034	52
1870	2.756012251e+6Hz	2.756012	2.756012	42
1880	2.755992773e+6Hz	2.755992	2.755992	29
1890	2.755983894e+6Hz	2.755983	2.755983	16
1900	2.755976870e+6Hz	2.755976	2.755976	7

Time (Sec)	Actual Reading Output frequency (MHz)	f_x	Frequency Number	Δf
1910	2.755960561e+6Hz	2.755960	2.755960	0
1920	2.755949437e+6Hz	2.755949	2.755949	34
1930	2.755926761e+6Hz	2.755926	2.755926	0
1940	2.755914376e+6Hz	2.755914	2.755914	15
1950	2.755911238e+6Hz	2.755911	2.755911	
1960	2.755893947e+6Hz	2.755893	2.755893	
1970	2.755923803e+6Hz	2.755923	2.755923	
1980	2.756580382e+6Hz	2.756580	2.756580	
1990	2.756618951e+6Hz	2.756618	2.756618	
2000	2.756628857e+6Hz	2.756628	2.756628	
2010	2.756666793e+6Hz	2.756666	2.756666	
2020	2.756728660e+6Hz	2.756728	2.756728	
2030	2.756724895e+6Hz	2.756724	2.756724	
2040	2.756712565e+6Hz	2.756712	2.756712	
2050	2.756705554e+6Hz	2.756705	2.756705	
2060	2.756702457e+6Hz	2.756702	2.756702	
2070	2.756702033e+6Hz	2.756702	2.756702	
2080	2.756701630e+6Hz	2.756701	2.756701	
2090	2.756699783e+6Hz	2.756699	2.756699	
2100	2.756702497e+6Hz	2.756702	2.756702	
2110	2.756698919e+6Hz	2.756698	2.756698	
2120	2.756761829e+6Hz	2.756761	2.756761	
2130	2.756811828e+6Hz	2.756811	2.756811	**300 µg Added**
2140	2.756594017e+6Hz	2.756594	2.756594	
2150	2.756302031e+6Hz	2.756302	2.756302	366
2160	2.756228929e+6Hz	2.756228	2.756228	92
2170	2.756210273e+6Hz	2.756210	2.756210	44
2180	2.756184904e+6Hz	2.756184	2.756184	33
2190	2.756177217e+6Hz	2.756177	2.756177	23
2200	2.756161519e+6Hz	2.756161	2.756161	31
2210	2.756146541e+6Hz	2.756146	2.756146	33
2220	2.756128398e+6Hz	2.756128	2.756128	28
2230	2.756118313e+6Hz	2.756118	2.756118	25
2240	2.756103874e+6Hz	2.756103	2.756103	36
2250	2.756082445e+6Hz	2.756082	2.756082	
2260	2.756073673e+6Hz	2.756073	2.756073	
2270	2.756071635e+6Hz	2.756071	2.756071	
2280	2.756048419e+6Hz	2.756048	2.756048	

Appendix 10

Time (Sec)	Actual Reading Output frequency (MHz)	f_x	Frequency Number	Δf
2290	2.756346013e+6Hz	2.756346	2.756346	
2300	2.756520930e+6Hz	2.756520	2.756520	
2310	2.756528746e+6Hz	2.756528	2.756528	
2320	2.756529697e+6Hz	2.756529	2.756529	
2330	2.756534773e+6Hz	2.756534	2.756534	
2340	2.756540784e+6Hz	2.756540	2.756540	
2350	2.756616864e+6Hz	2.756616	2.756616	
2360	2.756683516e+6Hz	2.756683	2.756683	
2370	2.756677705e+6Hz	2.756677	2.756677	
2380	2.756671376e+6Hz	2.756671	2.756671	
2390	2.756656420e+6Hz	2.756656	2.756656	
2400	2.756647742e+6Hz	2.756647	2.756647	
2410	2.756639282e+6Hz	2.756639	2.756639	
2420	2.756627591e+6Hz	2.756627	2.756627	
2430	2.756622265e+6Hz	2.756622	2.756622	
2440	2.756608862e+6Hz	2.756608	2.756608	
2450	2.756610126e+6Hz	2.756610	2.756610	
2460	2.756604389e+6Hz	2.756604	2.756604	
2470	2.756594202e+6Hz	2.756594	2.756594	
2480	2.756586723e+6Hz	2.756586	2.756586	
2490	2.756573210e+6Hz	2.756573	2.756573	
2500	2.756566092e+6Hz	2.756566	2.756566	
2510	2.756554256e+6Hz	2.756554	2.756554	
2520	2.756547922e+6Hz	2.756547	2.756547	
2530	2.756542649e+6Hz	2.756542	2.756542	
2540	2.756525889e+6Hz	2.756525	2.756525	
2550	2.756524698e+6Hz	2.756524	2.756524	
2560	2.756518541e+6Hz	2.756518	2.756518	
2570	2.756514989e+6Hz	2.756514	2.756514	
2580	2.756525040e+6Hz	2.756525	2.756525	
2590	2.756519684e+6Hz	2.756519	2.756519	
2600	2.756524225e+6Hz	2.756524	2.756524	
2610	2.756535005e+6Hz	2.756535	2.756535	**90 µg Added**
2620	2.756480833e+6Hz	2.756480	2.756480	
2630	2.756339187e+6Hz	2.756339	2.756339	141
2640	2.756341939e+6Hz	2.756341	2.756341	21
2650	2.756320193e+6Hz	2.756320	2.756320	29
2660	2.756312930e+6Hz	2.756312	2.756312	8
2670	2.756313602e+6Hz	2.756313	2.756313	0
2680	2.756329173e+6Hz	2.756329	2.756329	56
2690	2.756369932e+6Hz	2.756369	2.756369	40
2700	2.756369019e+6Hz	2.756369	2.756369	16
2710	2.756353185e+6Hz	2.756353	2.756353	19
2720	2.756350835e+6Hz	2.756350	2.756350	7
2730	2.756346837e+6Hz	2.756346	2.756346	16
2740	2.756334446e+6Hz	2.756334	2.756334	
2750	2.756324453e+6Hz	2.756324	2.756324	
2760	2.756313186e+6Hz	2.756313	2.756313	
2770	2.756297879e+6Hz	2.756297	2.756297	
2780	2.756627129e+6Hz	2.756627	2.756627	
2790	2.756631484e+6Hz	2.756631	2.756631	
2800	2.756640285e+6Hz	2.756640	2.756640	
2810	2.756667281e+6Hz	2.756667	2.756667	
2820	2.756650131e+6Hz	2.756650	2.756650	
2830	2.756642758e+6Hz	2.756642	2.756642	
2840	2.756645611e+6Hz	2.756645	2.756645	
2850	2.756644511e+6Hz	2.756644	2.756644	
2860	2.756640940e+6Hz	2.756640	2.756640	
2870	2.756637280e+6Hz	2.756637	2.756637	
2880	2.756642496e+6Hz	2.756642	2.756642	
2890	2.756644080e+6Hz	2.756644	2.756644	
2900	2.756650446e+6Hz	2.756650	2.756650	
2910	2.756655078e+6Hz	2.756655	2.756655	
2920	2.756657226e+6Hz	2.756657	2.756657	

The third Column (f_x) is the function for changing the output reading format (2nd Column) to number and the 4th column is the output frequency in the number format with 6 digits.

The last column is the frequency difference between output without sample and the output after applying the sample. The rolling average method is used here between every 30 seconds (3 readings) and the highest value is considered as a Δf.